


GIDL: GENERALIZED INTERFERENCE DETECTION AND LOCALIZATION SYSTEM

A DISSERTATION
SUBMITTED TO THE DEPARTMENT OF AERONAUTICS AND ASTRONAUTICS
AND THE COMMITTEE ON GRADUATE STUDIES
OF STANFORD UNIVERSITY
IN PARTIAL FULFILLMENT OF THE REQUIREMENTS
FOR THE DEGREE OF
DOCTOR OF PHILOSOPHY

Konstantin G. Gromov
March 2002

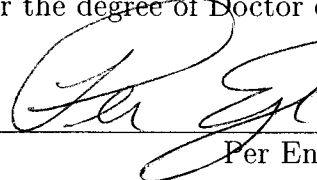
© Copyright 2002
by
Konstantin G. Gromov

I certify that I have read this dissertation and that in my opinion it is fully adequate, in scope and in quality, as a dissertation for the degree of Doctor of Philosophy.



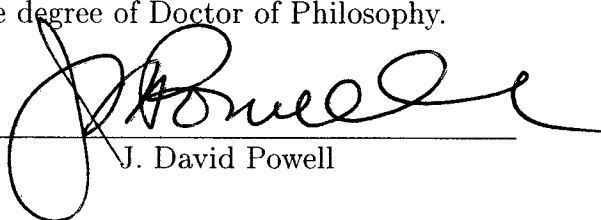
Bradford W. Parkinson
(Principal Advisor)

I certify that I have read this dissertation and that in my opinion it is fully adequate, in scope and in quality, as a dissertation for the degree of Doctor of Philosophy.



Per Enge

I certify that I have read this dissertation and that in my opinion it is fully adequate, in scope and in quality, as a dissertation for the degree of Doctor of Philosophy.



J. David Powell

Approved for the University Committee on Graduate Studies:

Dean of Graduate Studies

}

Abstract

The Local Area Augmentation System (LAAS) and the Wide Area Augmentation System (WAAS) are being developed by the U.S. Federal Aviation Administration (FAA) to provide satellite navigation performance compliant with the stringent requirements for aircraft precision approach and landing. A primary design goal of both systems is to insure that signal-in-space failures are detected by ground facilities and to exclude the affected measurements before differential corrections are broadcast to users. One such failure is unintentional interference or intentional jamming in the GPS frequency band. To protect integrity, LAAS and WAAS ground facilities must quickly detect the presence of any hazardous interference falling within the restricted band used by GPS. To protect availability, ground personnel must be able to quickly locate and deactivate the interference source.

In order to serve this purpose, the prototype Generalized Interference Detection and Localization System (GIDL) has been developed. This prototype includes four antennae and RF sections slaved to a common clock to allow detection and determination of a three-dimensional interference location. Measurements of differential signal propagation delays across the multiple baselines between the GIDL antennae are combined to estimate the location of the undesired interference transmitter. The GIDL system can be implemented in parallel with a three- or four-receiver LAAS ground facility (sharing components with the LAAS reference receivers and processors) or as a separate installation to support nearby LAAS and WAAS sites.

This dissertation describes the GIDL theory and GIDL receiver design and derives theoretical predictions of the ability of the GIDL to accurately locate interference sources. The GIDL System has been successfully demonstrated to the Federal Aviation Administration (FAA).

}

Acknowledgments

I would like to thank my advisor, Professor Bradford W. Parkinson, for providing me with the freedom and latitude to pursue this research. His technical insight and management skills have been a great source of inspiration to me. Additionally, his skills as a teacher, advisor, and mentor are much appreciated. I would also like to thank Professor Per Enge for always making time to provide me with his technical expertise and guidance, which helped me to overcome difficulties in the past years. I thank my defense and reading committees, including Professor J. David Powell, Professor J. Christian Gerdes and Dr. Sam Pullen.

I would like to thank Dr. Boris Pervan, Dr. Dennis Akos, and Dr. Todd Walter for all their comments, discussions, guidance and time which they have provided me. All the members of the Stanford GPS, LAAS and WAAS Laboratories are greatly appreciated for their friendship, support, and team work. I appreciate very much all the support and help which I got from various people during my years at Stanford University. The help of Sally Gressens at the Aero Astro Student offices was instrumental in getting through all official procedures, applications, etc. I would like to express my appreciation to Fiona Walter for her thorough reading and editing of my thesis drafts and for her suggestions and comments on my writing.

Funding for this research was provided by the Satellite Program Office of the Federal Aviation Administration. I am very grateful for this support. Without it this project probably would not have happened.

The Department of Aeronautics and Astronautics and Stanford University are gratefully acknowledged for establishing the best environment for the pursuit of graduate studies.

I also want to thank my parents, Ludmila and Gennadiy Gromov for their support and encouragement.

Last but not least, I would like to express my highest respect and appreciation to my friend, Irene.

Contents

Abstract	v
Acknowledgments	vii
1 Introduction	1
1.1 Motivation	2
1.2 Background	5
1.2.1 Navigation Requirements and Terminology for Precision Landing .	5
1.2.2 Overview of GPS and GPS-Based Systems	8
1.2.3 Interference Threats to GPS, LAAS and WAAS (Overview)	14
1.3 Previous Interference Detection and Localization Work	15
1.3.1 Multisite Radar Systems (MSRS)	17
1.3.2 Passive Localization and Signal Processing	20
1.3.3 Hyperbolic Navigation Systems	23
1.3.4 GPS Receiver and Interference Detection	24
1.3.5 Software Radio	25
1.3.6 Current Research or Competitors	26
1.4 Contributions	28
1.5 Notes on Terminology	30
1.6 Dissertation Outline	31

2	GIDL Concepts and Theory	33
2.1	Simplified GIDL Concept	34
2.2	Jammer Detection	35
2.2.1	Signal and Interference Model Formulation	36
2.2.2	Criteria for Optimum Signal Detection in GIDL	42
2.2.3	Detection of Stochastic Signals	47
2.3	Jammer Localization	55
2.3.1	Jammer Position and Velocity Measurement Methods. One-Stage And Two-Stage Algorithms	55
2.3.2	One-Stage Optimum Coordinate Measurement In GIDL Using Tem- poral Signal Parameters	57
2.3.3	Signal TDOA Measurement For Two-Stage Radiation Source Lo- calization By GIDL	61
2.3.4	Maximum Attainable Accuracy of Maximum Likelihood Estimates of Informative Parameters	67
2.3.5	Maximum Attainable Estimation Accuracy of Signal TDOAs in GIDL	72
2.4	Resultant Jammer Coordinate Measurement Using Two-Stage Algorithms .	77
2.4.1	Resultant Coordinate Measurement Formation	77
2.4.2	Examples of Two-Stage Algorithm Applications to Jammer Coor- dinate Estimation	84
2.5	Range and Coverage of GIDL System	89
2.5.1	Reference Jammer	101
2.6	Expected GIDL Performance	101
3	GIDL Hardware Design	107
3.1	Software Radio Concept	108
3.1.1	Introduction	108
3.1.2	Front End Configuration	108
3.1.3	Software Signal Processing	111
3.1.4	GIDL Front End Design	112

3.2	GIDL Hardware Philosophy	117
3.3	GIDL Realization	118
3.3.1	GIDL Hardware Concept	118
3.3.2	GIDL Frequency Plan	118
3.3.3	GIDL Construction	121
3.4	GIDL Display Software	129
3.5	Construction of an Experimental GPS Jammer	129
4	Software Radio and GIDL System Calibration	133
4.1	Introduction	133
4.2	GPS Signal Structure	134
4.3	GPS Software Signal Processing	135
4.3.1	Spread Spectrum Signal Acquisition	136
4.3.2	Acquisition Via Parallel Code Phase Search	137
4.4	System Calibration Using GPS Signals	139
4.5	Experimental Results of System Calibration	145
5	GIDL Implementation	151
5.1	Introduction To Implementation Details	151
5.2	Data flow in GIDL	151
5.3	Implemented algorithms and assumptions	153
5.4	Calibration by GPS in detail	154
5.4.1	Initial Search of Frequency/Time space for presence of GPS Signal	157
5.4.2	Detection of the GPS data bit flips in the collected data	162
5.4.3	Carrier frequency calculation and master clock calibration	166
5.4.4	Precise PR estimation and differential delay calculation	168
5.4.5	Calibration Coefficient Calculation	172
5.5	Jammer Detection and TDOA Estimation	173
5.5.1	Jammer Detection	173
5.5.2	Jammer Signal TDOA Estimation	173
5.6	Why GIDL needs a 12-bit ADC	179

6	Experimental Setup and Results	183
6.1	Cable Experiments	183
6.2	Roof-Top Experiments	189
6.3	Experimental Setup for Full GIDL System Test	193
6.4	Data Collection and Demonstration Modes	198
6.5	Experimental Results of Jammer Localization	199
7	GIDL Applications	211
7.1	Applications to LAAS	211
7.2	Aircraft Application	212
7.3	Other Applications	213
7.4	GIDL Hardware as a Flexible Research Platform	213
7.4.1	Experiment on Aided GPS Signal Detection	213
7.4.2	SQM Application	214
7.4.3	Modifications for Multiple Frequencies	215
7.4.4	Experiments With New GPS Signals	215
8	Conclusions and Future Work	217
8.1	Specific Contributions	218
8.2	Recommendations for Future Research	219
8.2.1	Short Baseline System to Mitigate CW Interference	219
8.2.2	Distributed GIDL System Concept	220
8.2.3	Incorporation into Integrity Monitoring Testbed	222
8.2.4	Test on Various Single Jammers	222
8.2.5	Test on Multiple Jammers	222
8.2.6	Optimization of Algorithms	222
8.3	Summary	223
A	Glossary	225
	Bibliography	231

List of Tables

1.1	ILS Signal-in-Space Specifications	7
6.1	Results of the Experiment Performed October 18, 2000. Azimuth and Range Referenced to Antenna 0; Measured values are mean and standard deviation of 50 runs for each jammer location.	200
6.2	Uncalibrated Jammer Localization in Demonstration Mode During First GIDL Experiment at Lake Lagunita	207
6.3	Uncalibrated Jammer Localization in Demonstration Mode During Second GIDL Experiment at lake Lagunita	208

}

List of Figures

1.1	Receiver Jamming Test Results	4
1.2	The Global Positioning System (GPS)	9
1.3	Constellation of the GPS Satellites around the Earth	9
1.4	GPS Signal Power	11
1.5	Local Area Augmentation System	12
1.6	Prior Art: Overview	16
1.7	(Passive) Radar	17
1.8	NAVSPASUR West	18
1.9	NAVSPASUR East	18
1.10	NAVSPASUR Antenna	19
1.11	One Step Processing or Filtered Beamformer	21
1.12	Two Step Processing or Multiplier-Correlator TDOA(RD) Estimator	21
2.1	Simplified GIDL Concepts	34
2.2	Structure of the optimum detector for stochastic signals with a known correlation (covariance) matrix	50
2.3	Detection characteristics of the optimum detector for stochastic signals with known correlation matrix, $P_{fa} = 10^{-4}$ and n : 10^3 and 10^4	54
2.4	Algorithm Classification	56
2.5	Configuration of the GIDL for Examples	85
2.6	Single Baseline System	91
2.7	-51 dBW/MHz Jammer Range and GIDL Coverage with 100m Baselines	94
2.8	“Star Antenna” Configuration for Analysis	95

2.9	Maximum Range and Coverage of the GIDL System With Baselines 12 m and 100 m and Star Configuration for Jammers of Various Powers (red circles are GIDL antenna locations and effective jammer range is not shown)	96
2.10	6 dB Difference in Antenna Gain Corresponds to x2 Improvement in Range	96
2.11	Error Ellipses for Constant Power Jammer: -33dBW/MHz	98
2.12	Error Ellipses for Constant Power Jammer: -43dBW/MHz	99
2.13	Error Ellipses for Constant Power Jammer: -53dBW/MHz	100
2.14	Effective Jammer Range and Expected GIDL Coverage	102
2.15	TDOA Jammer Localization. SOP (Hyperbolas) and Error boundaries ($\pm 0.7\text{m}$).	103
2.16	TDOA Jammer Localization. SOP (Hyperbolas) and Error boundaries ($\pm 0.7\text{m}$), Zoomed.	104
2.17	Expected GIDL Performance: Error Ellipses for the GIDL Setup	105
2.18	Expected GIDL Performance: Expected Variations of the Errors	106
3.1	Typical Front End Implementation	109
3.2	Software Radio Direct Digitization Front End Implementation	110
3.3	Frequency Domain Depiction of the Various Output Stages of a Bandpass Sampling Front End	116
3.4	GIDL Realization Concept	119
3.5	GIDL Frequency Plan: Analog Mixing	119
3.6	GIDL Frequency Plan: Sampling With Aliasing	120
3.7	Front, Back, and Gain Controller of GIDL Receiver	122
3.8	RF and IF Sections of the GIDL Receiver	122
3.9	Clock and Power Sections of the GIDL Receiver	123
3.10	Diagram of GIDL Hardware Setup	123
3.11	Reference Oscillator and System Clock Diagram	124
3.12	Diagram of RF Section and ADC	124
3.13	Complete Block Diagram of the Built GIDL Receiver	125
3.14	ICS-650 Two channel ADC Board Block Diagram	127
3.15	ICS-650 Two Channel ADC board Specifications	128
3.16	Real-Time GIDL Display Software (Simulation)	130

3.17	-70 dBW/MHz Interference Source	131
4.1	Parallel PRN Code Phase Search Acquisition Block Diagram	138
4.2	GIDL Calibration Setup	139
4.3	Pseudorange and Doppler Frequency Estimation Process	141
4.4	GPS Signal Detection: Correlation of 1 ms of GPS signal with Spectrum of Reconstructed Carrier from 1 ms	142
4.5	Spectrum of Reconstructed GPS Carrier from 12 ms of Data	143
4.6	GPS Correlation peak for PRN 6 obtained from 13 ms of data	144
4.7	GIDL Calibration: Results of Clock and Delay Calibration	147
4.8	GIDL Calibration: Results for Data Runs 1—15; Number of SVs per Each Run: 5 5 4 4 4 6 6 5 5 4 5 5 4 4 4	148
4.9	GIDL Calibration: Results for the 20 Data Runs	149
5.1	Data flow in GIDL System	152
5.2	Calibration by GPS: overview of the process	155
5.3	Calculation of SV Doppler frequency and expected propagation delay	156
5.4	Process of initial "1 ms" search for correlation	157
5.5	MATLAB code to search 1(2) ms of data for Doppler frequency and C/A code offset	158
5.6	Correlation and Circular correlation	160
5.7	MATLAB code to detect data bit flips occurrence in the data	163
5.8	Typical complex correlation peaks for data bit flips detection	164
5.9	MATLAB Code to find master clock offset, and all relevant frequencies	165
5.10	Precise pseudorange estimation	169
5.11	Correlation peaks and normalized maximums for the fine C/A code delay search	171
5.12	Calibration coefficient calculation	172
5.13	PSD of the signal in the absence and presence of the jammer	174
5.14	Process of the TDOA estimation for jamming signal	175
5.15	MATLAB code to estimate jammer signal TDOAs for each baseline	176
5.16	Various stages of the obtaining jammer correlation	177

5.17	MATLAB code to calibrate TDOAs and find jammer location	180
6.1	Experimental Setup for Cable Experiment	184
6.2	Correlation of the first and second channel data for experiment with 50 ft cable. Horizontal axis shows number of samples from the beginning of data set, and vertical axis shows amplitude of the correlation peaks in internal (relative) units.	185
6.3	Scaled correlation of the first and second channel data for experiment with 50 ft cable. Horizontal axis shows number of samples from the beginning of data set, and vertical axis shows scaled amplitude of the correlation peaks such that maximum is equal to one.	187
6.4	Scaled correlation of the first and second channel data for experiment with 4 ft cable. Horizontal axis shows number of samples from the beginning of data set, and vertical axis shows scaled amplitude of the correlation peaks such that maximum is equal to one.	188
6.5	Rooftop Test Range 1	189
6.6	Rooftop Test Range 2	190
6.7	Plot of the Results from the Roof Experiments (1–5 m results are good, 6–11 m results are severely affected by multipath)	191
6.8	Summary of the Results from the Roof Experiments	192
6.9	Summary of the Results from the Roof Experiments in Graph Form	192
6.10	GIDL Receive Antenna and Experimental Jammer	194
6.11	GIDL Experimental Setups on Lake Lagunita; A0, A1, A2, A3—GIDL Antenna Locations; J1, J2, J3—Surveyed Locations of the Jammer; Obs.—Direction Finder (Observer) Location	196
6.12	Optical Direction Finder, Used for Independent Jammer Azimuth Verification	197
6.13	GIDL base station (GIDL receiver, processing computer, etc.) was located in the bed of HEPL truck during experiments at Lake Lagunita	198
6.14	Jammer localization results on October 18, 2000, with jammer at location 1, summary of 50 independent experiments	201

6.15	Jammer localization results on October 18, 2000, with jammer at location 1, summary of 50 independent experiments (zoomed)	202
6.16	Jammer localization results on October 18, 2000, with jammer at location 2, summary of 50 independent experiments	203
6.17	Jammer localization results on October 18, 2000, with jammer at location 2, summary of 50 independent experiments (zoomed)	204
6.18	Jammer localization results on October 18, 2000, with jammer at location 3, summary of 50 independent experiments	205
6.19	Jammer localization results on October 18, 2000, with jammer at location 3, summary of 50 independent experiments (zoomed)	206
6.20	Results of the Experiment Performed October 18, 2000. Surveyed (red \times) and GIDL measured mean location (green \square) for each jammer with corresponding $\pm 1\sigma$ error bars.	207
6.21	Uncalibrated Jammer Localization in Demonstration Mode During First GIDL Experiment at Lake Lagunita. Surveyed (red \times) and GIDL measured location (green \square) for each jammer.	208
6.22	Uncalibrated Jammer Localization in Demonstration Mode During Second GIDL Experiment at lake Lagunita. Surveyed (red \times) and GIDL measured location (green \square) for each jammer.	208
8.1	Distributed GIDL System	220

}

Chapter 1

Introduction

Development and completion of the Global Positioning System (GPS) was the most significant navigational achievement of the 20th century. GPS allows users to know their location anywhere on Earth thereby opening up multiple possibilities for various applications. One of the applications of GPS navigation is aviation. It has been shown that GPS can be seamlessly used for en-route navigation and landing of airplanes.

There are two systems currently under development for this purpose: the Local Area Augmentation System (LAAS), which primarily targets precision navigation for landing, and the Wide Area Augmentation System (WAAS), which can be used for en-route navigation and non-precision approaches.

Along with these GPS opportunities come some problems associated with GPS signals. GPS signals are very weak and can be easily jammed by unintentional or intentional interference. A solution to this problem is needed. Various approaches to the solution of this problem can be taken: implementation of more robust signal processing algorithms; development of adaptive antennae with null steering; or timely localization and mitigation of the source of interference. This thesis addresses the last issue: finding and locating sources of GPS interference.

When GPS was invented, it was designed to be a military system, with only partial utility for civilians. It actually was anticipated that at some point in time the system would be jammed. However, civilians are now the primary GPS users and lengthy outages due to jamming is unacceptable for airplane users. Thus, another part of the system must be

developed and tested, such that a jammer (hostile signal) presence is both detected and located. This thesis proposes a solution to this problem.

At Stanford University, ongoing effort focuses on research, development, implementation, and testing of LAAS architectures and architecture subsystems. This thesis advances the development of the GIDL receiver and algorithms as an adjunct to the Stanford LAAS prototype.

Since source localization has been studied almost since the invention of the radio, there are a significant number of algorithms which could be used in the GIDL system. Several ways to implement interference source localization are interferometry, time-of-arrival differential system, spatial spectrum estimation, phased antenna array, etc. The majority of this work concentrates on the interferometric, or time-of-arrival, techniques. Analysis and experimental results are included in this thesis.

This work examined possible theoretical solutions to jammer or interferer localization problems, chose the subset of the most interesting solutions, and then developed experimental hardware allowing implementation of these algorithms. Upon completion of the hardware and algorithm development, the prototype system was successfully field tested for the Federal Aviation Administration (FAA).

During the field test, this prototype GIDL was set up at Lake Lagunita on the Stanford campus, along with a conventional optical direction finder. The interference source was placed in various locations in the dry lake bed. The GIDL reported locations of the source, as well as direction to the source from the location of the optical direction finder. GIDL's reported directions and optically observed directions were the same. Mr. Carl McCullough, Director of the FAA's Office of Communications, Navigation and Surveillance Systems was present at the demonstration. He was completely satisfied with the system performance.

1.1 Motivation

Modern society seeks more and more accurate navigation solutions to fulfill its needs. These methods of navigation must not only be accurate but also reliable due to continuously decreasing tolerance of failures, delays and costs in such systems. Recently, the

Federal Aviation Administration (FAA) announced their “zero accidents” policy, which requires airlines to have perfect navigation from takeoff to landing. The same could be said about modern construction workers, which have to know where to build or dig precisely, to avoid interference with existing communications or structures. Farmers and their machinery can utilize precise navigation to operate farm equipment automatically in bad visibility conditions or at night, or to do precision farming, when the exact location of various soils must be noted. Over time these and other applications will demand additional reliable navigation technology.

During the last twenty years, the Global Positioning System (GPS) has revolutionized the field of navigation. At almost any time, in any weather, anywhere on Earth, a receiver can obtain signals from at least four of the GPS satellites and then compute its position. This was unthinkable prior to the development of GPS.

The application of GPS to commercial aviation has been especially alluring in recent years by providing seamless satellite navigation from takeoff to touchdown. While these are very exciting possibilities, some technical challenges still exist. The GPS Risk Assessment Study [1] by the Applied Physics Laboratory at John Hopkins University stated that there are only two significant GPS risks to the GPS based aircraft navigation and guidance systems: interference and ionosphere propagation effects. In response, the central focus of this research has been to study various algorithms and techniques of interference detection and localization, to build experimental hardware which could be used to test the algorithms and techniques, and to demonstrate localization of an interference source in real time.

An interference source can disrupt an airplane’s ability to safely navigate or land. Additionally, navigation outages due to interference are also costly and disrupt normal airport and aircraft operations. Therefore, it is necessary to stop an interference source in real time, or as fast as it is practically possible.

To protect GPS based systems from jamming, to reduce outage time, to improve availability, and to quickly and accurately locate interference sources some sort of interference detection and localization system is needed. In technical terms, this means improvement in system availability and reduction of outage duration. (see Section 1.2.1 for a complete definition of these terms).

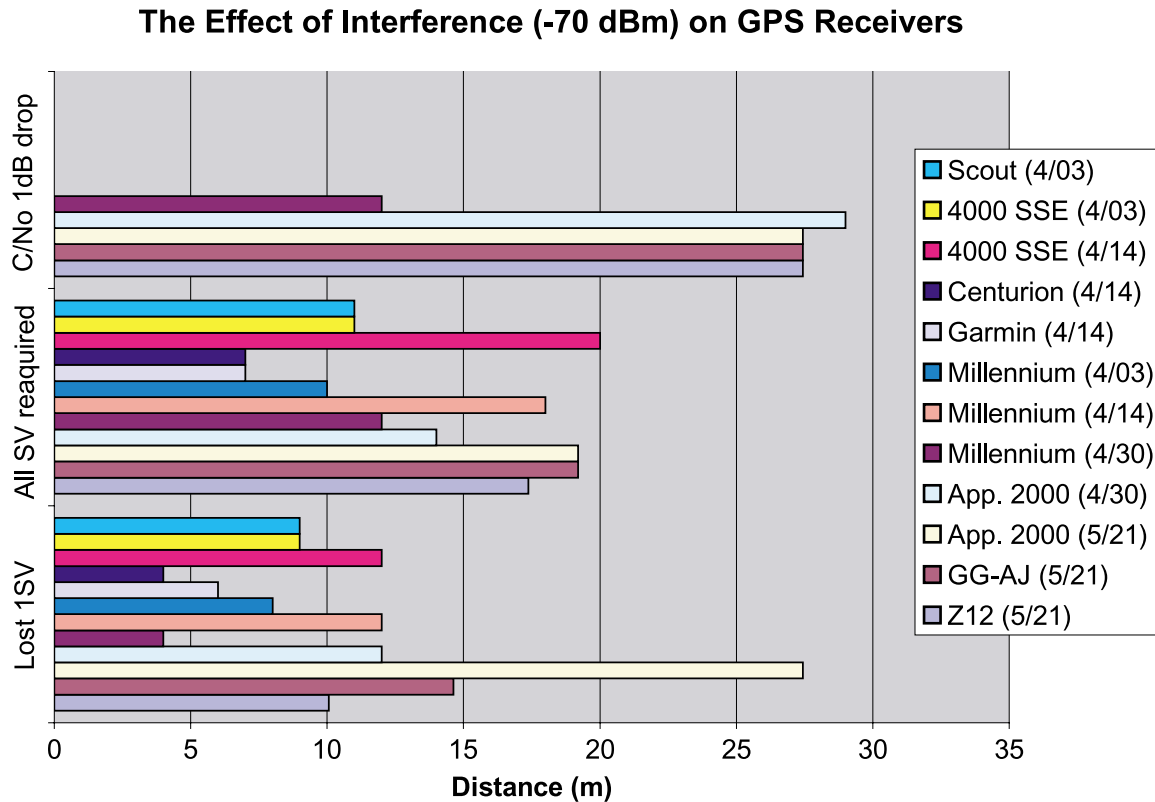


Figure 1.1: Receiver Jamming Test Results

A number of GPS receivers have been tested with regard to susceptibility to interference in order to provide a bench mark on the range of a jammer.

The interference source used for the testing is a white noise source with power of -70 dBW/MHz. Experimental results are summarized in Figure 1.1. In this test, the interference source was moved closer to the receiver, and the jammer locations at which the first satellite and all satellites were lost were recorded. Then, the jammer was moved away from the receiver, and the range at which all satellites were reacquired was recorded. These results show that at a range of about 10 meters, this specific jammer becomes a threat. These results scale to a jammer of a different power, proportionally to the square root of the jammer power (see Section 2.5.1), and provide further confirmation of the need for an interference detection/localization subsystem within the current GPS navigation framework. This very weak jammer poses a threat to GPS-based aircraft navigation only at ranges

10-25 meters, so it was safe to use it for experiments. But from these data follows (see Section 2.5.1) that jammer with power of 0 dBW/MHz would pose a threat to GPS-based aircraft navigation at ranges 31-80 kilometers!

1.2 Background

This section provides only a brief overview of GPS, GPS-based systems, and jammer localization concepts. Detailed descriptions of these concepts can be found in [2, 3, 4, 5, 6, 7] and a multitude of other books and articles which have been published about GPS. The actual government specification for the GPS signal format is known as ICD-200 [8]. Good sources for up-to-date information on GPS and GPS related subjects are the journal, *NAVIGATION*, and proceedings of ION GPS conferences. Additionally, this section also provides definitions for system metrics and FAA landing requirements necessary for use in the remainder of the thesis.

1.2.1 Navigation Requirements and Terminology for Precision Landing

Traditionally, the overall quality and utility of a given navigation and guidance system for aircraft precision approach and landing (both ground facilities and aircraft hardware) has been rated according to a three-tiered structure based on minimum achievable altitude [9]. The tiers, or categories, are as follows [9]:

Category I. If the horizontal visibility on the runway, known as Runway Visual Range (RVR), is greater than 2400 ft, a *Category I* navigation and guidance system may deliver an aircraft down to a decision height (DH) of 200 ft. If the pilot is unable to see the runway at the DH, a missed approach must be executed.

Category II. If RVR is greater than 1200 ft, a *Category II* navigation and guidance system may deliver an aircraft down to a DH of 100 ft. Again, if

the pilot is unable to see the runway at the DH, a missed approach must be executed.

Category III. While *Category III* ground facilities are generally designed for automatic landing, some variability is allowed, depending on the quality of the specific ground installation and the degree of fault tolerance (via redundant avionics) of the onboard guidance system. Thus, three sub-classes of *Category III* systems are possible:

- *Cat. IIIa.* Ranges from $DH > 50$ ft and $RVR > 700$ ft to automatic landing.
- *Cat. IIIb.* Automatic landing and rollout.
- *Cat. IIIc.* Automatic landing, rollout and taxi.

Four fundamental parameters provide the bases for allocation of specific requirements for Category I, II, and III navigation systems [10, 11]. These metrics are each affected by signal interference.

Accuracy. Accuracy is the measure of the navigation output deviation from truth under fault-free conditions—often specified in terms of 95% performance.

Integrity. Integrity is the ability of a system to provide timely warnings to users when the system should not be used for navigation. *Integrity risk* is the probability of an undetected navigation system error or failure that results in hazardously misleading information (HMI) onboard the aircraft.

Continuity. Continuity is the likelihood that the navigation signal-in-space supports accuracy and integrity requirements for the duration of the intended operation. *Continuity risk* is the probability of a detected but unscheduled navigation function interruption after an approach has been initiated.

Availability. Availability is the fraction of time the navigation function is usable (as determined by its compliance with the accuracy, integrity, and continuity requirements) before the approach is initiated.

	Vertical Accuracy at DH — 95 % ft	Integrity Risk (per approach)	Continuity Risk (per 15 sec)
Category I	14.5	—	—
Category II	6.1	10^{-7}	4×10^{-6}
Category III	2.1 (50 ft DH)	0.5×10^{-9}	2×10^{-6}

Table 1.1: ILS Signal-in-Space Specifications

The International Civil Aviation Organization (ICAO) specifications (95% probability) of the Instrument Landing System (ILS) signal-in-space plus airborne glideslope receiver and the integrity and continuity specifications for ILS signal-in-space only are given in Table 1.1 [12, 13]. For a Category III ILS, the vertical accuracy required is roughly two feet at a 50 ft altitude. This altitude is generally achieved at the runway threshold. At this point, vertical navigation is obtained primarily from a radar altimeter onboard the aircraft. It is also immediately clear from Table 1.1 that for Category II/III navigation, ILS must operate with extremely high integrity and continuity. The *vertical protection limit (VPL)* — the maximum safe (mean) glideslope deviation — for ILS integrity monitoring is roughly equivalent to 1.1 m at the 50 ft DH. In the event of an anomaly which causes this protection limit to be exceeded, the maximum time allowed to alert the aircraft of the condition is 2 sec [12]. In addition, while the actual ILS navigation availability at a single-ILS airport is 99.15%, the desired level of availability for a new navigation aid is at least 99.9% [14].

The ILS specifications, of course, are also representative of the required performance for a given GPS-based navigation system that is intended to replace ILS. The current specifications for LAAS are given in [15]. Table 1.1 (along with a navigation availability guideline of 99.9%) serves to provide a quantitative guideline for current ILS precision landing navigation requirements.

1.2.2 Overview of GPS and GPS-Based Systems

GPS overview

Without the Global Positioning System (GPS), none of the new navigation and landing systems would exist. GPS NAVSTAR has been introduced and developed in the last three decades by the US Department of Defense (DoD). Its primary goal is to provide continuous navigation throughout the globe for the US military. It also happens that the system has a signal available free of charge for civilian use, which provides this same service to the public.

The Global Positioning System (GPS) consists of three segments: the space segment, the control segment, and the user segment, as shown in Figure 1.2. The control segment tracks each satellite and periodically uploads to the satellite its prediction of future satellite positions and satellite clock time corrections. These predictions are then continuously transmitted by the satellite to the user as a part of the navigation message. The space segment consists of 24 satellites, each of which continuously transmits a ranging signal that includes the navigation message stating current position and time correction. The user receiver tracks the ranging signals of selected satellites and calculates three-dimensional position and local time.

The Global Positioning System (GPS), is a passive satellite-based ranging system (see Figure 1.3). Timing of signal travel from spacecraft to user provides the basis for range measurement. The typical user receiver obtains ranges from four (or more) satellites and with knowledge of the spacecraft locations, can solve for the three components of its position and the deviation of its receiver clock from GPS time.

GPS provides global coverage with a nominal 24 space vehicle (SV) constellation¹, in which each SV is continuously broadcasting an L-band signal. The portion of the transmission normally accessible to the civil user is comprised of an L-band carrier modulated with a pseudorandom noise (PRN) code and data stream. A unique PRN code is used for each spacecraft. For a given SV, ranging is based on measuring the offset between the received PRN code phase and an identical code generated internally in the receiver. The

¹There are currently 28 SV's on orbit and being used.

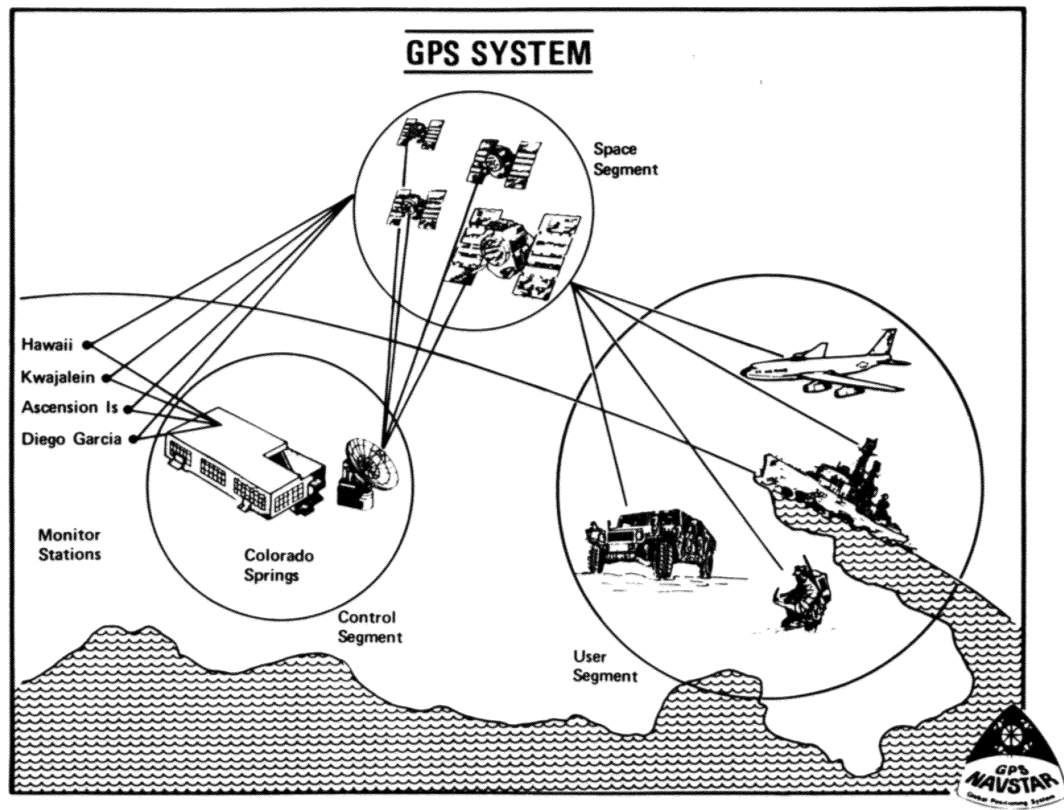


Figure 1.2: The Global Positioning System (GPS)

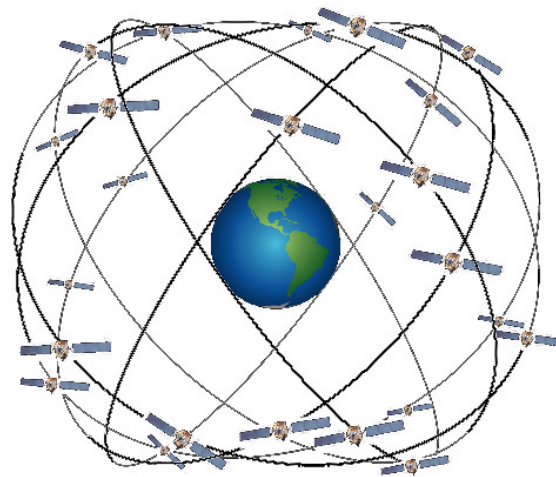


Figure 1.3: Constellation of the GPS Satellites around the Earth

incoming data stream provides the receiver with the necessary information on spacecraft location [16].

Standard single frequency civil GPS positioning accuracy is limited to roughly 10 meters (95% probability) by a number of error sources. Furthermore, although the GPS Operational Control Segment (OCS) does monitor the end-to-end performance of the navigation system, it does not have the means to provide timely (a few seconds) alarms to the user in the event of a satellite or OCS ground segment failure.

The power of GPS signals is also very low, making it susceptible to intentional or unintentional interference or jamming. Such interference or jamming can prevent the user receiver from tracking GPS signals or receiving them properly.

Clearly, GPS civil aviation applications — particularly for precision approach and landing — is contingent upon significant improvements in navigation accuracy, integrity and availability (see Section 1.2.1). Timely detection and localization of the interferer or jammer would improve both system integrity and availability.

GPS Signal Structure, Power Levels and Interference

A brief description of GPS signals is now provided to help better understand the problems associated with such signals.

As mentioned earlier, GPS satellites fly about 20,000 km above the Earth (Figure 1.4). Each of the satellites transmits a spread spectrum signal, with unique spreading sequence, which defines the satellite number. Total power of the transmitted signal is about 30 W. This power is spread in the spectrum domain over 20.46 MHz, and it shines on the whole Earth. In any given location on Earth, the total power of the signal is only -160 dBW. The highest power density of this spread spectrum signal is -220 dBW/Hz, when the nominal background noise level is about -205 dBW/Hz. Thus, the signal lies about 15 dB below the background noise level. To visualize how low GPS power is, think about a 30 W light bulb shining on the whole globe from 20,000 km away.

The GPS spread spectrum signal (Figure 1.4) has a processing gain of about 60 dB, which brings the maximum achievable Signal-to-Noise Ratio (SNR) with respect to the background noise to about 45 dB. In most cases, achievable SNR is less than that maximum. So, if a jamming signal with power 45 dB greater than the noise floor is introduced

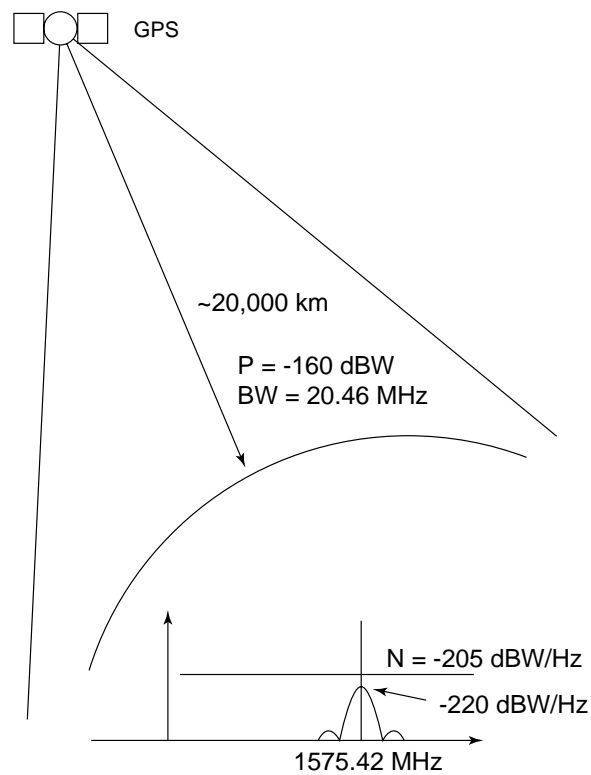


Figure 1.4: GPS Signal Power

in the receiver location, the receiver will be jammed completely. This jamming power corresponds to $-205 + 45 = -160$ dBW/Hz power density. If we integrate jamming power over all GPS frequency bands of 20 MHz (this is more than necessary, it would be enough to have it over 2 MHz in the center of the GPS band) this yields a critical jammer power of -87 dBW, or $2 \cdot 10^{-9}$ W, if it is located right next to the GPS receiver. (For the detailed discussion on the jammer range see Section 2.5 and for the plot of the jammer range depending on the jammer power see Figure 2.14.)

GPS relies on the aforementioned weak signals for all of its navigation measurements. Therefore, these signals must be protected. It has been shown [17] that these signals can be easily jammed by intentional or unintentional interference, out-of-band emissions, communication and broadcast malfunctioning. Intentional jammers are relatively simple and inexpensive (about 100 dollars in parts or less) to build. A jammer of 1W in power would interfere with all signals in the radius of about 100 km [18]. Unintentional jamming of the

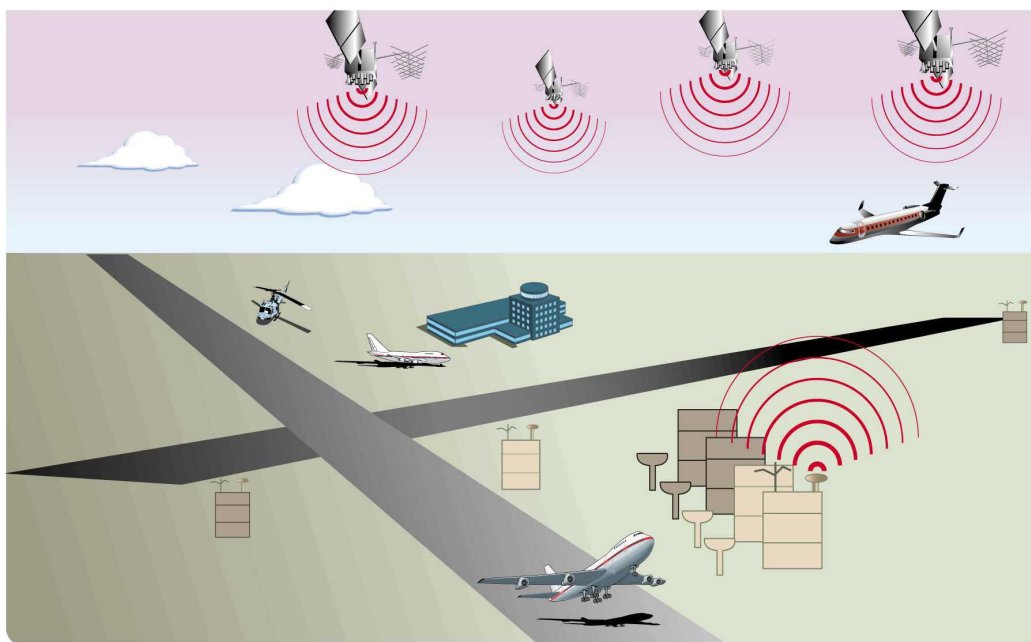


Figure 1.5: Local Area Augmentation System

GPS signals has happened in the past [19].

LAAS overview

GPS is a very convenient and highly precise navigation system but it lacks some characteristics which are necessary for an airplane navigation and landing system. Namely, any airplane navigation system must meet specifications not only in accuracy, but also in continuity, integrity, and availability.

The Local Area Augmentation System (LAAS) is a ground-based differential GPS system being implemented by the Federal Aviation Administration (FAA) for aircraft precision approach and landing (Figure 1.5). LAAS will adequately provide precision approach service for those airports that are not covered by the FAA's Wide Area Augmentation System (WAAS) and is intended to provide Category II and Category III performance in the future [20] (See section 1.2.1 for definitions of Category I, II, and III performance). A primary design goal for LAAS is to insure that failures occurring in the ground or space segments of GPS be eliminated by the ground system before differential corrections are

broadcast to users. One such failure is unintentional interference or intentional jamming in the GPS frequency band. To protect integrity, the ground and air must quickly detect the presence of interference. To protect availability, ground personnel must also be able to locate and disable the interference source. The Generalized Interference Detection and Localization (GIDL) system will be able to assist ground personnel in finding interference sources, by providing estimated locations of any interfering signals that lie outside the tolerable LAAS interference environment (specified in Appendix H of the RTCA LAAS MASPS [21]).

In order to serve this purpose, the GIDL System has been developed. GIDL can improve LAAS availability by accurately estimating the location of the source, and specifically, its direction from the GIDL location. GIDL activities can be implemented in parallel with reference receiver functions and can share components with the reference receivers and processors in LAAS ground stations.

WAAS overview

The Wide Area Augmentation System (WAAS) is a safety-critical system consisting of a signal-in-space plus a ground network to support enroute through precision approach air navigation. It is designed to augment GPS so that it can be used as the primary navigation sensor. The WAAS augments GPS with the following three services: a ranging function, which improves availability and continuity; differential GPS corrections, which improve accuracy; and integrity monitoring, which improves safety. For more detailed description of WAAS see [2].

Other GPS-Based Systems

Due to the quantity of other GPS-based systems, details of these systems are not provided here. For informational purposes, a few are listed here. All these systems or applications would be affected by the presence of a jamming or interfering signal in various ways. Other GPS-based applications include: Land Vehicle Navigation and Tracking; Marine; Air Traffic Control; General Aviation; Surveying; Attitude Determination; Geodesy; Test Range Instrumentation; etc..

1.2.3 Interference Threats to GPS, LAAS and WAAS (Overview)

There are numerous sources of radio frequency interference (RFI) to a GPS receiver. These sources may be on the same vehicle as the receiver, on other vehicles or ground-based. Interference may result from harmonics, intermodulation products of on-board electronic devices, direct continuous wave (CW) and broad/narrow band noise RFI emissions that may fall within the GPS L1 band (1563 to 1587 MHz). This section presents an overview of the different possible interference classifications.

Classification of Interference

Depending on its bandwidth, RFI can be classified as broadband, narrow band or continuous wave (CW). Interference may also be pulsed (gated on/off) or continuous.

Narrowband Interference: Narrowband interference is modeled as a pure tone RFI, consisting of a continuous wave (CW), at a specified frequency. When the frequency of CW interference coincides with that of a GPS signal, it is described as being coherent. Non-coherent CW interference does not coincide with any spectral line of the GPS signal.

Broadband Interference: Broadband interference and thermal noise have a flat power spectral density over a wide range of frequencies, specifically including the GPS L1 band, 1563 through 1587 MHz. This type of interference can be modelled as Additive White Gaussian Noise (AWGN).

Pulsed Interference: Pulsed interference is present only a fraction of the time. It is therefore characterized by a pulse duty cycle, i.e., the fraction of time which the pulse is on, pulse repetition rate or pulse width, and peak power. This type of interference can be broadband or CW pulses.

Sources of Interference to GPS

One source for interference to GPS receivers is radios using the civil aviation band, 118 MHz to 136 MHz. This band, within the very high frequency (VHF) range spanning 30 MHz to

300 MHz, is set aside for air to ground voice and data communication. Civil aviation VHF voice bands consist of 25 kHz channels. The 12th and 13th harmonics of several 25 kHz bands fall directly within the GPS spectrum. For example, the 12th harmonic of the VHF channel 131.25 MHz = 12×131.25 MHz = 1575 MHz, the center of the GPS L1 spectrum. The 13th harmonics of the channels 121.150, 121.175 and 121.200 MHz also fall within the GPS band [22, 23].

Another potential source of GPS interference comes from the introduction of High Definition Television (HDTV). HDTV is a new TV standard currently being adopted by the FCC, which will transmit wide screen video and audio at resolutions up to five times greater than current television. Since the signals are digital, HDTV transmitters will not have to maintain the stringent out-of-band signal suppression currently used by analog TV. The current FCC minimum requirements for TV out-of-band signal suppression will be inadequate to prevent significant HDTV interference to GPS.

Other sources of interference include pulsed radar signals, improperly filtered TV signals, and accidental transmissions by radio frequency (RF) experimenters, etc.

1.3 Previous Interference Detection and Localization Work

This work is based on previous results from the areas of parameter estimation, passive localization, hyperbolic navigation systems, nonlinear optimization, and digital signal processing. The parameter estimation and nonlinear optimization results are fairly classical in nature, and reviewed as needed; the other areas are reviewed in this section.

A simple diagram on how GIDL is related to and based upon different fields of knowledge and previous work is shown in Figure 1.6. GIDL theory combines and uses ideas from several not quite overlapping areas of knowledge: GPS, advanced signal processing, interference detection, Multisite Radar Systems (MSRS), adaptive antenna arrays, beamforming and null steering, RF and microwave engineering, signal source localization from moving platform, etc. The most important of these supporting disciplines are now introduced.

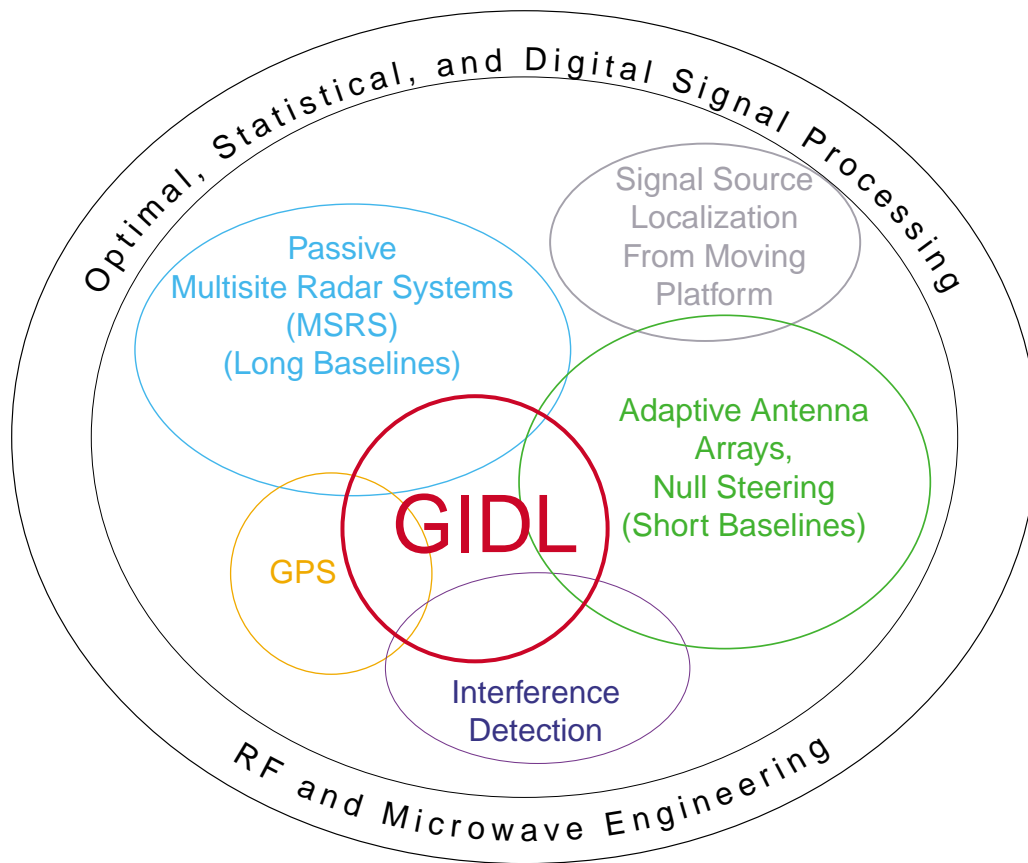


Figure 1.6: Prior Art: Overview

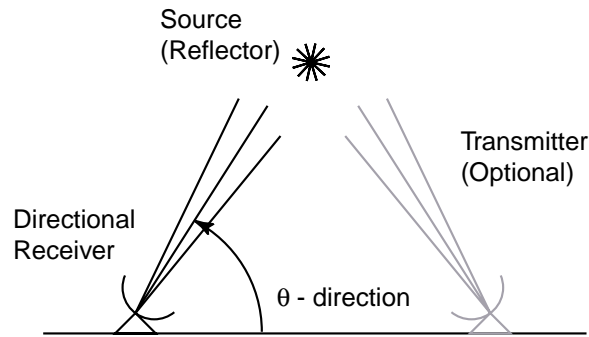


Figure 1.7: (Passive) Radar

1.3.1 Multisite Radar Systems (MSRS)

It is well known that the earliest radars were bistatic Continuous Wave (CW) radars. They detected an object as it crossed the transmitting station-receiving station baseline by measuring the beat frequency of its Doppler-shifted reflection and direct signal propagating from the transmitting station to the receiving station. After the invention of the duplexer at the US Naval Research Laboratory in 1936, which provided a means of using a common antenna for both transmitting and receiving, monostatic radars became practical and interest in bistatic radars became dormant. The interest in bistatic radars was revived again in the 1950s [24, 25].

The concept of the passive radar is shown in Figure 1.7. If the target is not transmitting, it is necessary to highlight the target by transmitted signal. If the target is active, a transmitter is not required. In the case of active radar, one antenna performs both functions, transmitter and receiver.

One of the first MSRS in the United States is the NAVSPASUR (Navy Space Surveillance System). It is a CW MSRS, in operation since 1960, that detects orbiting objects as they pass through the electronic “fence” over the continental United States. The system includes three groups of stations interspersed along a great circle at 33.5°N latitude from Fort Stewart, Georgia, to San Diego, California about 3500 km apart (Figures 1.8 and 1.9). Each group contains one central transmitting station and two receiving stations, one on each side of the transmitting station, separated from it by 400-500 km. Operational frequency lies in the range of 214-219 MHz. The large linear arrays of the transmitting stations generate

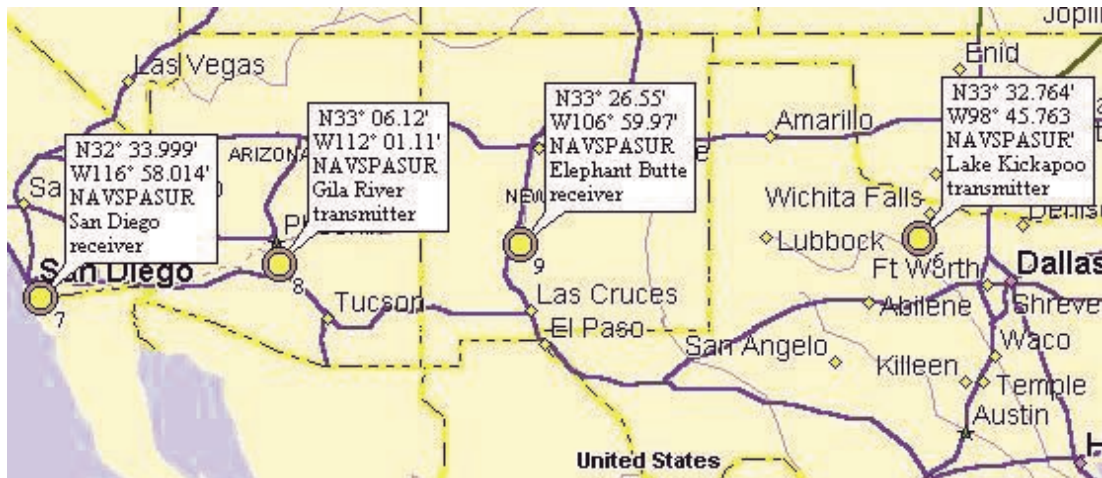


Figure 1.8: NAVSPASUR West

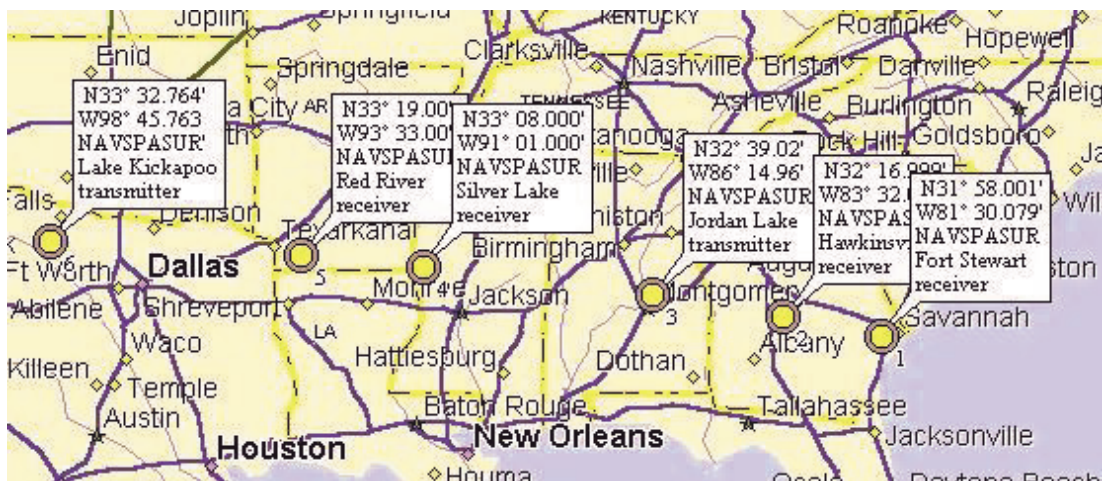


Figure 1.9: NAVSPASUR East



Figure 1.10: NAVSPASUR Antenna

stationary, vertical, coplanar fan beams, oriented along the great circle. The length of the linear transmitting arrays of the east and west groups are 1600m, while the transmitting array of the central group located at Kickapoo Lake, Texas (Figure 1.10), is about 3300m long. Four receiving stations contain eight linear phase-measuring arrays each of 120 m in length and one additional alerting array. The main purpose of these stations is to detect objects at low and medium orbits. In 1986 the NAVSPASUR was upgraded to double its range from 7500 to 15000 Nm [26, 24, 27, 25].

From 1972-1975, the Applied Physics Laboratory of the Johns Hopkins University conducted two empirical investigations into the advantages and problems of MSRS created by integration of radar and beacon airspace surveillance systems. The initial experiment was conducted using ATC radars and beacons located in the Washington-Baltimore area. The MSRS included two sites separated by 25 Nm. At each site a radar and a beacon were used.

The Multistatic Measurement System (MMS) was deployed in 1978-1980 at the Kwajalein Missile Test Range (Marshall Islands) as a part of the Kiernan Re-entry Measurement Site (KREMS). The high-power Tradex L-band and Altair UHF radars at Roi-Namur Island are utilized to illuminate targets and to receive target echoes.

In the late 1970s under the sponsorship of the US Air Force (USAF) the Precision Location/Strike System (PLSS) was developed. The purpose of this system is to reconnoiter

hostile air defense means, to locate and identify hostile radars and to point striking weapons with high accuracy. The system works on the principle of hyperbolic location. At three spatially separated points, TDOAs of pulse signals from a hostile radar are measured by three aircrafts flying at a height of 15-20 km. Aircraft positions are known with high accuracy achieved by the radio navigational system. Obtained information is transmitted to the ground-based data fusion and control center. The prototype of the PLSS is the ALSS developed in 1972 [28, 29, 30].

All these systems have baselines on the order of at least tens or hundreds of kilometers. GIDL is attempting to provide a performance assessment for source localization involving much smaller baselines.

1.3.2 Passive Localization and Signal Processing

As it relates to this thesis, probably the most important result reported in the passive localization literature has to do with the canonical form of the maximum likelihood (ML) estimator of source location parameters given the received sensor signals. Bangs and Schultheiss [31], Carter [32], and Owsley and Swope [33] showed that the ML estimate of source position is that which maximizes the power in the output of the filtered beamformer shown in Figure 1.11. This form has intuitive appeal, but is very costly to implement, requiring a search over a nonconvex, difficult-to-compute functional. An optimal one step detector/localizer is considered in the works of Dubrovina [34], Kailath [35], Farina [36], and others. These one step optimal detector/localizers provide the best performance but are very complicated and hard to implement.

In [37] and [38], Hahn and Weinstein showed that, in the small-error region (where the ML estimator is efficient), the ML estimator can be implemented as a two-step process, where, in the first step, intersensor delays (range differences (RD) or time difference of arrival (TDOA)) are measured, and, in the second step, source position is extracted from the measured delays (see Figure 1.12). (This approach was also suggested by Ng [39].) Thus, given an efficient way to measure intersensor delay (i.e., RD or TDOA) from time-series data, a method for extracting source parameter information from the measured RDs would provide a quick, accurate solution to the passive localization problem. A suboptimum, two

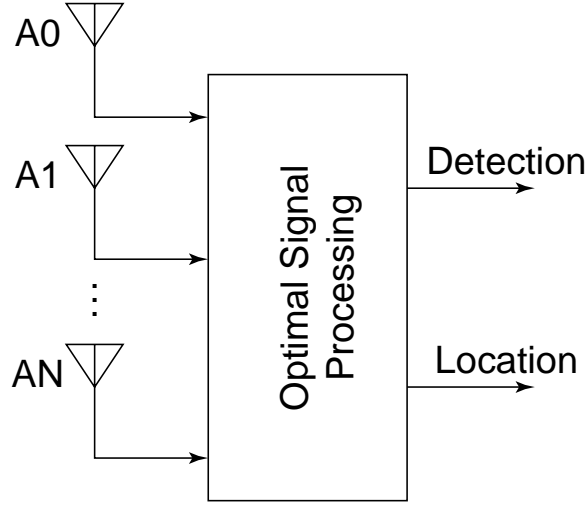


Figure 1.11: One Step Processing or Filtered Beamformer

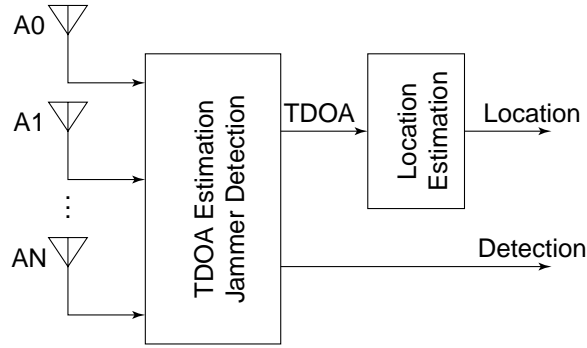


Figure 1.12: Two Step Processing or Multiplier-Correlator TDOA(RD) Estimator

step, detector/localizer is considered in the works Brad [40], Chan [41], Hann [42], and others. These two step suboptimal detectors/localizers approach optimal performance, and are simpler to implement than one step algorithms.

RD or TDOA estimation

In the case of estimating the vector of intersensor RDs, often referred to (given scaling by the speed of light or sound) as time differences of arrival (TDOA), computationally inexpensive ML methods are available. Hahn and Tretter [42, 43], and later Ng [44], studying the multisource case, proposed an RD vector estimator implemented as a set of filtered

multiplier-correlators, followed by a linear post-processor. This structure is inexpensive to implement and, to first order in the square of the typical sensor noise to signal ratio, is unbiased with variance equal to the Cramer-Rao lower bound (CRB) [45]. It should be pointed out that for sensor signal to noise ratios below one, the CRB becomes unachievable [46, 47, 48]. Although as noted in [46, 49], for the two-sensor case, the cross-correlator nearly achieves the tighter Ziv-Zakai bounds [50, 51, 52], the multi-sensor case remains unstudied. As an aside, Hahn notes in [43] that the multiplier-correlator structure has the advantage over the steered beamformer of allowing different noise spectra at different sensors.

For completeness, the bibliography includes references on the measurement of intersensor RD and TDOAs. The estimation of RD via spectral operations is discussed in [53, 54, 55, 56, 57, 58, 59]; cross-correlation-based methods are presented in [60, 61, 62, 63, 64, 65]; and, the tracking of a time-varying RD is discussed in [66, 67, 68, 69, 70, 71, 72]. Finally, bounds on the performance of intersensor RD estimators are considered in [46, 73, 49, 47, 64, 48].

TDOA-Based Position Estimation

The estimation of position from RDs has been fairly well studied in the passive localization literature for the special case of the source far from an array with collinear elements. In [43], Hahn derives the Cramer-Rao bound (CRB) and a closed-form maximum likelihood (ML) estimator for the source position given a set of unbiased, CRB-variance RDs. A similar estimator was derived by Weinstein [74]. These techniques are made possible by the fact that, under the source-far-from-a-collinear-element-array assumption, the intermediate variables are linear in the measurements. In general, intermediate variables linear in the measurements cannot be found, and the ML estimate will be given as the solution of a difficult nonlinear least-squares problem.

Bounds on the variance of unbiased position and velocity estimators are discussed in [31, 32, 75, 76, 77, 74, 78, 79, 61]. References [77, 74] are concerned with the behavior of information inequality variance bounds as a function of the source-sensor geometry.

These techniques and methods form a theoretical background for GIDL operations.

Particularly chosen techniques (TDOA) are considered in detail in the theoretical chapter. To limit the scope of this thesis work, only TDOA based algorithms have been fully implemented and tested.

Multisource Localization

Finally, a note on multisource localization. Wax and Kailath [35] derive a canonical form for the ML estimator of the positions of multiple, possibly correlated sources. The likelihood function is the filtered output of a bank of beamformers, each trained on a different source. In the uncorrelated-source, low-SNR case, the likelihood function reduces to the sum of single-source likelihood functions. Unfortunately, the likelihood function is expensive to compute and nonconvex; accordingly, without a good *a priori* situation estimate, the associated ML estimate will be extremely costly to compute. Multisource RD estimation has been treated in [80, 81, 82, 44].

In the special case of far-field sources (i.e., source location characterized by its direction only), Schmidt's MUSIC algorithm [83] and the ESPRIT algorithm of Paulraj, Roy, and Kailath [84] have become widely used. These techniques decompose the correlation matrix of sensor signals into subspaces associated with source signals and noise, and extract the various signal direction arrivals from the appropriate eigenvectors.

Most of the mentioned references are concerned with a more theoretical approach to the solution of the problem. One of the ideas behind the GIDL is to develop a flexible research platform, which would allow for experimental implementation of the above-mentioned techniques and algorithms, and experimental comparison of their performance along with difficulty of implementation. As it will be shown later, a GIDL receiver constructed in such a way that most of the signal processing is done in software. This allows for implementation and testing of almost all the mentioned and described algorithms, by programming them in software, without changing receiver hardware.

1.3.3 Hyperbolic Navigation Systems

TDOA or range-difference-based localization is widely-used in hyperbolic navigation systems; accordingly, this dissertation builds on and extends many results reported in that

literature.

A so-called hyperbolic navigation system — see [85, 86] for tutorial reviews — consists of a set of transmitters and a receiver, or station. The transmitters have accurate synchronized clocks precisely known, and, except for brief identification messages, transmit the same signal at the same time. The signals arrive at the station with time delays proportional to the station-transmitter range plus the difference in transmit time. A station can then compare the relative arrival times of the incoming signals to estimate the vector of inter-transmitter RDs and subsequently estimate its location relative to the set of transmitters. If the receiver is equipped with a clock synchronized to the transmitter clocks, then the received signals may be used to estimate the various station-transmitter ranges, and, in turn, station position. Usually, the mobile station clock is not synchronized with the transmitter clocks, and the measured transmitter ranges will all be corrupted by the same unknown bias. The resulting biased range measurements are termed pseudoranges (PR) [87]. This PR idea is extensively used in GPS.

1.3.4 GPS Receiver and Interference Detection

The GPS receiver can be designed with precautions against interference; namely, bandpass RF filtering to minimize out-of-band interference, pulse blanking to reduce the effects of high-level pulse interference and prevent Low Noise Amplifier (LNA) overload, adequate number of quantizing levels, and appropriate Automatic Gain Control (AGC) to ensure full processing gain, and careful design of the code and carrier tracking loops.

However, sufficiently high levels of interference will overload any type of radionavigation system, and GPS, even with its spread spectrum, is no exception. Note that taking advantage of the GPS signal processing gain by itself is not only the strategy. For example, study [2] indicates that an interferer with power 14 dB greater than the desired signal will typically disrupt GPS receiver operation. However, if a narrow-band interferer were “notched out”(band-stop filtered) in frequency before correlation, only a modest degradation in tracking accuracy (due to signal distortion) would be noticed.

Under most circumstances, narrow-band or broad-band interference of sufficient level to disrupt the GPS receiver is well above the thermal noise level, either in peak power

spectral density, total power, or both. Under these circumstances, either a total power measurement or a crude spectral density measurement (e.g., using upper band/lower band comparison or more elaborate but still simple, discrete Fourier transform (DFT) processing) can be effective in reliably detecting the presence of interference [23, 88]. When interference is detected, various actions can be taken:

1. Alert the Kalman filter to the interference, give lower weight to the measurements, and use alternate sensors such as an inertial measurement unit during the limited period where interference is present.
2. Reduce the Delay Lock Loop (DLL) tracking loop filter bandwidths.
3. Alert the integrity-monitoring system of the interference.
4. Utilize adaptive antenna nulling or notch filter techniques (adaptive frequency notching).

There are multiple papers on the various jamming detection and mitigation techniques for GPS receivers. All the above mentioned ideas and techniques can be tested by the GIDL receiver and serve as a basis and background for the GIDL receiver design.

1.3.5 Software Radio

The software radio has been described as the most revolutionary advance in receiver design since the advent of the superheterodyne concept in 1918 by Edwin Armstrong. In addition, the Institute of Electrical and Electronics Engineers (IEEE) devoted the May 1995 Communication Magazine exclusively to the software radio. The fundamental design philosophy is simple. An analog-to-digital converter (ADC) should be placed as near as possible to the antenna in the chain of front end components and the resulting samples should be processed using a programmable microprocessor.

This configuration offers a number of advantages over the traditional receiver implementation. The most notable include: 1) The removal of analog signal processing components and their associated nonlinear, temperature-based, and age-based performance characteristics. 2) A single antenna/front end configuration can be used to receive and demodulate a variety of distinct radio frequency (RF) transmissions. 3) The software radio provides

the ultimate simulation/testing environment. In order to evaluate a specific algorithm, there is no need to replace hardware components or develop additional simulations—simply make the modification in the software, compile the code, and download to the processor for real-time execution and evaluation of performance. For more information on the software radio see [89, 90, 91, 92, 93, 94, 95, 96, 97].

Software radio techniques are used to calibrate the GIDL. For detailed description of the software radio and GIDL system calibration see Chapter 4.

1.3.6 Current Research or Competitors

There are presently only a few papers which address interference direction and location finding in the GPS Band. Most of the technical literature focuses on trying to find only direction to the source of interference. The following seven readings provide a quick summary and overview of the current publications related to the GPS interference localization.

- Shih-Chieh Leung et al., “Analysis of Algorithms for GPS Interferer Direction Finding” [98]: Two algorithms, MUSIC (Multiple Signal Classification) and PRIME (Polynomial Root Intersection for Multidimensional Estimation), are applied to interferer direction finding problem, which concerns finding the number of interference emitters and their directions. A two dimensional planar array antenna with seven elements (very short baseline array) is used in this study. The algorithms can operate on either pre-correlation phase measurements (for the case of the strong signal) or post correlation phase measurements, derived from the carrier tracking loop (for the case of the weak signal). Results from this study have shown that these methods have the potential for detecting multiple emitters within one tenth of the antenna beamwidth. Only simulation results present in the paper.
- E. Michael Geyer et al., “Airborne GPS RFI Localization Algorithms” [99]: This GPS Interference Source Location and Avoidance System was developed by the U.S. DOT Volpe National Transportation Systems Center. The system is called the Aircraft RFI Localization and Avoidance System (ARLAS). ARLAS has three major subsystems: (1) a GPS receiver and roof-mounted patch antenna; (2) gyros with capability to measure roll, pitch and heading; and (3) a personal computer containing

software which process receiver and gyro data and estimate the location of an interferer. SNR, aircraft position and attitude measurements are utilized to estimate the location of the interference. In time of the publication flight tests of the integrated system have not yet been conducted and the results must be viewed as preliminary. No overall performance numbers for the system are given in the paper.

- Dignius-Jan Moelker, “Multiple Antennae for Advanced GNSS Multipath Mitigation and Multipath Direction Finding” [100]: This paper proposes and studies integrated multipath direction finding and multipath mitigation techniques for GNSS. These techniques are based on the hybrid combination of multiple antennae and multiple correlators per receiver channel. The author of this paper uses a short baseline antenna array (phase array) and utilizes post-correlation measurements to deduce direction to the source of multipath. Two multipath direction finding algorithms are considered. The first is an extension of the Multipath Estimating Delay Lock Loop (MEDLL) and the second uses Multiple Signal Classification (MUSIC). The feasibility of both techniques is demonstrated by measurements, which indicate an achievable direction estimation error of 4.9 degrees for the MEDLL-extension and 1.5 degrees for MUSIC. All measurements are done with two antennae and two NovAtel prototype MEDLL receivers.
- Jose M. Blas et al., “A Low Cost GPS Adaptive Antenna Array” [101]: Again, this paper discusses baseband processing, for a short baseline phased array antenna. The author utilizes the Mitel GPS Chipset to obtain post-correlation measurements.
- A. Brown et al., “Jammer and Interference Location System - Design and Initial Test Results” [102]: NAVSYS Corporation approached solution of jammer detection and location problem through a network centric approach where data is collected from both specialized GPS receiver equipment and conventional GPS user equipment acting as jammer sensors. The data from these sensors is relayed over a data link or network to a Master Station that can use the data to derive the various jammer locations. NAVSYS Corporation is building three types of sensors. The first uses the diagnostic data (C/N0) generated from conventional GPS user equipment to allow it to act as a jammer sensor. The second sensor identifies the Angle-of Arrival (AOA)

of the jammer signals at the sensor. The data from one moving AOA sensor collected over a period of time. The third sensor collects data snapshots of the jammer's RF spectrum at multiple locations. No performance figures for this system were given in the paper.

- J. Wohlfel et al., "Location of GPS Interferers" [103]: The described system, according to the paper, consists of a short baseline three antenna array; a high sensitivity, three channel, fast scanning receiver; three interferometric direction finding processors; a state-of-the-art signal processor, and a DAT tape drive. The paper does not provide detailed description of the system and performance figures.
- Shau-Shiun Jan and Per Enge, "Finding Source of Electromagnetic Interference (EMI) to GPS Using a Network Sensors" [104]: This paper considers two methods to estimate jammer location. One method is based on jammer bearing measurements at different points along the sensor trajectory, or from the sensor array. Another method is based on the Doppler shift of the jammer frequency caused by the relative motion between the sensor and jammer.

1.4 Contributions

The initial goal of this research was to deduce and demonstrate an optimized design for an interference localization system. In the course of this research, it was discovered that no single optimum algorithm exists which would cover all the possible scenarios. An optimum interference localization system design depends on the requirements of the overall system, and specific system installation. Since these various algorithms can share common hardware, the only difference comes in the processing algorithms. This dissertation presents an analysis of these interference detection and localization algorithms, and a hardware design capable of testing all these algorithms. One of these algorithms was tested utilizing the prototype GIDL hardware. Results from the extensive testing under realistic conditions are presented. In addition, this dissertation describes other interference detection and localization algorithms studied, and presents the tradeoff among the various algorithms.

Taken together, these contributions introduce the Generalized Interference Detection and Localization (GIDL) System solution to the problem of interference and jammer localization in the GPS frequency band. This solution is cost efficient compared to other previously studied solutions, for example jammer localization system by airplane [99].

The newly developed Generalized Interference Detection and Localization System provides the solutions to constantly monitor GPS signal environment and detect interference as soon as it appears. When interference is detected it estimates direction to the source of interference and its location. The GIDL hardware allows for implementation and testing of a variety of detection and localization algorithms. It performs the role of a flexible development platform and solution for the jammer threat since various types and numbers of sources may be accommodated.

The specific contributions of this research are the following:

1. Developed the first Time Difference of Arrival (TDOA) system to find the location of GPS jammers that is compatible with the currently recommended LAAS installation.
2. Developed GIDL signal processing algorithms to detect the presence of interference in the GPS band and to estimate the location of the jammer. These algorithms include algorithms to estimate and measure the Time Difference of Arrival (TDOA) for unknown weak signals (jamming signals), and algorithms to estimate range and direction to the source of interference from measured TDOA.
3. Developed Software GPS Receiver algorithms to calibrate the GIDL system delays and clock offsets using the GPS satellite signals.
4. Designed, developed, and built a flexible research platform for the GIDL system development and digital signal processing of signals in GPS frequency band. This platform is a completely digital, common clock, four channel digital signal processing receiver solution. It can be used to develop and verify various GIDL algorithms, including long and short baseline GIDL algorithms and to demonstrate aided detection of very weak GPS signals. A user friendly graphical interface to GIDL programmed in MATLAB also has been developed for easy interaction with the GIDL system.

Experimentally demonstrated detection of weak signals, and finding azimuth and range to their source in real time, including demonstrated localization of the moving jammer. Compared error analysis with experiment.

1.5 Notes on Terminology

This dissertation necessarily contains terms and abbreviations from electrical engineering, mathematics and related fields, which may be unfamiliar to aerospace engineers. To minimize both confusion and repetition, a glossary of terms and acronyms is provided in Appendix A.

The technology of the GIDL system, and related systems such as MSRS and sonar, has evolved over a number of years. Sometimes work done in one field uses different terminology for similar work done in another application. Theoretical work adds more confusion in terminology. The unfortunate result is that “translation” is sometimes required when going from one application to another. The same *things* are described in different *words*. An attempt has been made to use consistent terminology throughout this work. When necessary, confusing terms or naming conventions are noted and explained.

One further note on history and nomenclature. The “Generalized Interference Detection and Localization” (GIDL) described herein was originally known as the “Interference Direction Finder” (IDF). However, the IDF is more a concept than a specific piece of hardware. A one channel GIDL-like system could be called a “Signal Quality Monitoring” (SQM) receiver, as the concept itself preceeded GIDL, and evolved from it. The original test bed for the GIDL, actually for IDF, was a combination of two SQM receivers patched together to form the first prototype (SQM today serves a purpose of detecting signal faults that originate on the satellite).

In the course of this research, various revisions, configurations, and names of the SQM/IDF/GIDL receiver were built, which eventually evolved into the final design described in subsequent chapters.

1.6 Dissertation Outline

This introduction described GPS, LAAS, and WAAS, and gives an explanation of how the GPS signal can become jammed, and what has been done to mitigate this problem. The Chapter 2 describes GIDL theory. After describing GIDL theory, the text turns in Chapter 3 to description and design considerations of the experimental hardware, and how to calibrate it in Chapter 4. Experiments performed with this hardware and results compared to the theoretically predicted performance are presented in Chapters 5 and 6. Finally, possible development and future plans are addressed in Chapters 7 and 8.

Appendices include supporting documentation such as a glossary and a description of the experimental studies on effects of jammers and mobile satellite communications on various GPS receivers.

}

Chapter 2

GIDL Concepts and Theory

This chapter discusses the theory behind GIDL operation. The discussion starts from the simplified GIDL concept, such that the reader gains a clear graphical picture of the methodology. The full theory is then developed.

There are two questions that have to be answered to protect a LAAS installation. First is there an interference source present? Second what is its location? Once a jammer has been detected, localization may begin. Therefore, following the discussion of the simplified GIDL concept, there is a section on how to detect the presence of a jammer, and then on possible ways to localize it, once it has been detected.

One method of localization is based on the time difference of arrival (or range difference). To limit the scope of this dissertation, only this approach has been fully studied, implemented and tested. Nevertheless, other approaches could be implemented and tested on the current GIDL hardware. This is left as the subject of future research.

The last section in this chapter covers questions on how far and how accurately it is possible to detect and localize a jammer. There are ways to improve detection/localization range relative to jamming range, and these methods are also discussed.

Sections 2.2 2.3 2.4 are conglomeration from References [105, 106, 107, 108, 109, 110]; they are based on translation from Russian of selected works by Chernyak, which is done with his permission. The author would like to thank V.S.Chernyak and other referenced authors, for their work in signal theory. This work would not be done without that.

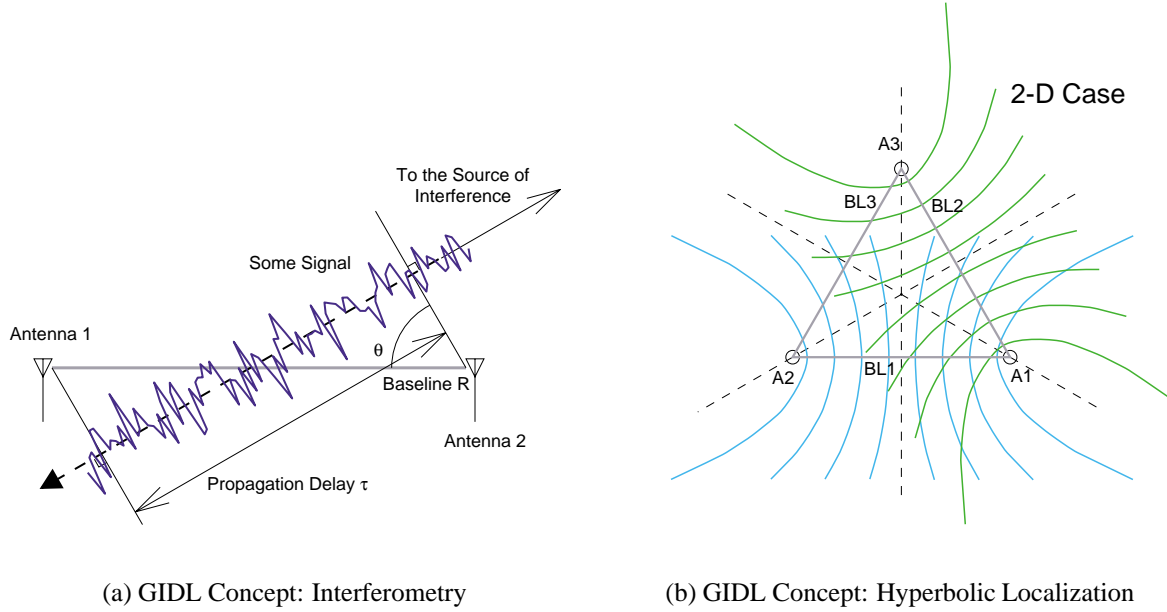


Figure 2.1: Simplified GIDL Concepts

2.1 Simplified GIDL Concept

Let us assume that we have a system containing two sensors (or antennae) and some signal source (jammer) located far enough away such that it is possible to assume that signal wavefronts from this source are planar with respect to the sensors' (antennae') baseline. This situation is shown in Figure 2.1(a).

If differential signal propagation delay time is measured between these two antennae, and signal propagation speed is known in the media (for example, the speed of light), the range difference (RD) measurement (or time difference of arrival (TDOA) measurement, which differs from RD measurements by a scale factor of propagation speed in the media) can be formed. The RDs are equal to the distance between antennae (the baseline) multiplied by the sine of the angle between antenna baseline and direction of the signal wavefronts (direction to the signal source, or direction of propagation, is orthogonal to the direction of wavefronts, and equal to $90^\circ - \theta$ degrees): $L \sin(\theta) = \tau c$, where c is propagation speed in the media, L is distance between antennae or baseline, τ is the time difference of arrival (or τc is range difference), and θ is the direction of the wavefront with respect to

the baseline. L and c are assumed to be known, and τ is the measurement. By inverting this equation, it is possible to find direction of the wavefronts, θ , or direction to the source $90^\circ - \theta$. There is an ambiguity in the solution as signal source can be on either side of the baseline, in a planar case, or on the cone in the case of 3D space. Multiple baselines can resolve this ambiguity.

When the assumption concerning a distant source is not valid it is necessary to take into account the fact that wavefronts from this source are spherical. In this case, it is also possible to form the TDOA (or RD) measurement, but now this measurement would define a hyperbola of possible source locations in 2D, or hyperboloid in 3D with antennae in the foci of these hyperbolas. This is shown in Figure 2.1(b). By intersecting hyperbolas from the multiple baselines, it is again possible to find the signal source location in 2D or 3D space.

From this simple concept it is easy to see that it is possible to locate the source of interference by means of a completely static system (without moving parts), through the use of omnidirectional antennae plus signal processing algorithms which let us estimate TDOA measurements. Questions to be answered include: how to detect the presence of interference; how to estimate TDOA, once the jamming signal is detected; how system performance depends on the length of the baselines; what is the possible performance with baselines of length compatible with the LAAS installation; and how is it possible to detect a jammer before it starts affecting GPS receivers which are to be protected? Answers to these questions are given in the following sections.

2.2 Jammer Detection

This section outlines algorithms which could be used for jammer detection and Time Difference of Arrival (TDOA) estimation. Details of the experimental algorithms are also shown. For the current GIDL configuration, the jammer is modeled as a stationary white noise-like signal, with no appreciative Doppler frequency shift.

2.2.1 Signal and Interference Model Formulation

The signal detection theory for GIDL may be considered a part of the general spatial-temporal signal processing theory. However, most practical results of that general theory relate to the processing of plane or spherical waves incident upon receiving antennae of given form and size, namely phased antenna arrays (PAAs) [111, 112, 113, 114]. GIDL systems have a number of features which must be taken into account when developing the signal detection and parameter estimation theories. The main features are as follows:

1. The number and arrangement of antennae may be arbitrary. Therefore, the detection theory should be developed independent of a specific system configuration.
2. The differences of signal propagation time from each source to spatially separated antennae (TDOAs) are, as a rule, much greater than the reciprocals of signal bandwidths. In particular, this does not permit separation of the temporal processing from the spatial processing of the sum of echoes and external interferences (which is usually possible for antenna arrays).
3. A jammer may be located at any range from a GIDL system, i.e., not necessarily in the far zone (far field) and possibly in the Fresnel's zone (near field) with respect to the whole antenna system of the GIDL. But it is assumed that jammers are located in the far zone of each individual antenna.
4. Mutual correlation of scattered signal fluctuations at the inputs of different antennae may vary widely—from complete correlation (as at different elements of normal antenna arrays) to zero correlation (when the antennae are separated by sufficiently large baselines). (For performed GIDL experiments antennae were located at the reasonably small distance from each other so correlation of the scattered signals was assumed.)

Of great importance is the choice of mathematical models for signals and interferences. On the one hand, these models should adequately reflect the principal features of actual signals and interferences. On the other hand, they must be suitable for deriving sufficiently simple and clear results which can be applied to practice. Generally accepted models have

been chosen for “useful” signals: *the deterministic signals* (signals with known waveform without unknown or random parameters, i.e., completely known signals), *the quasideterministic signals* (signals with known waveform but containing unknown or random parameters) and *stochastic signals* (random signals with unknown waveform). Deterministic and quasideterministic signals will also be called regular signals (to emphasize their known waveform).

Deterministic signals are widely used in detection theory as a mathematical model. Employing this model is often the simplest way to reveal some principal relationships that hold for actual signals. Thus, the deterministic signal model is warranted and practically convenient.

The classical detection theory usually assumes informative signal parameters, such as time and direction (angle) of arrival (TOA and AOA), Doppler shift, and other parameters, to be known *a priori* [115, 26, 116, 117, 118, 114]. The same assumption is exploited in the detection theory for GIDL. In other words, the detection problem is usually formulated as the statistical decision problem of whether a jammer is present within the considered Space Resolution Cell (SRC) of the GIDL.

Consider a set of wanted signals at the inputs of m spatially separated receiving antennae of a GIDL system. In a complex form, $\mathbf{S}^*(t) = [S_1^*(t), \dots, S_m^*(t)]$. Here, and in subsequent text, the asterisk means complex conjugation for scalars but complex conjugation and transposition (Hermitian conjugation) for vectors and matrices. The wanted signal at the input of the i^{th} antenna can be written in the form

$$S_i(t) = a_{si} \exp(-j\varphi_{si}) s_0(t - t_{si}) \exp[j(\omega_0 + \Omega_{si})(t - t_{si})] \quad (2.1)$$

where a_{si} is the r.m.s. (effective) value; φ_{si} is the initial phase; t_{si} is the signal propagation delay; ω_0 and Ω_{si} are the carrier frequency and the Doppler frequency shift, respectively. $s_0(t)$ is the normalized complex envelope (waveform). That is

$$\frac{1}{2} \int_{-\infty}^{\infty} |S_i(t)|^2 dt = \frac{a_{si}^2}{2} \int_{-\infty}^{\infty} |s_0(t - t_{si})|^2 dt = a_{si}^2 T_s = E_i \quad (2.2)$$

where T_s is the signal duration (assumed finite or finite observation time) and E_i is the signal energy at the input of the i^{th} antenna.

It is reasonable to synthesize and analyze detectors for GIDL in the frequency domain rather than in the time domain (see Section 2.2.2). The spectrum of the signal of (2.1) is

$$\Psi_i(\omega) = a_{si} \exp(-j\varphi_{si}) \Psi_0(\omega - \omega_0 - \Omega_{si}) \exp(-j\omega t_{si}) \quad (2.3)$$

where $\Psi_0(\omega)$ is the Fourier transformation of $s_0(t)$ so that

$$(1/2\pi) \int_{-\infty}^{\infty} |\Psi_0(\omega)|^2 d\omega = \int_{-\infty}^{\infty} |s_0(t)|^2 dt = 2T_s \quad (2.4)$$

Sometimes it is necessary to take into account the antenna directivity pattern (ADP). Then, instead of (2.3), $\Psi_i(\omega)$ becomes

$$\Psi_i(\omega) = a_{si} \exp(-j\varphi_{si}) g_i(\beta_{si}, \varepsilon_{si}, \omega) \Psi_0(\omega - \omega_0 - \Omega_{si}) \exp(-j\omega t_{si}) \quad (2.5)$$

where $g_i(\beta_{si}, \varepsilon_{si}, \omega)$ is the normalized ADP of the i^{th} antenna [$g_i(\beta_{si}, \varepsilon_{si}, \omega) \leq 1$] depending, in general, on frequency; and $\beta_{si}, \varepsilon_{si}$ are the interferer angle coordinates with respect to the i^{th} antenna.

Equations (2.1)–(2.5) are also valid for quasideterministic signals when some or all parameters are unknown or random, also assuming the complex envelope, $s_0(t)$, and hence its spectrum, $\Psi_0(\omega)$, are known.

Signals transmitted by sources of “noise” radiation and received by the GIDL system will be modeled as stochastic signals. The term “stochastic” instead of the simpler term “random” is used here in order to distinguish between these signals and quasideterministic signals with random parameters. Sometimes stochastic signals are called “noise signals,” although the term “noise” is usually associated with some signal contamination. In GIDL these signals are “useful” (wanted signals) so it will be more appropriate to call them “stochastic” signals. Such signals may be written in the form of (2.1), (2.3) or (2.5), assuming $s_0(t)$ and hence, $\Psi_0(\omega)$, to be realizations of random processes.

It is assumed here and in what follows that the stochastic signals are realizations of *complex, zero-mean, narrowband* ($\Delta\omega \ll \omega_0$ where $\Delta\omega$ is the power spectrum bandwidth), *stationary Gaussian stochastic processes* within the observation interval $(-T/2, T/2)$. Note, however, that statistical coupling between processes at the inputs of different antennae is not necessarily stationary.

The Gaussian stochastic process may be considered as a proper characterization for transmissions of many radiation sources observed by GIDL including noise-like jammers. This model permits exploiting well-developed mathematical techniques. As is well known, a multivariable, stationary, zero-mean Gaussian process can be completely determined by its correlation (covariance) matrix or by the power spectral density (PSD) matrix. For the considered stochastic processes and variables with zero mean, correlation functions and matrices coincide with covariance functions and matrices, respectively. (It is not a good model for sine wave jammer, which could be considered separately, but that beyond the scope of this work.)

In writing a stochastic signal in the form of (2.1), (2.3) or (2.5), the parameters a_{si} , φ_{si} , $i = \overline{1, m}$ (it is worth noticing that the overbar at integers means enumeration of possible values), are assumed to be constant within the observation time interval. At the same time the complex envelope, $s_0(t)$, varies rapidly so that each observation interval contains many correlation intervals of $s_0(t)$. Such a model is appropriate for signals from many radiation sources observed by a GIDL. For stochastic signals of this type, it is reasonable to introduce the so-called *conditional correlation matrices* at the fixed values of parameters characterizing intensity (power), differential phase shift and (or) time delay. When these values are known, a stochastic signal is present with the *deterministic correlation matrix*; when they are unknown or random, it is a stochastic signal with the *quasideterministic correlation matrix*.

An arbitrary element of the correlation matrix (“conditional” is omitted for the sake of brevity) for complex stochastic signals at the inputs of m receiving antennae of a GIDL can be written as follows:

$$B_{ik}(t_1, t_2) = 0.5 \overline{S_i(t_1) S_k^*(t_2)}, \quad i, k = \overline{1, m} \quad (2.6)$$

The overbar here and in the sequel denotes the expectation, in this case, over the set of complex envelopes, $s_0(t)$. The factor 0.5 has been introduced for the variance, $B_{ii}(0)$, to coincide with the variance (power) of the real part of a signal, $\text{Re} S_i(t)$. That is, $B_{ii}(0) = 0.5 \overline{|S_i(t)|^2} = \overline{[\text{Re} S_i(t)]^2}$ since $\overline{[\text{Im} S_i(t)]^2} = \overline{[\text{Re} S_i(t)]^2}$. Substituting (2.1) into (2.6) and

averaging yields

$$B_{ik}(t_1, t_2) = \sqrt{P_{si}P_{sk}\rho_s}(t_1 - t_2 + \tau_{sik}) \times \exp\{j[(\omega - 0 + \Omega_{si})(t_1 - t_2) - \Delta\Omega_{sik}t_2 + \omega_0\tau_{sik} + \Delta\varphi_{sik}]\} \quad (2.7)$$

In (2.7) the following notations apply:

$$\tau_{sik} = t_{sk} - t_{si}; \quad \Delta\Omega_{sik} = \Omega_{sk} - \Omega_{si}; \quad P_i = a_{si}^2; \quad (2.8)$$

and

$$\rho(t_1 - t_2) = 0.5\overline{s_0(t_1)s_0^*(t_2)} \quad (2.9)$$

which is the correlation function of the signal complex envelope, $s_0(t)$. Doppler phase shifts are included in the differential phase, $\Delta\varphi_{sik}$. In (2.7) ω_0 is the conventional (usually unknown) carrier frequency of the stochastic signal from a stationary (with respect to the receiving antennae) radiation source. When a radiation source moves, the frequency, $\omega_0 + \Omega_{si}$, $i = \overline{1, m}$, is perceived as a carrier frequency. Nevertheless, it is convenient to separate ω_0 from Ω_{si} . Note that in (2.8), t_{si} is the one-way signal propagation delay (from a source to the i^{th} antenna) and Ω_{si} is the Doppler frequency caused by the one-way source range variations relative to the i^{th} antenna.

In (2.7), the autocorrelation functions (i.e., at $i = k$, $i, k = \overline{1, m}$) depend on the difference, $(t_1 - t_2)$, which means that the signal is stationary. At the same time, the mutual correlation functions (i.e., at $i \neq k$) depend also on the time itself, t_2 , which indicates the nonstationary coupling between signals at different antennae. When the differential phase shifts accumulated during the observation time interval and caused by the Doppler frequency differences may be neglected (i.e., $|\Delta\Omega_{sik}T| \ll 2\pi$), then signals at all antennae are not only stationary but stationary coupled processes.

The correlation function (2.7) corresponds to the “instantaneous” power spectrum [119]

$$\begin{aligned} \Phi_{ik}(\omega, t) &= \int_{-\infty}^{\infty} B_{ik}(t, t - x) \exp(-j\omega x) dx \\ &= (\sqrt{P_{si}P_{sk}}/\Delta f_s) F_s(\omega - \omega_0 - \Omega_{sk}) \exp[j(\omega\tau_{sik} + \Delta\psi_{sik})] \\ &\quad \times \exp(-j\Delta\Omega_{sik}) \end{aligned} \quad (2.10)$$

where $\Delta\psi_{sik} = \Delta\varphi_{sik} + \Delta\Omega_{sik}t_{si} = \varphi_{sk} - \varphi_{si} + \Delta\Omega_{sik}t_{si}$; Δf_s is the bandwidth of the signal power spectrum; and $F_s(\omega)$ is the dimensionless normalized power spectrum of the complex envelope [see (2.9)]:

$$\begin{aligned} F_s(\omega) &= \Delta f_s \int_{-\infty}^{\infty} \rho_s(x) \exp(-j\omega x) dx; \\ (1/2\pi\Delta f_s) \int_{-\infty}^{\infty} F_s(\omega) d\omega &= 1 \end{aligned} \quad (2.11)$$

If the Doppler frequency differences at individual antennae may be neglected, this assumption is reasonable while GIDL antennae are stationary, ($|\Delta\Omega_{sik}T| \ll 2\pi$, $i, k = \overline{1, m}$), then

$$\Phi_{ik}(\omega, t) = \Phi_{ik}(\omega) = (\sqrt{P_{si}P_{sk}}/\Delta f - s)F_s(\omega - \omega_0) \exp[j(\omega\tau_{sik} + \Delta\psi_{sik})] \quad (2.12)$$

Here $\Delta\psi_{sik} = \Delta\varphi_{sik} = \varphi_{sk} - \varphi_{si}$. At $i = k$, Equations (2.12) and (2.8) yield the signal power spectrum at an arbitrary receiving antenna.

Self-noises of the receiver system are modeled as white, zero-mean, stationary Gaussian processes mutually independent at different RF channels. Therefore,

$$\begin{aligned} B_{ik}(t_1, t_2) &= 0.5\overline{n_i(t_1)n_k^*(t_2)} = \sqrt{N_iN_k}\delta_{ik}\delta(t_1 - t_2); \\ \Phi_{ik}(\omega) &= \sqrt{N_iN_k}\delta_{ik}, \quad i, k = \overline{1, m} \end{aligned} \quad (2.13)$$

where N_i is the one-sided noise power spectral density at the i^{th} channel; δ_{ik} is Kronecker's symbol ($\delta_{ik} = 1$ if $i = k$, $\delta_{ik} = 0$ if $i \neq k$); $\delta(t)$ is Dirac's delta function.

For GIDL, apart from temporal correlation, an important role is played by *the inter-antenna (spatial) correlation of complex amplitude fluctuations* (after signal delay equalization). Just as with the temporal correlation, one should consider extreme situations first. Being completely spatially correlated, the complex amplitudes at the inputs of different receiving antennae are tightly coupled and fluctuate simultaneously. Since the initial phases are tightly coupled as well, such signals may naturally be called “spatially coherent signals.” In particular, deterministic signals and stochastic signals with deterministic correlation matrices are spatially coherent. Conversely, when there is no correlation between complex amplitudes at the inputs of different antennae (or, in the more general case, complex amplitudes are statistically independent), such signals may be called “spatially

incoherent signals.” Quasideterministic signals and stochastic signals with a quasideterministic correlation matrix can be either spatially coherent or incoherent. Of course, the intermediate cases of partial temporal or spatial correlation are possible.

It is important to stress that spatial (interantenna) correlation of complex amplitudes and their temporal correlation (in each RF channel individually) are independent signal features.

2.2.2 Criteria for Optimum Signal Detection in GIDL

As is well known, for a number of “classical” optimality criteria for statistical decisions (the Bayes criteria, the Neyman-Pearson criterion, etc.), optimum signal processing is reduced to the likelihood ratio test. The specific criteria differ only by threshold levels. This means that the likelihood ratio criterion may be considered as a sufficiently universal optimality criterion which determines the structure of optimum detectors, i.e., signal processing algorithms up to the threshold comparison.

In this work, the *likelihood ratio criterion* is used for the synthesis of optimum detection algorithms. For the performance analysis of optimum and simplified suboptimum algorithms, the detection characteristics are used which present the detection probability as a function of the Signal-to-Noise Ratio (SNR) at the inputs of antennae with the probability of the false alarm as a parameter.

A set of overall signals received by m antennae of a GIDL in the time interval $(-T/2, T/2)$ represents a vector of overall signals which can be written in a complex form as follows: $\mathbf{X}^*(t) = [X_1^*(t), \dots, X_m^*(t)]$. This may be a sum of wanted signals, $\mathbf{S}(t)$, external interferences, $\mathbf{J}(t)$, and receiver system self-noises (thermal noises), $\mathbf{N}(t)$, i.e., $\mathbf{X}(t) = \mathbf{S}(t) + \mathbf{J}(t) + \mathbf{N}(t)$, or a sum of external interferences and self-noises only, i.e., $\mathbf{X}(t) = \mathbf{J}(t) + \mathbf{N}(t)$, where $\mathbf{J}^*(t) = [J_1^*(t), \dots, J_m^*(t)]$ and $\mathbf{N}^*(t) = [N_1^*(t), \dots, N_m^*(t)]$ (asterisk with scalars denotes the complex conjugate but the same asterisk with vectors and matrices denotes complex conjugate and transpose (Hermitian conjugate)). In particular cases external interferences may be absent.

Such a representation of overall received signals, wanted signals, external interferences and noises is valid for an arbitrary m -channel receiving system. Features of GIDL can

be revealed after the substitution of the specific expressions for signals, interferences and self-noises corresponding to mathematical models introduced in Section 2.2.1. Taking into account the assumed Gaussian probability distribution for noises and external interferences and imposing no constraints on the GIDL configuration, it is possible to write the known general likelihood ratio relationship for regular signals, Λ (e.g., [105])

$$\Lambda = \exp \left\{ \operatorname{Re} \int_{-T/2}^{T/2} \int_{-T/2}^{T/2} \mathbf{S}^*(t_1, \boldsymbol{\Theta}) \mathbf{R}(t_1, t_2) \mathbf{X}(t_2) dt_1 dt_2 - 0.5 \int_{-T/2}^{T/2} \int_{-T/2}^{T/2} \mathbf{S}^*(t_1, \boldsymbol{\Theta}) \mathbf{R}(t_1, t_2) \mathbf{S}(t_2, \boldsymbol{\Theta}) dt_1 dt_2 \right\} \quad (2.14)$$

where $\boldsymbol{\Theta}$ is the vector of signal parameters, and the $m \times m$ matrix $\mathbf{R}(t_1, t_2)$ is the solution of the integral-matrix equation

$$\int_{-T/2}^{T/2} \mathbf{B}(t_1, t) \mathbf{R}(t, t_2) dt = \mathbf{I} \delta(t_1 - t_2), \quad -T/2 \leq (t_1, t_2) \leq T/2 \quad (2.15)$$

In (2.15) \mathbf{I} is the identity matrix of the order m ; $\delta(t)$ is the Dirac delta-function.

The kernel of Equation (2.15) is the $m \times m$ space-time correlation (covariance) matrix of the sum of external interferences and receiver system self-noises at the inputs of spatially separated receiving stations, $\mathbf{B}(t_1, t_2)$. For the synthesis of optimum detection structures, as a rule, it is assumed that this matrix is known, i.e., the sum of self-noises and external interferences is a Gaussian zero-mean random process with deterministic correlation (covariance) matrix (see Section 2.2.1). Of course, in most practical situations the correlation matrix at least of external interferences contains unknown or random parameters, i.e., it should be considered as a quasideterministic matrix. Optimum detection algorithms derived under the assumption of a deterministic correlation matrix, $\mathbf{B}(t_1, t_2)$, are of great importance. They determine the potential performance level for any detection algorithms.

It should be noted that in the case of jammer detection in a background of receiver system thermal self-noises, the correlation matrix of these noises may often be considered a deterministic one.

In signal (jammer) detection problems, it is assumed that the interferences are stationary and, in the case of their interantenna correlation, stationary coupled during the observation time interval $(-T/2, T/2)$. This assumption simplifies detection problems significantly

and at the same time often holds in practice. Nonstationarity of interferences does not have sufficient time to manifest itself in a short time interval, T . The motion of interference sources (e.g., jammers) in space leads to nonstationary coupling of spatially correlated interferences (see Section 2.2.1). However, strong interantenna correlation is possible (after proper delay equalization) if the baselengths between antennae are not too large. In these cases differential Doppler frequency shifts of each interference at the inputs of any pair of antennae, $\Delta\Omega_{i,k}$, $i, k = \overline{1, m}$, are often small, i.e., $\|\Delta\Omega_{i,k}T\| \ll 1$, so that the nonstationarity of interference coupling may be neglected.

For stationary and stationary coupled interferences, $\mathbf{B}(t_1, t_2) = \mathbf{B}(t_1 - t_2)$ and $\mathbf{R}(t_1, t_2) = \mathbf{R}(t_1 - t_2)$. Now it is convenient to transfer from the time domain to the frequency domain. Let us denote the power spectral density (PSD) of the sum of interferences and self-noises by $\Phi(\omega)$ which is the Fourier transformation of $\mathbf{B}(t_1 - t_2)$. The Fourier transformation of $\mathbf{R}(t_1 - t_2)$ is denoted by $\mathbf{f}(\omega)$. The observation time interval, T , is usually much longer than the correlation interval of interferences, and all signals fall within the observation interval. It is now possible to replace the limits of integrals in (2.15) by infinity and solve this system of equations with the help of the Fourier transformation. Equation (2.15) becomes

$$\Phi(\omega)\mathbf{f}(\omega) = \mathbf{I} \quad (2.16)$$

The likelihood ratio in the frequency domain takes the form

$$\Lambda = \exp \left\{ \operatorname{Re} \frac{1}{2\pi} \int_{-\infty}^{\infty} \Phi^*(\omega, \Theta) \mathbf{f}(\omega) \chi(\omega) d\omega - \frac{1}{4\pi} \int_{-\infty}^{\infty} \Phi^*(\omega, \Theta) \mathbf{f}(\omega) \Phi(\omega) d\omega \right\} \quad (2.17)$$

where

$$\Phi^*(\omega) = [\Phi_1^*(\omega, \Theta), \dots, \Phi_m^*(\omega, \Theta)]; \chi(\omega) = [\chi_1^*(\omega), \dots, \chi_m^*(\omega)] \quad (2.18)$$

are the vectors of the Fourier transformations (the spectra) of the wanted signals, $\mathbf{S}^*(t) = [S_1^*(t), \dots, S_m^*(t)]$, and of the overall signals, $\mathbf{X}^*(t) = [X_1^*(t), \dots, X_m^*(t)]$, received during the time interval $(-T/2, T/2)$, respectively. It is seen that the system of integral equations used to solve for the functions of time, $R_{ik}(t_1 - t_2)$, $i, k = \overline{1, m}$, has been transformed into the much simpler system of functional equations to solve for the spectral functions,

$f_{ik}(\omega)$, $i, k = \overline{1, m}$. This is one of the most important advantages of the spectral approach. Another advantage which is especially significant for the GIDL investigations is that the signal envelope delays in the time domain are transformed into “phasors” (phase factors) in the frequency domain. If, for instance, the wanted signal is $S_i(t) = a_{si} \exp(-j\varphi_{si}) s_0(t - t_{si}) \exp[j\omega_0(t - t_{si})]$, then its spectrum is $\Psi_i(\omega) = a_{si} \exp(-j\varphi_{si}) \Psi_0(\omega - \omega_0) \exp(-j\omega t_{si})$ (see Section 2.2.1).

It follows from (2.16) that in (2.17), $\mathbf{f}(\omega) = \Phi^{-1}(\omega)$, i.e., the inverse of the PSD matrix for the external interferences and self-noises, $\Phi(\omega)$.

When wanted signals are deterministic (i.e., vector Θ is known), the second integrals in (2.14) and (2.17) may be discarded since they have no effect on received signal processing. By taking the natural logarithm of Λ we have, from (2.17), the optimum processing algorithm for deterministic signals

$$\ln \Lambda = L = \operatorname{Re} \frac{1}{2\pi} \int_{-\infty}^{\infty} \Phi^*(\omega, \Theta) \mathbf{f}(\omega) \chi(\omega) d\omega \quad (2.19)$$

The decision of whether a jammer is present in the GIDL resolution cell being probed can be obtained by comparing the decision variable L with a predetermined threshold which, in its turn, is determined by the allowable false alarm probability (the Neyman-Pearson criterion).

When wanted signals contain random parameters Θ , i.e., the signals are quasideterministic (e.g., fluctuating), the likelihood ratio (2.17) should be considered as conditional at a fixed Θ . The unconditional likelihood ratio can be obtained by averaging over Θ .

$$\begin{aligned} \tilde{\Lambda} &= \int_{\Theta} w(\Theta) \Lambda(\Theta) d\Theta = \int_{\Theta} w(\Theta) \exp[L(\Theta)] \\ &\times \exp \left[-\frac{1}{4\pi} \int_{-\infty}^{\infty} \Phi^*(\omega, \Theta) \mathbf{f}(\omega) \Phi(\omega, \Theta) d\omega \right] d\Theta \end{aligned} \quad (2.20)$$

where $w(\Theta)$ is the Probability Density Function (PDF) of Θ ; $L(\Theta)$ is determined by (2.19) and the integrals are taken over the total domain of $w(\Theta)$. The unconditional likelihood ratio determines the optimum processing algorithm for signals containing random parameters. The processing result (the decision variable $\tilde{\Lambda}$) should be compared with a threshold to make a decision as to the presence of jammer.

In many cases, the PDF, $w(\Theta)$, is not known or parameters Θ are nonrandom though unknown. In these cases an adaptive approach may be used. Following this approach, algorithm (2.19) is utilized which is optimum for known Θ , but in this case unknown Θ is replaced by its maximum likelihood estimate $\hat{\Theta}$ [120]. Then, instead of (2.19) we have

$$L = \text{Re} \frac{1}{2\pi} \int_{-\infty}^{\infty} \Phi^*(\omega, \hat{\Theta}) \mathbf{f}(\omega) \chi(\omega) d\omega \quad (2.21)$$

This algorithm is often called “the generalized likelihood ratio algorithm” (see, e.g., [121]).

The stochastic wanted signal, according to models introduced in Section 2.2.1, does not differ by its features from interferences. The log-likelihood ratio optimum processing algorithm in the frequency domain for Gaussian signals with deterministic correlation (covariance) matrices can be written in the form

$$L = \frac{1}{2\pi} \int_{-\infty}^{\infty} \chi^*(\omega) [\mathbf{f}(\omega) - \mathbf{f}_{\text{SI}}(\omega)] \chi(\omega) d\omega \quad (2.22)$$

where $\mathbf{f}(\omega)$ is the inverse matrix for the PSD matrix of the sum of external interferences and self-noises, $\Phi(\omega)$; $\mathbf{f}_{\text{SI}}(\omega)$ is the inverse matrix for the PSD matrix of the sum of wanted signals, external interferences and self-noises, $\Phi_{\text{SI}}(\omega) = \Phi_{\text{S}}(\omega) + \Phi(\omega)$.

When mutual phase shifts and/or intensities of wanted stochastic signals at the inputs of receiving antennae are random, correlation (covariance) matrices of such signals are quasideterministic. It means that $\Phi_{\text{SI}}(\omega)$ and hence, $\mathbf{f}_{\text{SI}}(\omega)$, contain random parameters, Θ . One can obtain the unconditional likelihood ratio by averaging over Θ :

$$\tilde{L} = \int_{\Theta} w(\Theta) \frac{\mathfrak{R}_1(\Theta)}{\mathfrak{R}_0} \exp \left\{ \frac{1}{4\pi} \int_{-\infty}^{\infty} \chi^*(\omega) [\mathbf{f}(\omega) - \mathbf{f}_{\text{SI}}(\omega)] \chi(\omega) d\omega \right\} d\Theta \quad (2.23)$$

where, as earlier, $w(\Theta)$ is the PDF of Θ ; the integral is taken over the domain of $w(\Theta)$; $\mathfrak{R}_1(\Theta)$ is the likelihood functional coefficient when the wanted signal is present; \mathfrak{R}_0 is the similar coefficient when the wanted signal is absent. If random parameters Θ are not connected with signal energy (for instance, phase shifts) then not only \mathfrak{R}_0 , but \mathfrak{R}_1 , does not depend on Θ . In these cases the ratio $\mathfrak{R}_1/\mathfrak{R}_0$, may be factored outside the integral sign and omitted.

Two remarks are necessary in closing. First, using the frequency domain in the above formulas does not mean that signal processing must be carried out in that domain. The frequency domain has been chosen here for simpler presentation of most relationships and for

the solution of principal equations. In practice, detection algorithms may be implemented in both the frequency and time domains depending on specific conditions. Second, here and in the subsequent sections continuous signals, interferences and noises are primarily considered in accordance with their actual physical form at the inputs of spatially separated antennae of any GIDL.

2.2.3 Detection of Stochastic Signals

As was mentioned in Section 2.2.1, detection of stochastic signals is the task of GIDL systems which receive signals from sources of “noise” radiation. The assumption that a correlation matrix of stochastic signals is completely known (deterministic correlation matrix) is a methodically convenient idealization similar to the assumption of the deterministic character of regular signals (Section 2.2.1).

There are a number of interference detection algorithms which could be used in GIDL. The choice of detection algorithm can depend on the operational situation, computational capacity of the GIDL, and other parameters. For the comprehensive analysis of detection algorithms for various signals and situations, the reader is referred to outside literature [88, 122, 123, 110].

In this section optimal detection of stochastic signals with known correlation matrices would be considered.

Synthesis of Optimum Detectors

For stochastic signal detection in a background of spatially uncorrelated interferences, Equation (2.22) takes the form

$$L = \frac{1}{2\pi} \int_{-\infty}^{\infty} \chi^*(\omega) [\mathbf{f}_n(\omega) - \mathbf{f}_{sn}(\omega)] \chi(\omega) d\omega \quad (2.24)$$

where $\chi(\omega)$ is the vector ($m \times 1$) of the Fourier transformations of received signals (realizations of sums of wanted signals plus noises or noises alone) at the inputs of m antennae within the observation time interval $(-T/2, T/2)$; $\mathbf{f}_n(\omega)$ and $\mathbf{f}_{sn}(\omega)$ are the inverse of the PSD noise and signal plus noise matrices, $\Phi_n(\omega)$ and $\Phi_{sn}(\omega)$, respectively. To specify the algorithm, L , the structure of the matrices $\mathbf{f}_n(\omega)$ and $\mathbf{f}_{sn}(\omega)$ should be revealed. By

the spatial independence of noises, $\Phi_n(\omega) = \mathbf{N}$ and $\mathbf{f}_n(\omega) = \mathbf{N}^{-1}$ are diagonal matrices. As was discussed in Section 2.2.1, Gaussian stochastic signals stationary within the interval $(-T/2, T/2)$ are stationary coupled when the differences between Doppler frequency shifts at the inputs of all antennae may be neglected: $\|\Delta\Omega_{si,k}T\| \ll 2\pi$, $i, k = \overline{1, m}$. In this case Doppler frequency shift common for all antennae may be included in the carrier frequency, ω_0 . And it is possible to write $\Phi_{sn}(\omega) = \mathbf{N} + \Phi_s(\omega)$ where an arbitrary element of the PSD matrix of the wanted signals at the inputs of m antennae, $\Phi_s(\omega)$, is determined by (2.12). To obtain $\mathbf{f}_{sn}(\omega) = \Phi_{sn}^{-1}(\omega)$, equation (2.12) is again used to form:

$$\Phi_{sn}(\omega) = \mathbf{N} + \Phi_s(\omega) = \mathbf{N} + F_s(\omega - \omega_0)\mathbf{U}(\omega)\mathbf{U}^*(\omega) \quad (2.25)$$

where $\mathbf{U}(\omega)$ is the m -dimensional vector with the following elements

$$U_i(\omega) = \sqrt{P_{si}/\Delta f_s} \exp[-j(\omega t_{si} + \varphi_{si})], \quad i = \overline{1, m} \quad (2.26)$$

For matrices having the form of (2.25), the simple inversion rule is used [114, 124]

$$\begin{aligned} \mathbf{f}_{sn}(\omega) &= \Phi_{sn}^{-1}(\omega) = \mathbf{N}^{-1} - \gamma F_s(\omega - \omega_0)\mathbf{N}^{-1}\mathbf{U}(\omega)\mathbf{U}^*(\omega)\mathbf{N}^{-1}; \\ \gamma &= [1 + F_s(\omega - \omega_0)\mathbf{U}^*(\omega)\mathbf{N}^{-1}\mathbf{U}(\omega)]^{-1} \end{aligned} \quad (2.27)$$

Substituting (2.26) into (2.27) yields the expression for each element of the matrix, $\mathbf{f}_{sn}(\omega)$:

$$f_{snik}(\omega) = \frac{1}{\sqrt{N_i N_k}} \left\{ \delta_{ik} - \frac{q_{si} q_{sk} F_s(\omega - \omega_0)}{1 + F_s(\omega - \omega_0) q_{s\Sigma}^2} \exp[j(\omega \tau_{sik} + \Delta\varphi_{sik})] \right\} \quad (2.28)$$

where

$$\tau_{sik} = t_{sk} - t_{si}; \quad \Delta\varphi_{sik} = \varphi_{sk} - \varphi_{si} \quad (2.29)$$

are the TDOA and phase difference of expected signals at the inputs of the i^{th} and k^{th} antennae;

$$q_{s\Sigma}^2 = \sum_{i=1}^m q_{si}^2 \quad (2.30)$$

and $q_{si}^2 = P_{si}/N_i \Delta f_s$ is the SNR at the input of the i^{th} antenna; δ_{ik} , is Kronecker's symbol. It follows from (2.29) that

$$\begin{aligned} \tau_{sik} &= -\tau_{ski}; \quad \Delta\varphi_{sik} = -\Delta\varphi_{ski}, \quad i, k = \overline{1, m} \\ \tau_{sik} + \tau_{skl} + \tau_{sli} &= 0; \quad \Delta\varphi_{sik} + \Delta\varphi_{skl} + \Delta\varphi_{sli} = 0, \quad i, k, l = \overline{1, m} \end{aligned} \quad (2.31)$$

Assigning (without loss of generality) the first antenna to be the “reference”, it is possible to write

$$\tau_{sik} = \tau_{si1} - \tau_{sk1}; \quad \Delta\varphi_{sik} = \Delta\varphi_{si1} - \Delta\varphi_{sk1} \quad (2.32)$$

Now taking into account that $f_{nik}(\omega) = \delta_{ik}/\sqrt{N_i N_k}$ and substituting this relationship, (2.28), and (2.32) into (2.24) yields the optimal algorithm in the form

$$L = \frac{1}{2\pi} \int_{-\infty}^{\infty} \left| H(\omega) \sum_{i=1}^m \frac{q_{si} \exp(-j\Delta\varphi_{si1})}{\sqrt{N_i}} \chi_i(\omega) \exp(-j\omega\tau_{si1}) \right|^2 d\omega \quad (2.33)$$

where

$$\|H(\omega)\|^2 = F_s(\omega - \omega_0)/[1 + F_s(\omega - \omega_0)q_{s\Sigma}^2] \quad (2.34)$$

When the condition $\|\Delta\Omega_{si,k}T\| \ll 2\pi$, $i, k = \overline{1, m}$ is not satisfied, the stationary Gaussian signals at the inputs of receiving antennae turn out to be nonstationary coupled. An arbitrary element of the correlation matrix then takes the form of (2.7) and an arbitrary element of the power spectral density (PSD) matrix takes the form of (2.10). The more complicated expression for the optimal signal processing must be considered instead of (2.24).

$$\begin{aligned} L = & \sum_{i=1}^m \sum_{k=1}^m \frac{1}{4\pi^2} \int_{-\infty}^{\infty} \int_{-\infty}^{\infty} \chi_i^*(\omega_1) \chi_k(\omega_2) \\ & \times \int_{-\infty}^{\infty} [\tilde{f}_{nik}(\omega_1, t) - \tilde{f}_{snik}(\omega_1, t)] \exp(j\omega_2 t) dt d\omega_1 d\omega_2 \end{aligned} \quad (2.35)$$

The functions $\tilde{f}_{nik}(\omega, t)$ and $\tilde{f}_{snik}(\omega, t)$ are Fourier transformations (with respect to the argument, t_1 , of the elements $R_{nik}(t_1, t_2)$ and $R_{snik}(t_1, t_2)$ of the matrices $\mathbf{R}_n(t_1, t_2)$ and $\mathbf{R}_{sn}(t_1, t_2)$, respectively). The last matrices are solutions of the equation (2.15). From (2.15) we can immediately obtain a system of equations for $\tilde{f}_{nik}(\omega, t)$ and $\tilde{f}_{snik}(\omega, t)$. By integrating over infinite limits, applying Fourier transformation to both sides with respect to the argument $t_1 - t_2$, carrying out the change of variables and employing (2.10) we have

$$\tilde{f}_{nik}(\omega, t) = (\delta_{ik}/N_i) \exp(-j\omega t), \quad i, k = \overline{1, m} \quad (2.36)$$

The functions $\tilde{f}_{snik}(\omega, t)$ can be found as solutions of the following system of equations

$$\begin{aligned} & \sum_{k=1}^m \sqrt{N_i N_k} [\delta_{ik} + q_{si} q_{sk} F_s(\omega - \omega_0 - \Omega_{si})] \\ & \times \exp\{j[(\omega - \Omega_{si})\tau_{sik} + \Delta\psi_{sik}]\} \tilde{f}_{snik}(\omega - \Delta\Omega_{sik}, t) \exp(j\omega t) = \delta_{ik}, \quad i, l = \overline{1, m} \end{aligned} \quad (2.37)$$

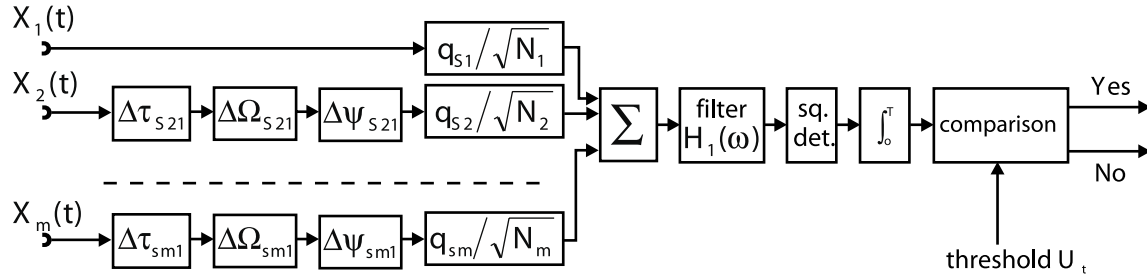


Figure 2.2: Structure of the optimum detector for stochastic signals with a known correlation (covariance) matrix

As can be verified by substitution these solutions take the form

$$\tilde{f}_{snik}(\omega, t) = \frac{\exp[-j[(\omega + \Delta\Omega_{sik})t]]}{\sqrt{N_i N_k}} \left[\delta_{ik} - \frac{q_{si} q_{sk} F_s(\omega - \omega_0 - \Omega_{si})}{1 + F_s(\omega - \omega_0 - \Omega_{si}) q_{s\Sigma}^2} \right] \times \exp \{ j[(\omega - \Omega_{si})\tau_{sik} + \Delta\psi_{sik}] \} \quad (2.38)$$

Using (2.36), (2.38) and (2.32) and assuming the first antenna to be the reference one yields the optimal processing algorithm (2.35) in the following form

$$L = \frac{1}{2\pi} \int_{-\infty}^{\infty} \left| H_1(\omega) \sum_{i=1}^m \frac{q_{si} \exp(-j\Delta\psi_{si1})}{\sqrt{N_i}} \chi_i(\omega - \Delta\Omega_{si1}) \exp[-j(\omega - \Omega_{s1})\tau_{si1}] \right|^2 d\omega \quad (2.39)$$

where

$$|H_1(\omega)|^2 = F_s(\omega - \omega_0 - \Omega_{s1}) / [1 + F_s(\omega - \omega_0 - \Omega_{s1}) q_{s\Sigma}^2] \quad (2.40)$$

Comparing (2.39) with (2.33) shows that determining the difference of expected signal Doppler frequencies at the inputs of receiving antennae requires equalization of the signal carrier frequencies before summation.

The structural scheme of the obtained optimum detector is presented in Figure 2.2. Received signals pass through delay lines, phase shifters and (if necessary) frequency shifters which provide equalization in time delays, phase and central (carrier) frequencies with respect to the reference antenna. Then weighted summation, filtration, square envelope detection and integration are carried out. It may be said that the scheme of Figure 2.2 provides an estimate of the power (energy) of the coherent weighted and filtered sums of (wanted) received signals. When input wanted signals are strong ($q_{s\Sigma}^2 \gg 1$), the filter in Figure 2.2

may be dropped. When input wanted signals are weak ($q_{s\Sigma}^2 \ll 1$) which more often occurs in practice, this filter is necessary and the squared modulus of its transfer function is equal to the PSD of the wanted signal at the reference antenna. If wanted signals are stationary coupled at the inputs of spatially separated antennae, frequency shifters $\Delta\Omega_{si1}$, $i = \overline{2, m}$, should be excluded from the scheme in Figure 2.2. (This is the case for practical GIDL demonstration.)

When the influence of antenna directivity patterns (ADP) is to be taken into account, then additional multipliers—complex ADPs, $g_i(\beta_{si}, \epsilon_{si}, \omega)$, should be included into the sums (2.33) and (2.39). It should be noted that the scheme in Figure 2.2 after the summator does not differ from the so called “energy receiver” which is the optimal monostatic detector for Gaussian stochastic signals.

Performance Analysis of Optimum Detectors

It is necessary to obtain the probability distribution of the variable, L , from (2.33) and (2.39) when wanted signals are absent and when they are present. It is seen from Figure 2.2 that the optimum processing includes a nonlinear operation: the square-law envelope detection of the sum of Gaussian stochastic processes. Therefore, the variable L is in general non-Gaussian (Rician). In this particular case, if discrete processing is employed and the signal PSD is rectangular with bandwidth, Δf_s , the variable L is chi-square distributed with $2\Delta f_s T$ degrees of freedom ($\Delta f_s T$ independent complex samples and each of these consists of two quadratures). However, usually $\Delta f_s T \gg 1$ (e.g., $\Delta f_s T \approx 10^3 - 10^4$). In this case it is possible to consider that the integration provides the effective normalization of the output process from the square envelope detector such that the variable L may be assumed to be Gaussian with practically sufficient accuracy. Then it is only necessary to derive mean values and variances of the variable L in the absence and in the presence of expected signals [106, 109, 110].

Let us consider the more general expression (2.39). The mean value can be written as

$$\begin{aligned} \overline{L} = & \frac{1}{2\pi} \int_{-\infty}^{\infty} |H_1(\omega)|^2 \sum_{i=1}^m \sum_{k=1}^m \frac{q_{si} q_{sk} \exp[-j(\Delta\psi_{si1} - \Delta\psi_{sk1})]}{\sqrt{N_i N_k}} \\ & \times \overline{\chi_i(\omega - \Delta\Omega_{si1}) \chi_k^*(\omega - \Delta\Omega_{sk1})} = \exp[-j(\omega - \Omega_{s1})(\tau_{si1} - \tau_{sk1})] d\omega \end{aligned} \quad (2.41)$$

The spectra, $\chi_i(\omega)$ and $\chi_k(\omega)$, are to be shifted by $\Delta\Omega_{si1}$ and $\Delta\Omega_{sk1}$, $i, k = \overline{2, m}$, respectively. Then signal central frequencies at all antennae become equal to $\omega_0 + \Omega_{si1}$ (since, according to (2.8), $\Omega_{si} + \Omega_{si1} = \Omega_{s1}$, $i = \overline{2, m}$). This means that all received signals turn out to be stationary coupled. Using (2.12) it can be shown that when wanted signals are present and $\Delta f_s T \gg 1$

$$\begin{aligned} \overline{\chi_i(\omega - \Delta\Omega_{si1})\chi_k^*(\omega - \Delta\Omega_{sk1})} &= 2T\Phi_{snik}(\omega - \Omega_{s1}) \\ &= 2T\sqrt{N_i N_k} \{\delta_{ik} + q_{si}q_{sk}F_s(\omega - \omega_0 - \Omega_{s1})\} \\ &\quad \times \exp\{j[(\omega - \Omega_{s1})\tau_{sik} + \Delta\psi_{sik}]\} \end{aligned} \quad (2.42)$$

If wanted signals are absent, $q_{si} = q_{sk} = 0$ in (2.42) and the right side of (2.42) is equal to $2TN_i\delta_{ik}$. Substituting (2.42) in (2.41) yields mean values of L in the absence and in the presence of wanted signals

$$m_{10} = m_1\{L_0\} = \bar{L}_0 = \frac{q_{s\Sigma}^2 T}{\pi} \int_{-\infty}^{\infty} \frac{F_s(\omega - \omega_0 - \Omega_{s1})d\omega}{1 + F_s(\omega - \omega_0 - \Omega_{s1})q_{s\Sigma}^2}; \quad (2.43)$$

$$m_{11} = m_1\{L_1\} = \bar{L}_1 = \frac{q_{s\Sigma}^2 T}{\pi} \int_{-\infty}^{\infty} F_s(\omega - \omega_0 - \Omega_{s1})d\omega \quad (2.44)$$

To calculate variances of L , the fourth moment of $\chi_i(\omega - \Delta\Omega_{si1})$, $i = \overline{1, m}$ should be obtained. For jointly Gaussian variables, the following expression of the fourth moment through the second moments is known [125]

$$\begin{aligned} &\overline{\chi_i(\omega_1 - \Delta\Omega_{si1})\chi_k^*(\omega_1 - \Delta\Omega_{sk1})\chi_p(\omega_2 - \Delta\Omega_{sp1})\chi_q^*(\omega_2 - \Delta\Omega_{sq1})} = \\ &= \overline{\chi_i(\omega_1 - \Delta\Omega_{si1})\chi_k^*(\omega_1 - \Delta\Omega_{sk1})\chi_p(\omega_2 - \Delta\Omega_{sp1})\chi_q^*(\omega_2 - \Delta\Omega_{sq1})} \\ &\quad + \overline{\chi_i(\omega_1 - \Delta\Omega_{si1})\chi_q^*(\omega_2 - \Delta\Omega_{sq1})\chi_k(\omega_1 - \Delta\Omega_{sk1})\chi_p^*(\omega_2 - \Delta\Omega_{sp1})} \end{aligned} \quad (2.45)$$

In addition,

$$\overline{\chi_i(\omega_1 - \Delta\Omega_{si1})\chi_q^*(\omega_2 - \Delta\Omega_{sq1})} = 4\pi\Phi_{iq}(\omega_1 - \Omega_{s1})\delta(\omega_1 - \omega_2) \quad (2.46)$$

Taking into account (2.45) and (2.46), it is possible to obtain expressions for variances of L when wanted signals are absent (M_{20}) and they are present (M_{21})

$$M_{20} = M_2\{L_0\} = \overline{L_0^2} - (\bar{L}_0)^2 = \frac{2(q_{s\Sigma}^2)^2 T}{\pi} \int_{-\infty}^{\infty} \frac{F_s^2(\omega - \omega_0 - \Omega_{s1})d\omega}{[1 + F_s(\omega - \omega_0 - \Omega_{s1})q_{s\Sigma}^2]^2}; \quad (2.47)$$

$$M_{21} = M_2\{L_1\} = \overline{L_1^2} - (\bar{L}_1)^2 = \frac{2(q_{s\Sigma}^2)^2 T}{\pi} \int_{-\infty}^{\infty} F_s^2(\omega - \omega_0 - \Omega_{s1}) d\omega \quad (2.48)$$

It is seen that the main energy parameter is the summed signal-to-noise ratio (SNR) at the inputs of all receiving antennae, $q_{s\Sigma}^2$. It should be noted that the number of antennae, m , has only an indirect effect through the sum, $q_{s\Sigma}^2 = \sum_{i=1}^m q_{si}^2$. Note that the mean values and variances of L depend on the duration of received signal realization (observation interval), T , and on certain integral parameters of signal power spectra.

Detection characteristics are determined by the expressions (2.43), (2.44), (2.47), and (2.48)

$$\begin{aligned} P_{fa} &= 0.5[1 - \text{erf}(y_0/\sqrt{2})]; \\ P_d &= 0.5[1 - \text{erf}(y_0/\sqrt{M_{20}/2M_{21}} - (m_{11} - m_{10})/\sqrt{2M_{21}})] \end{aligned} \quad (2.49)$$

where $\text{erf}(x)$ is the error function, and y_0 is the threshold level. For a given false alarm probability, P_{fa} , it is possible to calculate y_0 from the first equation of (2.49). Substituting y_0 in the second equation of (2.49) yields detection probability, P_d .

The obtained results are valid for the case where wanted signals are stationary coupled at the inputs of spatially separated receiving antennae, and the optimal signal processing is determined by (2.33). For this case, Ω_{s1} in (2.43), (2.44), (2.47) and (2.48) should be omitted (set to zero).

Example.

Let a jammer PSD have the rectangular form, as expected for a broadband stationary jammers. This model approximates the jammer used during GIDL experiments and demonstrations.

$$F_s(\omega - \omega_0 - \Omega_{s1}) = \begin{cases} 1, & |\omega - \omega_0 - \Omega_{s1}| \leq \Delta\omega_s/2; \\ 0, & |\omega - \omega_0 - \Omega_{s1}| > \Delta\omega_s/2 \end{cases} \quad (2.50)$$

Then from (2.43), (2.44), and (2.47)-(2.50), it follows that

$$\begin{aligned} m_{10} &= \frac{2q_{s\Sigma}^2 n}{1 + q_{s\Sigma}^2}; & m_{11} &= 2q_{s\Sigma}^2 n; \\ M_{20} &= \frac{4(q_{s\Sigma}^2)^2 n}{(1 + q_{s\Sigma}^2)^2}; & M_{21} &= 4(q_{s\Sigma}^2)^2 n; \end{aligned} \quad (2.51)$$

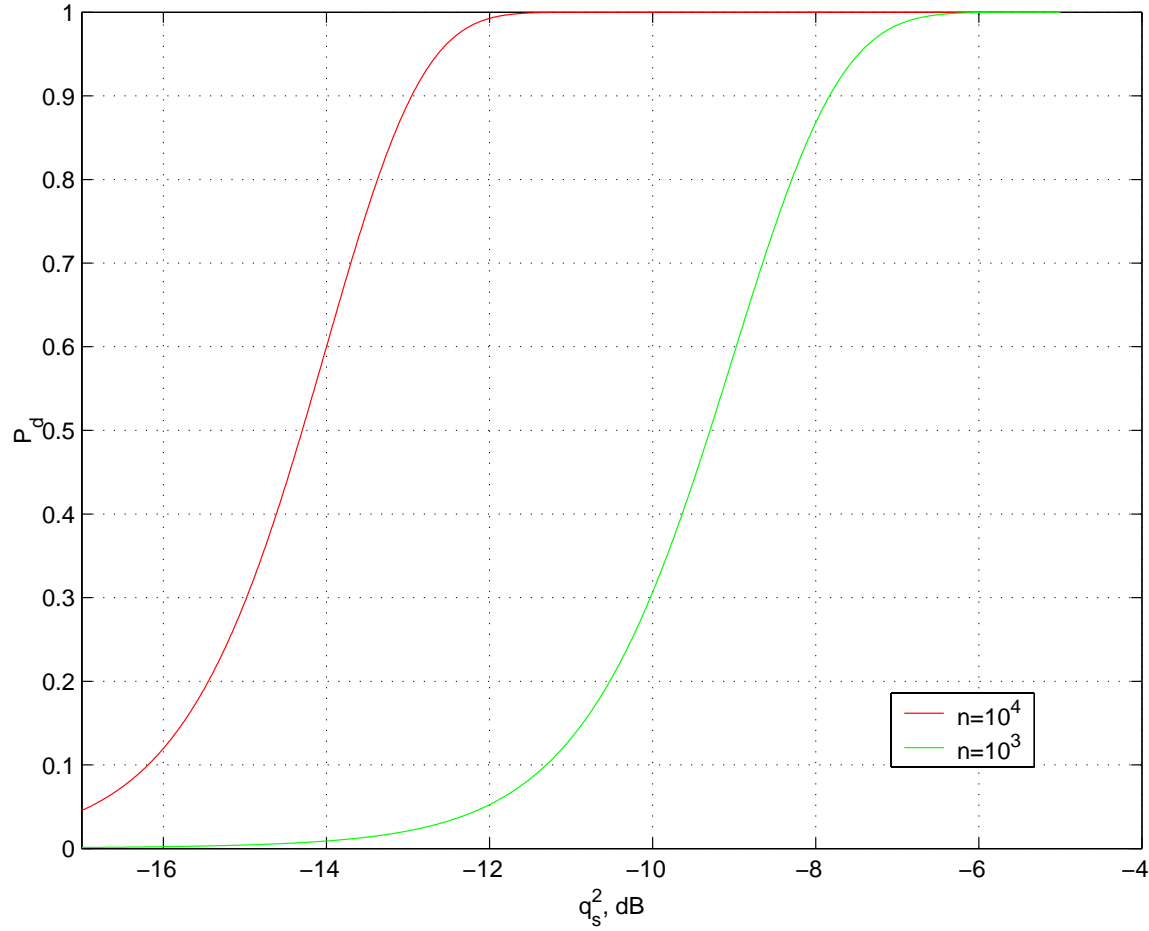


Figure 2.3: Detection characteristics of the optimum detector for stochastic signals with known correlation matrix, $P_{fa} = 10^{-4}$ and n : 10^3 and 10^4

$$\begin{aligned}
 P_{fa} &= 0.5[1 - \text{erf}(y_0/\sqrt{2})]; \\
 P_d &= 0.5 \left\{ 1 - \text{erf} \left[\frac{y_0 - q_{s\Sigma}^2 \sqrt{n}}{\sqrt{n}(1 + q_{s\Sigma}^2)} \right] \right\}
 \end{aligned} \tag{2.52}$$

The signal accumulation (integration) factor, $n = \Delta f_s T$, is determined by the number of independent samples of a stochastic process accumulated by the integrator in Figure 2.2.

Detection characteristics calculated from (2.52) are plotted in Figure 2.3 for $P_{fa} = 10^{-4}$ and two values of n : 10^3 and 10^4 .

2.3 Jammer Localization

Once a jammer has been detected, localization may begin, which is the ultimate goal of the GIDL. This section would discuss possible ways to localize it.

2.3.1 Jammer Position and Velocity Measurement Methods. One-Stage And Two-Stage Algorithms

Two approaches are possible to the problem of composite measurement formation from individual measurements. It is possible to combine signals received by all antennae and estimate jammer coordinates (and their derivatives) directly from all individual measurements of this summed signal. Such one-stage algorithms are considered in section 2.3.2. Two-stage algorithms are much simpler and more widely used. At the first stage, jammer coordinates are estimated with respect to selected in advance pair of antennae (not all possible pairs of antennae are used), yielding so-called jammer local, or “primary”, coordinates. At the second stage, these local coordinate estimates are combined so as to form a resultant composite measurement, i.e., the estimates of global, or “final” jammer coordinates and, possibly, their derivatives in a GIDL coordinate reference system referenced to a specific time.

Using the hyperbolic method, the position of a jammer is determined via range differences (RD) of the jammer with respect to spatially separated antennae. Therefore, it is also called the range-difference measurement method. Each measured value of the jammer range difference relative to a pair of antennae gives rise to the surface of position (SOP) being a hyperboloid of revolution with its foci at these antennae sites. The jammer position in space is determined by the intersection point of three hyperboloids. Jammer range errors rapidly increase (approximately in the square law) with the increase of jammer range.

The hyperbolic method is used where the one-way signal propagation time from a jammer to receiving antennae (i.e., the jammer range or range sum) cannot be measured [126, 127, 108], which is always the case for GIDL. The range difference of a jammer with respect to each pair of receiving antennae is evaluated using the TDOA measurement with the help of a correlation technique. In the simplest case, signals received by a pair of receiving

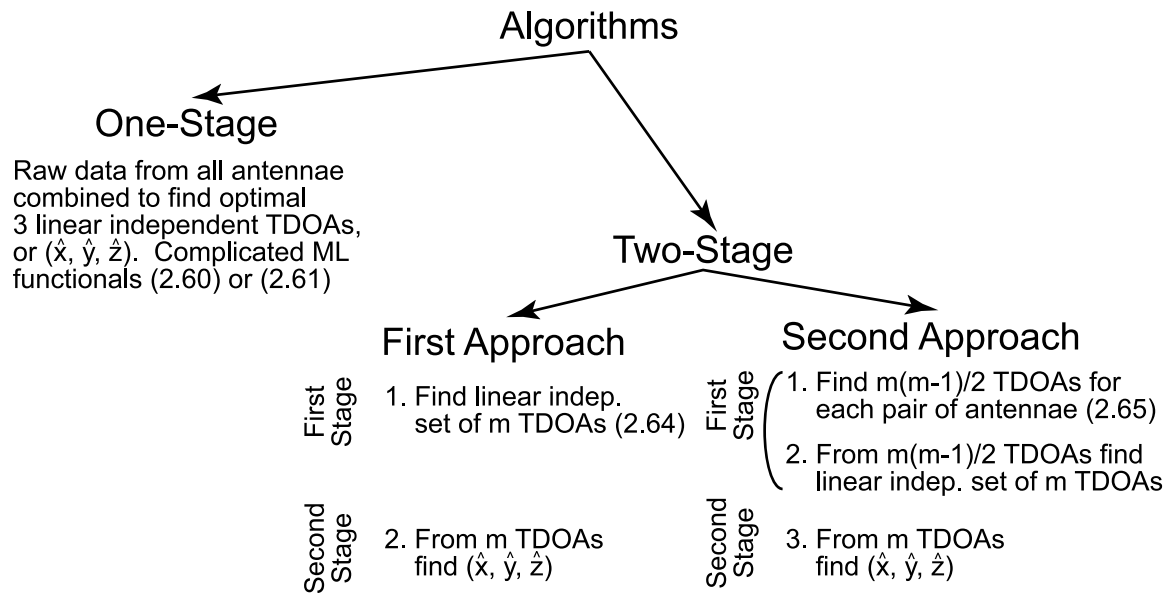


Figure 2.4: Algorithm Classification

antennae from a radiation source are conveyed to correlator inputs with the signal from one of the antennae has been passed through a variable delay line. A delay value corresponding to the maximum of the correlator output, cancels out the signal TDOA at the correlator inputs. Having measured this delay value, one can calculate the range difference from the radiation source to the receiving stations. It should be emphasized that this procedure does not require *a priori* information for either the signal waveform or the time of signal transmission by the source. These properties make the hyperbolic method suitable for radiation source localization when signal waveforms are *a priori* unknown. To obtain three spatial coordinates of a radiation source (e.g., a jammer) using the hyperbolic method, at least four receiving antennae are necessary. (If jammer altitude is known, the three.)

Graphical representation of the classification to one-stage and two stage algorithms and to first a second approaches for the two-stage algorithm is shown in Figure 2.4.

2.3.2 One-Stage Optimum Coordinate Measurement In GIDL Using Temporal Signal Parameters

One of the important advantages of GIDL is the ability to determine three coordinates of a jammer with high accuracy using only temporal signal parameter measurements. Such temporal parameters are signal TDOAs at each pair of receiving antennae, determining range differences for a radiation source.

One-stage optimum algorithms for the jammer spatial position determination using temporal signal parameter measurements are now considered [106, 110]. One-stage algorithms permit direct jammer localization in space using signal parameter estimation even with a redundant number of antennae. These algorithms may determine the three jammer spatial coordinates themselves or three linearly independent TDOAs, τ_{12} , τ_{13} , τ_{14} , where numbering of antennae is arbitrary without any loss of generality. For a known geometry of antennae, the problem of determining the jammer coordinates is then reduced to the problem of a conversion of variables. As is well known, such a conversion is mutually single-valued if its Jacobian is non-zero. (There is still exists possibility of the ambiguity that could be resolved separately.) Due to the to one-to-one correspondence, the optimality of signal TDOA estimates in accordance with any criterion ensures the optimality of coordinate estimates according to the same criterion.

A priori probability distributions of signal parameters to be estimated, are usually much wider than their likelihood functions. Therefore, the maximum likelihood criterion for estimate optimization is adopted. The signal and interference models are assumed to be the same as for the detection problems (see Section 2.2.1).

Stochastic signals and interferences are assumed to be stationary and stationary coupled Gaussian random processes as before. The likelihood ratio with respect to the vector, Θ , of unknown parameters can be written from (2.23)

$$\Lambda = \frac{\mathfrak{R}_1(\Theta)}{\mathfrak{R}_0} \exp \left\{ \frac{1}{4\pi} \int_{-\infty}^{\infty} \chi^*(\omega) [\mathbf{f}(\omega) - \mathbf{f}_{\text{sl}}(\omega, \Theta)] \chi(\omega) d\omega \right\} \quad (2.53)$$

Here \mathfrak{R}_1 is likelihood functional coefficient when the wanted signal is present; \mathfrak{R}_0 is the similar coefficient when the wanted signal is absent. It can be shown that in the general case (taking into account possible dependence, \mathfrak{R}_1 , on Θ), a likelihood equation system

determining the optimum estimate of the n -dimensional vector, Θ , is given by

$$\sum_{i=1}^m \sum_{k=1}^m \frac{1}{2\pi} \int_{-\infty}^{\infty} [2T \partial \Phi_{slik}^*(\omega, \Theta) / \partial \Theta_l] f_{slik}(\omega, \Theta) + \chi_i^*(\omega) \chi_k(\omega) [\partial f_{slik}(\omega, \Theta) / \partial \Theta_l] d\omega = 0, \quad l = \overline{1, n} \quad (2.54)$$

where $\Phi_{slik}(\omega, \Theta)$, $f_{slik}(\omega, \Theta)$, and $\chi_i(\omega)$ are the elements of the matrices, $\Phi_{sI}(\omega, \Theta)$ and $\mathbf{f}_{sI}(\omega, \Theta)$, and the vector, $\chi(\omega)$.

Consider the practical case where interference spatial correlation is absent or may be neglected and the signal correlation matrix is quasideterministic. Let us start from the estimation of three linearly independent TDOAs. In a GIDL containing m receiving antennae there are $m(m-1)/2$ pairs of antennae, and $m(m-1)/2$ different TDOAs, τ_{slik} , $i, k = \overline{1, m}$, $i < k$. However, only $m-1$ TDOAs among these are linearly independent (see (2.31)). Let us denote these TDOAs by $\tau_{s12}, \dots, \tau_{s1m}$ (numbering of antennae is arbitrary). In the three-dimensional physical space, three linearly independent TDOAs determine all those remaining. For a GIDL of known geometry:

$$\tau_{slik} = \tilde{h}_{ik}(\tau_{s12}, \tau_{s13}, \tau_{s14}), \quad \begin{cases} k \geq 5, & i = 1; \\ k \geq i + 1, & i > 1, \end{cases} \quad i, k = \overline{1, m}. \quad (2.55)$$

Here, a signal model with mutually independent initial phases of the correlation matrix is assumed, with signal intensities (variances) known. Under these assumptions, the vector, Θ , contains $m(m-1)/2$ noninformative phase differences and three informative TDOAs

$$\Theta = (\Delta\varphi_{s12}, \dots, \Delta\varphi_{sm(m-1)}, \tau_{s12}, \tau_{s13}, \tau_{s14}) \quad (2.56)$$

Assuming the noises to be white, we can employ expressions (2.25)-(2.30) for $\Phi_{slik}(\omega, \Theta)$ and $f_{slik}(\omega, \Theta)$. When the vector, Θ , of unknown parameters is expressed by (2.56), the first term under the integral in (2.54) is equal to zero since \Re_1 in (2.53) does not depend on Θ (all unknown parameters do not relate to signal energy). Substituting (2.28) we can

transform (2.54) to the form

$$\begin{aligned}
L = & \operatorname{Re} \sum_{k=2}^4 \frac{q_{s1} q_{sk} \exp(j\Delta\varphi_{s1k})}{\sqrt{N_1 N_k}} \frac{1}{2\pi} \int_{-\infty}^{\infty} \chi_1^*(\omega) \chi_k(\omega) |H(\omega)|^2 \exp(j\omega\tau_{s1k}) d\omega \\
& + \operatorname{Re} \sum_{i=1}^{m-1} \sum_{k=i+1; \text{for } i=1 \text{ } k \neq 2,3,4} \frac{q_{si} q_{sk} \exp(j\Delta\varphi_{sik})}{\sqrt{N_i N_k}} \frac{1}{2\pi} \int_{-\infty}^{\infty} \chi_i^*(\omega) \chi_k(\omega) |H(\omega)|^2 \\
& \times \exp[j\omega \tilde{h}_{ik}(\tau_{s12}, \tau_{s13}, \tau_{s14})] d\omega \rightarrow \max(\Delta\varphi_{s12}, \dots, \Delta\varphi_{sm(m-1)}, \tau_{s12}, \tau_{s13}, \tau_{s14})
\end{aligned} \quad (2.57)$$

where the squared modulus of the filter frequency response is given by

$$\|H(\omega)\|^2 = \frac{F_s(\omega - \omega_0)}{1 + F_s(\omega - \omega_0) q_{s\Sigma}^2}; \quad q_{s\Sigma}^2 = \sum_{i=1}^m q_{si}^2 \quad (2.58)$$

Here $F_s(\omega - \omega_0)$ is the normalized PSD of the signal complex envelope [see (2.11)]; ω_0 is the carrier frequency. Maximum L in (2.57) for independent $\Delta\varphi_{sik}$ is reached when each term of the sum has its own maxima. Hence the maximum likelihood estimates of $\Delta\varphi_{sik}$ are as follows:

$$\widehat{\Delta\varphi_{sik}} = -\arg \left[\frac{1}{2\pi} \int_{-\infty}^{\infty} \chi_i^*(\omega) \chi_k(\omega) |H(\omega)|^2 \exp(j\omega\tau_{sik}) d\omega \right] \quad (2.59)$$

where τ_{sik} for $i = 1, k \geq 5$ and for $i > 1, k \geq i + 1$ are determined by (2.55). To obtain an optimum (maximum likelihood) algorithm for estimating τ_{s12} , τ_{s13} and τ_{s14} , (2.57) is substituted into (2.59). The optimum estimation algorithm is given by

$$\begin{aligned}
L = & \sum_{k=2}^4 \frac{q_{s1} q_{sk}}{\sqrt{N_1 N_k}} \left| \frac{1}{2\pi} \int_{-\infty}^{\infty} \chi_1^*(\omega) \chi_k(\omega) |H(\omega)|^2 \exp(j\omega\tau_{s1k}) d\omega \right| \\
& + \sum_{i=1}^{m-1} \sum_{k=i+1; \text{for } i=1 \text{ } k \neq 2,3,4} \frac{q_{si} q_{sk}}{\sqrt{N_i N_k}} \left| \frac{1}{2\pi} \int_{-\infty}^{\infty} \chi_i^*(\omega) \chi_k(\omega) |H(\omega)|^2 \right. \\
& \times \exp[j\omega \tilde{h}_{ik}(\tau_{s12}, \tau_{s13}, \tau_{s14})] d\omega \left. \right| \rightarrow \max(\tau_{s12}, \tau_{s13}, \tau_{s14})
\end{aligned} \quad (2.60)$$

Thus, the one-stage algorithm (2.60) for optimum estimation of the independent signal TDOAs, τ_{s12} , τ_{s13} , τ_{s14} , requires performing the following procedures. The input signal at each antenna undergoes preliminary filtration. From the outputs of the filters, the signals from all antennae are applied to the inputs of correlators for all $m(m-1)/2$ pairs of antennae. Then the values of $\hat{\tau}_{s12}$, $\hat{\tau}_{s13}$, $\hat{\tau}_{s14}$ are determined. These correspond to maxima of

the moduli of estimates of correlation between signals received by the first and the second, the first and the third, and the first and the fourth antennae. Numbering of pairs of antennae is arbitrary. It is reasonable to use those pairs whose moduli maxima are large and have the largest effective baselengths. Knowing $\hat{\tau}_{s12}, \hat{\tau}_{s13}, \hat{\tau}_{s14}$, the point in space corresponding to this triad is determined and the values of functions $\tilde{h}_{ik}(\hat{\tau}_{s12}, \hat{\tau}_{s13}, \hat{\tau}_{s14})$ are calculated. For a known GIDL geometry, this may be done using relationships from [26] and other publications. The quantity, L , is then evaluated according to (2.60). Using a suitable selection of combinations of $\hat{\tau}_{s12}, \hat{\tau}_{s13}, \hat{\tau}_{s14}$, a maximum of L is achieved. The combination of $\hat{\tau}_{s12}, \hat{\tau}_{s13}, \hat{\tau}_{s14}$ for which L reaches its maximum is adopted as an optimum estimate. This combination determines an optimum estimate of the radiation source's three spatial coordinates. Of course, only those maxima of L are taken into account which exceed a predetermined detection threshold.

As for regular signals, the one-to-one correspondence between the set of triads, $\hat{\tau}_{s12}, \hat{\tau}_{s13}, \hat{\tau}_{s14}$, and the set of points with spatial coordinates $(\hat{x}, \hat{y}, \hat{z})$ in the three-dimensional space leads to the optimum algorithm (2.60) being rewritten in another equivalent form

$$L = \sum_{i=1}^{m-1} \sum_{k=i+1}^m \frac{q_{si}q_{sk}}{\sqrt{N_i N_k}} \left| \frac{1}{2\pi} \int_{-\infty}^{\infty} \chi_i^*(\omega) \chi_k(\omega) |H(\omega)|^2 \times \exp[j\omega \tau_{sik}(x, y, z)] d\omega \right| \quad (2.61)$$

$\rightarrow \max(x, y, z)$

The algorithm (2.61) can be derived directly from (2.53) and (2.54) in a similar manner to (2.60). If $\tau_{sik}, i, k = \overline{1, m}, i < k$, are expressed as functions of spatial coordinates, then $\tau_{sik} = \tau_{sik}(x, y, z)$.

This approach requires analyzing all points in the whole region where radiation sources may exist. The former approach, according to (2.60), permits reduction of the entire spatial search region to one or several small regions in the vicinities of points determined by the values of $\hat{\tau}_{s12}, \hat{\tau}_{s13}, \hat{\tau}_{s14}$ corresponding to maxima of three cross-correlation estimate moduli. In this case the search for cross-correlation envelope maxima is necessary. However, (2.60) is more complicated to compute than (2.61). As in the case of regular signals (see above), the best implementation is likely a combination of both approaches. First, large correlation peaks should be found and values of $\hat{\tau}_{s12}, \hat{\tau}_{s13}, \hat{\tau}_{s14}$ plus the spatial coordinates $(\hat{x}, \hat{y}, \hat{z})$ of corresponding points should be determined. Then the algorithm (2.61) may be employed in the vicinities of those points.

Let us turn to the case where signal intensities are unknown (random). The most realistic situation in which intensity fluctuations at the inputs of different antennae are completely mutually dependent is now considered. In this case, the vector, Θ , in (2.56) has an additional parameter which may (without loss of generality) be assumed to be the SNR at the first antenna, q_{s1}^2 . Then $q_{rmsi}^2 = A_{i1}^2 q_{s1}^2, i = \overline{2, m}$, where A_{i1}^2 are the known quantities. The substitution of this expression in (2.54) and (2.57) shows that q_{si}^2 is a common factor which does not influence the estimates of $\Delta\varphi_{sik}$ and $\hat{\tau}_{s12}, \hat{\tau}_{s13}, \hat{\tau}_{s14}$. This means that if unknown quantities, q_{si} , are replaced by $A_{i1}, i = \overline{2, m}$ the algorithm (2.60) and its equivalent (2.61) are optimal for unknown mutually dependent signal intensities.

2.3.3 Signal TDOA Measurement For Two-Stage Radiation Source Localization By GIDL

For GIDL, the first stage of two-stage radiation source localization implies measurement algorithms for signal TDOAs which are proportional to the jammer (radiation source) range differences. The most interesting stochastic signals in practice have quasideterministic correlation (covariance) matrices containing random phases and variances (signal intensities, see Section 2.2.1); these are now considered. For a GIDL with m receiving antennae, two different approaches are possible for the optimum TDOA estimation. The first approach (which may be referred to as a one-step approach) implies direct optimal estimation of $m - 1$ linearly independent signal TDOAs, $\tau_{s12}, \dots, \tau_{s1m}$, utilizing signals received by all the m antennae. These $m - 1$ optimum TDOA estimates, $\hat{\tau}_{s12}, \dots, \hat{\tau}_{s1m}$, are used for the optimal estimation of radiation source spatial coordinates, $\hat{x}, \hat{y}, \hat{z}$, at the second stage of a radiation source localization algorithm. The second approach (which may be referred to as a two-step approach) implies at the first step optimal estimation of all the $m(m-1)/2$ signal TDOAs, $\tau_{sik}, i, k = \overline{1, m}, i < k$, individually. Then, at the second step, optimum estimates, $\hat{\tau}_{s12}, \dots, \hat{\tau}_{s1m}$, of $m - 1$ linearly independent TDOAs are calculated using the obtained estimates, $\hat{\tau}_{s12}, \dots, \hat{\tau}_{s1m}, \hat{\tau}_{s23}, \dots, \hat{\tau}_{s2m}, \dots, \hat{\tau}_{s(m-1)m}$. The second stage of a two-stage source localization algorithm is the same as the first approach alone (see, e.g., [128, 110]).

An optimum algorithm for TDOA estimation according to the first approach can be derived as in Section 2.3.2. Using (2.57) without (2.55) an optimum algorithm evolves in

the form

$$L = \text{Re} \sum_{i=1}^{m-1} \sum_{k=i+1}^m \frac{q_{si} q_{sk} \exp(j\Delta\varphi_{sik})}{\sqrt{N_i N_k}} \frac{1}{2\pi} \int_{-\infty}^{\infty} \chi_i^*(\omega) \chi_k(\omega) |H(\omega)|^2 \times \exp[j\omega(\tau_{s1k} - \tau_{s1i})] d\omega \rightarrow \max(\Delta\varphi_{s12}, \dots, \Delta\varphi_{sm(m-1)}, \tau_{s12}, \tau_{s13}, \tau_{s14}) \quad (2.62)$$

where it should be taken into account that $\tau_{s11} = 0$. Assuming (as in Section 2.3.2) all phases, $\Delta\varphi_{sik}$, $i, k = \overline{1, m}$, $i < k$, to be mutually independent it is possible to obtain their maximum likelihood estimates

$$\widehat{\Delta\varphi_{sik}} = -\arg \left\{ \frac{1}{2\pi} \int_{-\infty}^{\infty} \chi_i^*(\omega) \chi_k(\omega) |H(\omega)|^2 \exp[j\omega(\tau_{s1k} - \tau_{s1i})] d\omega \right\} \quad (2.63)$$

and substitute them for random phases, $\Delta\varphi_{sik}$, in (2.62). Then the optimum signal TDOA estimation algorithm takes the form

$$L = \sum_{i=1}^{m-1} \sum_{k=i+1}^m \frac{q_{si} q_{sk}}{\sqrt{N_i N_k}} \left| \frac{1}{2\pi} \int_{-\infty}^{\infty} \chi_i^*(\omega) \chi_k(\omega) |H(\omega)|^2 \times \exp[j\omega(\tau_{s1k} - \tau_{s1i})] d\omega \right| \rightarrow \max(\tau_{s12}, \dots, \tau_{s1m}) \quad (2.64)$$

It can be seen that this algorithm is not much simpler than the one-stage algorithms (2.60) and (2.61) though it does not yet locate a radiation source in space.

The optimal TDOA measurement algorithm according to the second approach mentioned above, can be derived in the same manner as (2.64). As a result we have

$$L = \sum_{i=1}^{m-1} \sum_{k=i+1}^m \frac{q_{si} q_{sk}}{\sqrt{N_i N_k}} \left| \frac{1}{2\pi} \int_{-\infty}^{\infty} \chi_i^*(\omega) \chi_k(\omega) |H(\omega)|^2 \times \exp(j\omega\tau_{sik}) d\omega \right| \rightarrow \max(\tau_{sik})$$

At this step, all TDOAs are assumed to be independent variables. Each term of the double sum contains only a single “its own” TDOA. Hence the sum reaches its maximum when all terms have their own maxima. The estimation algorithm takes the form

$$L = \left| \frac{1}{2\pi} \int_{-\infty}^{\infty} \chi_i^*(\omega) \chi_k(\omega) |H(\omega)|^2 \times \exp(j\omega\tau_{sik}) d\omega \right| \rightarrow \max(\tau_{sik}). \quad i, k = \overline{1, m}; \quad i < k \quad (2.65)$$

In accordance with (2.34), when input SNRs are sufficiently large ($q_{s\Sigma}^2 \gg 1$), the filters with the squared amplitude response, $|H(\omega)|^2$, may be excluded. On the contrary, for weak input signals ($q_{s\Sigma}^2 \ll 1$), $|H(\omega)|^2 = F_s(\omega - \omega_0)$, where the filter must be included.

It follows from (2.65) that the required estimate of a signal TDOA at each pair of receiving antennae is the delay value at one of the two correlator inputs which corresponds to a maximum of the estimate modulus of the cross-correlation of filtered signals and interferences received by that pair of antennae. Obviously, this measurement procedure is much simpler than (2.64).

Knowing TDOAs, $\hat{\tau}_{s12}, \dots, \hat{\tau}_{s1m}, \hat{\tau}_{s23}, \dots, \hat{\tau}_{s2m}, \dots, \hat{\tau}_{s(m-1)m}$, one can obtain optimum estimates of linearly independent TDOAs, $\hat{\tau}_{s12}, \dots, \hat{\tau}_{s1m}$. Furthermore, if the algorithm (2.65) is used with the filter $\|H(\omega)\|^2$ from (2.34) we may obtain efficient estimates, $\hat{\tau}_{s12\text{opt}}, \dots, \hat{\tau}_{s1m\text{opt}}$, i.e., unbiased estimates with minimal attainable variances that are determined by the Cramer-Rao bound [42, 129]. In fact, the vector, τ_s , of all $m(m-1)/2$ TDOAs, $\tau_s = [\hat{\tau}_{s12}, \dots, \hat{\tau}_{s1m}, \hat{\tau}_{s23}, \dots, \hat{\tau}_{s2m}, \dots, \hat{\tau}_{s(m-1)m}]^t$, is linearly related to the vector, τ_{s1} , of linearly independent TDOAs, $\tau_{s1} = (\hat{\tau}_{s12}, \dots, \hat{\tau}_{s1m})^t$, so that

$$\tau_s = \mathbf{A} \tau_{s1} \quad (2.66)$$

where the $m(m-1)/2 \times (m-1)$ matrix \mathbf{A} is given by

$$\mathbf{A} = \|A_{ik1n}\| = \begin{bmatrix} A_{1212} & A_{1213} & \dots & A_{121m} \\ \dots & \dots & \dots & \dots \\ A_{1m12} & A_{1m13} & \dots & A_{1m1m} \\ A_{2312} & A_{2313} & \dots & A_{231m} \\ \dots & \dots & \dots & \dots \\ A_{2m12} & A_{2m13} & \dots & A_{2m1m} \\ \dots & \dots & \dots & \dots \\ A_{(m-1)m12} & A_{(m-1)m13} & \dots & A_{(m-1)m1m} \end{bmatrix}; A_{ik1n} = \delta_{kn} - \delta_{in}. \quad (2.67)$$

Let the covariance matrix of the unbiased estimates, $\hat{\tau}_{sik}$, $i, k = \overline{1, m}, i < k$, obtained from (2.65) be denoted by $\tilde{\mathbf{B}}$. Then the optimum estimate of the vector, τ_{s1} , is given by a known relationship derived from the weighted least squares method (see Section 2.4.1 and [42, 129])

$$\hat{\tau}_{s1\text{opt}} = (\mathbf{A} \tilde{\mathbf{B}}^{-1} \mathbf{A})^{-1} \mathbf{A}^t \tilde{\mathbf{B}}^{-1} \hat{\tau}_s \quad (2.68)$$

As it has been shown in [42, 129], the vector, $\hat{\tau}_{s1\text{opt}} = (\hat{\tau}_{s12\text{opt}}, \dots, \hat{\tau}_{s1m\text{opt}})^t$, obtained according to (2.68) and (2.65), is the vector of efficient estimates. The covariance matrix,

\mathbf{B}_{eff} , of the estimates, $\hat{\tau}_{\text{slopt}}$, is the inverse of the Fisher Information Matrix (FIM) and is given by

$$\mathbf{B}_{\text{eff}} = (\mathbf{A}^t \tilde{\mathbf{B}}^{-1} \mathbf{A})^{-1} \quad (2.69)$$

The matrix, $\tilde{\mathbf{B}}$, in (2.68) and (2.69) is an $m(m-1)/2 \times m(m-1)/2$ symmetric matrix whose entries, $\overline{b_{ikln}}$, are the variances and covariances of signal TDOA estimates, $\hat{\tau}_{sik}$ and $\hat{\tau}_{sln}$, i.e., $\overline{b_{ikln}} = \overline{\hat{\tau}_{sik} \hat{\tau}_{sln}}$, $i, l = \overline{1, (m-1)}$, $k = \overline{(i+1), m}$, $n = \overline{(l+1), m}$. It is clear that $b_{ikln} = 0$ when all the subscripts i, k, l, n are different, for such a pair of correlators has no common inputs. The sign of the covariance is changed if the correlator inputs at one of the correlators of each pair are switched, i.e., $\overline{b_{ikln}} = \overline{\hat{\tau}_{sik} \hat{\tau}_{sin}} = -\overline{b_{ikni}} = -\overline{\hat{\tau}_{sik} \hat{\tau}_{sni}}$ and $\overline{b_{ikln}} = \overline{\hat{\tau}_{sik} \hat{\tau}_{sin}} = -\overline{b_{klin}} = -\overline{\hat{\tau}_{ski} \hat{\tau}_{sin}}$. Corresponding expressions for the variances, $\overline{b_{ikik}} = \overline{\hat{\tau}_{sik} \hat{\tau}_{sik}}$, and the covariances, $\overline{b_{ikln}} = \overline{\hat{\tau}_{sik} \hat{\tau}_{sin}}$, are presented in [129] for wideband stochastic processes (it is worth recalling that the overbar at random quantities means averaging over the corresponding ensemble, whereas the overbar at integers means enumeration of possible values). For the assumed models of narrowband complex signals and white noises (see Section 2.2.1) and using our notations those expressions can be rewritten as follows

$$\begin{aligned} \sigma^2(\hat{\tau}_{sik}) &= \overline{\hat{\tau}_{sik} \hat{\tau}_{sik}} \\ &= \frac{\pi}{T} \frac{\int_{-\infty}^{\infty} (\omega - \omega_0)^2 |H(\omega)|^4 [1 + q_{si}^2 F_s(\omega - \omega_0) + q_{sk}^2 F_s(\omega - \omega_0)] d\omega}{q_{si}^2 q_{sk}^2 \left[\int_{-\infty}^{\infty} (\omega - \omega_0)^2 |H(\omega)|^2 F_s(\omega - \omega_0) d\omega \right]^2}; \end{aligned} \quad (2.70)$$

$$\begin{aligned} \sigma^2(\hat{\tau}_{sik}) \sigma^2(\hat{\tau}_{sin}) \rho(\hat{\tau}_{sik}, \hat{\tau}_{sin}) &= \overline{\hat{\tau}_{sik} \hat{\tau}_{sin}} \\ &= \frac{\pi}{T} \frac{\int_{-\infty}^{\infty} (\omega - \omega_0)^2 |H(\omega)|^4 F_s(\omega - \omega_0) d\omega}{q_{si}^2 \left[\int_{-\infty}^{\infty} (\omega - \omega_0)^2 |H(\omega)|^2 F_s(\omega - \omega_0) d\omega \right]^2} \end{aligned} \quad (2.71)$$

Example 1.

Consider an application of the second approach to TDOA optimum estimation. Let the signal PSD have a rectangular form, i.e., be determined by (2.50) for $\Omega_{s1} = 0$. It follows from (2.34) that in this case $|H(\omega)|^2 = 1/(1 + q_{s\Sigma}^2)$ and $|H(\omega)|^4 = 1/(1 + q_{s\Sigma}^2)^2$ in the frequency band $(\omega_0 - \Delta\omega_s/2, \omega_0 + \Delta\omega_s/2)$. Substituting these quantities in (2.70) and

(2.71) yields

$$\sigma^2(\hat{\tau}_{sik}) = \frac{1(1 + q_{si}^2 + q_{sk}^2)}{2q_{si}^2 q_{sk}^2 \Delta f_s T \pi^2 \Delta f_s^2}; \quad \sigma^2(\hat{\tau}_{sik}) \sigma^2(\hat{\tau}_{sin}) \rho(\hat{\tau}_{sik}, \hat{\tau}_{sin}) = \frac{3}{2q_{si}^2 \Delta f_s T \pi^2 \Delta f_s^2} \quad (2.72)$$

The correlation coefficient, $\rho(\hat{\tau}_{sik}, \hat{\tau}_{sin})$, is given from (2.72) by

$$\rho(\hat{\tau}_{sik}, \hat{\tau}_{sin}) = \frac{q_{sk} q_{sn}}{\sqrt{(1 + q_{si}^2 + q_{sk}^2)(1 + q_{si}^2 + q_{sn}^2)}} \quad (2.73)$$

It is important to note that, as follows from (2.73), when the input SNRs are small ($q_{si}^2 \ll 1, q_{sk}^2 \ll 1, q_{sn}^2 \ll 1$) signal TDOA estimates at different pairs of antennae (with one common antenna in each pair) are weakly correlated. It should be also noted that small input SNRs do not necessarily lead to low accuracy of TDOA estimates. It can be seen from (2.72) that a large accumulation (integration) factor, $\Delta f_s T$, may offset low input SNRs. For instance, even if $q_{si}^2 = q_{sk}^2 = q_{sn}^2 = -10$ dB and $\Delta f_s T = 10^3 - 10^4$, the attainable r.m.s error of signal TDOA estimates according to (2.72) does not exceed $0.135/\Delta f_s - 0.043/\Delta f_s$, i.e., a small fraction of the correlation interval. This feature of correlation measurements is similar to the corresponding feature of correlation detection.

To simplify mathematical manipulations, a two-dimensional case and a GIDL containing three receiving antennae with equal SNRs at the inputs of all antennae, i.e., $q_{si}^2 = q_{sk}^2 = q_{sn}^2$ is now considered. The matrices \mathbf{A} and $\tilde{\mathbf{B}}$ according to (2.67) and (2.72) are then

$$\mathbf{A} = \begin{bmatrix} 1 & 0 \\ 0 & 1 \\ -1 & 1 \end{bmatrix}; \quad \mathbf{A}^t = \begin{bmatrix} 1 & 0 & -1 \\ 0 & 1 & 1 \end{bmatrix}; \quad (2.74)$$

$$\tilde{\mathbf{B}} = \frac{3}{2q_s^2 \Delta f_s T \pi^2 \Delta f_s^2} \begin{bmatrix} \frac{1+2q_s^2}{q_s^2} & 1 & -1 \\ 1 & \frac{1+2q_s^2}{q_s^2} & 1 \\ -1 & 1 & \frac{1+2q_s^2}{q_s^2} \end{bmatrix} \quad (2.75)$$

Where, $\rho(\hat{\tau}_{s12}, \hat{\tau}_{s13}) = \rho(\hat{\tau}_{s13}, \hat{\tau}_{s23}) = -\rho(\hat{\tau}_{s12}, \hat{\tau}_{s23})$. The inverse of $\tilde{\mathbf{B}}$ can be easily obtained:

$$\tilde{\mathbf{B}}^{-1} = \frac{2q_s^6 \Delta f_s T \pi^2 \Delta f_s^2}{3(1 + 3q_s^2)} \begin{bmatrix} \frac{1+4q_s^2+3q_s^4}{(1+3q_s^2)q_s^2} & -1 & 1 \\ -1 & \frac{1+4q_s^2+3q_s^4}{(1+3q_s^2)q_s^2} & -1 \\ 1 & -1 & \frac{1+4q_s^2+3q_s^4}{(1+3q_s^2)q_s^2} \end{bmatrix} \quad (2.76)$$

Substituting (2.74) and (2.76) in to (2.69) yields the covariance matrix, \mathbf{B}_{eff} , of optimum (efficient) estimates of the linearly independent TDOAs, $\hat{\tau}_{s12\text{opt}}, \hat{\tau}_{s13\text{opt}}$

$$\mathbf{B}_{\text{eff}} = (\mathbf{A}^t \tilde{\mathbf{B}}^{-1} \mathbf{A})^{-1} = \frac{1 + 3q_s^2}{2q_s^4 \Delta f_s T \pi^2 \Delta f_s^2} \begin{pmatrix} 2 & 1 \\ 1 & 2 \end{pmatrix} \quad (2.77)$$

Using (2.74), (2.76) and (2.77) permits one to obtain the optimum algorithm for $\hat{\tau}_{s12\text{opt}}, \hat{\tau}_{s13\text{opt}}$ estimation in accordance with (2.68)

$$\hat{\tau}_{s1\text{opt}} = \begin{pmatrix} \hat{\tau}_{s12\text{opt}} \\ \hat{\tau}_{s13\text{opt}} \end{pmatrix} = \frac{1}{3} \begin{pmatrix} 2 & 1 & -1 \\ 1 & 2 & 1 \end{pmatrix} \begin{pmatrix} \hat{\tau}_{s12} \\ \hat{\tau}_{s13} \\ \hat{\tau}_{s23} \end{pmatrix} = \frac{1}{3} \begin{pmatrix} 2\hat{\tau}_{s12} + \hat{\tau}_{s13} - \hat{\tau}_{s23} \\ \hat{\tau}_{s12} + 2\hat{\tau}_{s13} + \hat{\tau}_{s23} \end{pmatrix} \quad (2.78)$$

Clearly, the second approach to the optimum TDOA estimation is simpler than the first one, since simultaneous adjustment of all linearly independent delays at the inputs of correlators to achieve a total maximum of the sum (2.64) is replaced by individual TDOA measurements at the inputs of each pair of antennae. In addition, this approach can yield efficient estimates of linearly independent TDOAs, whereas the first approach results in a maximum likelihood and hence, only asymptotically efficient estimates.

Example 2.

Let us evaluate the covariance matrix, \mathbf{B}' , for optimal estimates, $\hat{\tau}_{s12\text{opt}}, \hat{\tau}_{s13\text{opt}}$, from Example 1 if the cross-correlation between measurements is ignored, i.e., if the measurement covariance matrix, $\tilde{\mathbf{B}}$ is diagonal (see (2.72) and (2.75)) then,

$$\tilde{\mathbf{B}} = \sigma^2(\hat{\tau}_{sik}) \mathbf{I} \frac{3(1 + 2q_s^2)}{2q_s^4 \Delta f_s T \pi^2 \Delta f_s^2} \mathbf{I}, \quad \hat{\tau}_{sik} \in (\hat{\tau}_{s12}, \hat{\tau}_{s13}, \hat{\tau}_{s23}) \quad (2.79)$$

where \mathbf{I} is the identity matrix. Using (2.74) and inverting $\tilde{\mathbf{B}}$ yields

$$\mathbf{B}' = (\mathbf{A}^t \tilde{\mathbf{B}}^{-1} \mathbf{A})^{-1} = \frac{1 + 2q_s^2}{2q_s^4 \Delta f_s T \pi^2 \Delta f_s^2} \begin{pmatrix} 2 & 1 \\ 1 & 2 \end{pmatrix} \quad (2.80)$$

It is seen that the matrix \mathbf{B}' is similar to the matrix \mathbf{B}_{eff} (2.77) but the variances of the estimates, $\hat{\tau}_{s12\text{opt}}, \hat{\tau}_{s13\text{opt}}$, are here less than in (2.77). Their ratio is equal to $(1 + 2q_s^2)/(1 +$

$3q_s^2$). It is clear, that ignoring cross-correlation between measurements leads to overvalued accuracy of the estimates, $\hat{\tau}_{s12\text{opt}}, \hat{\tau}_{s13\text{opt}}$. However, for low input SNRs ($q^2 \ll 1$) this overvaluation may often be neglected.

2.3.4 Maximum Attainable Accuracy of Maximum Likelihood Estimates of Informative Parameters

The problem of jammer position and velocity estimation in GIDL is a typical problem of multidimensional parameter estimation. It is acceptable to characterize the accuracy of multidimensional estimators with the help of a vector of biases and an Error Covariance Matrix (ECM). Explicit analytical expressions for direct ECM calculation for specific estimation algorithms are usually difficult to derive. In those cases where ECM calculations are necessary, computer simulation is used.

It is known that maximum likelihood estimates are asymptotically unbiased and efficient under certain, usually satisfied, regularity conditions (e.g., [130]). Therefore, analysis of the ECM for efficient estimates is widely used for the accuracy analysis of maximum likelihood estimates of the same parameters, especially when requirements for estimation accuracy are sufficiently high so that the conditions of asymptotic efficiency are approximately satisfied. An ECM of efficient estimates presents the Cramér-Rao lower bound for estimate errors. It is a reliable approximation of attainable errors when the observation time is long enough (or, more correctly, when the product of the observation time by the signal bandwidth is large enough). The advantage of such an approach is that the ECM of efficient estimates is the inverse of the Fisher Information Matrix (FIM), so that it determines the maximum attainable accuracy inherent in Likelihood Functions or Functionals (LF) of estimated parameters regardless of specific estimation algorithms.

The “FIM technique” (or the “Cramér-Rao lower bound” technique) is usually employed in the cases where all unknown parameters of an LF are to be estimated. However, in practice, LFs often contain not only informative (useful) parameters, but also noninformative (stray or nuisance) parameters. According to the “classical” procedure, an FIM for all parameters is to be calculated and inverted for obtaining the corresponding ECM. Only a part of this ECM will be the ECM of informative parameters. When the number of

stray parameters is large (typical for GIDL), the dimension of the FIM also becomes large making inversion difficult.

To overcome this difficulty, averaging of the original LF over stray parameters is commonly employed. The averaged LF is used for both the synthesis of informative parameter estimators and the accuracy analysis with the help of FIM [131, 113, 114]. This technique is quite expedient when stray parameters are random with known probability distributions. However, it cannot be used when probability distributions are unknown or those parameters are unknown but not random. It should be noted that maximum likelihood estimates of informative parameters have been derived in Sections 2.3.2–2.3.3 using LF maximization with respect to all parameters (including strays) without averaging. It is desirable to simplify calculations of the ECM of efficient estimates with the help of the “FIM technique” without averaging over stray parameters.

A Technique for Deriving ECM of Efficient Estimates of Informative Parameters by Inverting a Special FIM

The special FIM takes into account stray parameters but its dimension is determined only by the number of informative parameters [107].

Let an LF take the form $\Lambda[\mathbf{X}(t), \boldsymbol{\alpha}, \boldsymbol{\beta}]$ where $\mathbf{X}(t)^t = [X_1(t), \dots, X_m(t)]$ is the vector of overall received signals, $\boldsymbol{\alpha}^t = (\alpha_1, \dots, \alpha_N)$ is the vector of informative parameters, and $\boldsymbol{\beta}^t = (\beta_1, \dots, \beta_M)$ is the vector of stray parameters. In general, estimates of $\boldsymbol{\alpha}$ are dependent on $\boldsymbol{\beta}$ and are obtained as a result of the joint solution of the $N + M$ likelihood equations:

$$\partial \ln \Lambda / \partial \alpha_i = 0, \quad i = \overline{1, N}; \quad \partial \ln \Lambda / \partial \beta_k = 0, \quad k = \overline{1, M} \quad (2.81)$$

The corresponding FIM for the estimates, $\hat{\boldsymbol{\alpha}}$ and $\hat{\boldsymbol{\beta}}$, may be partitioned as follows:

$$\mathbf{J}^{(\alpha, \beta)} = \begin{pmatrix} \mathbf{J}^{(\alpha\alpha)} & \mathbf{J}^{(\alpha\beta)} \\ \mathbf{J}^{(\beta\alpha)} & \mathbf{J}^{(\beta\beta)} \end{pmatrix} \quad (2.82)$$

where $\mathbf{J}^{(\alpha\alpha)}$ and $\mathbf{J}^{(\beta\beta)}$ are the $N \times N$ and $M \times M$ square matrices, respectively, with the entries

$$\begin{aligned} \mathbf{J}_{np}^{(\alpha\alpha)} &= -E\{\partial^2 \ln \Lambda[\mathbf{X}(t), \boldsymbol{\alpha}_0, \boldsymbol{\beta}_0] / \partial \alpha_n \partial \alpha_p\}, \quad n, p = \overline{1, N}; \\ \mathbf{J}_{np}^{(\beta\beta)} &= -E\{\partial^2 \ln \Lambda[\mathbf{X}(t), \boldsymbol{\alpha}_0, \boldsymbol{\beta}_0] / \partial \beta_n \partial \beta_p\}, \quad n, p = \overline{1, M}, \end{aligned} \quad (2.83)$$

and $\mathbf{J}^{(\alpha\beta)} = [\mathbf{J}^{(\beta\alpha)}]^t$ where $\mathbf{J}^{(\alpha\beta)}$ is the $N \times M$ rectangular matrix with the following elements

$$\mathbf{J}_{np}^{(\alpha\beta)} = -E\{\partial^2 \ln \Lambda[\mathbf{X}(t), \boldsymbol{\alpha}_0, \boldsymbol{\beta}_0] / \partial \alpha_n \partial \beta_p\}, \quad n = \overline{1, N}, \quad p = \overline{1, M} \quad (2.84)$$

All derivatives are taken at the true values of parameters, $\boldsymbol{\alpha}_0$ and $\boldsymbol{\beta}_0$. “ E ” means expected value, i.e., the average over the ensemble of $\mathbf{X}(t)$. Such a notation here is more convenient than the overbar that was used in previous sections. This will be used in subsequent text.

The inverse of the $(N + M) \times (N + M)$ matrix (2.82) is the ECM of the jointly efficient estimates, $\hat{\boldsymbol{\alpha}}$ and $\hat{\boldsymbol{\beta}}$. The upper right portion is the only part of interest, i.e., in the $N \times N$ ECM matrix for the efficient estimates of informative parameters, $\hat{\boldsymbol{\alpha}}$. Let us denote it by $\mathbf{D}^{(\alpha\alpha)}$. The inversion of the matrix, $\mathbf{J}^{(\alpha\beta)}$, (2.82) may be bypassed using a known result on the inverse of a partitioned matrix. Then

$$\mathbf{D}^{(\alpha\alpha)} = \{\mathbf{J}^{(\alpha\alpha)} - \mathbf{J}^{(\alpha\beta)}[\mathbf{J}^{(\beta\beta)}]^{-1}\mathbf{J}^{(\beta\alpha)}\}^{-1} \quad (2.85)$$

The expression in braces is denoted by $\tilde{\mathbf{J}}^{(\alpha)}$:

$$\tilde{\mathbf{J}}^{(\alpha)} = \mathbf{J}^{(\alpha\alpha)} - \mathbf{J}^{(\alpha\beta)}[\mathbf{J}^{(\beta\beta)}]^{-1}\mathbf{J}^{(\beta\alpha)} \quad (2.86)$$

so that

$$\mathbf{D}^{(\alpha\alpha)} = [\tilde{\mathbf{J}}^{(\alpha)}]^{-1} \quad (2.87)$$

It is seen that the inversion of the $(N + M) \times (N + M)$ matrix, $\mathbf{J}^{(\alpha\beta)}$, (2.82) is replaced by the inversion first of the $M \times M$ matrix, $\mathbf{J}^{(\beta\beta)}$, and then of the $N \times N$ matrix, $\tilde{\mathbf{J}}^{(\alpha)}$.

The matrix $\tilde{\mathbf{J}}^{(\alpha)}$ may be considered an “FIM” of informative parameters taking into account the influence of stray parameters. Calculation of $\tilde{\mathbf{J}}^{(\alpha)}$ may be in many cases significantly simplified in comparison with (2.86), by excluding the calculation and inversion of $\mathbf{J}^{(\beta\beta)}$. To do this, an LF of informative parameters, $\tilde{\Lambda}[\mathbf{X}(t), \boldsymbol{\alpha}]$, should be derived such that an FIM calculated according to the usual technique coincides with $\tilde{\mathbf{J}}^{(\alpha)}$. That is,

$$-E\{\partial^2 \ln \tilde{\Lambda}[\mathbf{X}(t), \boldsymbol{\alpha}] / \partial \alpha_n \partial \beta_p\} = \tilde{\mathbf{J}}_{np}^{(\alpha)}, \quad n, p = \overline{1, N} \quad (2.88)$$

To derive the required $\tilde{\Lambda}[\mathbf{X}(t), \boldsymbol{\alpha}]$, the likelihood equations in (2.81) for $\boldsymbol{\beta}$ should be averaged over the ensemble of overall received signals, $\mathbf{X}(t)$. Assume that the system of equations has been solved,

$$-E\{\partial \ln \Lambda[\mathbf{X}(t), \boldsymbol{\alpha}, \boldsymbol{\beta}] / \partial \beta_k\} = 0, \quad k = \overline{1, M} \quad (2.89)$$

β can be expressed in terms of α . Denoting the solutions of (2.89) by $\beta = \mathbf{u}(\alpha)$, they are substituted into the original LF for β . Now it can be shown that, at least near the true values of the estimated parameters, where the logarithm of the original LF can be well approximated by the first (linear and square) terms of a Taylor-series expansion at the true point (α_0, β_0) the obtained LF, $\Lambda[\mathbf{X}(t), \alpha, \mathbf{u}(\alpha)]$, is just the required LF, $\tilde{\Lambda}[\mathbf{X}(t), \alpha]$. That is, condition (2.88) is satisfied. Let the following equation be valid in the vicinity of the point (α_0, β_0) :

$$\begin{aligned} \ln \Lambda[\mathbf{X}(t), \alpha, \beta] = & \ln \Lambda(0) + [\partial \ln \Lambda(0) / \partial \alpha]^t (\alpha - \alpha_0) \\ & + [\partial \ln \Lambda(0) / \partial \beta]^t (\beta - \beta_0) + 0.5(\alpha - \alpha_0)^t [\partial^2 \ln \Lambda(0) / \partial \alpha^2] (\alpha - \alpha_0) \\ & + 0.5(\beta - \beta_0)^t [\partial^2 \ln \Lambda(0) / \partial \beta^2] (\beta - \beta_0) \\ & + (\alpha - \alpha_0)^t [\partial^2 \ln \Lambda(0) / \partial \alpha \partial \beta] (\beta - \beta_0) \end{aligned} \quad (2.90)$$

where $\Lambda(0) = \Lambda[\mathbf{X}(t), \alpha_0, \beta_0]$ and in brackets are the vectors of the first derivatives and the matrices of the second derivatives of the LF with respect to parameters $\alpha_1, \dots, \alpha_N$ and β_1, \dots, β_M at the point (α_0, β_0) . Substitute (2.90) into (2.89) taking into account that

$$\mathbb{E}[\partial \ln \Lambda(0) / \partial \alpha] = \mathbb{E}[\partial \ln \Lambda(0) / \partial \beta] = 0 \quad (2.91)$$

while the averaged matrices of the second derivatives coincide with the corresponding FIMs. A system of linear equations results from which the required matrix function, $\beta = \mathbf{u}(\alpha)$, can be found:

$$\beta - \beta_0 = -[\mathbf{J}^{(\beta\beta)}]^{-1} \mathbf{J}^{(\alpha\beta)} (\alpha - \alpha_0). \quad (2.92)$$

Substituting (2.92) into (2.90) yields $\ln \Lambda[\mathbf{X}(t), \alpha, \mathbf{u}(\alpha)]$ which is equal to a logarithm of the desired LF, $\ln \tilde{\Lambda}[\mathbf{X}(t), \alpha]$. Indeed, if $\ln \Lambda[\mathbf{X}(t), \alpha, \mathbf{u}(\alpha)]$ is differentiated twice with respect to α at the point α_0 and averaged over the ensemble of $\mathbf{X}(t)$, the matrix $\tilde{\mathbf{J}}^{(\alpha)}$ (2.86) will be obtained in the right-hand side of (2.90). This means that the LF, $\ln \Lambda[\mathbf{X}(t), \alpha, \mathbf{u}(\alpha)]$, satisfies the condition (2.88).

Thus to derive an LF containing only informative parameters but taking into account the presence of stray parameters, one must solve likelihood equations which are averaged over input received signals for the stray parameters. Then the stray parameters are expressed in terms of the informative ones and substituted into the original LF for the stray parameters.

Applications to Gaussian Likelihood Functionals

The general approach developed above is now applied to Gaussian LFs which are used in signal parameter estimation for GIDL. Let us consider now a stochastic signal in GIDL, i.e., an m -dimensional complex Gaussian random process with zero-mean. Unknown parameters are in the covariance (correlation) matrix of a signal. A system of likelihood equations averaged over received signal realizations takes the form

$$\sum_{i=1}^m \sum_{k=1}^m \int_{-T/2}^{T/2} \int_{-T/2}^{T/2} \{ [\partial B_{\text{sn } ik}^*(t_1, t_2, \boldsymbol{\alpha}, \boldsymbol{\beta}) / \partial \beta_l] R_{\text{sn } ik}(t_1, t_2, \boldsymbol{\alpha}, \boldsymbol{\beta}) + B_{\text{sn } ik}^*(t_1, t_2, \boldsymbol{\alpha}_0, \boldsymbol{\beta}_0) [\partial R_{\text{sn } ik}(t_1, t_2, \boldsymbol{\alpha}, \boldsymbol{\beta}) / \partial \beta_l] \} dt_1 dt_2 = 0 \quad (2.93)$$

($R_{\text{sn } ik}(t_1, t_2, \boldsymbol{\alpha}, \boldsymbol{\beta})$ is the element of the matrix $\mathbf{R}_{\text{sn}}(t_1, t_2, \boldsymbol{\alpha}, \boldsymbol{\beta})$, which is solution of the equation (2.15)) and an arbitrary element of the FIM of informative parameters is given by

$$\begin{aligned} \tilde{J}_{np}^{(\alpha)} = & - \sum_{i=1}^m \sum_{k=1}^m \int_{-T/2}^{T/2} \int_{-T/2}^{T/2} \{ \partial B_{\text{sn } ik}^*(t_1, t_2, \boldsymbol{\alpha}_0, \mathbf{u}_2(\boldsymbol{\alpha}_0)) / \partial \alpha_l \} \\ & \times \{ \partial R_{\text{sn } ik}(t_1, t_2, \boldsymbol{\alpha}_0, \mathbf{u}_2(\boldsymbol{\alpha}_0)) / \partial \alpha_l \} dt_1 dt_2 = 0 \quad n, p = \overline{1, N} \end{aligned} \quad (2.94)$$

where $\mathbf{u}_2(\boldsymbol{\alpha})$ is the vector of the solutions of the system (2.93). The remaining notations are the same as in (2.14) and (2.15). The subscript “sn” denotes a sum of “useful” signals and noises. If this sum is a sum of jointly stationary processes and the observation time, T , is much greater than their correlation intervals, it is convenient to pass into the frequency domain (as for regular signals). Thus,

$$\begin{aligned} \tilde{J}_{np}^{(\alpha)} = & - \sum_{i=1}^m \sum_{k=1}^m \frac{1}{2\pi} \int_{-\infty}^{\infty} \{ \partial \Phi_{\text{sn } ik}^*[\omega \boldsymbol{\alpha}_0, \mathbf{u}_3(\boldsymbol{\alpha}_0)] / \partial \alpha_n \} \\ & \times \{ \partial f_{\text{sn } ik}[\omega, \boldsymbol{\alpha}_0, \mathbf{u}_3(\boldsymbol{\alpha}_0)] / \partial \alpha_p \} d\omega, \quad n, p = \overline{1, N} \end{aligned} \quad (2.95)$$

instead of (2.94), where $\mathbf{u}_3(\boldsymbol{\alpha})$ is the solution of the system of likelihood equations averaged over received signal realizations

$$\begin{aligned} & \sum_{i=1}^m \sum_{k=1}^m \frac{1}{2\pi} \int_{-\infty}^{\infty} \{ [\partial \Phi_{\text{sn } ik}^*(\omega \boldsymbol{\alpha}, \boldsymbol{\beta}) / \partial \beta_l] f_{\text{sn } ik}(\omega \boldsymbol{\alpha}, \boldsymbol{\beta}) \\ & + \Phi_{\text{sn } ik}^*(\omega \boldsymbol{\alpha}_0, \boldsymbol{\beta}_0) [\partial f_{\text{sn } ik}(\omega, \boldsymbol{\alpha}, \boldsymbol{\beta}) / \partial \beta_l] \} d\omega; \quad l = \overline{1, M} \end{aligned} \quad (2.96)$$

Using the obtained general results maximum attainable accuracies can be analyzed (Cramér-Rao bounds) for signal temporal and spatial parameter estimates in GIDL.

2.3.5 Maximum Attainable Estimation Accuracy of Signal TDOAs in GIDL

Now the general technique developed in Section 2.3.4 is applied to GIDL. Consider a GIDL containing m receiving antennae with short-term spatial coherence. Assume that spatial correlations of external noises are either absent or ignored.

One-Stage Estimation Algorithms

A vector of unknown signal parameters contains three (our space is three-dimensional) informative parameters, $\tau_{s12}, \tau_{s13}, \tau_{s14}$ (or spatial coordinates, x, y, z), and the following stray parameters: $m(m-1)/2$ phases, $(\Delta\varphi_{sik})$, of the signal covariance (correlation) matrix, and m power SNRs, (q_{si}^2) , where $i, k = \overline{1, m}, i < k$. In order to simplify the notation in subsequent derivations, the subscript “s” denoting “signal” is dropped. It can be shown that solutions of the averaged likelihood equations (2.96) for q_i^2 do not depend on τ_{ik} . Therefore, the general expression (2.95) for an arbitrary FIM element of the estimates, $\hat{\tau}_{12}, \hat{\tau}_{13}, \hat{\tau}_{14}$, takes the form

$$\begin{aligned} \tilde{J}_{np}^{(\tau)} = & - \sum_{i=1}^m \sum_{k=1}^m \frac{T}{2\pi} \int_{-\infty}^{\infty} \{ \partial \Phi_{ik}^*[\omega, \boldsymbol{\tau}^0, \Delta\boldsymbol{\varphi}(\boldsymbol{\tau}^0)] / \partial \tau_{1(n+1)} \} \\ & \times \{ \partial f_{ik}[\omega, \boldsymbol{\alpha}^0, \Delta\boldsymbol{\varphi}(\boldsymbol{\tau}^0)] / \partial \tau_{1(p+1)} \} d\omega, \quad n, p = 1, 2, 3 \end{aligned} \quad (2.97)$$

Using expressions (2.25)-(2.28) for $\Phi_{snik}(\omega)$ and $f_{snik}(\omega)$, and substituting results into (2.97) yields

$$\begin{aligned} \tilde{J}_{np}^{(\tau)} = & - \sum_{i=1}^m \sum_{k=1}^m \frac{q_i^2 q_k^2 T}{2\pi} \int_{-\infty}^{\infty} \frac{F^2(\omega - \omega_0)}{1 + F(\omega - \omega_0) q_\sigma^2} \\ & \times \left(\omega \frac{\partial \tau_{ik}}{\partial \tau_{1(n+1)}} + \frac{\partial \Delta\varphi_{ik}}{\partial \tau_{1(n+1)}} \right) \left(\omega \frac{\partial \tau_{ik}}{\partial \tau_{1(p+1)}} + \frac{\partial \Delta\varphi_{ik}}{\partial \tau_{1(p+1)}} d\omega \right). \end{aligned} \quad (2.98)$$

The dependence of $\Delta\boldsymbol{\varphi}$ on $\boldsymbol{\tau}$ can be determined from (2.96) setting $\beta_l = \Delta\varphi_{rs}$. Since all $\Delta\varphi_{rs}$ for different r, s are assumed to be independent parameters, all terms in the double sum of (2.96) are equal to zero for each combination of r, s , excluding two complex conjugate terms with subscripts “rs” and “sr.” In addition, the first term under the integration sign

in (2.96) is equal to zero for all i, k since $\Delta\varphi_{ik}$ and τ_{ik} are nonenergetic signal parameters.

Then solving Equation (2.96) for $\Delta\varphi_{ik}$ yields

$$\Delta\varphi_{ik} = \Delta\varphi_{ik}^0 - \arg \frac{T}{\pi} \int_{-\infty}^{\infty} \frac{F^2(\omega - \omega_0) \exp[j\omega(\tau_{ik} - \tau_{ik}^0)]}{1 + F(\omega - \omega_0)q_\sigma^2} d\omega \quad (2.99)$$

To obtain the derivatives $\partial\Delta\varphi_{ik}/\partial\tau_{1(n+1)}$ from (2.99), the equation

$$\frac{\partial \arg Z(\alpha)}{\partial \alpha} = \frac{\text{Im}[(\partial Z(\alpha)/\partial \alpha)Z^*(\alpha)]}{\|Z(\alpha)\|^2}$$

is used while taking into account that

$$\partial\Delta\varphi_{ik}/\partial\tau_{1(n+1)} = (\partial\Delta\varphi_{ik}/\partial\tau_{ik})[\partial\tau_{ik}/\partial\tau_{1(n+1)}]$$

As a result,

$$\frac{\partial\Delta\varphi_{ik}}{\partial\tau_{1(n+1)}} = -\tilde{\omega} \frac{\partial\tau_{ik}}{\partial\tau_{1(n+1)}}, \quad i, k = \overline{1, m}; \quad i < k; \quad n = 1, 2, 3 \quad (2.100)$$

where $\tilde{\omega}$ is the mean frequency of the generalized signal power spectrum

$$\tilde{\omega} = \frac{1}{2\pi\Delta f_e} \int_{-\infty}^{\infty} \frac{\omega F^2(\omega - \omega_0)}{1 + F(\omega - \omega_0)q_\sigma^2} d\omega \quad (2.101)$$

and Δf_e may be considered as the “equivalent” signal bandwidth

$$\Delta f_e = \frac{1}{2\pi} \int_{-\infty}^{\infty} \frac{F^2(\omega - \omega_0)}{1 + F(\omega - \omega_0)q_\sigma^2} d\omega \quad (2.102)$$

It is convenient to also introduce the mean squared bandwidth of the generalized power spectrum

$$\overline{\overline{\Delta\omega^2}} = \frac{1}{2\pi\Delta f_e} \int_{-\infty}^{\infty} \frac{(\omega - \tilde{\omega})^2 F^2(\omega - \omega_0)}{1 + F(\omega - \omega_0)q_\sigma^2} d\omega \quad (2.103)$$

It is seen that Δf_e , $\tilde{\omega}$ and $\overline{\overline{\Delta\omega^2}}$ depend on the total input SNR, q_σ^2 (2.30). This dependence vanishes for weak signals ($q_\sigma^2 \ll 1$). Furthermore, $\tilde{\omega}$ and $\overline{\overline{\Delta\omega^2}}$ do not depend on q_σ^2 for strong signals ($q_\sigma^2 \gg 1$) or for a rectangular signal spectrum [(2.50) at $\Omega_{si} = 0$]. Let us substitute (2.100) into (2.98) taking into account (2.103) and the identity $\tau_{ik} = \tau_{1k} - \tau_{1i}$ [see (2.31)]. Then an arbitrary element of the FIM takes the form

$$\tilde{J}_{np}^{(\tau)} = 2\Delta f_e T \overline{\overline{\Delta\omega^2}} \sum_{i=1}^{m-1} \sum_{k=i+1}^m q_i^2 q_k^2 \left(\frac{\partial\tau_{1k}}{\partial\tau_{1(n+1)}} - \frac{\partial\tau_{1i}}{\partial\tau_{1(n+1)}} \right) \left(\frac{\partial\tau_{1k}}{\partial\tau_{1(p+1)}} - \frac{\partial\tau_{1i}}{\partial\tau_{1(p+1)}} \right), \quad n, p = 1, 2, 3 \quad (2.104)$$

The derivatives are determined from (2.55):

$$\frac{\partial \tau_{1k}}{\partial \tau_{1(n+1)}} = \begin{cases} \delta_{k(n+1)}, & k \leq 4 \\ \frac{\partial \tilde{h}_{1k}(\tau_{12}, \tau_{13}, \tau_{14})}{\partial \tau_{1(n+1)}}, & k > 4 \end{cases} \quad (2.105)$$

The inverse of the 3×3 FIM with the elements of (2.104) is the ECM of the efficient estimates, $\hat{\tau}_{12}, \hat{\tau}_{13}, \hat{\tau}_{14}$, i.e., the Cramér-Rao lower bound on errors of the one-stage estimation of TDOAs, $\hat{\tau}_{12}, \hat{\tau}_{13}, \hat{\tau}_{14}$.

When the number, m , of receiving stations is $2 \leq m \leq 4$ such that the number of linearly independent TDOAs does not exceed the dimensionality of space (3D), (2.104) and (2.105) yield:

$$\tilde{J}_{np}^{(\tau)} = 2\Delta f_e T \overline{\Delta \omega^2} q_{n+1}^2 (\delta_{np} q_\sigma^2 - Q_{p+1}^2), \quad n, p = \overline{1, m-1} \quad (2.106)$$

where δ_{np} is the Kronecker delta function.

Due to the mutual single-valued relations between each triad, $\hat{\tau}_{12}, \hat{\tau}_{13}, \hat{\tau}_{14}$, and the corresponding point in space with the coordinates, $\hat{x}, \hat{y}, \hat{z}$, the ECM of efficient estimates, $\hat{\tau}_{12}, \hat{\tau}_{13}, \hat{\tau}_{14}$, fully determines the ECM of efficient estimates, $\hat{x}, \hat{y}, \hat{z}$. This may be presented in an explicit form. In (2.104), the derivatives with respect to $\tau_{12}, \tau_{13}, \tau_{14}$ should be replaced by the derivatives with respect to x, y, z . Then, instead of (2.105),

$$\frac{\partial \tau_{1k}}{\partial x} = \frac{1}{c} \frac{\partial \Delta R_{1k}}{\partial x}; \quad \frac{\partial \tau_{1k}}{\partial y} = \frac{1}{c} \frac{\partial \Delta R_{1k}}{\partial y}; \quad \frac{\partial \tau_{1k}}{\partial z} = \frac{1}{c} \frac{\partial \Delta R_{1k}}{\partial z}; \quad k = \overline{1, m} \quad (2.107)$$

where c is the velocity of light and the relationships for range differences, ΔR_{1k} , are presented in Section 2.3.1. Substituting (2.107) into (2.104) yields an arbitrary element of the FIM, $\tilde{\mathbf{J}}^{(x,y,z)}$, say $\tilde{J}_{xy}^{(x,y,z)}$

$$\tilde{J}_{xy}^{(x,y,z)} = \frac{2\Delta f_e T \overline{\Delta \omega^2}}{c^2} \sum_{i=1}^{m-1} \sum_{k=i+1}^m q_i^2 q_k^2 \left(\frac{\partial \Delta R_{1k}}{\partial x} - \frac{\partial \Delta R_{1i}}{\partial x} \right) \left(\frac{\partial \Delta R_{1k}}{\partial y} - \frac{\partial \Delta R_{1i}}{\partial y} \right)$$

or in a slightly different form (since $\Delta R_{1k} - \Delta R_{1i} = \Delta R_{ik}$)

$$\tilde{J}_{xy}^{(x,y,z)} = \frac{2\Delta f_e T \overline{\Delta \omega^2}}{c^2} \sum_{i=1}^{m-1} \sum_{k=i+1}^m q_i^2 q_k^2 \left(\frac{\partial \Delta R_{ik}}{\partial x} \frac{\partial \Delta R_{ik}}{\partial y} \right) \quad (2.108)$$

It should be taken into account that $\Delta R_{11} = \Delta R_{ii} = 0$. The remaining elements of the FIM, $\tilde{\mathbf{J}}^{(x,y,z)}$, can be written by replacing the derivatives in parenthesis in accordance with

(2.107). Inverting this 3×3 FIM yields the ECM of efficient estimates of the radiation source spatial coordinates, i.e., the Cramér-Rao lower bound on errors of the one-stage estimation of x, y, z .

Example 1.

Let us obtain the ECM of efficient TDOA estimates (the Cramér-Rao lower bound on errors) for a particular case where the number of linearly independent TDOAs does not exceed the dimensionality of space (3D) ($2 \leq m \leq 4$) and the signal PSD has a rectangular form within the bandwidth $(\omega_0 - \Delta\omega/2, \omega_0 + \Delta\omega/2)$ [see (2.50) at $\Omega_{si} = 0$]. In this case, from (2.102) and (2.103), $\Delta f_e = \Delta f / (1 + q_\Sigma^2)$, $\overline{\Delta\omega^2} = 4\pi^2 \Delta f^2 / 12$. Substituting in (2.106) and inverting the FIM yields the minimum attainable variances of efficient estimates, $\hat{\tau}_{12}, \hat{\tau}_{13}, \hat{\tau}_{14}$,

$$\sigma_{\text{eff}}^2(\hat{\tau}_{1(n+1)}) = \frac{q_1^2 + q_{n+1}^2}{q_1^2 q_{n+1}^2} \frac{1 + q_\Sigma^2}{q_\Sigma^2} \frac{1}{\Delta f T} \frac{3}{2\pi^2 \Delta f^2} \quad (2.109)$$

and the correlation coefficient of the efficient estimates

$$\rho_{\text{eff}}[\hat{\tau}_{(n+1)}, \hat{\tau}_{(p+1)}] = \frac{q_{n+1} q_{p+1}}{\sqrt{(q_1^2 + q_{n+1}^2)(q_1^2 + q_{p+1}^2)}} \quad (2.110)$$

In (2.109) and (2.110), $n, p = \overline{1, m-1}$ and $2 \leq m \leq 4$. An increase in the number of antennae would lead to increasing the estimation accuracy due to redundant measurements.

For equal SNRs at the inputs of stations, $q_1^2 = q_{n+1}^2 = q_{p+1}^2 = q^2$, (2.109) and (2.110) yield

$$\sigma_{\text{eff}}^2(\hat{\tau}_{1(n+1)}) = \frac{1 + mq^2}{mq^4} \frac{1}{\Delta f T} \frac{3}{\pi^2 \Delta f^2}; \quad \rho_{\text{eff}}[\hat{\tau}_{(n+1)}, \hat{\tau}_{(p+1)}] = 0.5 \quad (2.111)$$

TDOA estimates derived in that example are efficient.

Consider now the maximum attainable accuracy of TDOA measurements at the first stage of two-stage algorithms for radiation source localization using the hyperbolic method. As shown in Section 2.3.3, in a GIDL with m antennae, $m-1$ linearly independent TDOAs are to be estimated at this stage. To obtain required expressions for an arbitrary element

of the $(m-1) \times (m-1)$ FIM it is sufficient to transform (2.105) taking into account the linear independence of all TDOAs of the τ_{1k} type:

$$\frac{\partial \tau_{1k}}{\partial \tau_{1(n+1)}} = \delta_{k(n+1)}, \quad k = \overline{2, m}; \quad n = \overline{1, m-1} \quad (2.112)$$

Substituting (2.112) into (2.104) yields (2.106). However, the number of antennae, m , may now be arbitrary, including the values of $m-1$ exceeding the dimensionality of space.

The $(m-1) \times (m-1)$ FIM with elements (2.106) can be easily inverted even when m is large. It may be presented as

$$\tilde{\mathbf{J}}^{(\tau)} = 2\delta f_e T \overline{\Delta \omega^2} [\mathbf{Q} - \mathbf{q}\mathbf{q}^t] \quad (2.113)$$

where \mathbf{Q} is the $(m-1) \times (m-1)$ diagonal matrix and \mathbf{q} is the $(m-1) \times 1$ vector

$$\mathbf{Q} = q_\Sigma^2 \text{diag}(q_2^2, \dots, q_m^2), \quad \mathbf{q} = (q_2^2, \dots, q_m^2)^t \quad (2.114)$$

Matrices of this structure (2.114) were discussed in Section 2.2.3 (Equation (2.25)). The inversion rule for such matrices was used there (e.g., [124]):

$$[\tilde{\mathbf{J}}^{(\tau)}]^{-1} = \mathbf{B}_{\text{eff}} = \frac{1}{2\delta f_e T \overline{\Delta \omega^2}} [\mathbf{Q}^{-1} + \gamma \mathbf{Q}^{-1} \mathbf{q}\mathbf{q}^t \mathbf{Q}^{-1}] \quad (2.115)$$

where

$$\gamma = [1 - \mathbf{q}^t \mathbf{Q}^{-1} \mathbf{q}]^{-1}. \quad (2.116)$$

Substituting (2.114) into (2.115) yields the ECM of efficient estimates, $\hat{\tau}_{12}, \dots, \hat{\tau}_{1m}$, (the Cramér-Rao lower bound on estimate errors)

$$\mathbf{B}_{\text{eff}} = \frac{1}{2\Delta f_e T \overline{\Delta \omega^2} q_\Sigma^2} \left\{ \text{diag} \left(\frac{1}{q_2^2}, \dots, \frac{1}{q_m^2} \right) + \frac{1}{q_1^2} \begin{pmatrix} 1 & \dots & 1 \\ \dots & \dots & \dots \\ 1 & \dots & 1 \end{pmatrix} \right\}. \quad (2.117)$$

It can be seen that the FIM and ECM of efficient estimates, $\hat{\tau}_{12}, \hat{\tau}_{13}, \hat{\tau}_{14}$, for one-stage TDOA estimation considered above, are particular cases of (2.113), (2.114) and (2.117). When all input SNRs are equal to each other, $q_i^2 = q^2$, $i = \overline{1, m}$, (2.117) takes the simplest form

$$\mathbf{B}_{\text{eff}} = \frac{1}{2\Delta f_e T \overline{\Delta \omega^2} m q^4} \begin{bmatrix} 2 & 1 & \dots & 1 \\ 1 & 2 & \dots & 1 \\ \dots & \dots & \dots & \dots \\ 1 & 1 & \dots & 2 \end{bmatrix}. \quad (2.118)$$

Example 2.

Consider again signals with a rectangular power spectrum [(2.50) at $\Omega_{si} = 0$] as in Example 1, but for an arbitrary number, m , of antennae. Substituting (2.102) and (2.103), $\Delta f_e = \Delta f / (1 + q_\Sigma^2)$, $\overline{\Delta \omega^2} = 4\pi^4 \Delta f^2 / 12$ into (2.117) yields (2.109) and (2.110). Thus these expressions do not depend on the number of antennae, m , nor on whether $m - 1$ exceeds the dimensionality of space (there is no explicit dependence on m , dependence on q_Σ^2 does not count, even it shows the usefulness of the additional measurement). For equal input SNRs from (2.118), Equation (2.111) again results.

It should be noted that for a GIDL with $m = 3$ antennae (2.118) coincides with (2.77). This confirms that the second approach to the first stage of a two-stage radiation source localization algorithm considered in Section 2.3.3 [see (2.68)] does yield efficient estimates of linearly independent TDOAs.

Maximum attainable accuracy of radiation source (e.g., jammer) localization in space using efficient estimates of linearly independent TDOAs, i.e., at the second stage of a two-stage source localization, will be considered in Section 2.4.2.

2.4 Resultant Jammer Coordinate Measurement Using Two-Stage Algorithms

2.4.1 Resultant Coordinate Measurement Formation

The main function of the second stage of two-stage jammer coordinate estimation algorithms is to combine signal parameter [or local (“primary”) coordinate] estimates obtained at the first stage with respect to individual antennae of a GIDL, so as to form a resultant composite measurement - the global (“final”) estimate of jammer coordinates and, possibly, their derivatives in a common reference coordinate system specified at a certain time.

The general characteristic of a jammer at each time moment is the vector of state, α , which may include all three jammer coordinates, their derivatives and other parameters [132, 113, 114, 133, 134]. This section considers only such vectors whose components can

be estimated within a short time interval. These may be spatial coordinates and velocity components which are measured by the Doppler method.

When a set of local coordinate estimates determines all unknown components of α unambiguously, i.e., a single point $\hat{\alpha}$ in the state space of the jammer, this point is adopted as the estimate of α . In this case optimum estimates of local coordinates ensure an optimum estimate, $\hat{\alpha}$, according to the same optimality criterion. However, the total number of measured local coordinates of a jammer often exceeds the dimensionality of the vector, α . In this case resultant measurement formation becomes a statistical problem of α estimation using redundant estimates of local jammer coordinates obtained by all channels (antennae) of a GIDL.

This problem is usually solved by the maximum likelihood method (when local coordinate estimates are Gaussian random variables) or by the least squares method (when probability distributions of those estimates are non-Gaussian or unknown). According to both maximum likelihood and minimum r.m.s. error criteria, such an estimate, $\hat{\alpha}$, is optimum when the following quadratic form is minimized

$$L = [\hat{\xi} - \mathbf{h}(\alpha)]^t \mathbf{B}_{\xi}^{-1} [\hat{\xi} - \mathbf{h}(\alpha)] \rightarrow \min(\alpha). \quad (2.119)$$

Here $\hat{\xi}$ is the vector of local coordinate estimates; $\mathbf{h}(\alpha)$ is the vector of known functions determining the dependence of the local coordinates, ξ , on the jammer state vector, α , i.e., $\xi = \mathbf{h}(\alpha)$; \mathbf{B}_{ξ}^{-1} is the inverse of the covariance matrix (in the case of maximum likelihood criterion) or the weight matrix (in the case of least squares method) of the estimates, $\hat{\xi}$. Errors in $\hat{\xi}$ are assumed to be additive. In general, $\hat{\xi}$ includes estimates of different local coordinates. The functions, $\xi_i = h_i(\alpha)$, are, as a rule, nonlinear. To obtain $\hat{\alpha}$ from (2.119), two approaches are usually exploited: linearization of functions, $\xi_i = h_i(\alpha)$, which yields estimates, $\hat{\alpha}$, in an explicit form and iterative procedures (the successive approximation method). Their combination is also possible.

The Linearization Method with Parallel Processing of Measurements from All Antennae of GIDL

The linearization method is used when an approximate value of α is known *a priori* and may be assumed as a reference value, α_{ref} . Then the purpose of measurements is to refine

2.4: Resultant Jammer Coordinate Measurement Using Two-Stage Algorithms 79

the estimate, α_{ref} . The difference between α_{ref} and the true value, α_0 , must be small enough such that linear terms of a Taylor series of each function, $\xi_i = h_i(\alpha)$, about $\alpha = \alpha_{\text{ref}}$ would approximate this function sufficiently well in the vicinity of α_{ref} , including α_0 . In this case

$$\mathbf{h}(\alpha) \approx \mathbf{h}(\alpha_{\text{ref}}) + \mathbf{H}(\alpha - \alpha_{\text{ref}}) \quad (2.120)$$

where $\mathbf{H} = \|\partial h_j(\alpha)/\partial \alpha_l\|_{\alpha=\alpha_{\text{ref}}}$ is the matrix of derivatives of functions $h_j(\alpha)$, $j = \overline{1, N}$ (N is the total number of measured local coordinates), with respect to all n components, α_l , $l = \overline{1, n}$, of the vector α at the point $\alpha = \alpha_{\text{ref}}$. Each row of this matrix represents projections of the gradient of one of the functions, $h_j(\alpha)$. Substituting the linearized function (2.120) into (2.119) and solving the likelihood equations, $\partial L/\partial \alpha = 0$, for α yield the optimum (maximum likelihood) estimate

$$\hat{\alpha} = \alpha_{\text{ref}} + (\mathbf{H}^t \mathbf{B}_{\xi}^{-1} \mathbf{H})^{-1} \mathbf{H}^t \mathbf{B}_{\xi}^{-1} [\hat{\xi} - \mathbf{h}(\alpha_{\text{ref}})] \quad (2.121)$$

The expression (2.121) can be presented in the form

$$\hat{\alpha} = \alpha_{\text{ref}} + \mathbf{K} [\hat{\xi} - \mathbf{h}(\alpha_{\text{ref}})] \quad (2.122)$$

where

$$\mathbf{K} = (\mathbf{H}^t \mathbf{B}_{\xi}^{-1} \mathbf{H})^{-1} \mathbf{H}^t \mathbf{B}_{\xi}^{-1} \quad (2.123)$$

is the $n \times N$ matrix of optimal weights used for adding differences, $\hat{\xi}_j - h_j(\alpha)$, $j = \overline{1, N}$, to each component $\alpha_{\text{ref}l}$, $l = \overline{1, n}$, of the vector α_{ref} . Each difference is the discrepancy between the measured value of the local coordinate, $\hat{\xi}_j$, and the value of ξ_j which would be measured if the jammer state vector was equal to α_{ref} and all measurement errors were absent. In other words, these are discrepancies between the measured values, $\hat{\xi}_j$, and the calculated (true) values of ξ_j corresponding to the jammer state vector, α_{ref} .

It is important to investigate the influence of both measurement errors in $\hat{\xi}$ and linearization errors on resultant errors of α . Substitute $\hat{\xi} = \mathbf{h}(\alpha_0) + \mathbf{e}$ into (2.121) where \mathbf{e} is the vector of random errors of local coordinate measurements. After some transformations, (2.121) takes the form [135]

$$\hat{\alpha} = \alpha_0 + (\mathbf{H}^t \mathbf{B}_{\xi}^{-1} \mathbf{H})^{-1} \mathbf{H}^t \mathbf{B}_{\xi}^{-1} \{ \mathbf{h}(\alpha_0) - [\mathbf{h}(\alpha_{\text{ref}}) + \mathbf{H}(\alpha_0 - \alpha_{\text{ref}})] + \mathbf{e} \} \quad (2.124)$$

It is possible to obtain the bias of the estimate $\hat{\alpha}$ by averaging \mathbf{e} in equation (2.124):

$$\mathbf{b} = \bar{\hat{\alpha}} - \alpha_0 = (\mathbf{H}^t \mathbf{B}_\xi^{-1} \mathbf{H})^{-1} \mathbf{H}^t \mathbf{B}_\xi^{-1} \{ \mathbf{h}(\alpha(\alpha_0)) - [\mathbf{H}(\alpha_0 - \alpha_{\text{ref}})] + \bar{\mathbf{e}} \} \quad (2.125)$$

The bias arises if $\bar{\mathbf{e}} \neq \mathbf{0}$, and/or if there are linearization errors, i.e., $\mathbf{h}(\alpha_0) - [\mathbf{h}(\alpha_{\text{ref}}) + \mathbf{H}(\alpha_0 - \alpha_{\text{ref}})] \neq \mathbf{0}$.

When each local coordinate estimator at each channel (antenna) is calibrated but a measurement bias remains, and the dependence of this bias on unknown parameters (for instance, SNR values) is known, these unknown parameters may be additionally included in the vector, α , to be estimated (if the dimensionality N of the measurement vector, $\hat{\xi}$, is sufficiently large). When maximum likelihood estimators process signal samples of a large size so that asymptotic properties of the estimators manifest themselves, $\bar{\mathbf{e}} = \mathbf{0}$.

The covariance matrix of the estimate, $\hat{\alpha}$, can be obtained from (2.124)

$$\mathbf{B}_\alpha = \overline{(\hat{\alpha} - \bar{\hat{\alpha}})(\hat{\alpha} - \bar{\hat{\alpha}})^t} = (\mathbf{H}^t \mathbf{B}_\xi^{-1} \mathbf{H})^{-1} \quad (2.126)$$

As can be seen from (2.121), calculating the estimate, $\hat{\alpha}$, requires calculating the matrix, \mathbf{B}_α , as a preliminary procedure, so that the covariance matrix, \mathbf{B}_α , is obtained together with the estimate, $\hat{\alpha}$. Since the nonlinear function, $\mathbf{h}(\alpha)$, in (2.119) is replaced by the linear function (2.120), the maximum likelihood estimate (2.121), (2.122) is an efficient estimate, $\hat{\alpha}$, given $\hat{\xi}$. This means that inverting the Fisher Information Matrix (FIM)

$$\left\| \frac{\partial^2 l(\hat{\xi}_1, \dots, \hat{\xi}_N, \alpha_1, \dots, \alpha_n)}{\partial \alpha_p \partial \alpha_q} \right\|, \quad p, q = \overline{1, n}$$

where L is determined by (2.119), yields (2.126), so that (2.126) is the Cramer-Rao lower bound on errors of vector, α , estimates given $\hat{\xi}$.

If the vector of local coordinate estimates, $\hat{\xi}$, is a Gaussian random vector, then the vector, $\hat{\alpha}$, is also Gaussian (due to linear dependence of $\hat{\alpha}$ on $\hat{\xi}$). In this case it is convenient to characterize the accuracy of $\hat{\alpha}$ by an error hyperellipsoid containing $\hat{\alpha}$ with the prescribed probability, P . The error hyperellipsoid equation is given by

$$(\hat{\alpha} - \bar{\hat{\alpha}})^t \mathbf{B}_\alpha^{-1} (\hat{\alpha} - \bar{\hat{\alpha}}) = k^2 \quad (2.127)$$

where the number k determines the size of the hyperellipsoid. This number is equal to the ratio of the principal semiaxes of the hyperellipsoid to the r.m.s. estimate errors of corresponding components along these semiaxes. The principal semiaxes of the hyperellipsoid do not coincide in general with coordinate axes unless the matrix \mathbf{B}_α is a diagonal one. However, since \mathbf{B}_α is a real positive definite symmetric matrix, there exists an orthogonal matrix, \mathbf{A} , that diagonalizes \mathbf{B}_α^{-1} : $\mathbf{A}\mathbf{B}_\alpha^{-1}\mathbf{A} = \tilde{\mathbf{B}}_\alpha^{-1}$ where $\tilde{\mathbf{B}}_\alpha^{-1}$ is a diagonal matrix with positive diagonal form. The number, k , is determined by the probability, P . For an n -dimensional vector, α , the probability that $\hat{\alpha}$ falls into the hyperellipsoid (2.127) is determined by the following expression [114, 135]:

$$P = P_n(k) = \frac{1}{\Gamma(n/2)} \int_0^{k^2/2} x^{n/2-1} \exp(-x) dx = \Gamma\left(\frac{k^2}{n}, \frac{n}{2}\right) \quad (2.128)$$

where $\Gamma(n/2)$ is the gamma-function; $\Gamma(k^2/2, n/2)$ is the incomplete gamma-function. Graphics and tables for $\Gamma(k^2/2, n/2)$ are presented in [114] and [136], respectively. In the particular cases of a one-dimensional, two-dimensional and three-dimensional vector, α , (2.128) is reduced to the form

$$P_1(k) = \text{erf}(k/\sqrt{2}); \quad P_2(k) = 1 - \exp(-k^2/2); \quad (2.129)$$

$$P_3(k) = \text{erf}(k/\sqrt{2}) - k\sqrt{2/\pi} \exp(-k^2/2)$$

where $\text{erf}(x)$ is error function.

Setting a fixed value of the probability, $P_n(k)$, one can calculate k from (2.128) or (2.129) and then using (2.127) construct an error ellipsoid (or hyperellipsoid) with principal semiaxes that are equal to $k\sigma_l$ where $\sigma_l^2, l = \overline{1, n}$, are diagonal elements of the diagonalized matrix, $\tilde{\mathbf{B}}_\alpha$.

It is often desirable to characterize accuracy of a multidimensional estimate, $\hat{\alpha}$, by a scalar parameter. Such a scalar measure of accuracy is the square root of the resultant second initial moment

$$\sigma_\Sigma(\hat{\alpha}) = \left[\sum_{l=1}^n (\hat{\alpha}_l - \alpha_{0l})^2 \right]^{1/2} = \left[\text{Tr}\mathbf{B}_\alpha + \sum_{l=1}^n b_l^2 \right]^{1/2} \quad (2.130)$$

where $\text{Tr}\mathbf{B}_\alpha$ is the trace of the matrix, \mathbf{B}_α ; b_l are the components of the bias vector (2.125) of estimates, $\hat{\alpha}$. When α contains only three jammer coordinates, e.g., $\alpha^t = (x, y, z)$ and $\hat{\alpha}$

is unbiased, the quantity $\sigma_{\Sigma}(\hat{\alpha})$ is often called the radius of the spherical r.m.s. error, r_{sph} . In a Cartesian coordinate system

$$r_{\text{sph}} = \sqrt{(\hat{x} - x_0)^2 + (\hat{y} - y_0)^2 + (\hat{z} - z_0)^2}; \quad (2.131)$$

in a spherical coordinate system

$$r_{\text{sph}} = \sqrt{(\hat{R} - R_0)^2 + R_0^2 \cos^2 \epsilon_0 (\hat{\beta} - \beta_0)^2 + R_0^2 (\hat{\epsilon} - \epsilon_0)^2} \quad (2.132)$$

Another scalar measure for jammer localization accuracy often used in practice is the Geometric Dilution of Precision (GDOP) which is defined either as the r.m.s. jammer position error (i.e. as (2.130) or [137]) or more often as the ratio of this r.m.s. jammer position error to the r.m.s. ranging error [135, 138, 139]. The latter definition is

$$\text{GDOP} = \sqrt{\text{Tr} \mathbf{B}_{\alpha}} / \sigma(R). \quad (2.133)$$

Following the definition (2.133), the GDOP indicates how much the ranging error is magnified by the geometric relations among the jammer and antenna positions in a GIDL.

The main drawback of the linearization method is that an approximate value, α_{ref} , of the estimated vector, α , must be known *a priori*. As mentioned above, α_{ref} must be sufficiently close to the true value, α_0 , such that the linear approximation (2.120) does not lead to a noticeable bias of estimates [see (2.125)]. It is important to note that this difficulty may often be overcome in GIDL. When there is no external jammer designation with required accuracy, preliminary measurements can be performed by a part of the total number of channels (antennae) (without redundancy) so as to obtain an unambiguous estimate of α . For instance, in GIDL, α_{ref} may be found by the hyperbolic method using three linearly independent TDOA measurements. Antennae with maximum effective baselengths between them with respect to the jammer direction should be selected. This provides better accuracy of α_{ref} .

Using preliminary nonredundant measurements from a portion of the total number of antennae for calculating the reference value, α_{ref} , of the jammer state vector, α , permits in many cases refinement of the accuracy of resultant maximum likelihood estimates (2.121)–(2.123) taking into account *a priori* information about the accuracy of α_{ref} . When α_{ref} is

2.4: Resultant Jammer Coordinate Measurement Using Two-Stage Algorithms 83

a Gaussian vector with the known covariance matrix, \mathbf{B}_{ref} , and errors of α_{ref} are close by an order of magnitude to expected errors of the optimum estimates, $\hat{\alpha}$ (see (2.126)), then instead of (2.123) the matrix, \mathbf{K} (2.122), takes the form [114, 134]

$$\mathbf{K} = (\mathbf{B}_{\text{ref}}^{-1} + \mathbf{H}^t \mathbf{B}_{\xi}^{-1} \mathbf{H})^{-1} \mathbf{H}^t \mathbf{B}_{\xi}^{-1}. \quad (2.134)$$

The inverse covariance matrix, $\mathbf{B}_{\text{ref}}^{-1}$ (the “accuracy matrix” [114]), of α_{ref} is additionally included in parentheses. Then the covariance matrix of the estimate, $\hat{\alpha}$, is given by

$$\mathbf{B}_{\alpha} = (\mathbf{B}_{\text{ref}}^{-1} + \mathbf{H}^t \mathbf{B}_{\xi}^{-1} \mathbf{H})^{-1}. \quad (2.135)$$

The estimate, $\hat{\alpha}$, obtained from (2.122) where the matrix, \mathbf{K} , is determined by (2.134) is an optimum estimate according to the maximum *a posteriori* probability criterion.

When signal complex amplitude fluctuations at different antennae are mutually statistically independent, then “noise” (random) errors of the jammer local coordinate measurements from different channels (antennae) are statistically independent also.

The Iteration Method

When one cannot “guess” the initial value, α_{ref} , sufficiently close to the true value, α_0 , so as to avoid noticeable linearization errors (see (2.125)), iteration methods may be directly applied to Equation (2.119). In principle, any extremum finding technique applicable to multidimensional nonlinear functions may be used. However, for large dimensionality of the jammer state vector, α , this problem becomes difficult. Several “semi-empirical” techniques have been proposed to solve the problem. In general, convergence of these iteration processes to the optimum estimate, $\hat{\alpha}$, has not been proven. However, when such procedures are used for practical calculations, their convergence to $\hat{\alpha}$ is usually achieved [140, 141]. Though an initial approximation, α_{ref} , is not necessary to be close to the true value, α_0 , most iteration techniques used the assumption that errors are “small” since linearized algorithms are employed at each step. Typically, measurements of all channels (antennae) are jointly taken into account (parallel measurement processing).

One group of iteration algorithms is based on Equation (2.121) [140, 142]:

$$\hat{\alpha}(k+1) = \hat{\alpha}(k) + [\mathbf{H}^t(k) \mathbf{B}_{\xi}^{-1} \mathbf{H}(k)]^{-1} \mathbf{H}^t(k) \mathbf{B}_{\xi}^{-1} \{\hat{\xi} - \mathbf{h}[\hat{\alpha}(k)]\} \quad (2.136)$$

where k is the number of iteration, $k = 0, 1, 2, \dots$; $\hat{\alpha}(0) = \alpha_{\text{ref}}$ is the initial approximation which can be chosen using *a priori* information or preliminary measurements. To ensure convergence of this procedure, it is desirable to choose $\hat{\alpha}(0)$ not too far from α_0 . The derivatives, $\mathbf{H}(k)$, are taken at the point $\hat{\alpha}(k)$.

Another approach is based on the gradient method. In this case [141, 142]

$$\hat{\alpha}(k+1) = \hat{\alpha}(k) + \mu \mathbf{H}^t(k) \mathbf{B}_{\xi}^{-1} \{\hat{\xi} - \mathbf{h}[\hat{\alpha}(k)]\} \quad (2.137)$$

where μ is the scalar constant ($\mu > 0$). Examples of successful applications of algorithms (2.136) and (2.137) are presented in [140, 141].

It is important to note that errors in antenna location lower the accuracy of resultant jammer state vector estimates. Therefore, antenna positions in a GIDL must be accurately known. When antenna localization errors are random and of the same order of magnitude as other errors, they may be included in measurements of local coordinates. It is then possible to optimize the estimate, $\hat{\alpha}$, including antenna localization errors [142]. Possible correlation between localization errors for different antennae should be taken into account. However, systematic errors (estimate biases) may have the most serious effect on the resultant jammer state estimation accuracy. Therefore, errors due to antenna site uncertainties, antenna orientation and time calibration must be minimized.

2.4.2 Examples of Two-Stage Algorithm Applications to Jammer Coordinate Estimation

In this subsection several numerical examples are presented for better understanding of the accuracy advantages of jammer position estimation in GIDL and for revealing the contributions of different local coordinate measurements to the resultant jammer localization accuracy.

Let us assume all estimates of local coordinates at the first stage of two-stage algorithms to be unbiased. Such an assumption reveals the dependence of jammer position r.m.s. errors on the number of antennae and system geometry as well as on the type of local coordinates. However, as was mentioned in Section 2.4.1, the problem of systematic errors caused by biases in local coordinate estimates is of great practical importance (see, e.g., [143]).

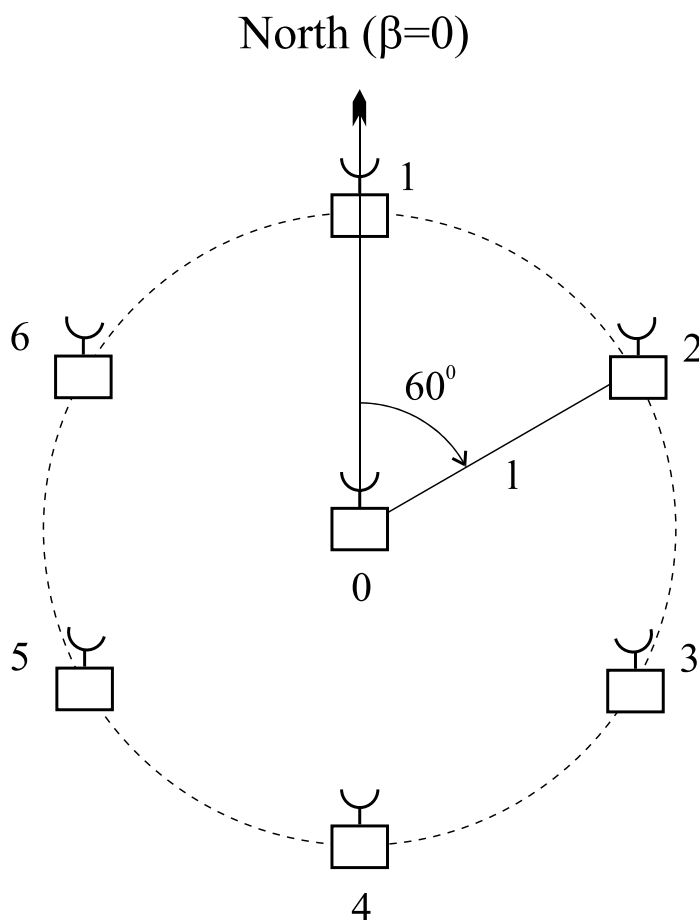


Figure 2.5: Configuration of the GIDL for Examples

Example 1.

Let a jammer be positioned at the point with the following spherical coordinates: range, R ; azimuth β ; elevation angle, ϵ . As a reference point, the coordinate system origin is considered. Let us assume that one antenna is located at the origin, and m other antennae are arranged uniformly along the circle of radius l m in the horizontal plane with the center at the coordinate origin, as shown in Figure 2.5. Antenna coordinates are: $L_i = l$ m, $\beta_i = 2\pi(i - 1)/m$, $\epsilon_i = 0$, $i = \overline{1, m}$.

Let a GIDL of the described above geometry estimate spatial coordinates of the jammer (a radiation source) by the hyperbolic method (range-difference-measurement method, see section 2.3.1). As noted in section 2.3.2, $m(m + 1)/2$ different TDOAs can be measured

in a GIDL containing $m + 1$ spatially separated receiving antennae but only m TDOAs among them are linearly independent. In fact, the TDOAs taken around any closed circuit of antennae add to zero [see (2.31)]. Following [42, 129] it has been shown in section 2.3.3, that estimates of all $m(m + 1)/2$ different TDOAs provide, under certain conditions, the efficient estimates of m linearly independent TDOAs. However, let us assume here that only m linearly independent signal TDOAs between the central antenna and each of the peripheral antennae are directly measured and used for jammer localization. Thus the vector of measurements takes the form: $\hat{\xi} = (\widehat{\Delta R}_1, \dots, \widehat{\Delta R}_m)^t$ where ΔR_i is the range difference from the jammer (the radiation source) to the central and the i^{th} peripheral antennae, i.e. $\Delta R_i = R - R_i$. Evidently, these range differences are proportional to corresponding TDOAs: $\Delta R_i = c\tau_{s0i}$ where c is the speed of light. It was shown in section 2.3.3 that though maximum likelihood TDOA estimates $\hat{\tau}_{s0i}$ are mutually correlated for different $i = \overline{1, m}$, this correlation is weak for weak input signals (low input SNRs). Therefore, assuming input signals to be weak, it is possible to ignore here correlation between different estimates so that the covariance matrix of measurements is: $\mathbf{B}_\xi = \sigma^2(\widehat{\Delta R})\mathbf{I}$ where $\sigma^2(\widehat{\Delta R})$ is the range difference measurement error variance (for simplicity, the same for all antennae) and \mathbf{I} is the identity matrix.

The exact expressions for elements of the covariance matrix \mathbf{B}_α (determining accuracy of the estimates \hat{R} , $\hat{\beta}$ and $\hat{\epsilon}$) can be obtained from (2.126) taking into account that

$$\xi_i = \Delta R_i = h_i(\alpha) = R \left[1 - \sqrt{1 - (2l/R) \cos \epsilon \cos(\beta - \beta_i) + l^2/R^2} \right]. \quad (2.138)$$

For the considered GIDL configuration (Figure 2.5) with “short baselines” ($l \ll R$) one may expand the right side of (2.138) into a Taylor series retaining only first terms. Note that a linear approximation is usually sufficient for accuracy analysis of angular coordinate estimates. This approximation implies the signal wavefront to be planar for the GIDL as a whole. To evaluate range errors as well as correlation between angular and range errors, the square approximation is necessary. As a result of calculations using equation (2.126) one can obtain for $m \geq 5$ (here $\rho(\cdot, \cdot)$ denotes the correlation coefficient):

$$\begin{aligned} \sigma(\hat{R}) &= \frac{2}{\sqrt{m}} \left(\frac{R}{L} \right)^2 \frac{1}{\sqrt{(1 - 0.5 \cos^2 \epsilon)^2 + 0.125 \cos^4 \epsilon}} \sigma(\widehat{\Delta R}); \\ \sigma(\hat{\beta}) &= \frac{2}{\sqrt{m}} \frac{1}{l \cos \epsilon} \sigma(\widehat{\Delta R}); \quad \sigma(\hat{\epsilon}) = \frac{2}{\sqrt{m}} \frac{1}{l \sin \epsilon} \sigma(\widehat{\Delta R}); \end{aligned}$$

2.4: Resultant Jammer Coordinate Measurement Using Two-Stage Algorithms 87

$$\begin{aligned}\rho(\hat{R}, \hat{\beta}) &= 0; \quad \rho(\hat{\beta}, \hat{\epsilon}) = 0; \\ \rho(\hat{R}, \hat{\epsilon}) &= \frac{3}{4\sqrt{2}} \frac{l}{R} \frac{\cos \epsilon (4 - 3 \cos^2 \epsilon)}{\sqrt{(1 - 0.5 \cos^2 \epsilon)^2 + 0.125 \cos^4 \epsilon}};\end{aligned}\quad (2.139)$$

for $m = 4$:

$$\begin{aligned}\sigma(\hat{R}) &= \left(\frac{R}{L}\right)^2 \frac{1}{\sqrt{(1 - 0.5 \cos^2 \epsilon)^2 + 0.125 \cos^4 \epsilon (1 + \cos 4\beta)}} \sigma(\widehat{\Delta R}); \\ \sigma(\hat{\beta}) &= \frac{1}{\sqrt{2}l \cos \epsilon} \sigma(\widehat{\Delta R}); \quad \sigma(\hat{\epsilon}) = \frac{1}{\sqrt{2}l \sin \epsilon} \sigma(\widehat{\Delta R}); \\ \rho(\hat{R}, \hat{\beta}) &= 0; \quad \rho(\hat{\beta}, \hat{\epsilon}) = 0; \\ \rho(\hat{R}, \hat{\epsilon}) &= \frac{3}{4\sqrt{2}} \frac{l}{R} \frac{\cos \epsilon [4 - \cos^2 \epsilon (3 + \cos 4\beta)]}{\sqrt{(1 - 0.5 \cos^2 \epsilon)^2 + 0.125 \cos^4 \epsilon (1 + \cos 4\beta)}}.\end{aligned}\quad (2.140)$$

It is seen that, within the frames of assumed approximations, for $m \geq 5$ the r.m.s. errors do not depend on the jammer range R and azimuth β . The estimates \hat{R} and $\hat{\beta}$ as well as $\hat{\beta}$ and $\hat{\epsilon}$ are mutually uncorrelated while \hat{R} and $\hat{\epsilon}$ are weakly correlated. For $m = 4$ the weak dependence of $\sigma(\hat{R})$ and $\rho(\hat{R}, \hat{\beta})$ on the jammer azimuth, β , appears.

For the minimal total number of antennae required to estimate all the three spatial coordinates of a radiation source, $m + 1 = 4$, the GIDL in the Figure 2.5 takes the form of a regular three-pointed star (antennae 0, 1, 3, and 5 only). For this case we have

$$\begin{aligned}\sigma(\hat{R}) &= \frac{2}{\sqrt{3}} \left(\frac{R}{L}\right)^2 \frac{1}{1 - 0.5 \cos^2 \epsilon} \sigma(\widehat{\Delta R}); \\ \sigma(\hat{\beta}) &= \frac{\sqrt{2}}{\sqrt{3}l \cos \epsilon} \frac{\sqrt{(1 - 0.5 \cos^2 \epsilon)^2 + 0.125 \cos^4 \epsilon \sin^2 3\beta}}{1 - 0.5 \cos^2 \epsilon} \sigma(\widehat{\Delta R}); \\ \sigma(\hat{\epsilon}) &= \frac{\sqrt{2}}{\sqrt{3}l \sin \epsilon} \frac{\sqrt{(1 - 0.5 \cos^2 \epsilon)^2 + 0.125 \cos^4 \epsilon \cos^2 3\beta}}{1 - 0.5 \cos^2 \epsilon} \sigma(\widehat{\Delta R}); \\ \rho(\hat{R}, \hat{\beta}) &= -\frac{\cos^2 \epsilon \sin 3\beta}{2\sqrt{2}\sqrt{(1 - 0.5 \cos^2 \epsilon)^2 + 0.125 \cos^4 \epsilon \sin^2 3\beta}}; \\ \rho(\hat{\beta}, \hat{\epsilon}) &= -\left\{ \cos \epsilon \sin 3\beta [\cos^3 \epsilon \sin 3\beta - (2l/R)(4 - \cos^2 \epsilon - 0.75 \cos^4 \epsilon)] \right\} \times \\ &\quad \left\{ 8\sqrt{[(1 - 0.5 \cos^2 \epsilon)^2 + 0.125 \cos^4 \epsilon \sin^2 3\beta][(1 - 0.5 \cos^2 \epsilon)^2 + 0.125 \cos^4 \epsilon \cos^2 3\beta]} \right\}^{-1}; \\ \rho(\hat{R}, \hat{\epsilon}) &= -\left\{ \cos \epsilon [\cos \epsilon \cos 3\beta - (l/2R)(12 - 7 \cos^2 \epsilon)] \right\}\end{aligned}$$

$$\times \left\{ 8 \left\{ (1 - 0.5 \cos^2 \epsilon)^2 + 0.125 \cos^4 \epsilon \cos^2 3\beta - (l/R) \cos \epsilon \cos 3\beta \right. \right. \\ \left. \left. \times [1 + \cos^2 \epsilon (1 - 0.875 \cos^2 \epsilon)] \right\} \right\}^{-1/2}. \quad (2.141)$$

When $m = 3$ correlation between the estimates appears, especially for low elevation angles, ϵ . It can also be seen that the r.m.s. angular errors are dependent on the jammer azimuth, β .

Example 2.

Let us evaluate the maximum attainable accuracy of the radiation source localization positioned as in Example 1 by the GIDL shown in Figure 2.5 when at the first stage of a two-stage localization algorithm all possible measurements of different TDOAs provide efficient estimates of linearly independent TDOAs (see Section 2.3.3). Let us consider for brevity only one the simplest variants where the GIDL is a regular three-pointed star (the azimuths of the peripheral stations are 0° , 120° and -120°). Let the signal have a rectangular PSD with the bandwidth Δf [see (2.50)], and the input SNRs, q^2 , be equal at all the antennae. It is easy to show according to (2.118), (2.111) that the ECM of range difference efficient estimates (the Cramer-Rao lower bound on errors) is given by

$$\mathbf{B}_{\Delta \text{Reff}} = \frac{3(1 + 4q^2)c^2}{8q^4 \Delta f T \pi^2 \Delta f^2} \begin{bmatrix} 2 & 1 & 1 \\ 1 & 2 & 1 \\ 1 & 1 & 2 \end{bmatrix}. \quad (2.142)$$

where c is the speed of light, T is the correlator integration time. To permit a simple comparison with the results from Example 1 let us assume r.m.s. error of each TDOA measurement to be $\sigma(\widehat{\Delta R})$ as before, the input SNRs, q^2 at all the antennae and other conditions to be equal to those of Example 1. Then it is possible to obtain

$$\mathbf{B}_{\Delta \text{Reff}} = \frac{1 + 4q^2}{4(1 + 2q^2)} \sigma^2(\widehat{\Delta R}) \begin{bmatrix} 2 & 1 & 1 \\ 1 & 2 & 1 \\ 1 & 1 & 2 \end{bmatrix} [\text{m}^2] \quad (2.143)$$

Expanding (2.138) into a Taylor series and retaining terms up to second order yields the following equations for the jammer range differences from the central to each of the three

peripheral antennae

$$\Delta R_{0i} = l \cos \epsilon \cos(\beta - \beta_i) - (l^2/2R)[1 - \cos^2 \epsilon \cos^2(\beta - \beta_i)] \quad (2.144)$$

where the notation is as in Example 1. The corresponding derivatives are

$$\begin{aligned} \partial \Delta R_{0i} / \partial R &= (l^2/2R^2)[1 - \cos^2 \epsilon \cos^2(\beta - \beta_i)]; \\ \partial \Delta R_{0i} / \partial \beta &= -l \cos \epsilon \sin(\beta - \beta_i)[1 + (l/R) \cos \epsilon \cos(\beta - \beta_i)]; \\ \partial \Delta R_{0i} / \partial \epsilon &= -l \sin \epsilon \cos(\beta - \beta_i)[1 + (l/R) \cos \epsilon \cos(\beta - \beta_i)]. \end{aligned} \quad (2.145)$$

Inverting the matrix (2.143), substituting (2.145) in (2.126) for l meters, R meters, $\beta = 0$, $\epsilon = 40^\circ$, $\beta_1 = 0$, $\beta_3 = 120^\circ$, and $\beta_5 = -120^\circ$ yields the covariance matrix of the estimate \mathbf{B}_α .

Comparing the minimum attainable r.m.s. errors of efficient unbiased estimates of the radiation source coordinates \mathbf{B}_α with corresponding errors from (2.141) it is possible to see significant advantages, namely, the azimuth r.m.s. error, elevation angle r.m.s. error are reduced while the range r.m.s. error is nearly the same. Such a reduction of the azimuth r.m.s. error is caused by the contribution of the large effective baselength between antennae number 3 and 5 (Figure 2.5), i.e. by high sensitivity of the range difference ΔR_{35} , to changes in the radiation source azimuth. This range difference was not included in the measurements in Example 1. At the same time the negative correlation between the range and elevation angular errors becomes higher.

2.5 Range and Coverage of GIDL System

There are two major characteristics to the GIDL system: (1) the maximum range and the coverage; (2) the accuracy of the jammer location. The first describes at what maximum range the system should be able to detect a jammer of a given power. This range needs to be greater than the effective radius of the jammer. The second characteristic describes how accurately the jammer can be located once it is detected. This section examines both characteristics, states expected performance, and lists aspects which provide improvement.

For the GIDL system, range and coverage are determined by jammer radiation characteristics. There are a variety of forms of radiation sources. They differ in waveform

structure, radiation power, bandwidth, etc. These may be sources of naturally occurring radiation or sources of deliberate active interferences designed to degrade performance or deny use of GPS signals. In what follows, a system is considered which is designed for detection, coordinate measurement and tracking of “point” sources radiating continuous stochastic (noise-like) signals. Mathematical models of such signals are described in Section 2.2.1.

GIDL system coverage is defined as the region of space in which a radiating source should be positioned such that with the chosen signal processing, information fusion algorithms, and detection criteria, the source detection probability will be no smaller than a required value at a fixed allowable false alarm probability. This limit assumes that the source radiates a stochastic signal with given power spectral density (PSD) in the directions of all receiving antennae.

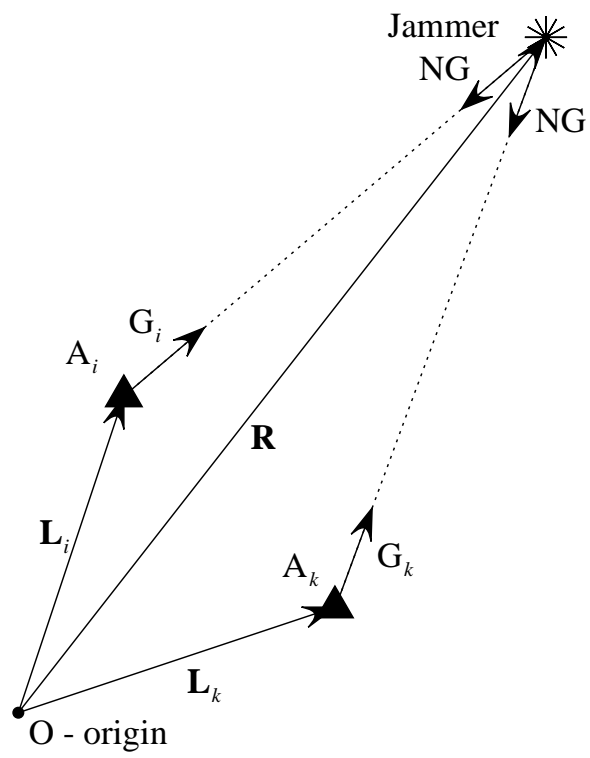
The PSD of radiation is assumed to be equal in all the GIDL antennae’ directions and constant within the signal bandwidth. Thus, a rather artificial jammer (here, a radiation source) is assumed. However, if sufficient *a priori* information is available, one may, of course, take into account characteristics of the actual radiation source including radiation PSD differences in the directions of different receiving stations, variations of PSD within the bandwidth, etc..

Let us consider range and coverage for a GIDL system locating a jammer via hyperbolic methods. Maximum range and coverage of the system is determined by looking at the post-processing signal-to-noise ratio of the received signals. That ratio is defined by setting probabilities of detection and false alarm.

Since TDOA measurements are based on mutual correlation processing of signals received by pairs of stations (Sections 2.3.1–2.3.3), the “cell” of such a system is a pair of receiving stations. The principal detection parameter for an arbitrary pair of stations with the numbers i, k ($i, k = \overline{1, m}$) is the signal-to-noise ratio (SNR) at the correlator output, $q_{\text{out cor } ik}^2$:

$$q_{\text{out cor } ik}^2 = q_{S_i}^2 q_{S_k}^2 n / (1 + q_{S_i}^2)(1 + q_{S_k}^2) \quad (2.146)$$

where $q_{S_i}^2, q_{S_k}^2$ are the power SNR at the antennae (at the correlator inputs) and $n = \Delta f_s T_s$ is the signal accumulation factor (assumed equal for all stations). For typical values, like

**Figure 2.6:** Single Baseline System

$n = 10^3 - 10^4$, the required high detection probabilities can be achieved at $q_{Si}^2 \ll 1$, $i = \overline{1, m}$, so that (2.146) may be simplified to

$$q_{\text{out cor } ik}^2 \approx q_{Si}^2 q_{Sk}^2 n, \quad i, k = \overline{1, m}, i \neq k \quad (2.147)$$

For the receiving antenna located at the point determined by the radius-vector \mathbf{L}_i ,

$$q_{Si}^2 = \frac{(NG)G_i\lambda^2\gamma_i}{(4\pi)^2 k T_{\text{eff } i} \|\mathbf{R} - \mathbf{L}_i\|^2}, \quad i = \overline{1, m} \quad (2.148)$$

where (NG) is the jamming signal PSD in the direction of all antennae; \mathbf{R} is the radius-vector of the signal source (jammer); γ_i is the total loss factor for the stochastic signal reception and processing; λ is the wavelength; k is the Boltzmann's constant ($k = 1.38 \times 10^{-23}$ W/Hz K); $T_{\text{eff } i}$ is the receiver effective noise temperature (K); and G_i is the antenna gain in the direction of the jammer.

Assume that we have a single baseline system as shown in Figure 2.6 and that the desired post-processing SNR ($q_{\text{out cor } ik}^2$) is set. Then using the link equation we can derive the maximum range and coverage for an antenna pair, A_i, A_k .

The quantity, $q_{Si}^2, i = \overline{1, m}$, has been determined by (2.148). Substituting (2.148) in (2.147) shows that at the fixed value of $n = \Delta f_S T_S$, the maximum range and coverage are determined by the inequality

$$\|\mathbf{R} - \mathbf{L}_i\|^2 \|\mathbf{R} - \mathbf{L}_k\|^2 \leq F_{1ik}^4 \quad (2.149)$$

where

$$F_{1ik}^4 = \frac{(NG)^2 G_i G_k \lambda^4 \gamma_i \gamma_k}{(4\pi)^4 k^2 T_{\text{eff } i} T_{\text{eff } k} q_{\text{out cor } ik}^2} \quad (2.150)$$

In (2.150), $q_{\text{out cor } ik}$ is the minimum value of output SNR affording the required detection characteristics.

When antenna mainbeam gains are not dependent on mainbeam pointing directions, then coverage area bounds in any plane passing through both stations are Cassini's ovals (see Figure 2.7). For long ranges these ovals approximate circles.

When the output false alarm probability, P_{fa} , the required output detection probability, $P_{d \text{ req}}$, and the chosen decision rule are specified, maximum range and coverage calculations are as follows. For each point in space, $\mathbf{R} = (R, \beta, \varepsilon)$, one can estimate q_{Si}^2 from

(2.148) and then $q_{\text{out corr } ik}^2$ from (2.147). Assuming the partial false alarm probabilities at the correlator output of all pairs of stations to be the same ($P_{\text{fa } ik} = P_{\text{fa } 0}$) one can obtain the detection probability, P_{dik} . Threshold exceedings in different pairs of stations under the condition $q_{Si}^2 \ll 1$ may be considered as statistically independent events. The output detection probability, P_d , can be calculated according to the decision rule chosen and using the obtained values of P_{dik} . The set of points, $\mathbf{R} = (R, \beta, \varepsilon)$, for which $P_d \geq P_{d \text{ req}}$ forms the coverage of the GIDL.

The approximate lower estimate for maximum detection range and coverage may be obtained combining individual coverages of each pair of stations.

Figure 2.7 represents the horizontal projection of the coverage of the GIDL containing four equal receiving antennae, with a baseline of 100m, and assumed jammer power - 51 dBW/MHz. The antennae are located in the form of a regular three-pointed star.

Equation (2.149) is the general equation. Let us now plug in numbers of interest and examine the results. Figure 2.8 shows the antenna array configuration which has been used to generate each plot shown in Figure 2.9. The maximum range and coverage for specific baselines and jammer powers are plotted in this second figure. This is the so-called “Star Antenna” configuration where the master antenna is located in the center and three other antennae are located at some distance from the central antenna and spaced 120° apart. This configuration produces three independent baselines. On each plot (2.9) three Cassini’s ovals are shown, one per baseline, with the intersection of these ovals being the coverage of the whole system. The top row of plots corresponds to baselines of 12 meters in length, with the bottom row representing baselines of 100 m. Note that for the weakest jammer and 100 m baseline there is no coverage. The jammer is simply too weak to be detected by two antennae simultaneously with the given system parameters. Other assumptions which were used in the generation of these plots include: $G_i = G_k = 1$ (antennae are omnidirectional with unity gain); postprocessing SNR, $q_{\text{out corr}}^2 = 50$ (set by probability of detection, $P_d \approx 0.75$, and probability of false alarm, $P_{fa} = 10^{-6}$); background white noise is $kT_{\text{eff}} = 4 \cdot 10^{-21}$ W/Hz; and processing losses are $\gamma_i = \gamma_k = 0.3$. Comparison of these plots with Figure 1.1 shows that the coverage of the GIDL is larger than the effective radius of the jammer, which is taken as a loss of the one satellite, and on average is about 10 m for a -70 dBW/MHz jammer. Note that it is possible to scale this number to a jammer of

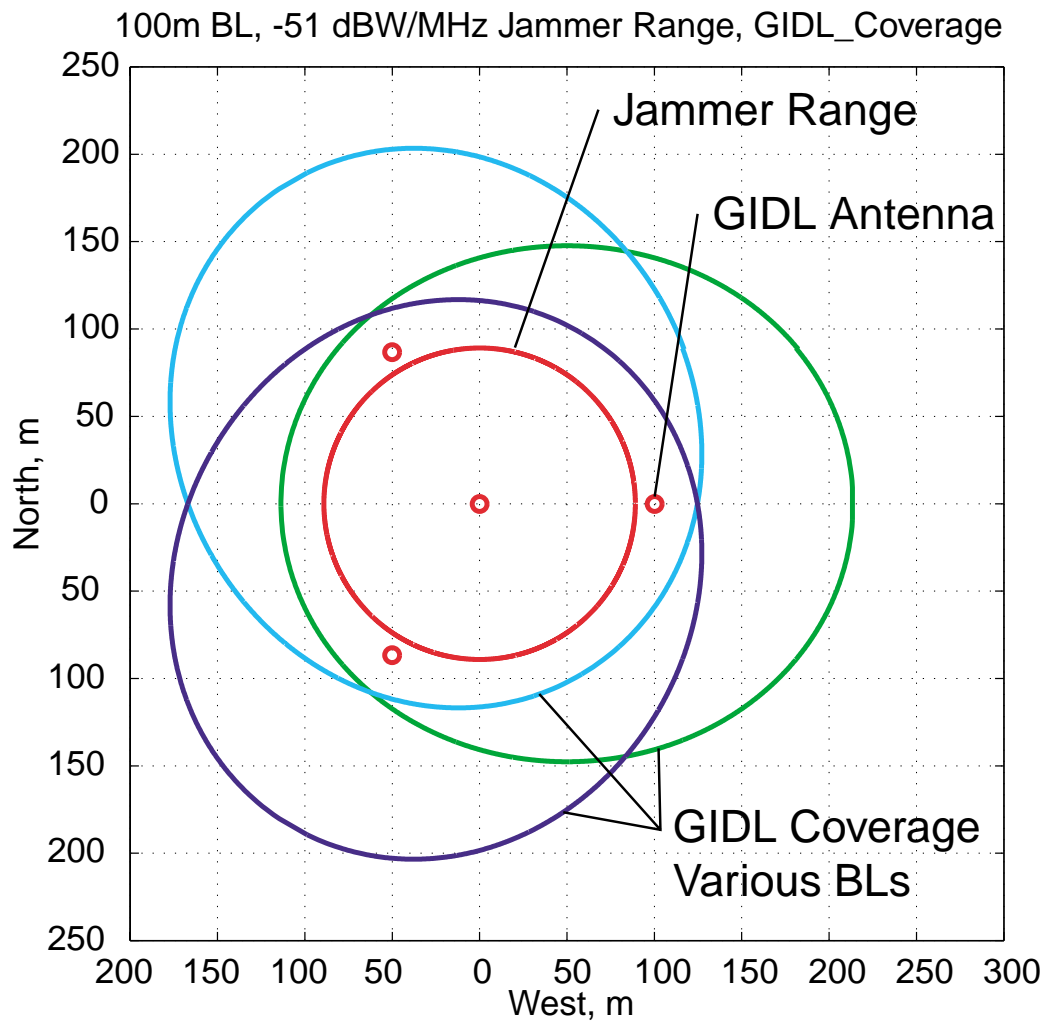


Figure 2.7: -51 dBW/MHz Jammer Range and GIDL Coverage with 100m Base-lines

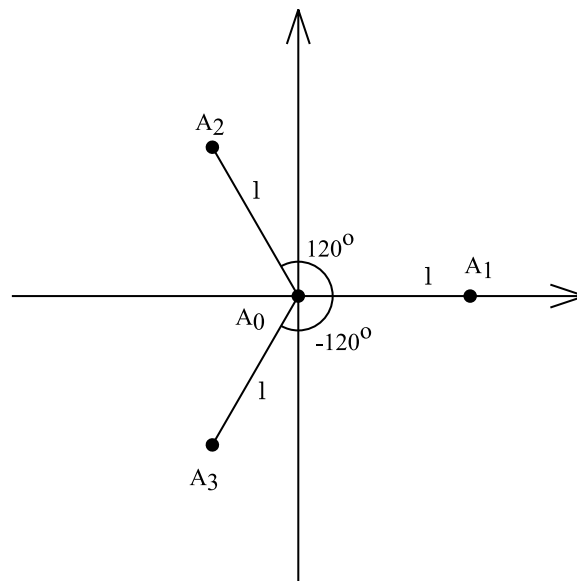


Figure 2.8: “Star Antenna” Configuration for Analysis

any power (see Figure 2.14, and Section 2.5.1).

Everything that has been said in the previous paragraph is true for a GPS receiver using the same antennae as the GIDL system, but by using different antennae it is possible to get a differential advantage of GIDL over a GPS receiver.

By using different antennae for GIDL and the GPS receiver, it is possible to improve the range of the GIDL and lessen the effective range of the ground jammer. The most probable direction for the interference signal is horizontal or along the ground. A typical antenna gain pattern of the GPS receiver is shown in Figure 2.10(GPS). It has low gain at low elevations, exactly where the jammers would most likely be located. On the contrary, if we use antenna patterns similar to that shown in Figure 2.10(GIDL), extra antenna gain results in the most probable jammer direction. Thus the small gain of the GPS antenna at low elevations shrinks the jammer effective radius for the GPS receiver (and also improve multipath performance of the GPS receiver), and the high gain of the GIDL antenna in the horizontal plane improves the jammer detection capability. For all calculations and analysis, it is assumed that all antennae are omnidirectional, so if this antenna pattern feature is present in the system, appropriate corrections to the calculations should be made.

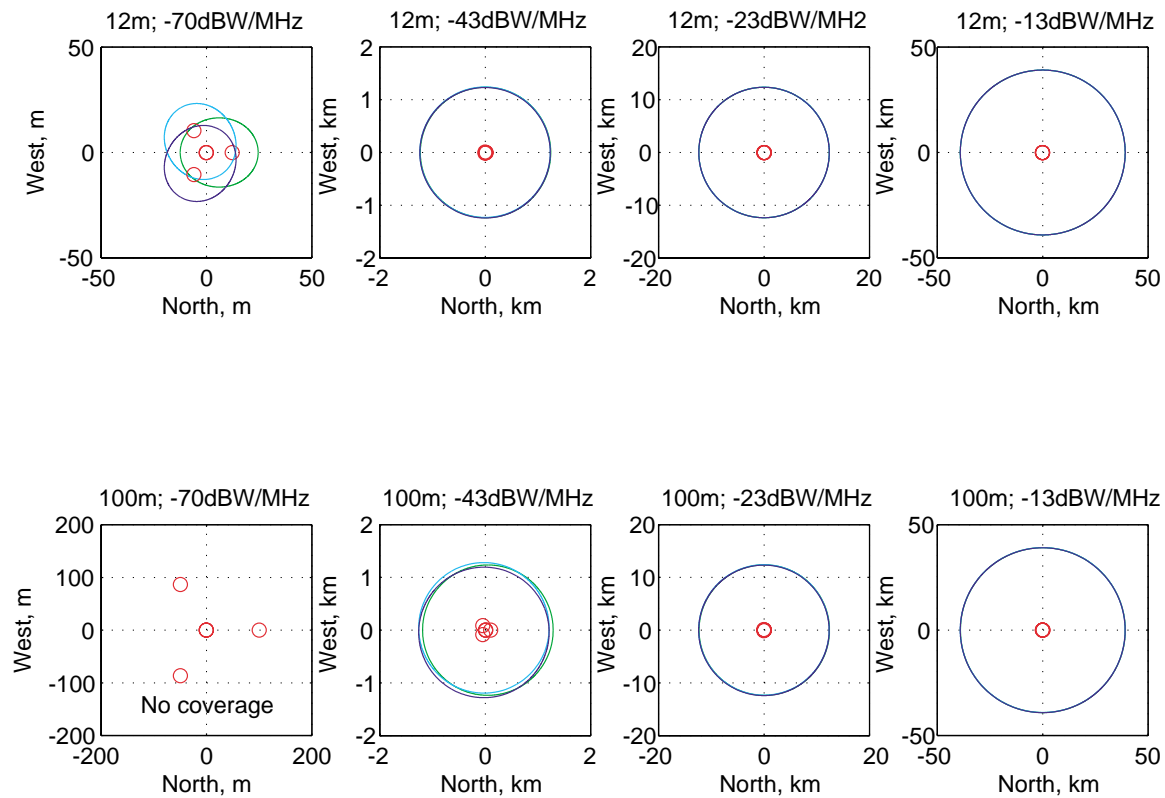


Figure 2.9: Maximum Range and Coverage of the GIDL System With Baselines 12 m and 100 m and Star Configuration for Jammers of Various Powers (red circles are GIDL antenna locations and effective jammer range is not shown)

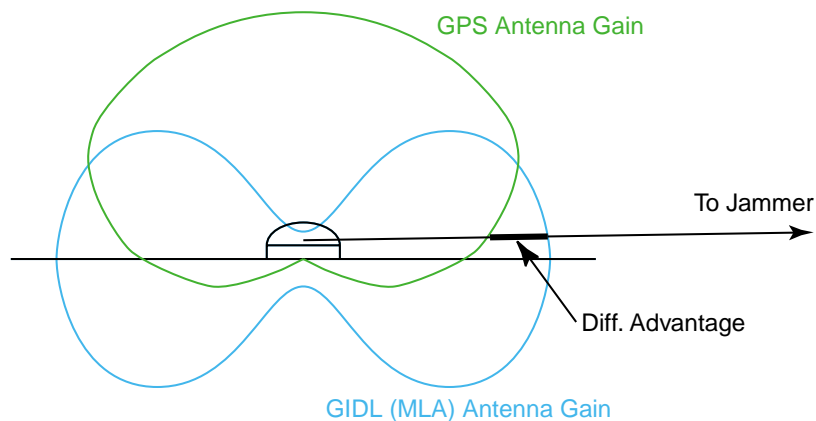


Figure 2.10: 6 dB Difference in Antenna Gain Corresponds to x2 Improvement in Range

Jammer Location Analysis The Stanford experimental GIDL system has only four antennae, which form three independent baselines. Jammer locations would lie on the intersection of three hyperbolas defined by these three baselines. In this special case it is possible to derive an analytical solution for the jammer location. Three baselines yield three range difference measurements, ΔR_i :

$$\Delta R_i = R \left(1 - \sqrt{1 - \frac{2l_i}{R} (\cos \epsilon \cos \epsilon_i \cos(\beta - \beta_i) + \sin \epsilon \sin \epsilon_i) + \frac{l_i^2}{R^2}} \right), \quad (2.151)$$

with unknowns: R range to the jammer, β azimuth of the jammer, ϵ elevation of the jammer; and system parameters (constants): l_i radius-vector of the i^{th} antenna, β_i azimuth of the i^{th} antenna, ϵ_i elevation of the i^{th} antenna.

An analytical solution to the jammer position, (R, β, ϵ) , was developed based on the measured signal delays, ΔR_i , and known system parameters.

It is possible to estimate the error covariance matrix (ECM) of possible jammer locations (see previous sections). Jammer location ECM is defined by

$$B_{\text{loc}} = (H^t B_{\Delta R_i}^{-1} H)^{-1}, \quad (2.152)$$

where $B_{\Delta R_i}$ is the ECM of measurements ΔR_i , and depends on the SNR in each antenna and

$$H = \begin{bmatrix} \frac{\partial \Delta R_1}{\partial R} & \frac{\partial \Delta R_1}{\partial \beta} & \frac{\partial \Delta R_1}{\partial \epsilon} \\ \frac{\partial \Delta R_2}{\partial R} & \frac{\partial \Delta R_2}{\partial \beta} & \frac{\partial \Delta R_2}{\partial \epsilon} \\ \frac{\partial \Delta R_3}{\partial R} & \frac{\partial \Delta R_3}{\partial \beta} & \frac{\partial \Delta R_3}{\partial \epsilon} \end{bmatrix}. \quad (2.153)$$

For the analysis of an assumed constant power jammer, depending on the jammer power and location, one would have to calculate SNR for each antenna, then compare it with the detection threshold, and only if it is above such a threshold, use it to estimate measurement errors.

In order to estimate the ECM of the measurements, the link equation is first used to estimate the SNR of the jammer as seen by each antenna

$$q_i^2 = \frac{P_j G_i \lambda^2 \gamma_i}{(2\pi)^2 k T_{\text{eff } i} |\mathbf{R} - \mathbf{L}_i|^2}. \quad (2.154)$$

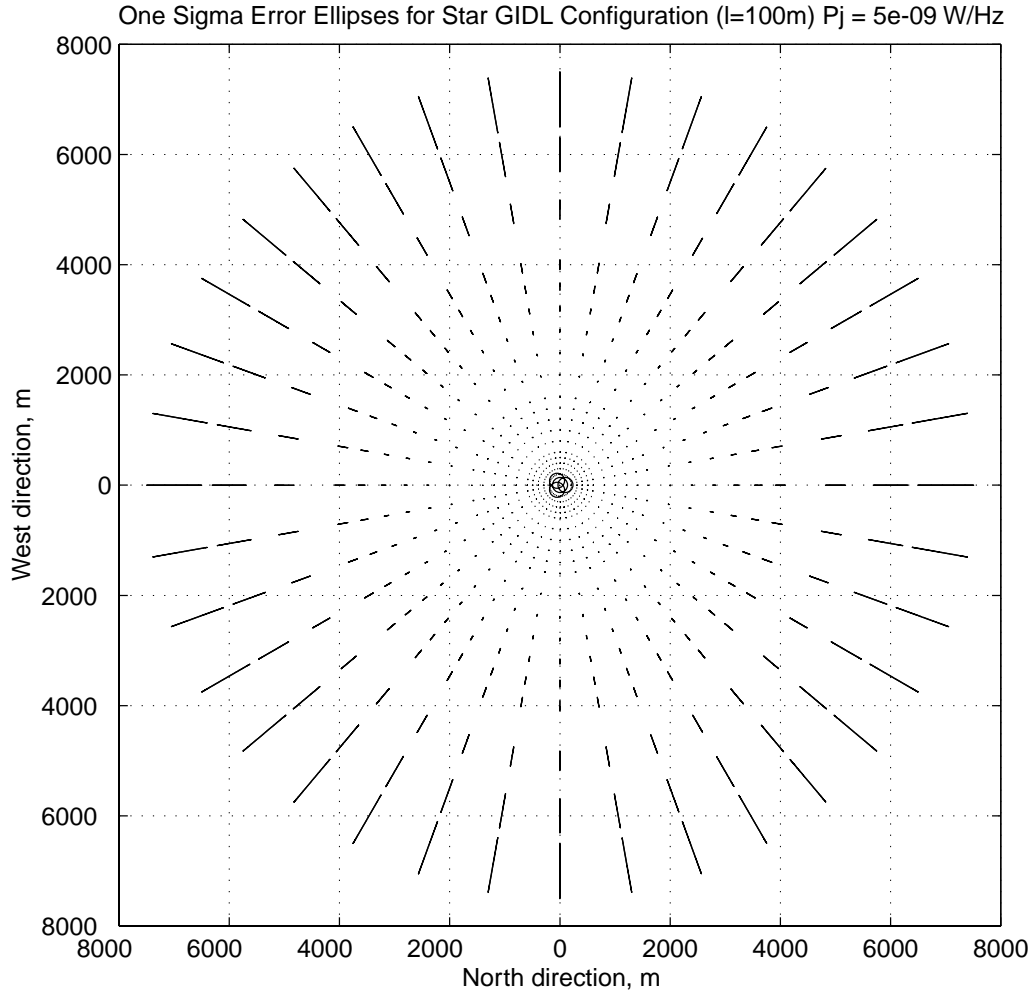


Figure 2.11: Error Ellipses for Constant Power Jammer: -33dBW/MHz

These estimates are then used to calculate the ECM of the measurements:

$$B_{\Delta R_i} = \frac{c^2}{\Delta f T} \frac{3}{2\pi^2 \Delta f^2} \frac{1 + q_1^2 + \dots + q_4^2}{q_1^2 + \dots + q_4^2} \times \left(\left(\begin{pmatrix} \frac{1}{q_2^2} & 0 & 0 \\ 0 & \frac{1}{q_3^2} & 0 \\ 0 & 0 & \frac{1}{q_4^2} \end{pmatrix} + \frac{1}{q_1^2} \begin{pmatrix} 1 & 1 & 1 \\ 1 & 1 & 1 \\ 1 & 1 & 1 \end{pmatrix} \right) \right) \quad (2.155)$$

Now when $B_{\Delta R_i}$ is known, ECM of the jammer location estimate may be calculated using Equation (2.152).

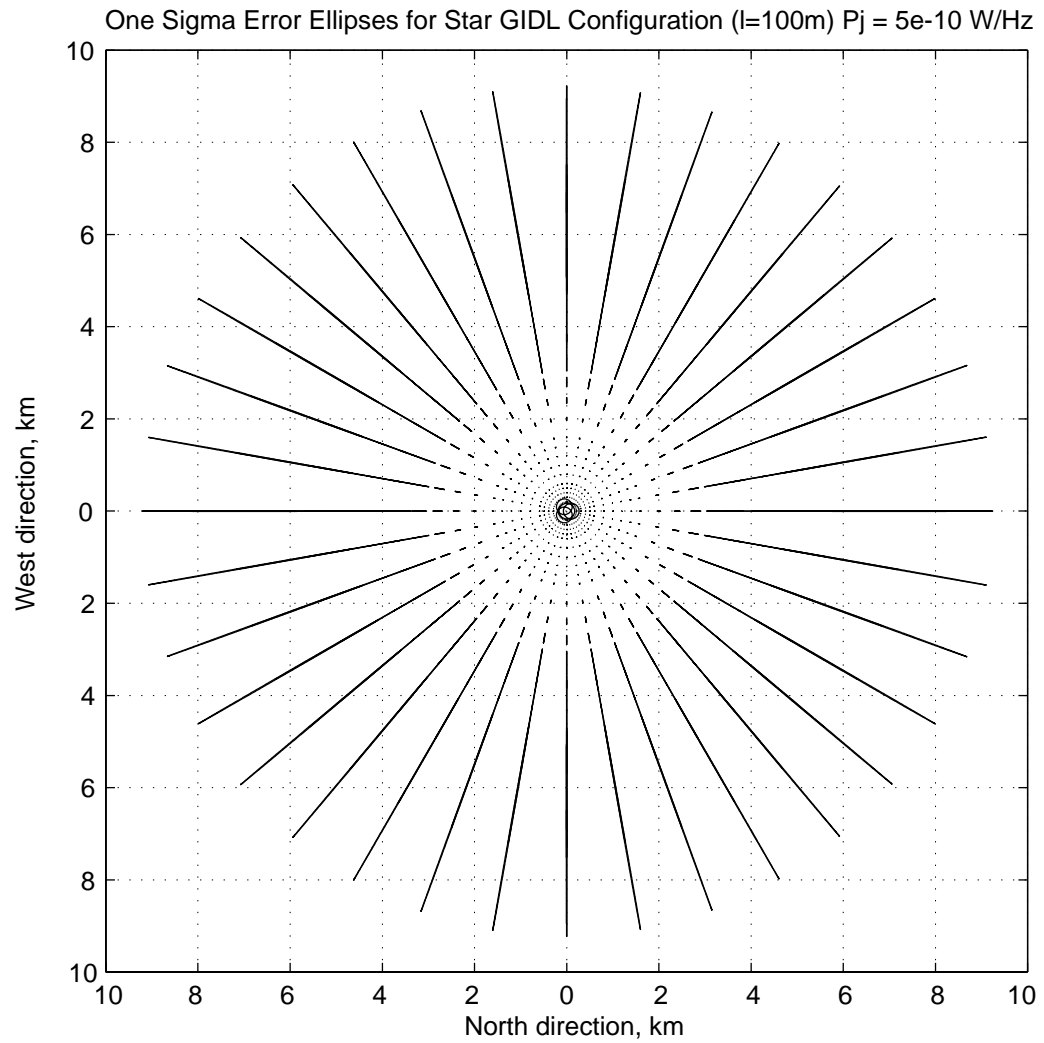


Figure 2.12: Error Ellipses for Constant Power Jammer: -43dBW/MHz

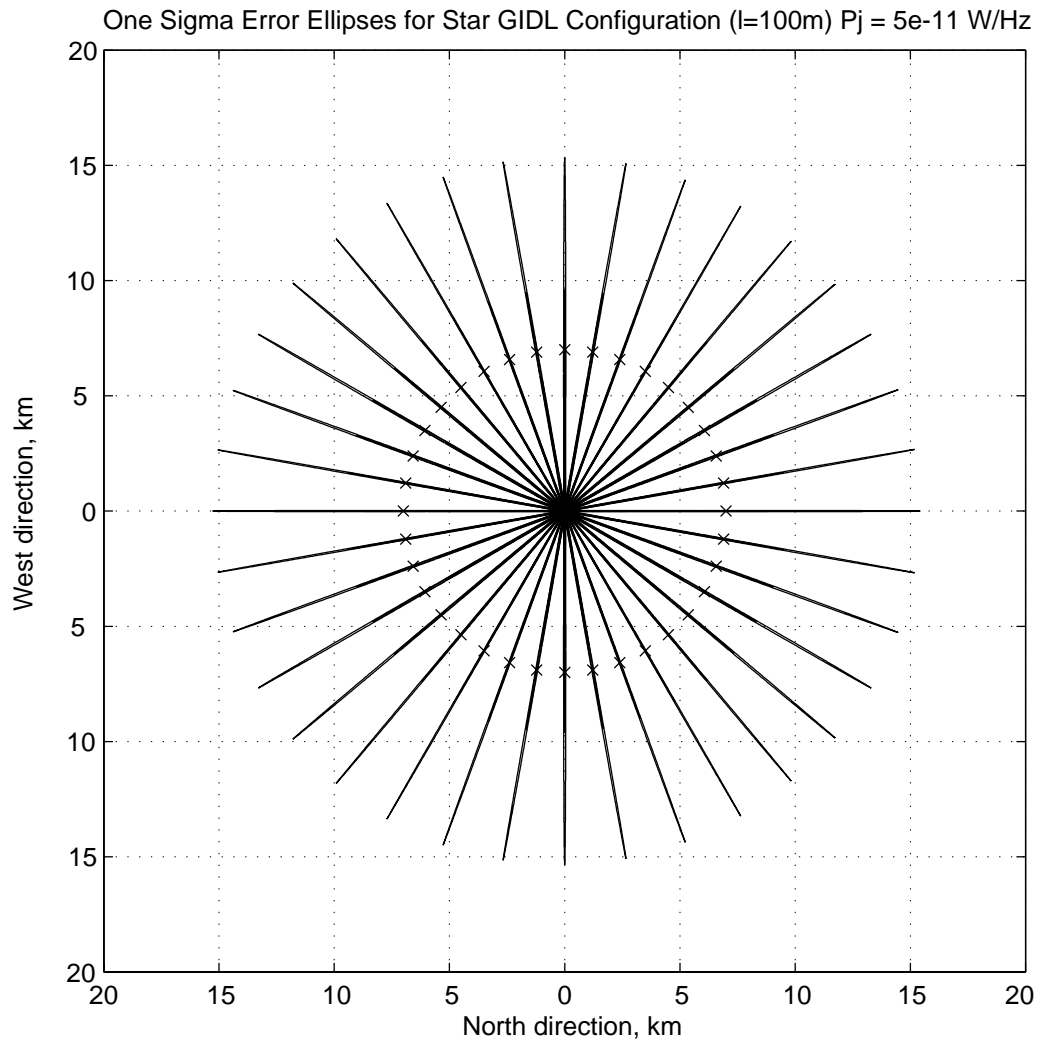


Figure 2.13: Error Ellipses for Constant Power Jammer: -53dBW/MHz

Knowing the ECM of the jammer position estimations, the expected system accuracy can be plotted in terms of error ellipses. Here, results of the analysis are presented for three types of jammer (relatively strong, weak and very weak). Results are shown in Figures 2.11, 2.12, and 2.13. A star antenna configuration is assumed with baselines of 100m. Jammers of specific power have been placed in various locations around the antenna array, and a horizontal projection of the error ellipses has been plotted. Each line on the plot is actually an error ellipse, narrow in azimuthal direction and wide in range. Thus for the relatively strong jammer one can see individual ellipses, and the resolution in range is good. For the weak jammer, good azimuthal resolution is still obtained, but the ellipses elongate in range direction (start to overlap), and for the very weak jammer, “x” marks the range at which the specified power of the jammer is undetectable (Figure 2.13). Plot of the range and azimuth accuracy versus range for the experimental GIDL setup for specific azimuth direction is shown in Figure 2.18.

2.5.1 Reference Jammer

To determine a jammer’s effective range, numerous experiments have been performed with a -70 dBW/MHz and other jammers (see the introduction chapter). From the data, it follows that this jammer would start affecting GPS receivers in the approximate range of 10m (this varies depending on receiver, but this is a good number to use). From the link equation it would follow that it is possible to scale that jammer range to the jammer of any power using the following equation

$$P_{\text{Jam0}} \sim R_{\text{Jam0}}, \quad R_x = R_0 \sqrt{\frac{GP_x}{P_0}} \quad (2.156)$$

In the Figure 2.14 effective jammer range is shown along with minimal range of the GIDL coverage. From this plot it is easy to see that GIDL range exceeds jammer range, so GIDL would be able to detect any jammer which would affect GPS in the protected region.

2.6 Expected GIDL Performance

It is possible to calculate expected GIDL performance for the antenna configuration used in the GIDL experiments and demonstrations. For a number of experiments, as described

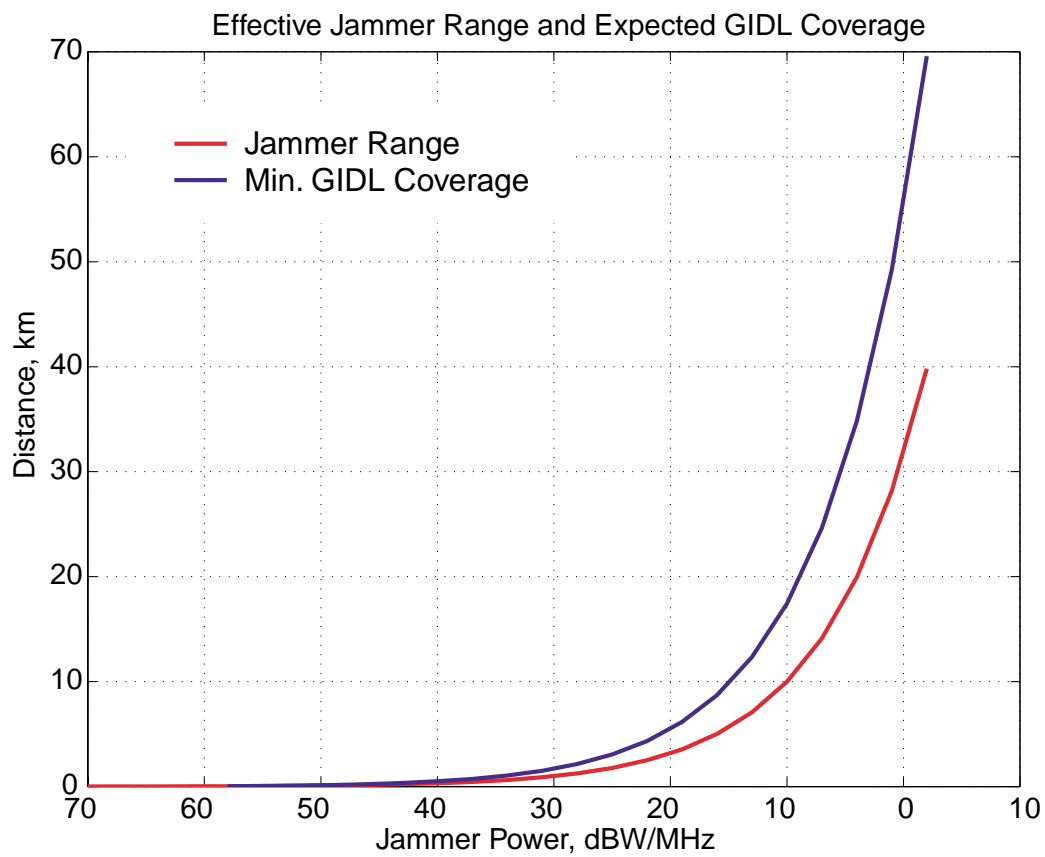


Figure 2.14: Effective Jammer Range and Expected GIDL Coverage

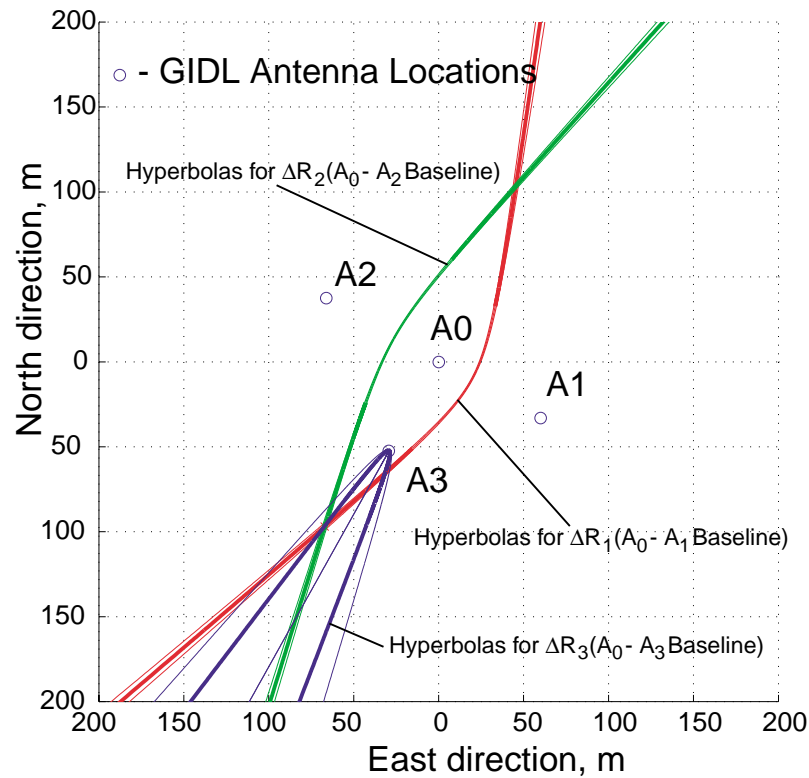


Figure 2.15: TDOA Jammer Localization. SOP (Hyperbolas) and Error boundaries ($\pm 0.7\text{m}$).

in Chapter 6, a semi-permanent GIDL configuration was used.

For this GIDL configuration, plots of jammer localization using the TDOA method were generated. Hyperbolas corresponding to TDOAs with expected errors of $\pm 0.7\text{m}$ are shown in Figures 2.15 and 2.16, with the left side of the figure showing the system as a whole and the right zooming in on jammer location and showing expected localization error boundaries (1σ).

In Figure 2.17 and Figure 2.18 it is assumed that a jammer with power -40 dBW/MHz is used during the experiments (as it was) and expected error ellipses for this jammer localization are plotted. Expected localization errors for direction are also plotted with azimuth of 193 degrees . This is an example of how the size of expected GIDL errors depends on the range from the GIDL system.

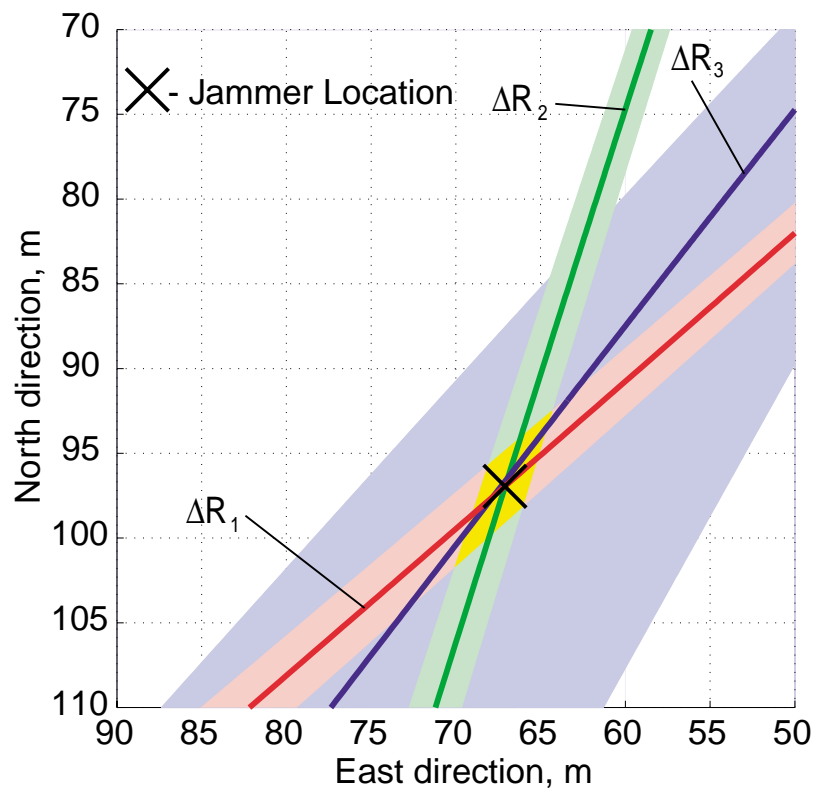


Figure 2.16: TDOA Jammer Localization. SOP (Hyperbolas) and Error boundaries ($\pm 0.7m$), Zoomed.

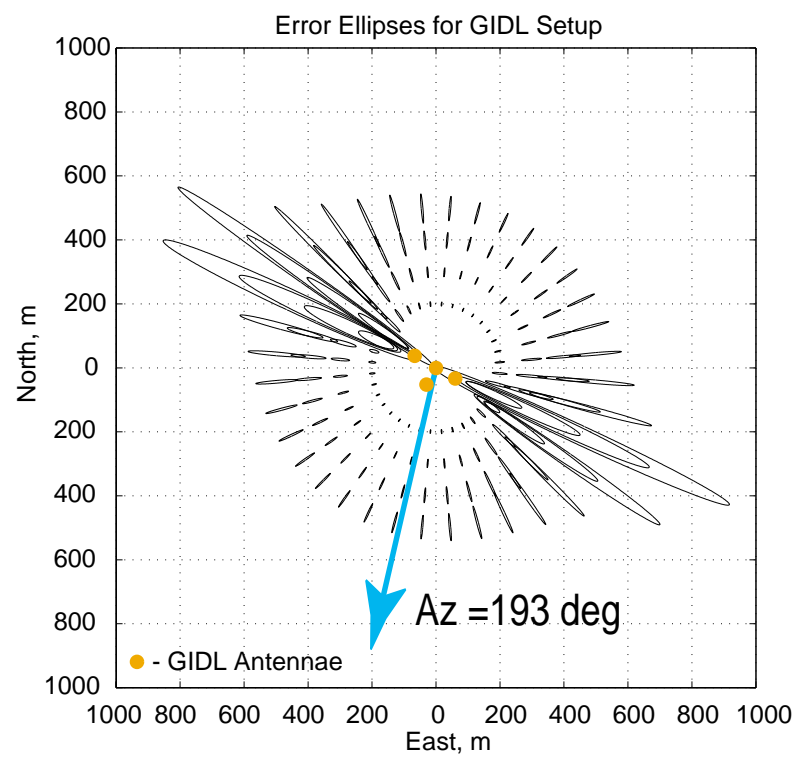


Figure 2.17: Expected GIDL Performance: Error Ellipses for the GIDL Setup

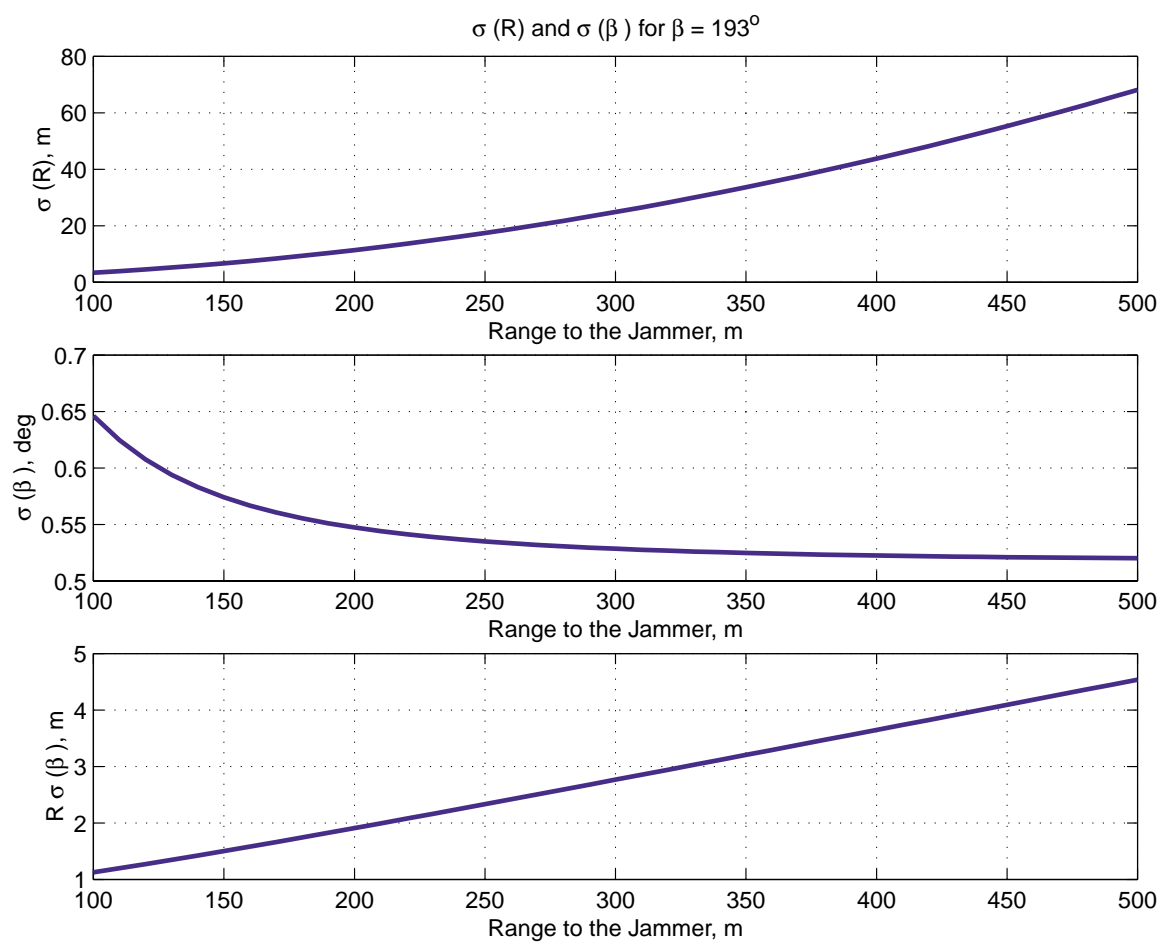


Figure 2.18: Expected GIDL Performance: Expected Variations of the Errors

Chapter 3

GIDL Hardware Design

The preceding chapter described the theory behind GIDL operation. To test the GIDL theory, and verify theoretical predictions in practice, experimental hardware was required. This chapter describes the GIDL prototype hardware that was built and used for testing the GIDL detection and localization algorithms.

This hardware was intended to be a very flexible research platform, which would allow testing of the largest subset of the GIDL algorithms. To achieve this goal, the software radio concept has been used in the GIDL receiver design. Some GIDL algorithms assume coherence between signals received by different antennae, so, the GIDL receiver had to be built as a multichannel coherent receiver. It has been shown that the minimum number of antennae to find jammer location in 3D space is four. So as a test platform for the GIDL system, a coherent four channel software radio receiver has been built. This chapter discusses constraints and tradeoffs in building such a receiver.

This chapter starts by describing the software radio approach to the receiver, then goes into a discussion of the practical issues in software radio implementation. After that, the frequency plan of the receiver is considered, and the chapter concludes with description of the overall structure of the as-built GIDL receiver.

3.1 Software Radio Concept

3.1.1 Introduction

As already mentioned in Chapter 1 the software radio offers a number of advantages over the traditional receiver implementation. It provides the ultimate simulation/testing environment. To evaluate a specific algorithms, all modifications to the receiver can be done in software.

There is a tremendous level of flexibility associated with a software radio design and this should be reflected in the implementation. Reducing the number of front end components typically involves increasing the sampling frequency. It is important to minimize not only the front end hardware, but also the required sampling frequency, as this determines the required amount of programmable processing power. The front end implementation was thoroughly investigated to determine the most suitable design.

Finally, it is important to recognize that this work is not exclusive to jammer detection. The software radio implementation is applicable to any RF transmission. Thus this research, particularly in the front end design, can be applied to the capture and processing of any signal. GIDL provides a platform in which the accuracy and integrity of the signal processing is both complex and critical, thus a software radio implementation will offer significant advantages over a traditional design.

There are two fundamental design objectives in the development of a software radio: 1) Position the ADC as near as possible to the antenna in the front end design. 2) Process the resulting samples using a programmable microprocessor. If it is possible to adhere to these objectives, there are a number of potential benefits that can be realized. Each of the objectives will be examined in detail, investigating the advantages of such an implementation as well as the obstacles involved.

3.1.2 Front End Configuration

The first objective is to place the ADC as near as possible to the antenna in the front end implementation. A traditional front end implementation is depicted in Figure 3.1. This configuration consists of multiple stages of frequency translation and amplification. The

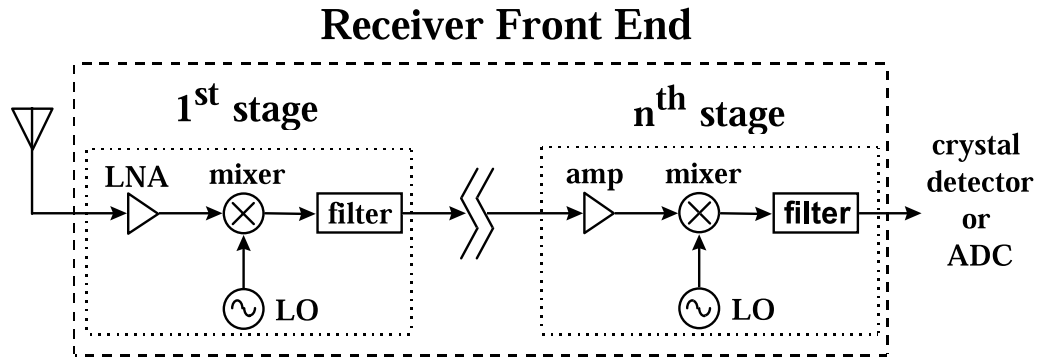


Figure 3.1: Typical Front End Implementation

benefit here is that the demand on each of the individual components is lessened. However, these multiple stages introduce additional analog components with some potential negative consequences. For example, oscillator performance is a function of both age and temperature. Mixers, and to a lesser extent amplifiers, exhibit nonlinear operating characteristics, resulting in intermodulation and spurious performance. Even filters can introduce unexpected problems. Suppose an LC filter is used as an intermediate element. If the inductor is not properly isolated, it can act as an antenna, injecting undesired noise into the system. All of these effects can be extremely difficult to model, and therefore simulate, making performance estimates troublesome.

It is impossible to place the ADC directly next to the antenna. Any RF transmission will require some degree of amplification and filtering. In a software radio, the goal is to minimize the number of analog components, and ideally sample the signal directly at the carrier frequency. An ideal software radio front end is depicted in Figure 3.2. This implementation samples the signal directly at RF, and greatly simplifies the front end design in terms of the number of components.

There are two ways to consider the required sampling rate of the ADC involved. One is based on the center frequency and the other is based on the information bandwidth. To obtain the entire band unambiguously, a sampling rate greater than twice the highest signal frequency is required. At the present time, there are only a handful of devices capable of operating at the required frequencies [144]. These are extremely expensive and even more challenging is the subsequent discrete processing which must occur at this same frequency.

Receiver Front End

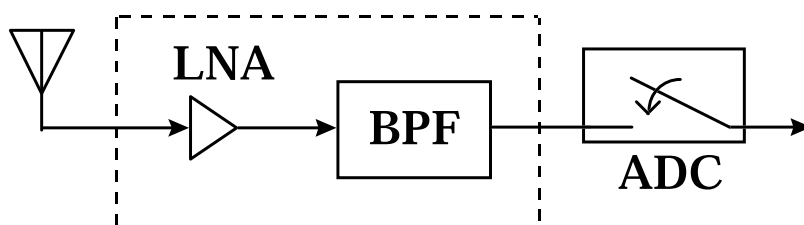


Figure 3.2: Software Radio Direct Digitization Front End Implementation

The practicality of this approach for signals broadcast in the UHF and higher bands is extremely limited by present technology. However, there is an alternative to the traditional sampling technique. The Nyquist sampling theorem requires that the absolute minimum sampling frequency be greater than twice the information bandwidth. This suggests that the ADC in Figure 3.2 could operate at a fraction of the rate necessary previously. It is important to recognize that this technique, known as bandpass sampling, requires the use of an appropriate amplifier, filter and ADC. It is possible then to sample an RF signal based solely on its information bandwidth [145, 146]. The various stages of local oscillators, mixers, and image reject filters are no longer necessary. Frequency translation is accomplished by intentionally aliasing the signal of interest.

Multi-stage receivers, as mentioned, can be complex, and could have a number of issues. Direct RF sampling receivers have their own limitations in selectivity, sensitivity, and are difficult to implement. Therefore, IF sampling is a reasonable compromise between the two and offers enough flexibility for the designer. An IF sampling receiver is a combination of both the multistage receiver and direct RF sampling receiver. In an IF sampling receiver, the RF signal is bandpass filtered, and using one mixing stage downconverted to some IF frequency, where it is again analog filtered to the desired bandwidth. Then the filtered signal is bandpass sampled by an ADC and transferred into the digital domain.

3.1.3 Software Signal Processing

In a true software radio the samples from the ADC depicted in Figure 3.2 are to be processed on a programmable microprocessor. This will provide the ultimate in receiver flexibility [97]. No time-consuming and costly hardware prototyping of different signal processing algorithms is necessary. If a different receiver architecture is desired, the appropriate programming is downloaded to the target processor and executed. If the ADC/microprocessor software radio platform is replacing analog-based signal processing, the procedure is much more deterministic, and therefore predictable, in nature. This is closely related to the simulation advantage of a software radio. The identical code being used for signal processing can be applied in the actual receiver. By reducing the number of front end components, their effects are minimized. Now more effort can be directed into developing higher accuracy models of the remaining components. Thus, with a software radio there should be little, if any, unexpected results in moving from simulation to receiver implementation. The flexibility of the software radio allows a single hardware configuration to serve as multiple radios. For example, a broadband antenna, amplifier, and filter could be used to capture a wide span of frequency spectrum, consisting of multiple transmissions. The microprocessor could selectively filter and decimate the desired frequency band, then recall the appropriate program to provide the desired processing. The implementation could process any number of analog and/or digital modulation formats.

The disadvantage to processing the resulting samples exclusively in software is the availability and cost of the required programmable computational power. However, available programmable processing power is exponentially increasing. According to Moore's Law microprocessor performance doubles every 18 months [147]. This statement has held true since the inception of the microprocessor. Therefore, the necessary computation power is likely to be available for any software radio implementation given the passage of sufficient time. The software radio, with its high level of flexibility, could be used to evaluate each of the various GIDL algorithms and designs.

3.1.4 GIDL Front End Design

The front end design and implementation constitutes half of the software radio development. This section will cover front end design for one channel of the GIDL receiver within the software radio guidelines. First, the basic front end design equations applicable to this type of implementation are reviewed. Next, the feasibility of sampling the signal directly at RF is investigated. Finally, the theory behind bandpass sampling, the preferred method of directly sampling at RF, is presented. In general, sensitivity and dynamic range are the most important factors in the hardware implementation of a front end design. There are well-known equations to calculate both the sensitivity and the dynamic range of a receiver, if the RF front end design is selected [96]. These equations, with slight modification, can be used to calculate the performance of an all digital receiver as well [148]. A generic RF front end consists of amplifiers, filters, and mixers, as depicted in Figure 3.1. Each component has three fundamental parameters: gain, noise figure and third order intercept point [149]. Three equations are used to determine the overall gain, noise figure and the resulting third order intermodulation point. The noise figure and third order intermodulation point in turn determine the sensitivity and dynamic range. First, system gain is given by:

$$G_t = G_1 G_2 \dots G_n \quad (3.1)$$

where G_t is the overall gain of the front end and G_i is the gain of the i^{th} component. The overall noise figure, F_t , can be written as:

$$F_t = F_1 + \frac{F_2 - 1}{G_1} + \frac{F_3 - 1}{G_1 G_2} + \dots + \frac{F_n - 1}{G_1 G_2 \dots G_n} \quad (3.2)$$

where F_i is the noise figure of the i^{th} component. The overall third order intermodulation point (a measure of the third-order intermodulation distortion, i.e. system nonlinearity, is given by intercept points, which are points on the graph of output power versus input power for the component or the system under consideration [149]), Q_{3t} , is:

$$Q_{3t} = \frac{G_t}{\frac{G_1}{Q_{31}} + \frac{G_1 G_2}{Q_{32}} + \dots + \frac{G_1 G_2 \dots G_n}{Q_{3n}}} \quad (3.3)$$

where Q_{3i} is the third order intermodulation product of each individual component.

The criteria used to determine the gain, noise figure and third order intermodulation product are: 1) The gain must be matched to a desired value (for example output signal amplitude should match input range of ADC), 2) The noise figure should be as low as possible, and 3) The third order intermodulation should be as high as possible. However, the noise figure and the third order intermodulation product are opposing parameters: the lower the noise figure, the lower the third order intermodulation product. In general, a compromise must be achieved between the noise figure and the third order intermodulation and this arrangement determines the desired gain value.

As an example, consider the implementation of a front end to receive the GPS signal. This example assumes that all necessary amplification and noise reduction filtering occurs directly at the RF carrier frequency, as would occur in the direct digitization front end depicted in Figure 3.2. In order to digitize the signal using an ADC, the power level should be at least -45 dBm. A total of 90 dB gain is chosen to amplify the signal to the desired power level. Since a single 90 dB gain amplifier is impractical due to non-linearities, the necessary gain can be obtained by cascading three identical commercially available amplifiers, each with the following specifications. Frequency range of 1-2 GHz, gain of 30 dB, noise figure: 2 dB, third order intermodulation point of 23 dBm. A bandpass filter centered at 1575.42 MHz with a 3 dB bandwidth of 24 MHz and an insertion loss of 1.0 dB is available to limit the out of band noise.

The above four components can be cascaded in different ways to obtain different designs. The general rule can be stated as follows. The closer the filter is placed to the antenna, the higher the noise figure and dynamic range. If the filter is placed far away from the antenna, the opposite is true. All the received GPS signals are close in amplitude, thus the dynamic range requirement on the receiver is low for GPS signals, and interference may require the increase of a receiver's dynamic range. All GPS signals have the same carrier frequency, with any deviation resulting strictly from the Doppler effect and the satellite frequency reference offset. Since each amplifier has 30 dB gain and a 2 dB noise figure, the filter can be placed at any position after the first amplifier, with a negligible effect on the overall noise figure.

However, in a practical implementation it is prudent to place the filter after the first amplifier in order to limit other signals from generating spurious responses. This arrangement

will limit out-of-band signals from getting into the second and third amplifiers. It is also possible to place the filter before the first amplifier to limit undesired signals. This arrangement will degrade the sensitivity by 1.0 dB, the insertion loss of the filter, and significantly increase the noise figure of the system.

In the practical implementation of a direct digitization front end, there is another factor that must be considered. If the final component prior to the ADC is an amplifier rather than a filter, additional noise will be folded, or aliased, into the resulting information band (assuming bandpass sampling is used). The amount of noise folded into this band will be proportional to the amount of amplification, in terms of both gain and bandwidth, between the last filter and the ADC. Thus to reduce this noise it is desirable to place another filter right before the ADC.

Direct RF Digitization

If the proposed front end design (depicted in Figure 3.2) is to be utilized, then the ADC will be required to sample the desired signal directly at RF. There are two vastly different ways to view the required sampling frequency for the ADC in a direct digitization approach. In this section the theory will first be presented and the GPS signal will be used as an example. Recall that GPS operates on an RF carrier of 1575.42 MHz and a first null bandwidth of approximately 2 MHz. These parameters provide the necessary information to determine the sampling frequency requirement. It is important to note an advantage in that any sampling directly at RF eliminates various front end components and their associated error contributions.

First, one can consider the minimum sampling frequency based on the RF carrier frequency, f_c , and information bandwidth, BW_I . The minimum allowable sampling frequency, f_s , in this case is given in Equation (3.4), which is the sampling theorem for low-pass signals).

$$f_s > 2 \left(f_c + \frac{BW_I}{2} \right) \quad (3.4)$$

The advantage to using this basis for the choice of sampling frequency is that the information in the range $[0, f_s/2]$ is uniquely identified. Therefore, this sampling frequency

provides the potential to recover any RF transmission in that frequency range. The disadvantages at the present time to this approach are numerous. In the case of GPS, this method would require a state-of-the-art ADC operating at a sampling frequency greater than 3 GHz. A related, and more difficult, problem is the processing of the resulting samples. There is no single processor solution available to this problem and any parallel processing implementation would be extremely expensive if it were even possible. Therefore, this type of implementation is impractical at the present time.

Second, the minimum sampling frequency of the information band is expressed in Equation (3.5).

$$f_s > 2BW_I \quad (3.5)$$

If the signal is bandlimited to its information bandwidth, then f_s represents the Nyquist rate. In the case of GPS, the information bandwidth can be approximated by the first null bandwidth, thus a sampling frequency requirement of about 4 MHz is imposed. If more of the GPS signal needs to be sampled, a higher sampling frequency can be used. This is a neat idea: sample a 1575.42 MHz RF carrier at about a 4 MHz rate and extract all the desired information. The technique itself is referred to as bandpass sampling or intentional aliasing. As with the previous approach, there are trade-offs in its implementation that are discussed in detail in the next subsection. However, the primary advantage to this technique is obvious — sampling occurs at a much lower rate and thus processing the resulting samples is a feasible operation.

Bandpass Sampling

Bandpass sampling is the technique of undersampling a modulated signal to achieve frequency translation via intentional aliasing [145, 146]. A high level frequency domain depiction of this process is presented in four stages in Figure 3.3 and is based on the direct digitization front end of Figure 3.2.

The signal enters through the antenna and is amplified by the low-noise amplifier (LNA) along with all frequencies within the bandwidth of the LNA (Stage 1). In a bandpass sampled system, the amplified signal would then pass through a narrow bandpass filter centered

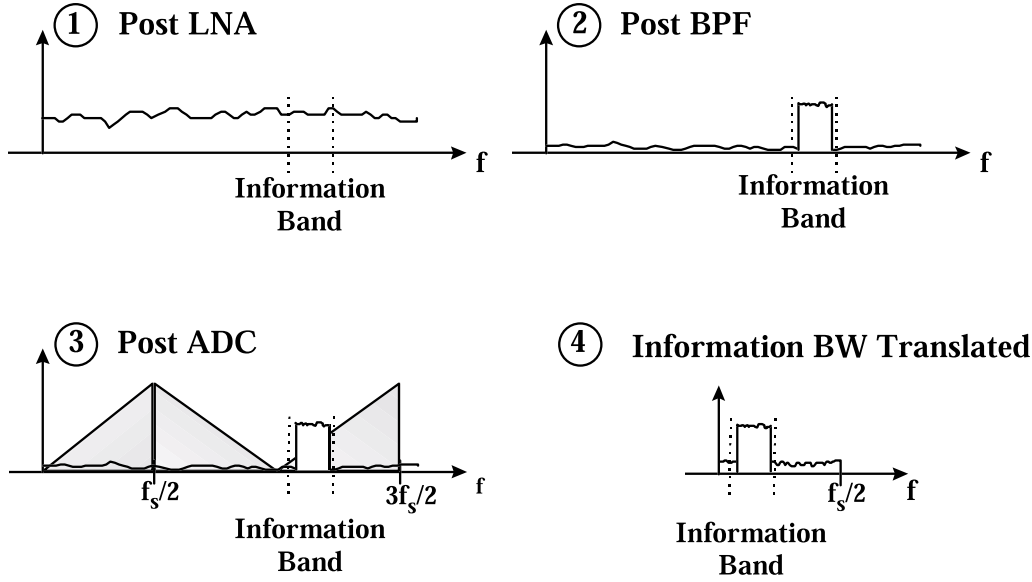


Figure 3.3: Frequency Domain Depiction of the Various Output Stages of a Band-pass Sampling Front End

about the carrier frequency. This filter would attenuate all frequencies outside of the information band (Stage 2). Next a sampling frequency, f_s , is chosen which defines the resulting sampled bandwidth, $[0, f_s/2]$, as well as the arrangement of the aliasing triangles depicted in Stage 3. After sampling, the information band along with the noise from each aliasing triangle is folded into the resulting sampled bandwidth (Stage 4). Thus the information band is translated without any analog downconversion stages.

First, the translation of the original carrier frequency, f_c , to the resulting intermediate frequency, f_{IF} , as a function of the sampling frequency, f_s , must be defined mathematically to obtain a more detailed understanding. This is presented in Equation (3.6) [95].

$$\text{if } \text{fix} \left(\frac{f_c}{\frac{f_s}{2}} \right) \text{ is } \begin{cases} \text{even, } f_{IF} = \text{rem}(f_c, f_s) \\ \text{odd, } f_{IF} = f_s - \text{rem}(f_c, f_s) \end{cases} \quad (3.6)$$

where $\text{fix}(a)$ is the truncated integer portion of argument, a , and $\text{rem}(a, b)$ is the remainder after division of a by b . It is important to recognize that Equation (3.6) provides a means of calculating the resulting intermediate frequency (IF) position. Associated with this IF are the corresponding modulation sidelobes that designate the information bandwidth. It is

important that f_s be chosen such that the entire information bandwidth is translated within the resulting sampled bandwidth. This can be ensured if the constraint in Equation (3.7) is met.

$$\frac{BW_I}{2} < f_{IF} < \frac{f_s - BW_I}{2} \quad (3.7)$$

If this constraint is not met, a portion of the information band of the signal can fold on top of itself, creating destructive interference.

Assuming an appropriate sampling frequency has been selected, the trade-offs in using bandpass sampling, as opposed to traditional sampling, can be discussed. Again, the primary advantage is that sampling frequency and consequent processing rate are proportional to the information bandwidth rather than the carrier frequency. However, bandpass sampling has some fairly unique hardware requirements that may be considered its disadvantage. One critical requirement is that the analog input bandwidth of the ADC must accommodate the RF carrier, although its sampling frequency can be much less as it is based on the information bandwidth. A narrow bandpass filter centered about the RF carrier is a second requirement. Ideally, this filter must attenuate all energy outside the information bandwidth. This is important as all frequencies, not only the information band, from 0 Hz to the input analog bandwidth of the ADC will fold into the resulting passband, thus affecting the SNR of the information band.

3.2 GIDL Hardware Philosophy

GIDL hardware philosophy is quite simple. Be as flexible as possible to allow testing of the largest subset of algorithms as discussed in Chapter 2.

The original idea for the experimental GIDL hardware was to build the ideal software radio, with direct RF sampling. Thus, it would consist of a filter, amplifier and ADC, as described in the previous section. But this realization was, in practice, expensive and unnecessarily difficult to implement. So an intermediate band pass sampling solution was chosen. The GIDL receiver was built as a single downconversion receiver with consequent bandpass sampling, leaving the remainder of the processing in the software (same as in the real software receiver).

The system was designed to be built out of relatively easily available components. This task has been successfully accomplished. The only custom parts in the system are the RF and IF filters, because they had to correspond to the chosen frequency plan, and have tight specifications.

3.3 GIDL Realization

This section describes actual GIDL hardware which has been built according to the ideas from the previous sections in this chapter.

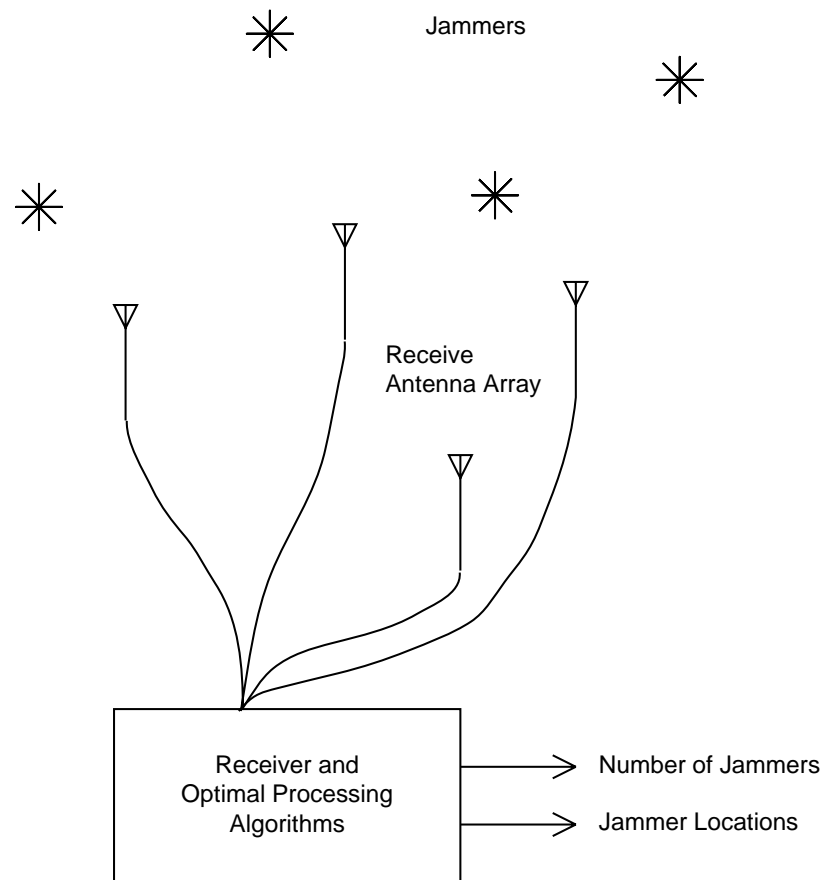
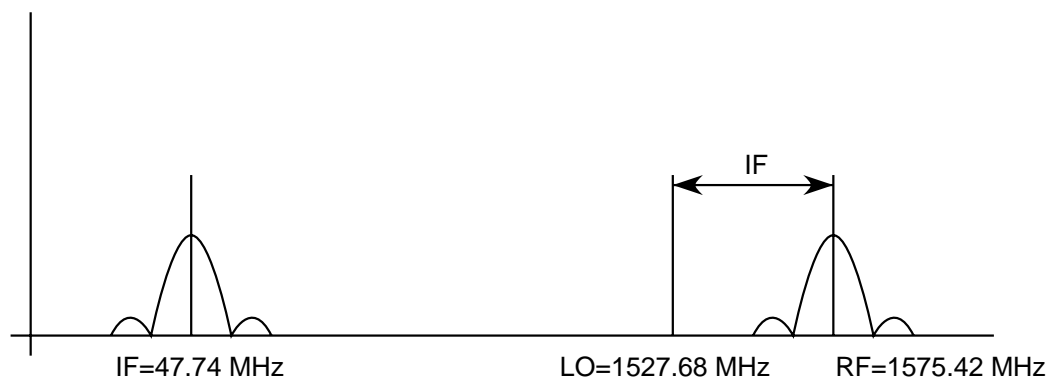
3.3.1 GIDL Hardware Concept

Conceptual design for the prototype GIDL receiver is shown in Figure 3.4. It consists of four RF inputs, which connect to the four antennae, some RF hardware and a processor to execute receiver processing algorithms. Outputs of the receiver are a jammer detection flag or number of jammers and their estimated location. The actual GIDL receiver follows this conceptual design. It is possible to build a receiver with four RF sections (i.e., with the ability to connect to four antennae). This type of receiver would operate from one common clock, making it a completely coherent system. There are some limitations to this prototype. Namely, it would have only four antennae, and the antenna locations would be limited by cable length from the receiver to the antenna.

3.3.2 GIDL Frequency Plan

As previously mentioned, the GIDL receiver is implemented with a single analog down-conversion/mixing stage. A second down-conversion is done by aliasing during ADC conversion. The remainder of the signal processing is completely digital. The system RF bandwidth is 24 MHz, and the IF bandwidth is 6 MHz, with a possible expansion to 17 MHz to protect wideband LAAS reference receivers (see Figures 3.5 and 3.6).

Figure 3.5 describes the single analog mixing done in the GIDL receiver when a filtered signal around the GPS center frequency of 1575.42 MHz is mixed with a local oscillator (LO) frequency at 1527.68 MHz. The mixing translates the GPS frequency and all signals

**Figure 3.4:** GIDL Realization Concept**Figure 3.5:** GIDL Frequency Plan: Analog Mixing

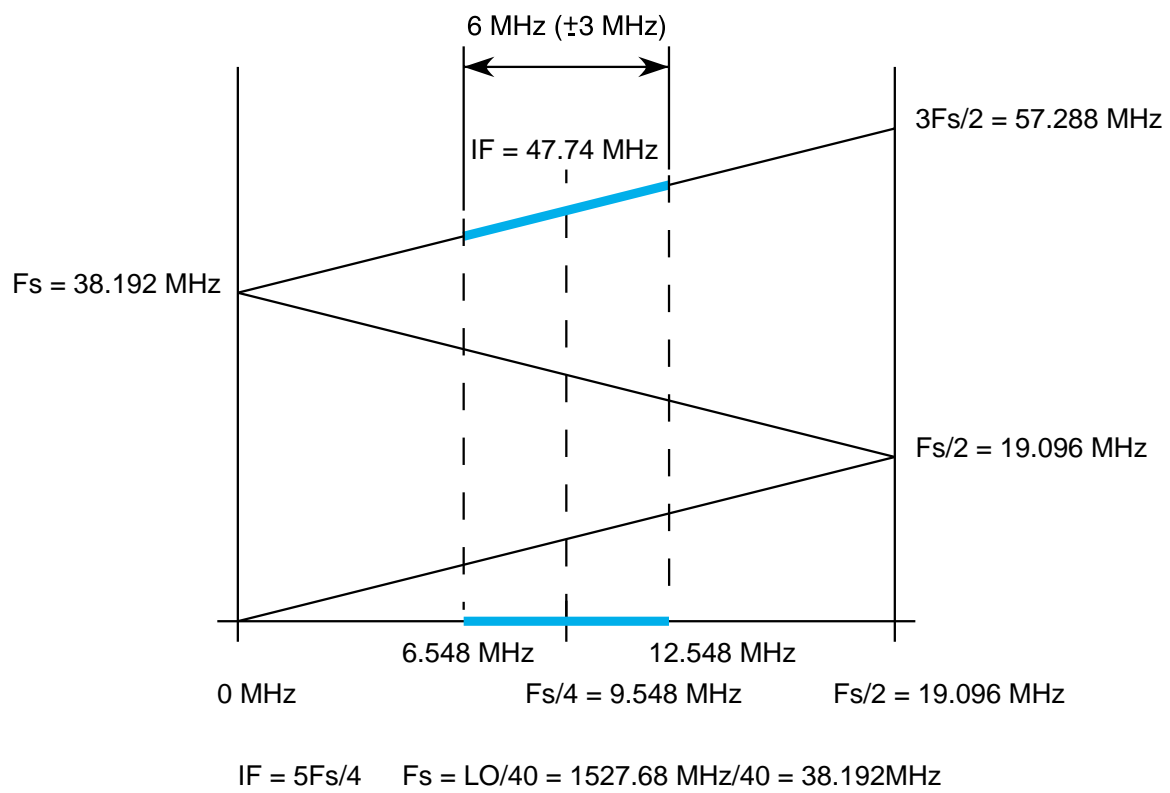


Figure 3.6: GIDL Frequency Plan: Sampling With Aliasing

around it to the IF frequency of 47.74 MHz. Figure 3.6 describes a bandpass sampling process in a GIDL receiver is another way to interpret bandpass sampling. The frequency axis is shown as a ladder which bends at the integer number of $f_s/2$ frequencies. Then the signal at any frequency after bandpass sampling would alias directly down on the ladder to the range $[0, f_s/2]$. In particular, the case of the GIDL receiver sampling frequency is chosen to be 38.192 MHz, which aliases the IF frequency of 47.74 MHz down to 9.548 MHz.

During the design stage of this receiver, the goal was to go to the digital domain as soon as possible. As mentioned, the GIDL receiver has only a single analog downconversion/mixing stage (Figure 3.5). Signal bandwidth is kept at 24 MHz until it goes to the IF filter. There is a second downconversion, but it is done simultaneously with sampling of the signal by aliasing during ADC conversion (Figure 3.6). Bandwidth of the IF filter was chosen to be 6 MHz, as a compromise between the resulting required digital signal processing and the bandwidth of the GPS signal, while still providing enough bandwidth to cover the main parts of the GPS band. Given sufficient digital signal processing capabilities, the IF bandwidth can be expanded to 8 MHz or more (up to 19 MHz) to satisfy the LAAS MASPS [150].

3.3.3 GIDL Construction

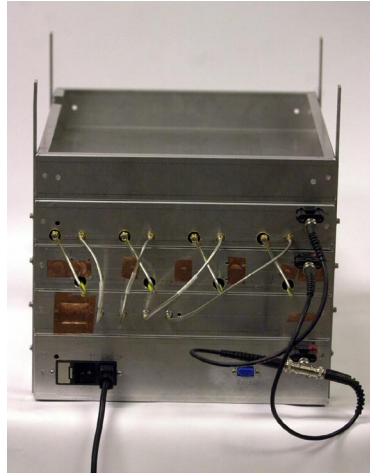
A 4-channel common-clock generic digital receiver was developed, which, operated in the GPS frequency band for the prototype GIDL system. A simplified block diagram of this receiver is shown in Figure 3.10 and pictures of this receiver and its individual modules are in Figures 3.7–3.9. The receiver consists of four identical RF and ADC sections, a clock section and a data collector and processing unit, or processing PC.

After digitization of the signal, the remainder of the processing is done completely digitally. (Note that the frequency plan design has the nominal carrier frequency aliased to $f_s/4$, which would make I and Q mixing extremely simple in the digital domain; sine and cosine waves would look like series of +1, -1 and 0s. This is a nice feature, reserved for future use, as processing can be done by specialized hardware, or a specialized DSP chip which is computationally efficient.)

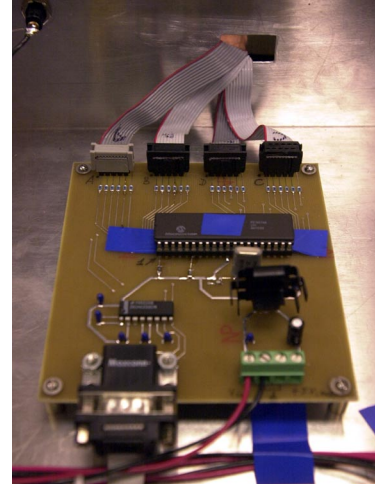
This receiver is a full common clock architecture, thus the key elements of the system



(a) Front Panel of the GIDL Experimental Receiver

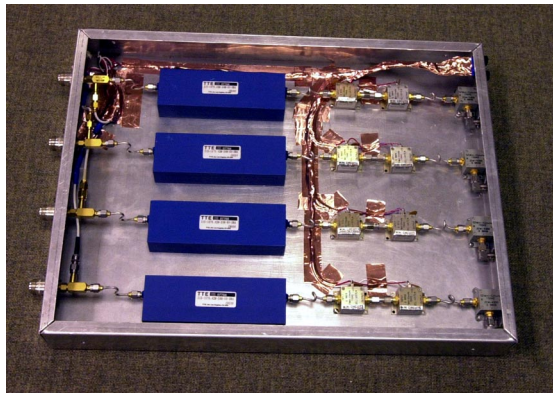


(b) Back Panel of the GIDL Experimental Receiver

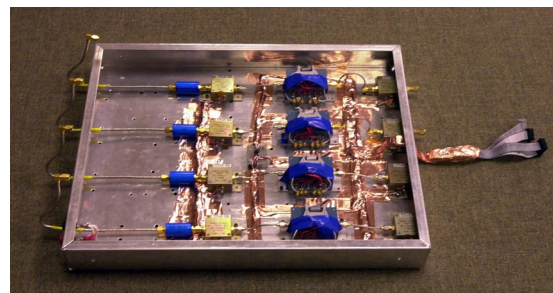


(c) Detail: Gain Control Microcontroller of GIDL Receiver with Attenuator Cables Attached

Figure 3.7: Front, Back, and Gain Controller of GIDL Receiver

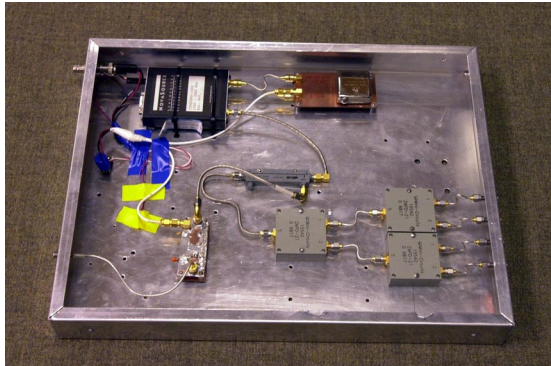


(a) RF Filters, RF Amplifiers and Mixers Section of GIDL Receiver

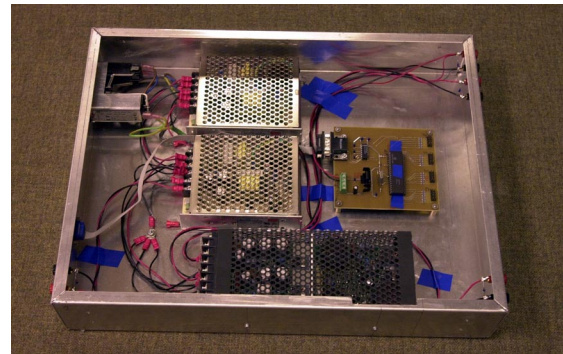


(b) IF Filters, IF Amplifiers and Gain Control Attenuators of GIDL Receiver

Figure 3.8: RF and IF Sections of the GIDL Receiver



(a) Master Clock, Synthesizer and Divide by 40
Circuit of GIDL Receiver



(b) Power Supply and Gain Control Microcon-
troller Assembly of GIDL Receiver

Figure 3.9: Clock and Power Sections of the GIDL Receiver

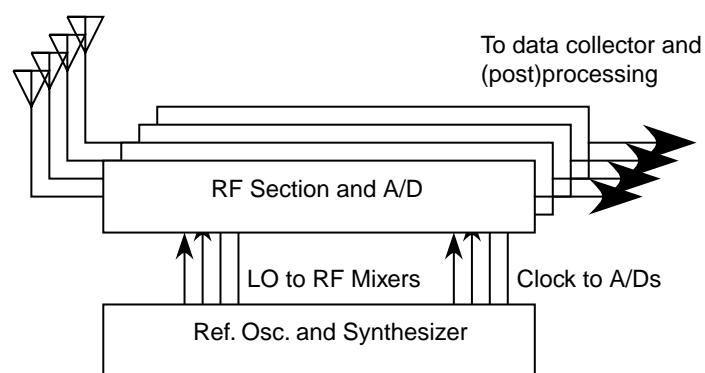


Figure 3.10: Diagram of GIDL Hardware Setup

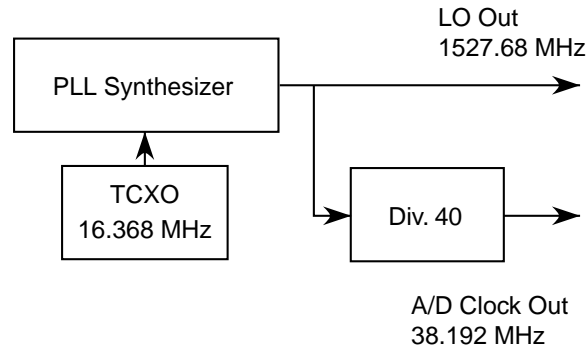


Figure 3.11: Reference Oscillator and System Clock Diagram

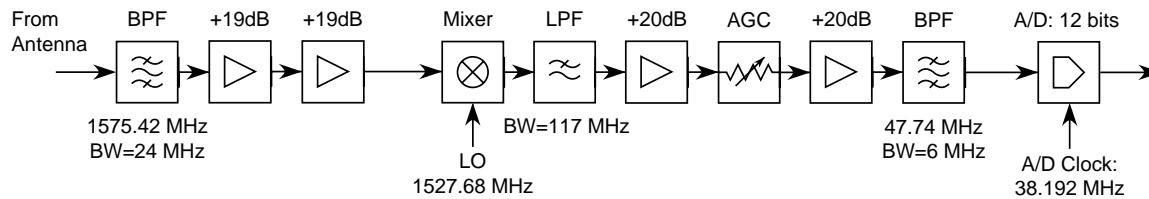


Figure 3.12: Diagram of RF Section and ADC

are the reference oscillator and synthesizer. The block diagram for this device is shown in Figure 3.11 and a picture of the real hardware is in Figure 3.9(a). The master clock for the system is a temperature-compensated crystal oscillator (TCXO) which runs at 16.368 MHz. The phase lock loop synthesizer is locked on this clock and generates a master frequency for the GIDL receiver, which is 1527.68 MHz. This frequency is used in analog mixing of the signal, to downconvert it to the IF. This frequency is divided by a factor of 40 by a static digital counter and then is used to drive the ADCs and to strobe a digital signal into the data collector. This frequency plan references all the frequencies to the single master (synthesizer) frequency, i.e., each receiver has only one error or uncertainty source in its frequency plan.

The combined block diagram for the RF section and ADC converter is shown in Figure 3.12. There are four of these channels in the GIDL receiver. The overall gain scheme assumes 25 dB gain in the active antenna. When the electronically controlled AGC attenuator is set to 0 (maximum gain), the ADC range is equal to twice the variance of ambient white noise assuming it is zero-mean. It is possible to sample ambient noise with the resolution of 12 bits.

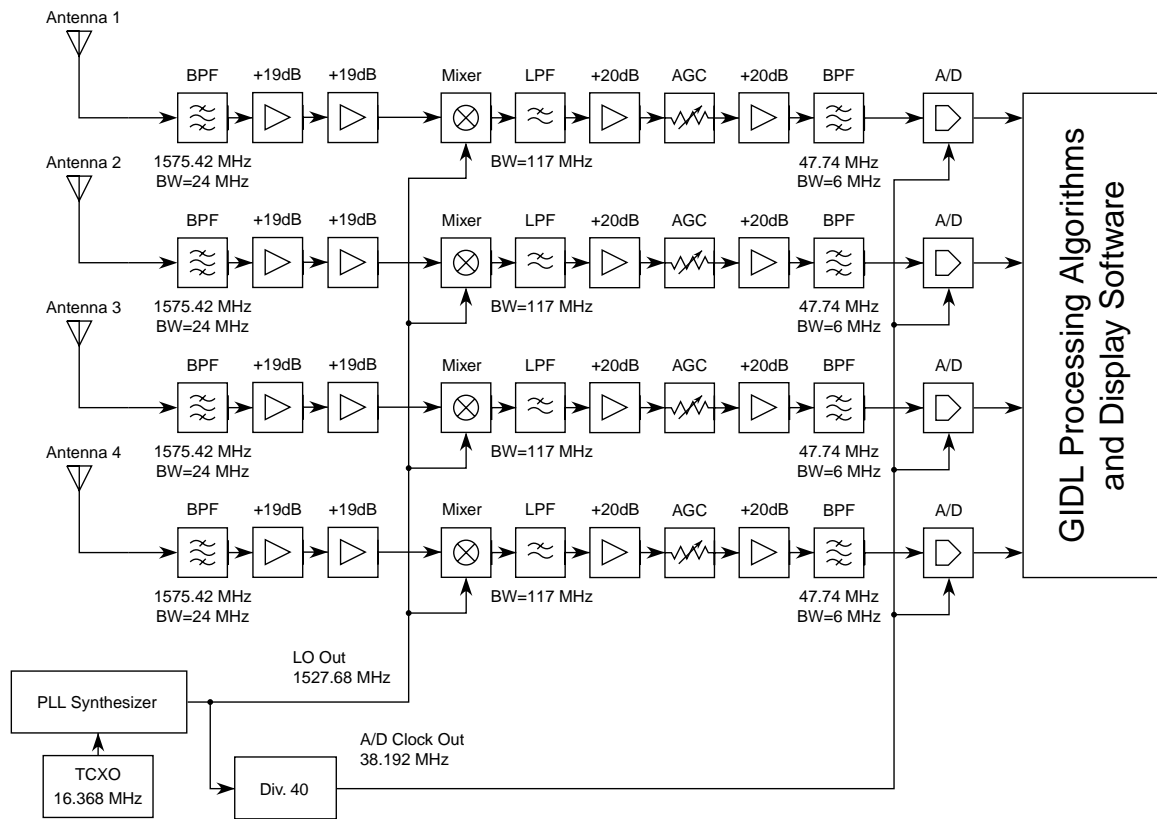


Figure 3.13: Complete Block Diagram of the Built GIDL Receiver

A complete GIDL receiver block diagram is shown in Figure 3.13. All the components from the antennae outputs up to the ADCs are assembled as the “GIDL receiver,” while the ADCs are installed inside the processing PC. IF signals from each of the channels have to be digitized, so four ADC converters operating in parallel are needed.

The original GIDL design included four external ADC boards running in parallel with the digital signal fed into a Xilinx-based data collection and processing board placed on a PCI bus of the host computer. The design allowed for preliminary digital processing in the hardware by programming the Xilinx chip, and trying to achieve real-time performance. Due to complexities of this arrangement and to limit the scope of this thesis, this arrangement has been changed to a simpler one, which allows for faster development and testing of algorithms, and a less complex configuration.

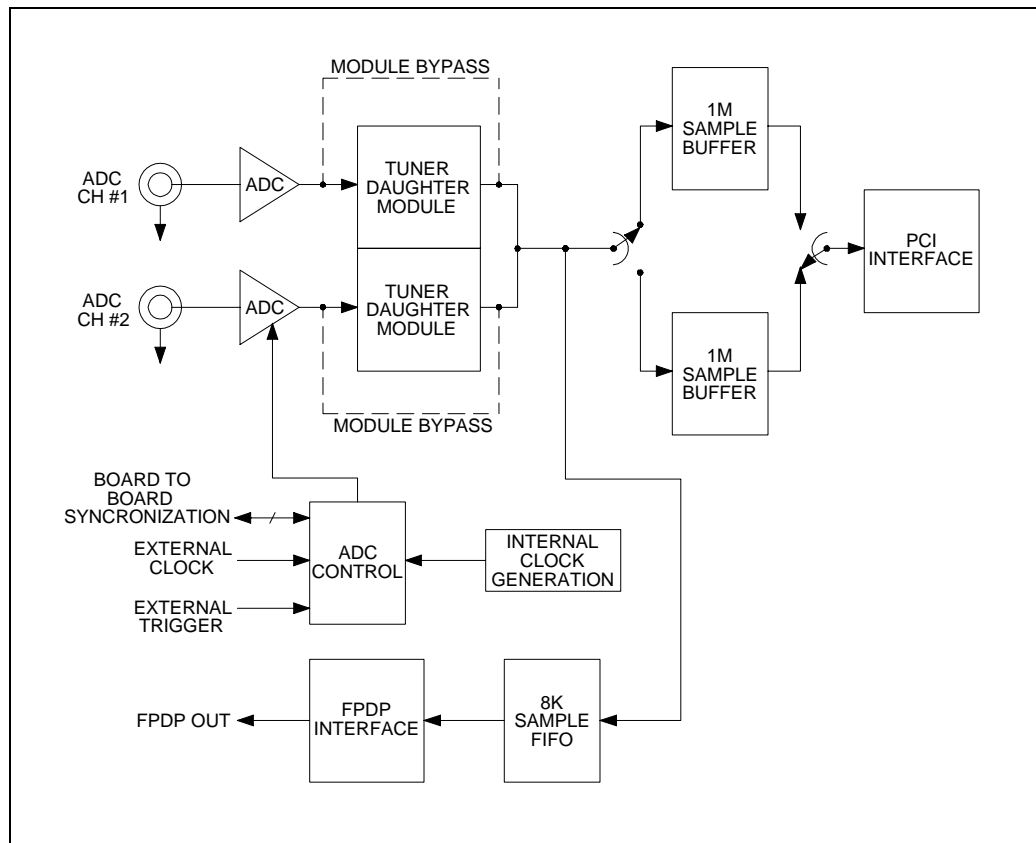
To collect four streams of digital data, two two-channel ADC boards have been used.

These boards are ICS-650 commercial of the shelf products, made by ICS Ltd. The boards have been configured to do synchronous sampling on all four channels. Each board allows synchronous sampling on two channels with sampling rate up to 65MHz, and 12-bit resolution. (12-bit resolution was one of the requirements for ADC boards due to accuracy and dynamic range requirements.) These boards allow for external or internal triggering and for an external and internal sampling clock. Internal triggering and external clock have been used in the experimental setup.

Each board has internal data memory and a swing buffer, which allows continuous data capture into PC memory using PCI DMA transfer. A block diagram of the ICS-650 ADC board is shown in Figure 3.14, and its specifications are in Figure 3.15. The continuous data capture feature of the ICS-650 board has not been used due to the limited bandwidth of the PCI bus. (The GIDL receiver is capturing data on 4 channels at sample rate 38.192MHz. This data is sampled at 12 bits, and is converted inside the ADC to 16 bits for convenience. This makes GIDL data rate equal to $38.192 \times 4 \times (16/8) = 305.536$ Mbytes per second, while the maximum PCI transfer rate is 132 Mbytes per second. There is a new PCI bus standard available now which would allow maximum transfer rate up to 528 Mbytes per second.) Data are collected into the cards' memory. When this memory is filled, data collection stops, and data is transferred into PC memory. Batch signal processing then starts.

An aluminum chassis hosts the RF/IF downconversion stages, master clock and synthesizer, and power supply. The ADCs are PCI cards and are installed into a data processing PC, which is set next to the GIDL receiver, as shown in Figure 6.13. All critical RF connections are done using semi-rigid RF cables to achieve the best connection performance, and extra care is taken in shielding the receiver internally and externally (note the copper tape inside and outside of the assemblies).

The completed GIDL receiver and its individual sections are shown in Figures 3.7–3.9. In Figure 3.7(a) it is possible to see four RF inputs located in the second from the top box, and non-filtered IF outputs located on the third from the top box. IF bandpass filters of various bandwidth are attached to these outputs (two of them attached in this figure). The output of these filters then goes directly into the ADC inside the processing PC. The top box of the assembly is empty. It is used for shielding, for carrying miscellaneous parts and cables during experiments, and for storage (to keep all the GIDL parts in the same

**Figure 3.14:** ICS-650 Two channel ADC Board Block Diagram

ICS -650 SPECIFICATIONS	
<u>ANALOG INPUT</u>	
No. of Analog Input Channels:	2
Analog Connector Type:	SMB Coaxial
Input Impedance:	50 Ohm
Full Scale Input:	± 1 Volt
Input Signal Bandwidth:	DC - 200 MHz (-3 dB point)
Max. Sampling Rate:	65 MHz/ch., 2 channels simultaneous
ADC Resolution:	12 bits
Sampling:	Rising edge of internal sample clock, rising or falling edge of external clock (programmable).
External trigger:	Sampling occurs on second clock edge following rising edge of external trigger. Trigger must remain high for at least one clock cycle.
SNR:	> 62 dB
SFDR:	<-80 dB
On-board Storage:	1 Msample/channel
<u>GENERAL</u>	
PCI bus Interface:	32-bit 33MHz, Master/Target Burst Mode (DMA) capable
Front Panel Interface:	FPDP 32-bit, 50 MHz
Environmental:	
Operating Temp:	-0° - 50°C (at entry point of forced air)
Storage Temp:	-40° - +85°C
Humidity:	90% non-condensing
Cooling:	Approximately 200 LFM
Power:	+5V @ 2.2A (without tuner module) +5V @ 2.9A (with tuner module)

Figure 3.15: ICS-650 Two Channel ADC board Specifications

place). The GIDL receiver assembly includes its own power supply, housed in the bottom chassis, so the system only requires a single 110 VAC power line. To provide antenna bias voltages, the system is configured such that it can supply any necessary voltage to the antenna preamplifier via the RF cable.

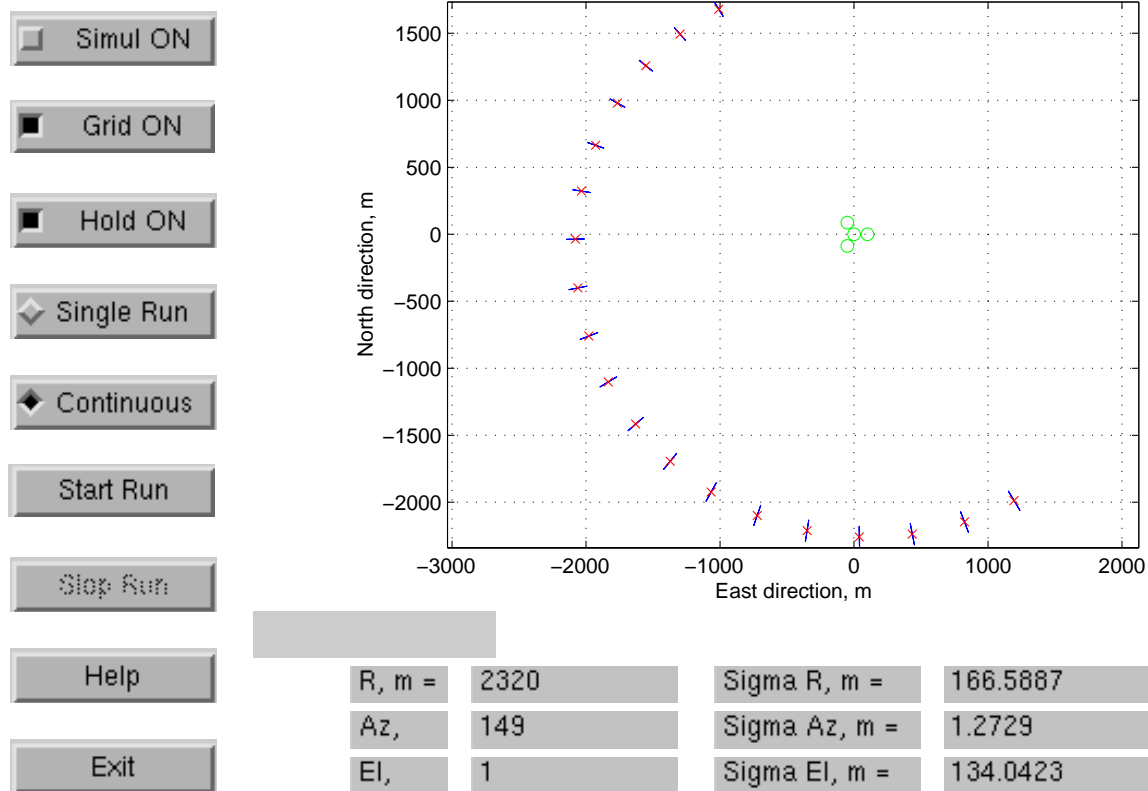
3.4 GIDL Display Software

The GIDL jammer positioning display software shows jammer position in real time and includes an option of tracking the location of the moving jammer, by plotting successive jammer locations as data is processed, i.e., with intervals of approximately 50 seconds. There is also an option to run it from simulated data or real data. In Figure 3.16, the display shows locations of the jammer as they appear in real-time, so it is easy to see that the jammer performs a spiral motion (data has been supplied by simulation code for this demonstration). In addition to jammer locations, this display also indicates calculated error ellipses (which look like little strikes), to assist in searching for the jammer. The display also has numeric information for the current jammer location, which includes calculated jammer location, and estimated localization errors (1σ) for that location.

As in all GIDL software, the display code is written in MATLAB. It accepts calculated jammer location for GIDL detection and localization software, calculates expected errors and shows this data on the screen. To orient the user, location of GIDL antennae is also shown on the screen, where the center of the screen corresponds to the reference point of the GIDL system. GIDL antenna locations are marked by circles on the display.

3.5 Construction of an Experimental GPS Jammer

Recently, much discussion has occurred regarding out-of-band emissions from handsets for the new mobile satellite communication services (MSS). These emissions are a significant GPS interference concern, so it was decided to develop a device which would imitate such emissions. Proposed specifications for out-of-band emissions from MSS state that power levels should be no more than -70 dBW/MHz. A jammer was created, shown in Figure 3.17, that generates white noise across the entire GPS band with a tunable power density

**Figure 3.16:** Real-Time GIDL Display Software (Simulation)

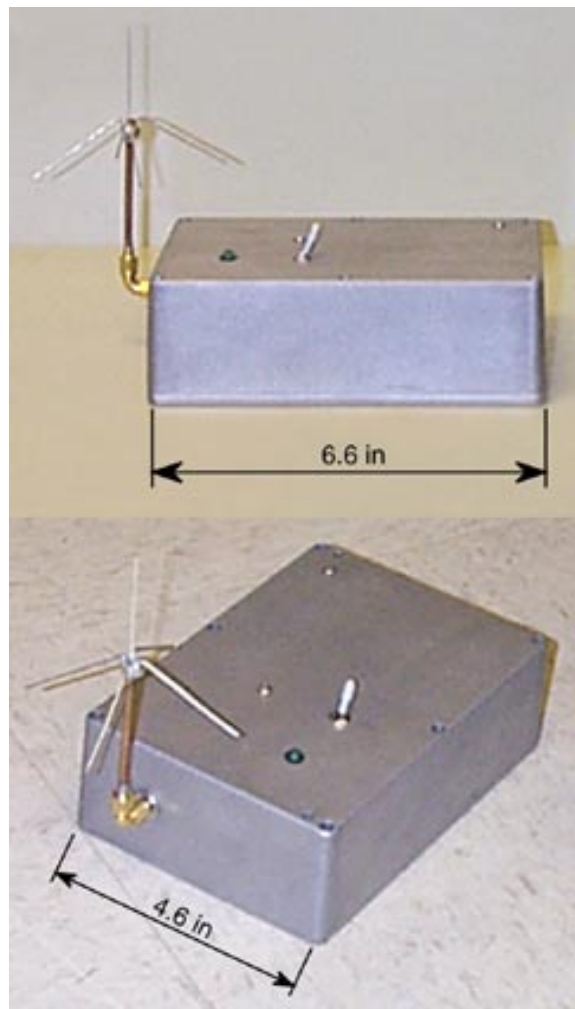


Figure 3.17: -70 dBW/MHz Interference Source

of -70 dBW/MHz. This noise source is completely autonomously operated and is battery powered. This jammer is an example of how easy and inexpensive it is to build GPS jammer.

This interference source can be used for other experiments besides interference direction finding. When it is turned on, it does not pose a significant threat to the non-participating GPS users. Interference tests have demonstrated that it does not affect typical GPS receivers at ranges over 30 meters.

For experiments with various power levels, an external attenuator has been attached to

the output of the described jammer to reduce jamming power level. For GIDL experiments, as described in Chapter 6, an external amplifier of 30 dB was attached to the jammer to increase its jamming range to approximately 316m.

Chapter 4

Software Radio and GIDL System Calibration

4.1 Introduction

The GIDL is designed to localize a jammer or interferer to the extent possible. All theoretical calculations assume perfect measurements, or measurements which contain some assumed distortion or noise. In most cases it is assumed that whatever is measured or received by the system is perfect and does not contain any errors introduced by the system itself.

A theoretical GIDL would have perfect components such that all the calculations would be valid. The real-life GIDL requires error analysis and calibration. The GIDL hardware is assembled using practical components and contains four channels. For the theory to be valid, these channels should be identical. However, there will be some variations in the hardware. The signals are received by real antennae (as opposed to identical theoretical ones) which introduce some delay that is not necessarily equal in each antenna. Connecting cables also introduce their own delays. The real-time clock is another source for error in the GIDL.

From the above, it follows that the GIDL is limited by these practical concerns but our performance projections are based on idealized calculations using it. Before doing this, it

is necessary to calibrate all system parameters which could introduce errors unaccounted for by the theory.

As mentioned in previous paragraphs, there are two things which are not accounted for in the theoretical calculations: differential delays in the GIDL receiver channels and the GIDL clock bias. Before one can make any useful measurements with the GIDL, these two errors must be calibrated. With respect to the clock calibration, it is both interesting and useful to track not only clock offset, but also offset with respect to changes in temperature and other factors, such as aging, changes due to shocks and vibration, instability in power supply, etc.

The easiest way to measure these errors is to set the transmitter in some known location, measure differential delays of the received signals in the system, and compare them with what one should expect if the system were ideal. For the clock calibration, it is necessary to compare clock data with some reference clock of known accuracy. However, calibrating the clock in this manner is neither feasible nor practical.

Fortunately, we have GPS. It transmits signals in the band of interest, and the GPS clock is one of the best clock signals available. It is possible to use GPS signals to calibrate both GIDL system unknowns: differential delays in the receiver channels and bias in the master clock. This calibration technique relies upon the fact that, most of the time, the jammer signal is not present, and GPS signals are readily receivable.

Before one can use GPS signals, they must first be obtained. The next section continues developing the concept of the software radio. Techniques used to receive GPS signals are then addressed. Section 4.4 goes on to explain how to use GPS signals for GIDL calibration.

4.2 GPS Signal Structure

As described in Section 1.2.2, GPS is a satellite-based radionavigation system deployed by the United States and managed by the U.S. Air Force. It was initially developed as a military technology for the U.S. Department of Defense but quickly evolved into a dual-use system as a result of the tremendous potential for civilian use. Two levels of service are now available: the military-specific Precise Positioning Service (GPS-PPS) and the

Standard Position Service (GPS-SPS) for widespread public use. The target software radio implementation is a GPS-SPS receiver utilizing the civilian component of GPS [8].

Extracting the GPS-SPS component from the multiple-frequency in-phase/quadrature GPS broadcast provides the following signal structure:

$$S_i(t) = \sqrt{2P}C_i(t)D_i(t)\cos(\omega_c t + \phi) \quad (4.1)$$

where S_i is the GPS-SPS broadcast from the i^{th} satellite, i indicates the satellite index, P is civil signal power, C_i is C/A, or PRN, code for the i^{th} satellite (1.023 Mbps), D_i is navigation data for the i^{th} satellite (50 bps), ω_c is equal to $2\pi f_c = 2\pi 1575.42 \times 10^6$, and ϕ is the phase offset.

Equation (4.1) assumes that each of the satellites is broadcasting on a common carrier frequency of 1575.42 MHz. This is indeed the case as GPS-SPS uses a CDMA spread spectrum modulation format. The spreading or PRN code for the GPS-SPS signal is known as the Coarse/Acquisition (C/A) code, hence the term in (4.1).

The C/A code has a chipping rate of 1.023 Mbps and a period of 1023 chips, or 1 ms. The C/A codes are a subset of the Gold code family, which is a collection of PRN codes that provides good multiple-access properties i.e. low cross correlation, for their periods [151]. Each satellite has a unique C/A code, which is produced from the modulo-2, sum of two, 1023 chip PRN codes, G1 and G2. G1 and G2 are generated using 10-stage maximal-length linear shift registers, initialized to all 1's, with tap positions specified by the generator polynomials.

For more details on the GPS signal structure and characteristics, see [2, 8].

4.3 GPS Software Signal Processing

Software signal processing can be considered the second half of software radio implementation. The software algorithms can be divided into three main areas: acquisition, code tracking, and carrier tracking. The algorithm of most interest to us is signal acquisition and pseudorange estimation from a single data set.

The most comprehensive software simulations of GPS signal acquisition and tracking were published by Zhuang [152] and Akos [89]. This section will review the underlying

theory in the algorithm implemented and provide a list of references for further study into their operation.

4.3.1 Spread Spectrum Signal Acquisition

Signal acquisition is the first step in processing the GPS signals. Acquisition here describes the three-parameter search required prior to the inception of code (and carrier tracking) [153]. The three parameters under investigation are PRN code, PRN code phase, and carrier frequency. The PRN code is the spreading code used for a particular satellite. In the case of GPS, the PRN code is the specific C/A code. This search space consists of any of the possible 32 GPS PRN codes. The second parameter is PRN code phase. This is the search for the specific code alignment in the received data. For example, when a GPS receiver takes its first sample of a GPS broadcast, that sample could occur at any location in the 1023-chip sequence. Determination of the PRN code phase, typically within half of a chip, allows a local synchronized version of the PRN code to be generated which is then correlated with the incoming signal to remove the spread spectrum modulation. The final parameter in the search is the carrier frequency, which can be considered the IF if downconversion or bandpass sampling is applied. For GPS this is equivalent to the 1575.42 MHz carrier or its resulting IF, which may initially appear to be deterministic given the front end implementation.

However, there are many factors which contribute to deviations from the expected value. The line-of-sight velocity, which results from the dynamics of the satellite and receiver, create a Doppler shift in the received carrier frequency. In addition, if a local oscillator (LO) is used to downconvert the incoming RF signal, its frequency drift proportional to the type of oscillator used will also influence the effective frequency. Typically, a search of -10 kHz to +10 kHz, in 500 Hz steps about the nominal IF, is adequate. This search space assumes that the line-of-sight dynamics are not extreme, such as in the case of a missile or rocket, and that the LO is of fairly high quality, such as a temperature-compensated or oven-controlled oscillator.

If no external information is available to the user, all parameters in the search space must be explored completely. This is known as a “cold start” in acquiring and tracking

GNSS signals. However, *a priori* knowledge can greatly reduce the search space, minimizing the time required for acquisition. For example, GPS satellites transmit almanac data which provides the approximate positions of all satellites in the constellation as a function of time along with each satellite's C/A code. Ideally, a receiver would store this information before it was powered down. Then, when the receiver was to be used again, it could utilize the almanac data, its internal clock for a time reference, and its last location to identify which satellites, and corresponding C/A codes should be visible along with an estimate of the Doppler frequency. This technique is known as a “warm start” and provides an intelligent starting point from which to base the search, thus minimizing acquisition time. However, if the receiver has been moved a significant distance since last used or it has not been used for such a long time that the almanac data is no longer valid, the initial guess of visible satellites is most likely incorrect and the receiver will revert to a cold start. There are also other techniques, such as knowledge of the probability density function of the unknown parameters, which can be used to search intelligently in an attempt to minimize search time [154, 155].

The bulk of commercial GPS receivers utilize an application-specific integrated circuit (ASIC) for code correlation, mixing in-phase and quadrature components to baseband, and accumulating the result over a given interval. The advantage of this is that the same hardware can be used for acquisition as well as tracking. However, this configuration restricts the type of acquisition algorithm. The software-radio approach allows the use of different algorithms for acquisition and signal tracking.

4.3.2 Acquisition Via Parallel Code Phase Search

The most recent development in GPS signal acquisition is the use of the frequency domain circular convolution [30]. The goal of this technique is to parallelize the code-phase search. In defining the acquisition search space, Equation (4.2) below:

$$\underbrace{\left(\left(\frac{1}{2} \right) 1023 \right)}_{\text{possible PRN Code phases}} \underbrace{\left(2 \left(\frac{10000}{500} \right) \right)}_{\text{possible frequencies}} \approx (2046)(40) = 81840 \text{ combinations} \quad (4.2)$$

indicates that the code phase contributes a much larger ambiguity (by a factor of 50) than that of the intermediate frequency (it is assumed that search is done in steps of half C/A

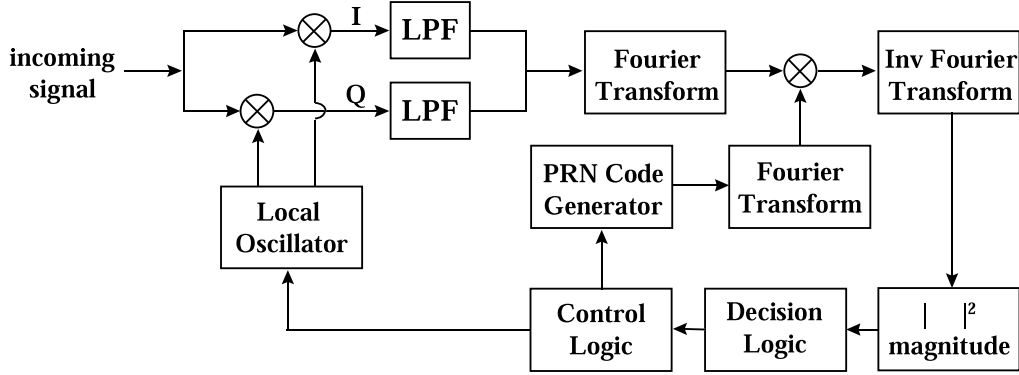


Figure 4.1: Parallel PRN Code Phase Search Acquisition Block Diagram

code chip in time domain, and in 500 Hz steps in frequency domain over ± 10 kHz of possible Doppler frequencies). Thus, a parallelization of the code-phase search will greatly reduce acquisition time. A block diagram of this technique is depicted in Figure 4.1.

The mathematical basis for the technique is illustrated in Equation (4.3) below.

$$\underbrace{x_1[n] * x_2[n]}_{\text{circular convolution}} \xleftrightarrow{\text{DFT}} X_1[k] X_2[k] \quad (4.3)$$

The inverse discrete Fourier transform (IDFT) of the product of two finite-duration n -point sequences corresponds to the circular convolution of their respective time domain sequences [156]. The incoming signal is mixed to baseband, generating the in-phase and quadrature components to be used as the real and imaginary inputs, respectively, in the calculation of the discrete Fourier transform (DFT). The result is multiplied by the complex conjugate of DFT of the complete PRN code. The magnitude of the IDFT is taken of the product, and the resulting sequence is the circular convolution of the two sequences.

The maximum value of the resulting sequence corresponds to the best estimate of the code-phase of the PRN sequence in the data set for the frequency tested. If this maximum value does not exceed a predetermined threshold, either the collected data does not contain a measurable signal with that PRN code or the frequency evaluated is incorrect. The remaining potential parameters, PRN codes and frequencies, can then be cycled through until acquisition is successful.

Note that all possible code phases are evaluated in a single operation using this technique. This approach reduces the search space for a single PRN code to only the frequency

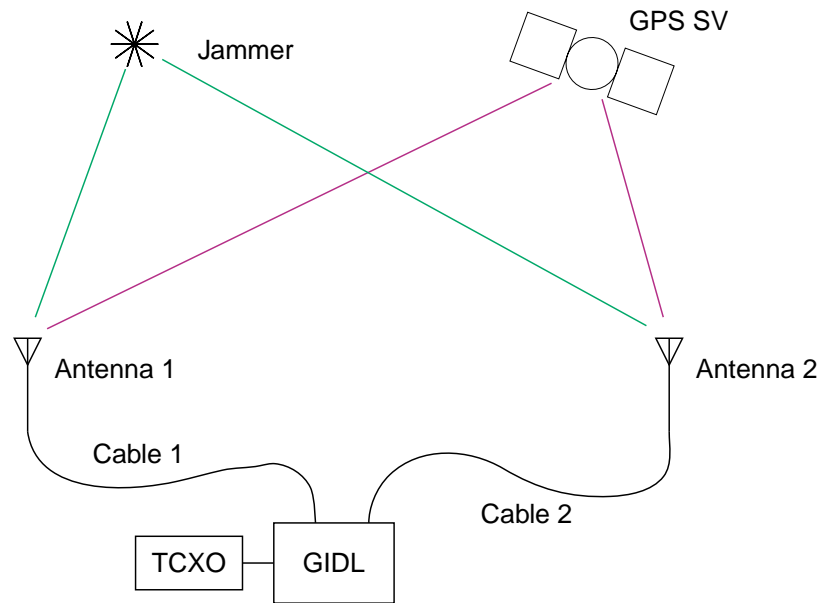


Figure 4.2: GIDL Calibration Setup

uncertainty. Thus the total search space for a single PRN code of more than 20000 different combinations has been reduced to only 40 candidates.

4.4 System Calibration Using GPS Signals

The concept behind the GIDL calibration setup is shown in Figure 4.2, which for simplicity shows only two GIDL antennae. Calibration of the GIDL using GPS signals is done in a batch form. When the GIDL is turned on, it is assumed that there is no interference present. If interference is present, it would be detected, and old, stored calibration data would be used. If the system is turned on for the first time with interference present, no calibration data is used, and GIDL would provide the best possible results for the jammer location without calibration.

For calibration, as for normal operation, 1 mega samples (MS) of data is collected simultaneously on all channels. This data size is limited by hardware, as discussed in Chapter 3. This 1 MS of data corresponds to 13.7 ms of captured signal. Along with the data collection, a time stamp from the GPS receiver is obtained along with ephemeris

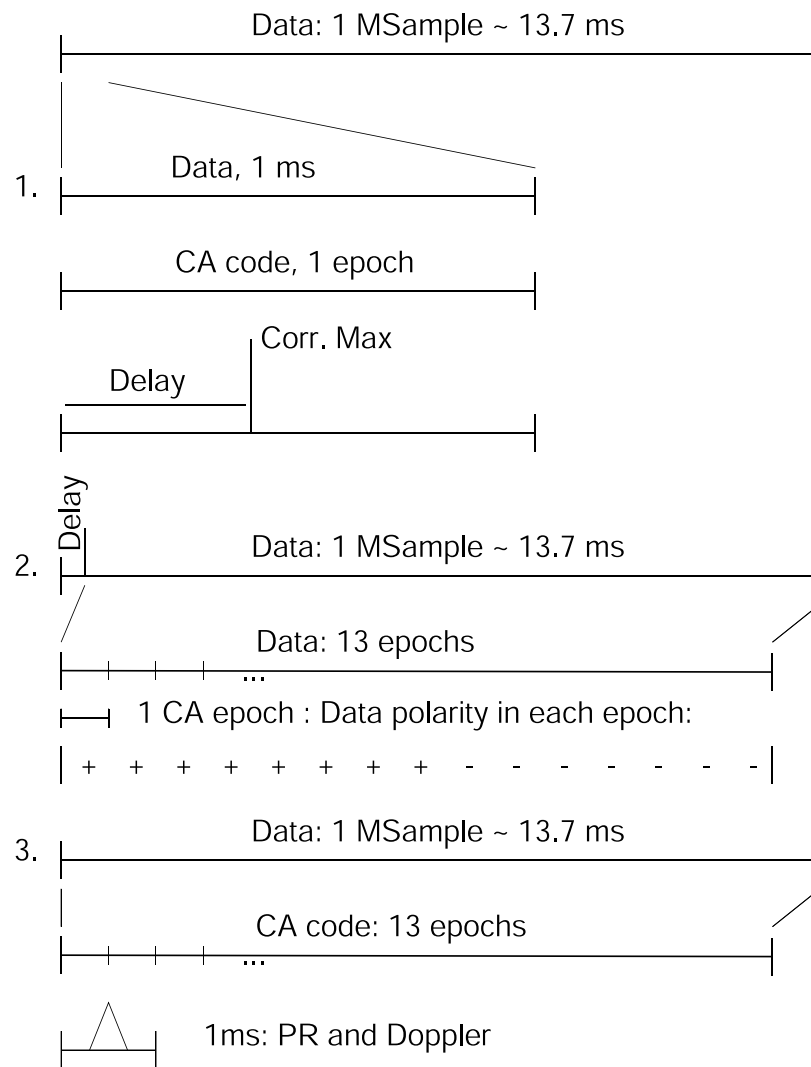
information and the number of satellites in view.

Data from each channel is used to estimate pseudoranges and Doppler frequencies for all satellites. This process is graphically presented in Figure 4.3. Only the first millisecond of data is used to find a rough correlation with the C/A code and to estimate code delay or pseudorange. Then the estimated delay is used to find the beginning of the C/A code in the data sample. In Figure 4.4, the correlation peak detected from 1 ms of data is shown as well as the spectrum of the reconstructed carrier signal.

Once the signal delay is found, each millisecond of data is correlated with one aligned epoch of C/A code. The restored carrier signal is used to find the data bits. Once the data bits are detected, a new C/A code is formed with the same length as the data set, and again data is correlated with this C/A code sequence. Now correlation has been completed for over 17 ms of data, so more energy of the signal is restored, and it is possible to reconstruct the carrier signal, as shown in Figure 4.5. Knowing the time and ephemeris from the GPS receiver and the surveyed location of the GIDL antenna, it is possible to calculate what frequency this signal should have and compare it to the frequency that is measured. This delta frequency defines the bias in the GIDL clock frequency. When that operation is completed, a new C/A code sequence can be generated, taking into account the GIDL clock bias estimate and GPS Doppler. This final sequence generates the best possible correlation peak when matched with the data. The correlation peak obtained from 13 ms of data is shown in Figure 4.6. The maximum of this correlation peak is used as the pseudorange measurement for a given channel and satellite.

This measurement procedure is repeated on each channel for every satellite in view. When it is completed, the ephemeris, time stamp, and surveyed GIDL antenna location are used to generate expected pseudorange differences for each antenna pair. These calculations are compared with measured pseudorange differences to obtain differential delays, which are estimates of the system biases of the GIDL. They are stored for future use.

Currently, the basic GIDL measurement is the TDOA of the signals to the antennae. Jammer direction and location is calculated on the basis of these measurements. These measurements must be done relative to the antennae; thus unknown delays in the cable and system should be calibrated out. Also, because a system clock has been used to calculate propagation delay, it too must be calibrated. To summarize, the major system unknowns

**Figure 4.3:** Pseudorange and Doppler Frequency Estimation Process

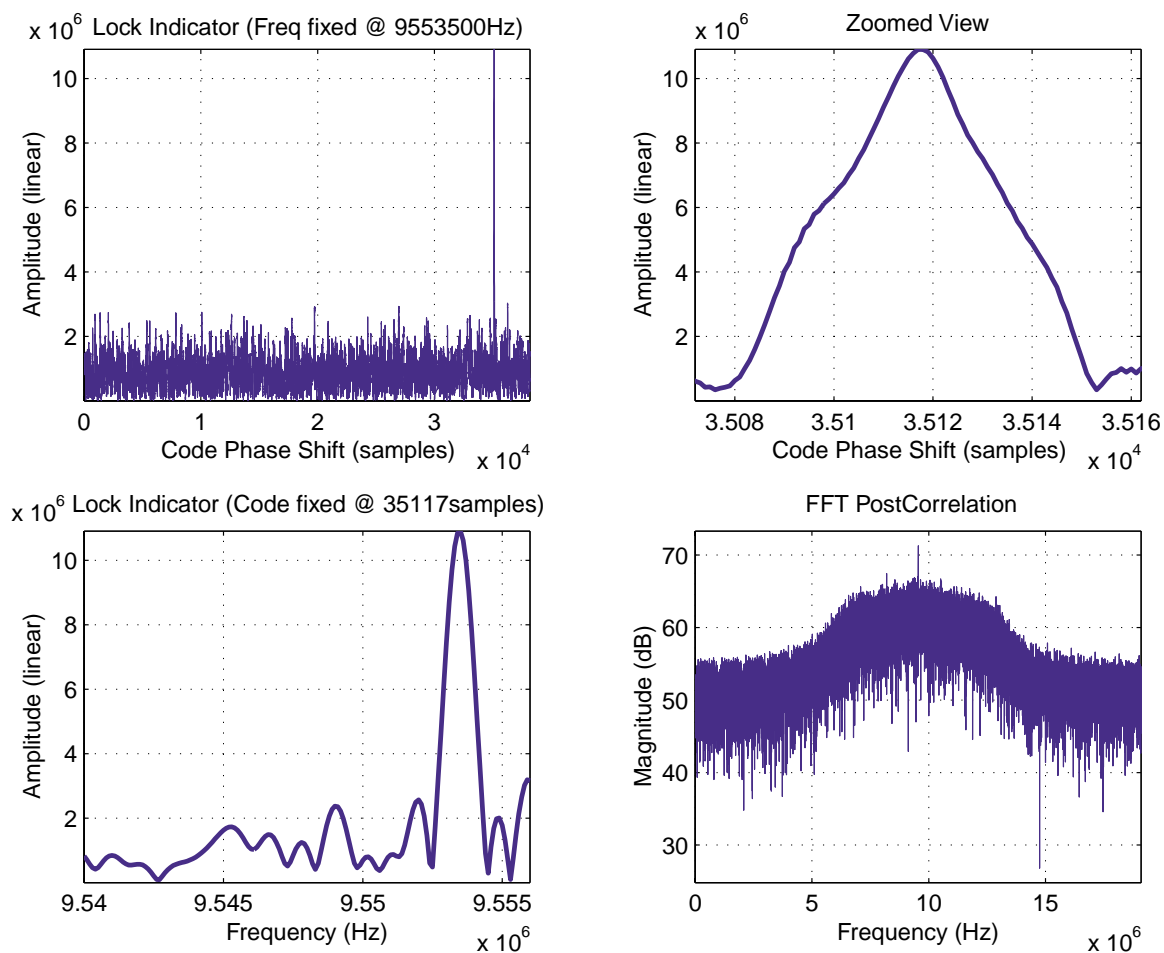


Figure 4.4: GPS Signal Detection: Correlation of 1 ms of GPS signal with Spectrum of Reconstructed Carrier from 1 ms

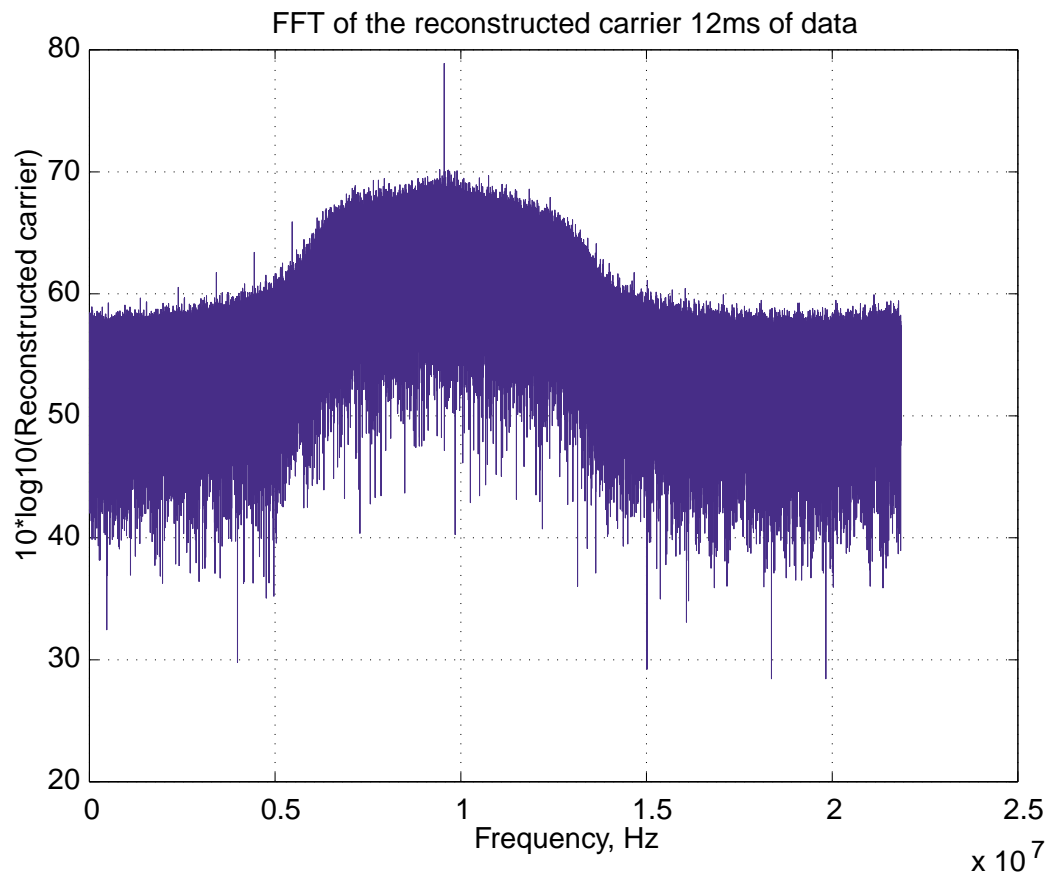


Figure 4.5: Spectrum of Reconstructed GPS Carrier from 12 ms of Data

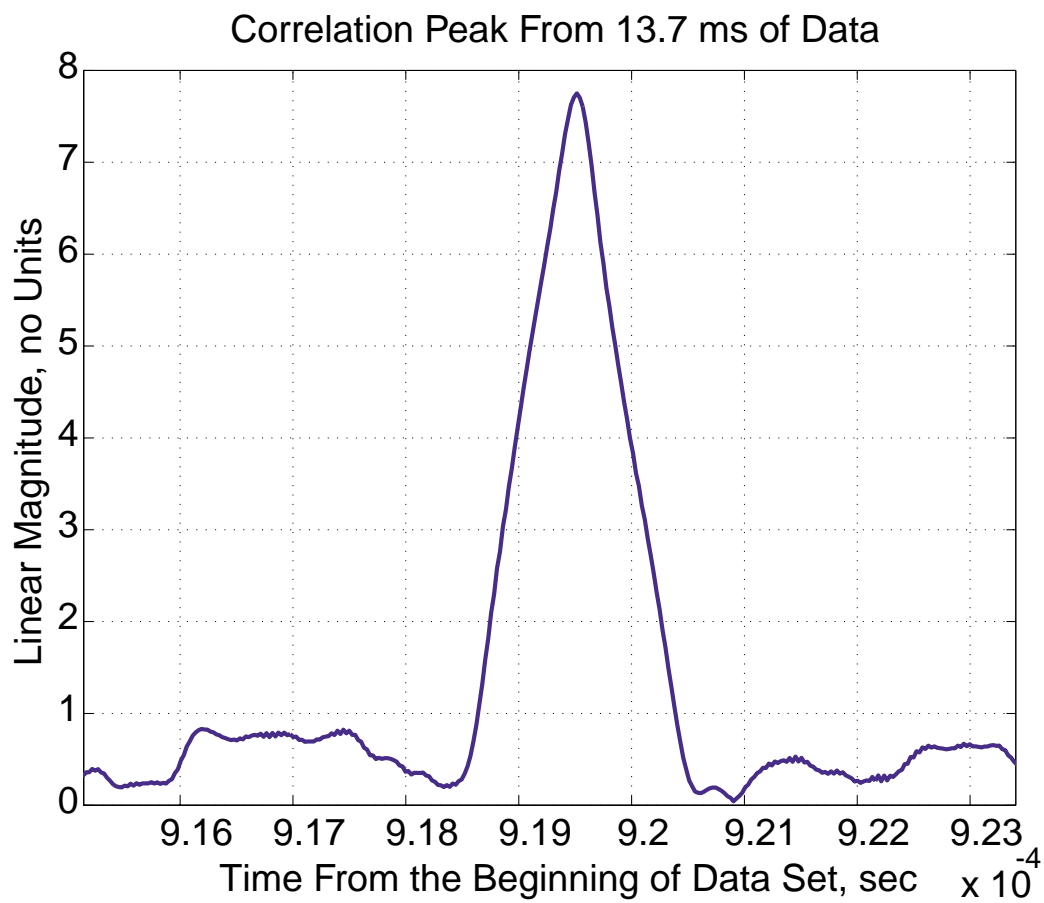


Figure 4.6: GPS Correlation peak for PRN 6 obtained from 13 ms of data

which should be calibrated are: relative delay in the antenna cables; offset in the master clock (TCXO); and variations with temperature and other factors (for example vibration, aging, humidity, variations in power supply voltage, etc.).

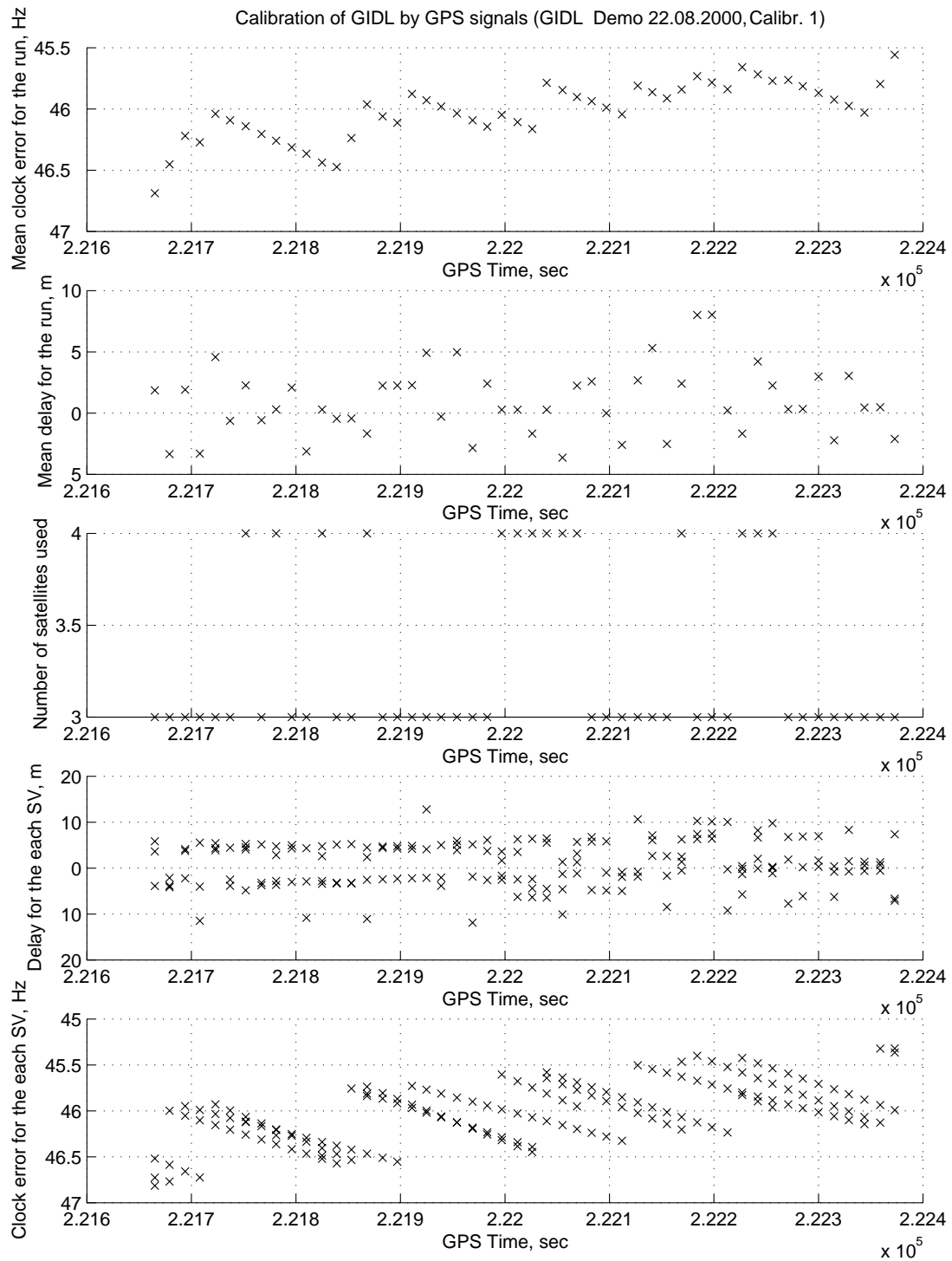
4.5 Experimental Results of System Calibration

Numerous experiments have been performed with the GIDL hardware and software. A significant focus has been on developing calibration software and performing calibration of the system. Experimental results of the system delay calibration and the clock calibration are shown in Figure 4.7. Fifty data sets have been collected a few minutes apart. Each data set was used to calculate the system clock error and system delay. Antenna locations and satellite geometry are known, as are the expected delay and the expected signal frequency. The satellite frequency is measured using the existing system, and the signal time difference of arrival is calculated. Next, the expected results are subtracted from the measured results, and the errors are plotted. The first plot in Figure 4.7 shows the average clock error for each given data run. Averaging is done over all satellites in view. The next plot shows the average system delay and also the average of all satellites in view. The third plot shows the number of satellites used, while the fourth shows delay errors for each individual satellite. The last plot shows the clock error based on each satellite measurement.

Figure 4.8 shows the running average of the clock estimation and the running average of the delay estimation. This means that propagation delay and frequency offset for the first data point have been obtained from the first data run, which had 5 good satellite signals, second data point have been obtained utilizing existing data and data collected in the second run which also had 5 good signals, same process was kept going on for 15 data runs, as it shown in Figure 4.8, or for 20 data runs as in Figure 4.9. For the GIDL experiments calibration data sets consisting of 50 or more runs were collected, with estimated propagation delay converging down to centimeters. It also shows three different ways in which one can estimate the top of the GPS correlation peak: maximum (as delay taking delay corresponding to the maximum of the correlation peak) , discriminator function (creating a discriminator function by shifting correlation peak by 1 sample, and looking for zero crossing) , and median (obtaining center of mass of the figure under correlation function) ,

for more detailed description of these methods see [2]. All three of these measurements are valid measurements, but the maximum measurement was decided upon as it is least susceptible to multipath errors. Figure 4.9 shows a running average for the number of runs of the system delay, based on the maximum of the correlation peak measurement. It converges to approximately 5.75 m. This error was primarily induced by the cables of different lengths used in the experimental setup.

These results shows that the system clock and system delays can be calibrated by means of the GPS signals. It takes several minutes to process one calibration data set depending on the number of satellites in view.

**Figure 4.7:** GIDL Calibration: Results of Clock and Delay Calibration

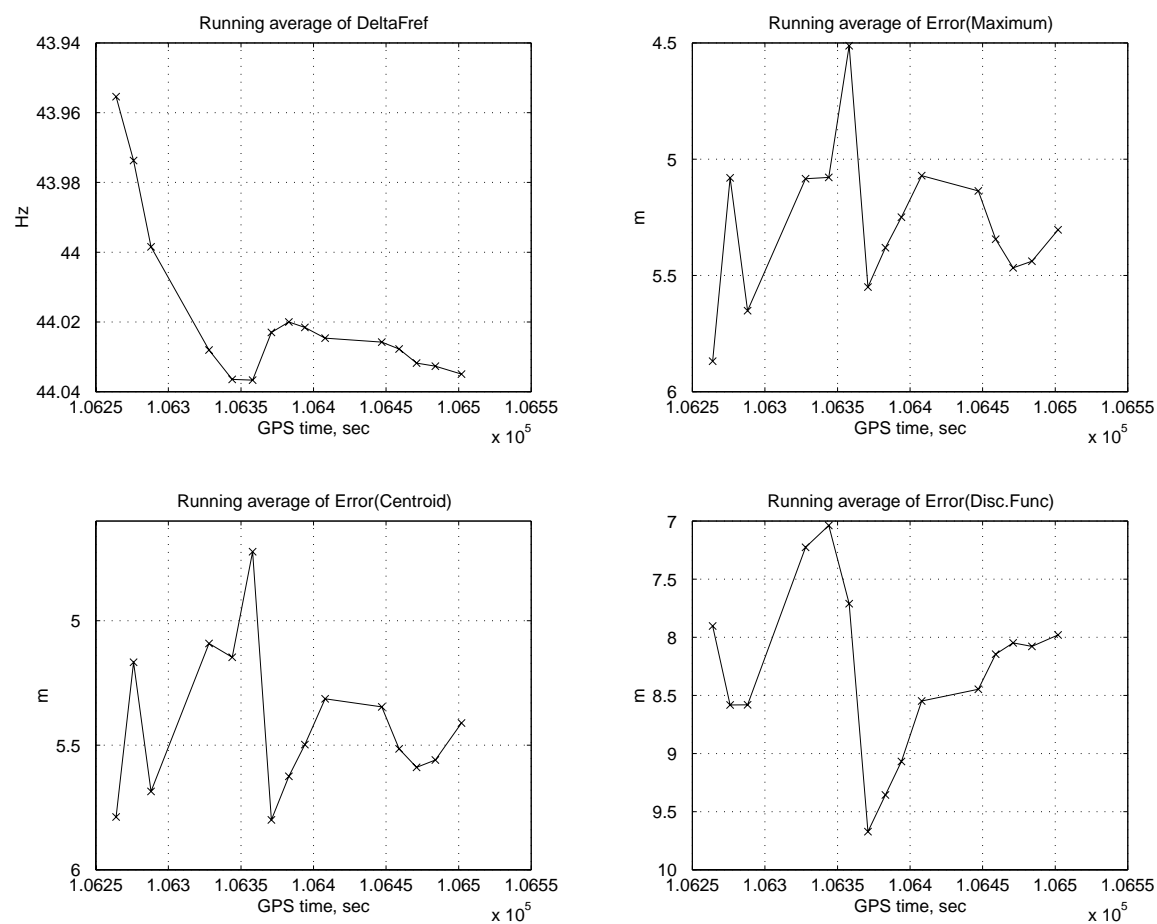
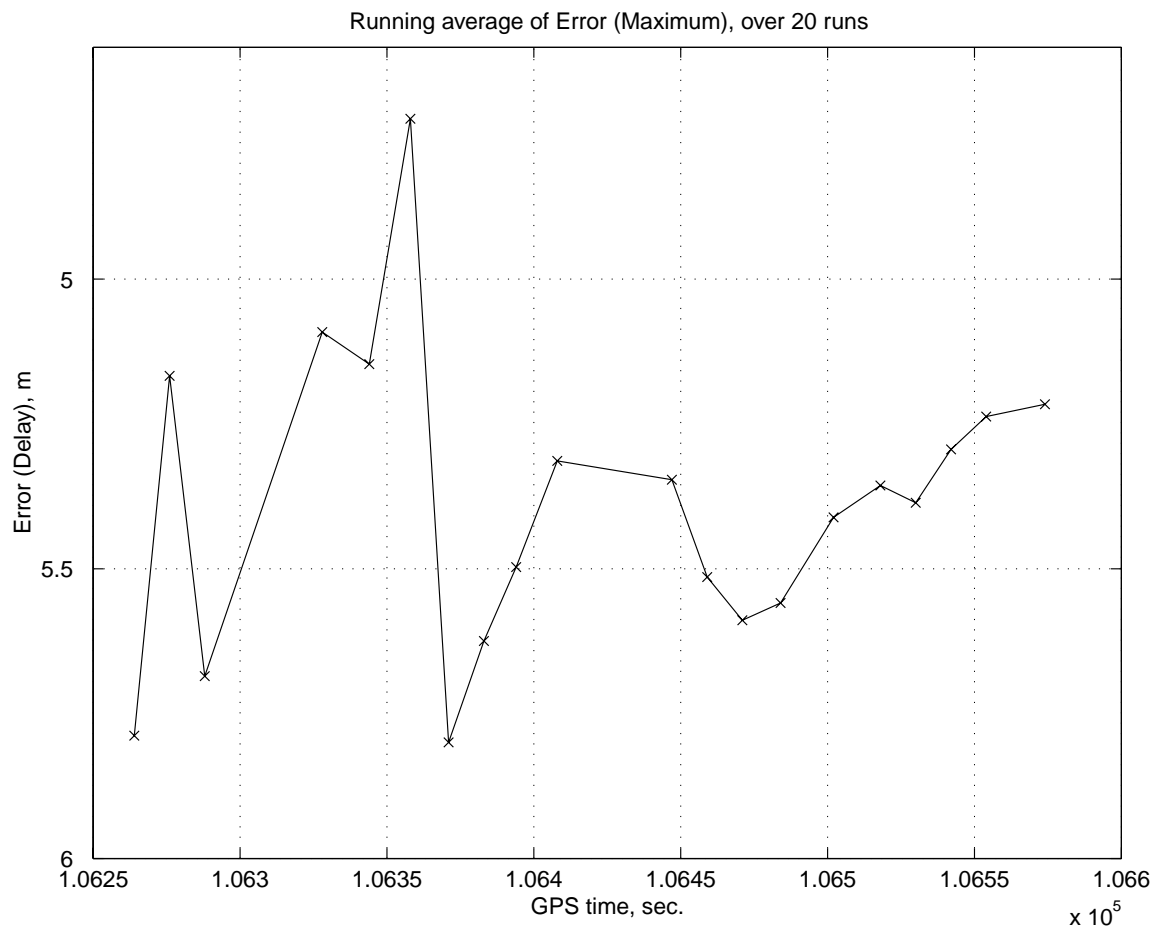


Figure 4.8: GIDL Calibration: Results for Data Runs 1—15; Number of SVs per Each Run: 5 5 4 4 4 6 6 5 5 4 5 5 4 4 4

**Figure 4.9:** GIDL Calibration: Results for the 20 Data Runs

}

Chapter 5

GIDL Implementation

5.1 Introduction To Implementation Details

This chapter will describe the practical aspects of the GIDL implementation and operation. Without going deeply into the theoretical considerations, it describes the algorithms and techniques used to calibrate GIDL and to obtain the jammer location. This chapter will shed more light on the “Generalized” nature of GIDL and possible extensions.

5.2 Data flow in GIDL

Data flow and software-hardware interaction is shown in Figure 5.1.

There are two types of data available for GIDL software. One is the raw ADCs data, and the other GPS data in the form of ephemerides and time tags. ADC data is available at all times and consists of 524288 samples for each GIDL channel. (The number of collected samples is determined by the memory capacity of the ADC cards, and currently it cannot exceed 524288 samples per ADC channel.) These data contain all signals information in the GPS frequency band (bandwidth of this band is defined by IF filters). It is a digitized signal downconverted from the GPS L1 frequency to the intermediate frequency of 9.548 MHz, and sampled at 38.192 MHz (GIDL frequency plan is discussed in section 3.3.2). Data from the Garmin GPS receiver is available, of course, only at times when the GPS signal is not jammed. The ephemerides and time data are used for GIDL calibration only.

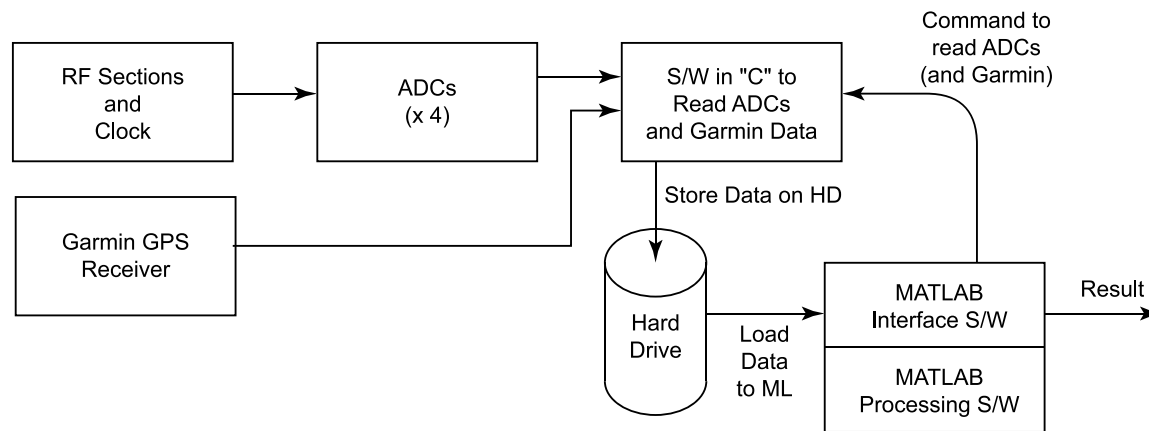


Figure 5.1: Data flow in GIDL System

User interface and control of the GIDL system is from within the environment. Custom interface software, written in “C,” interacts with ADCs, Garmin GPS receiver, and gain control attenuators (not shown in Figure 5.1 for clarity). On command from the user or the processing algorithms, the interface software reads data from ADCs and stores it to the hard drive for processing. In calibration mode it also reads ephemerides data and time from the Garmin GPS receiver. The MATLAB processing software then reads this data from the hard drive. The GIDL processing software actually defines what function the GIDL receiver is performing. This allows extraordinary flexibility in the system. The algorithms that have been implemented are discussed later in this chapter.

Resolution of the ADC is 12 bits, with ADC hardware patching these 12 bits with zeros to make 16-bit word. These 16-bit words are saved as integers in ASCII format in the data file, four values in a row corresponding to four simultaneous readings from all four ADCs. This format of the data file is chosen for the convenience of debugging, and readability by a number of programs, including MATLAB.

Several operational modes are used in the GIDL software. In the *data collection* mode, a preset number of data sets from ADCs are collected and stored by the hard drive, without further processing at the time of collection. If this data is going to be used for calibration, then ephemerides and time data are also collected from the Garmin GPS receiver. (Time stamp and ephemerides are needed in order to obtain location of the GPS satellites, which

are used as signal sources at known locations for GIDL calibration. A GPS receiver capable of providing this information could be implemented in software as part of the GIDL receiver, but that is beyond the scope of this work, so a Garmin GPS receiver was used in order to supply GIDL with time stamp and ephemerides data.) This mode is used to obtain calibration data, jammer localization data for postprocessing, statistics on data processing, and debugging data. In the *demonstration* mode, one data set is collected and then used to localize the jammer. This mode is a one-shot trigger and has been used to demonstrate the GIDL system. The last mode is *continuous operation* mode. In this mode, the ADCs are sampled, the Garmin data is collected and processed, and then this operation is repeated.

All of the above is done completely independent from the processing algorithms. This sets a framework for the processing algorithms without choosing specific algorithms to implement. Thus various processing algorithms, based on various assumptions can be implemented and tested. This feature makes GIDL “general,” it allows a framework for development and testing of jammer detection and localization algorithms, and possibly algorithms for other applications.

Reiterating, the basic GIDL hardware and software allows for various detection and localization algorithms to be tried by providing baseband sampled signal of the GPS frequency band and a way to pass this data (along with some additional GPS data) to processing algorithms that can be experimented with as appropriate.

5.3 Implemented algorithms and assumptions

In parallel with development of the flexible GIDL hardware, significant work has been done in studying various algorithms and implementations suitable for testing on the experimental hardware. There are a large number of detection and localization algorithms that have been considered in the literature for various types of signal and antenna configurations. All of these algorithms can be implemented and tested on the experimental hardware by changing processing software (and possibly by changing antenna configuration). For example, adaptive algorithms could be implemented to test the signal for the presence of various types of jamming via probabilistic hypothesis on a specific signal. A CW jammer smart antenna arrangement (for example combination of the short and long baselines in the same system),

combined with processing algorithms, would allow resolution of the cycle ambiguity and precise jammer localization. (This would have to be studied in detail in the future work.) Optimum jammer detection and localization algorithms are presented in Chapter 2.

To limit the scope of this thesis (as has been mentioned in Section 2.2) only white Gaussian noise sources are considered for interference. These sources are easy to build, and are effective jammers for the GPS signal. Detection and localization algorithms for other types of the jammers can be added to GIDL software to extend its functionality. This extension will be the subject of future research and development.

There are three functions that the GIDL system must perform to mitigate interference: system calibration, jammer detection, and jammer localization. These functions are performed by processing software via control from either the interface software or the system user. In the operational mode, data would be first collected then tested for jamming. If jamming were not present then it would be used for calibration. If jamming were present, then jammer location would be deduced from the data. Understanding of the GIDL software is predicated on the solution of each of these problems.

5.4 Calibration by GPS in detail

A number of operations must be performed to calibrate GIDL using GPS signals. The theory of GIDL calibration via GPS signals is described in Section 4.4. This section considers the actual implementation details.

Figure 5.2 shows an outline of the GIDL calibration process. After calibration data has been collected (either directly or because it was determined that no jammer is present) data from the Garmin GPS receiver, is also logged to disk. This information which includes a precise time stamp, the satellites in view and their ephemerides, is then used to calculate the precise location of the GPS satellites and the Doppler frequency shift for each satellite due relative motion. Then knowledge of the exact GIDL antenna locations¹ is utilized in order to calculate expected propagation delay of the signal from each SV along the each baseline

¹To reduce the scope of this work the exact GIDL antenna locations have been determined by survey GPS receivers, but it is anticipated that GIDL software can also perform this function, making the system completely self-calibrating.

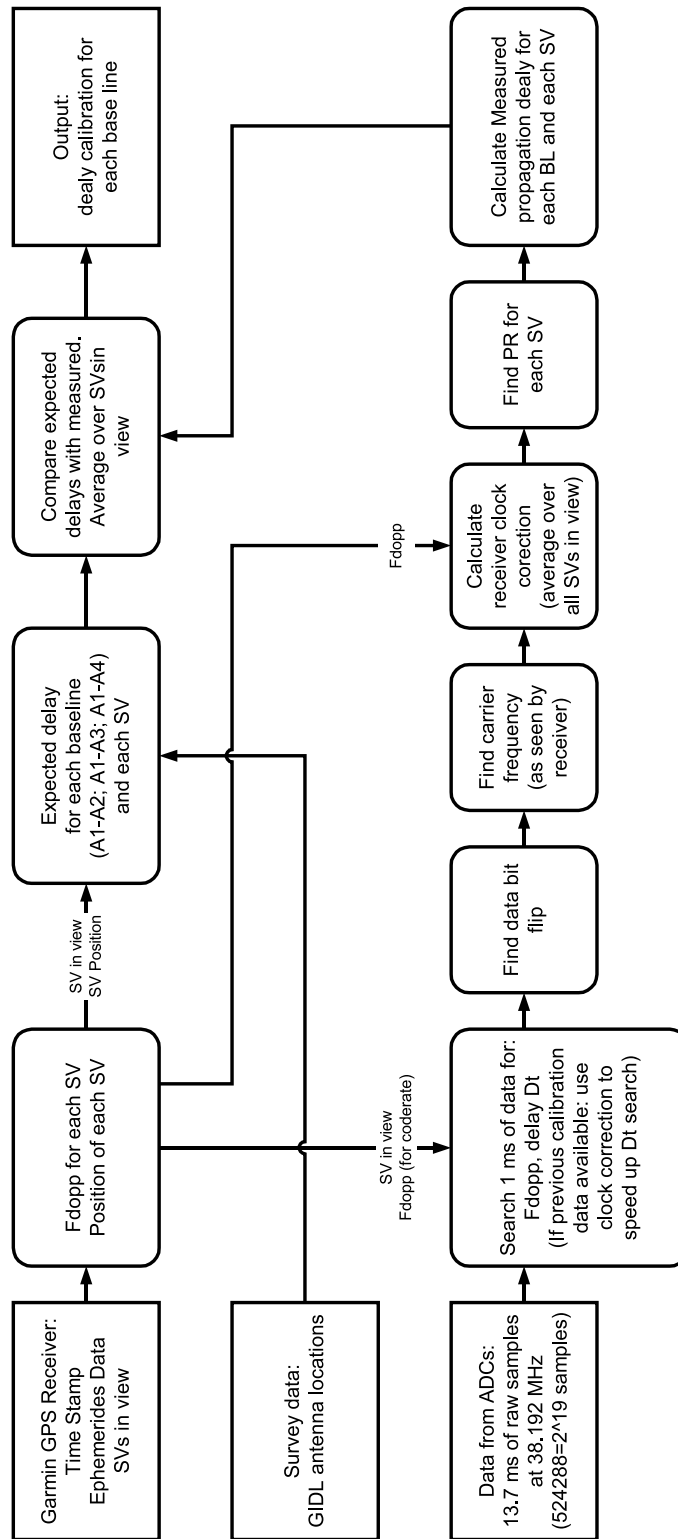


Figure 5.2: Calibration by GPS: overview of the process

```

% Constants
c = 299792458.0; % Speed of light, m/s
fs = 38192000; % Nominal Sampling frequency, Hz
L1 = 1575420000; % Frequency of L1, Hz

% Loading antenna locations in ENU coordinates. Format of the file Ant_Locations_ENU.dat
% is the following: First line is " 0 0 0 0", i.e. Master Antenna is located at the
% origin; second, third and fourth lines are location of the Ant. #2, #3, #4 in ENU
% coordinates relative to Ant. #1. (meters)
load Ant_Locations_ENU.dat
AntLocENU = Ant_Locations_ENU'; % Antenna locations are vectors, i.e. columns
clear Ant_Locations_ENU

% Loading ant. locations in XYZ coordinates. Format of the GIDL_Ant_Locations_XYZ.dat
% is the following: first line is location of Antenna #1 (Master) in XYZ WGS84,
% i.e. absolute location of the antenna, second, third and fourth lines -
% location of the Ant. #2, #3, #4 in XYZ relative to Antenna #1. (meters)
load Ant_Locations_XYZ.dat
AntLocXYZ = Ant_Locations_XYZ'; % Antenna locations are vectors, i.e. columns
clear Ant_Locations_XYZ

% Loading Garmin data file
load garmin.dat
% Format of the file: each line contains:
% gps_tow rcvr_tow rcvr_wn num_sv_in_viw fix(xD) (ephemeris)
% (ephemeris) are: svid toc toe af0 af1 af2 ura e sqrt_a dn m0 w omg0 i0
%
%          odot idot cus cuc cis cic crs crc iod
% Number of lines in the file would correspond to the number of tracked SVs
[NSV, n] = size(garmin); % NSV - how many Satellites are tracked
GPSTime = garmin(1, 1); % GPS time, sec
WN = garmin(1,3); % GPS Week number

% Let's calculated expected delays for each baseline:
% A1-A2; A1-A3; A1-A4, and for each satellite in view.
% Let's also calculate a Doppler frequency for each satellite in view.
for k=1:NSV,
    PRN(k) = garmin(k,6);
    % let's get ephemerides for the tracked SV:
    eph(1) = garmin(k,1);
    eph(2:24) = garmin(k, 6:28);
    % Solve for position of satellite
    Ttr = eph(1); % Time of transmission of the signal from SV (Ttr = Tor - PR/c;)
    [Xsat(:,k), Trel(k)] = satpos(eph, Ttr); % Find location of SV
    [XsatOld, TrelOld] = satpos(eph, Ttr-1); % Find location of SV one second ago

    Ant1toSV = Xsat(:,k) - AntLocXYZ(:,1); % Vector from Ant1 (master antenna) to SV
    % Let's make it to be a unit vector:
    Ant1toSVU = Ant1toSV/sqrt(Ant1toSV(1)^2 + Ant1toSV(2)^2 + Ant1toSV(3)^2);

    % "Doppler Velocity" - velocity of SV towards Ant #1: (See Blue book p. 411)
    Vdopp(k) = -(Ant1toSVU)*(Xsat(:,k)-XsatOld); % m/s
    Fdopp(k) = Vdopp(k)*L1/c; % Doppler frequency, Hz <-----

    % Now let's find projection of the BLs on LOS, this would correspond to the
    % delay in the signal received in Ant #2 with respect to ant1
    % if Delay < 0 Slave Ant. Receives signal before Ant #1 (Master)
    % Delay measured in meters <-----
    Delay(1,k) = -1*(Ant1toSVU' * (AntLocXYZ(:,2))); % AntLocXYZ(:,k) is location <-----
    Delay(2,k) = -1*(Ant1toSVU' * (AntLocXYZ(:,3))); % of slave antenna with <-----
    Delay(3,k) = -1*(Ant1toSVU' * (AntLocXYZ(:,4))); % respect to Ant #1. <-----
end

```

Figure 5.3: Calculation of SV Doppler frequency and expected propagation delay

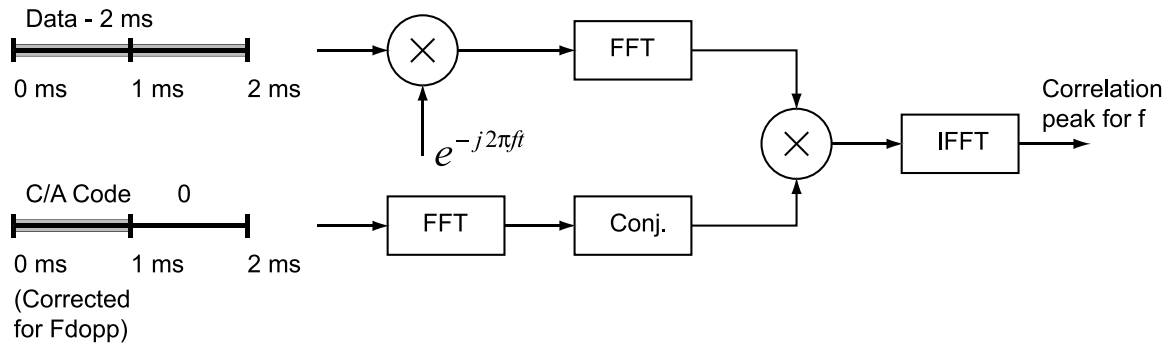


Figure 5.4: Process of initial "1 ms" search for correlation

from the master antenna (A1) to each other antenna (A2, A3, A4). These operations are standard, and the MATLAB source code to perform them is shown in Figure 5.3 (note that the arrows in the code points to the results of the segment shown).

After obtaining the expected delay for each satellite in view and base line combination, the actual delays have to be measured. In order to get these actual delay measurements and to calibrate the receiver master clock, the following operations have to be done. First, the leading millisecond of data is searched for the presence of the GPS signal. Second, the whole data set is searched for the presence of the data bit flips. Third, the whole data set is utilized to find the residual GPS carrier frequency, and by knowing the Doppler frequency of the satellites in view, the system clock is then calibrated. Fourth, precise pseudorange (PR) is calculated using the entire data set. Lastly, by subtracting the obtained PR, the measured differential delay is calculated. Now I will consider each of these steps in detail.

5.4.1 Initial Search of Frequency/Time space for presence of GPS Signal

This initial frequency/time space search is equivalent to initial signal acquisition performed by a regular GPS receiver. The difference is that this search is done on the same data for all possible delays and frequencies. An outline of the process is shown in Figure 5.4, and code to perform this search is shown in Figure 5.5. It is assumed that the Doppler frequency of the signal is known, and that the antennae are stationary. Although these assumptions improve accuracy and performance, they are not necessary for this section of the code to

```

% Sampled data is in data variable, it has length of 2^19 samples
% Fdopp - Doppler frequency for the given PRN, from time and ephemerides data
% Some constants and assumptions:
Fref = 16368000; % Hz, Reference oscillator frequency
satprn=PRN;      % Set PRN number to search
fs=38192000;     % Sampling frequency, Hz
fc=38192000/4;   % Resulting carrier frequency Hz;
maxdop=8000;     % Maximum Possible Doppler in Hz
dopbinwid= 250;  % Initial Doppler Bin Width in Hz
L1 = 1575420000; % Hz, L1 GPS Frequency
Fref0 = 16368000; % Hz, nominal frequency for ref. oscillator

% Let's do Frequency/time delay space search for the rough estimate of the
% GPS signal. (Trying to find GPS signal)
NS1ms = round(fs/1000); % Number of samples in 1 ms

stime=[0:1:(2*NS1ms-1)]/fs; % time scale : 2 ms
data = (data-(mean(data))); % subtract off dc component, if exists
gpsdata = data(1:2*NS1ms); % Take first 2 ms of data
coderate = (L1+Fdopp)/1540; % Actual code rate, corrected for Doppler
cacode = zeros(1, 2*NS1ms);
cacode(1:NS1ms) = cacode4(satprn, fs, NS1ms, coderate, 0); % Generate 1 ms (1 CA epoch)
freqcaconj=conj(fft(cacode));

if CalFlag ~= 1,
    lockdet=zeros(NS1ms,round(2*maxdop/dopbinwid+1)); % 38192 samples = 1 ms
    inda=1;
    % Starting First Search by fft:
    for freq=(fc-maxdop):dopbinwid:(fc+maxdop)
        mixgps =gpsdata .* exp(-i*2*pi*freq*stime);
        freqgps=fft(mixgps);
        outinter=ifft( freqgps .* freqcaconj );
        lockdet(:,inda)=((abs(outinter(1:NS1ms))))';
        inda=inda+1;
    end
    doppfreq = (fc-maxdop):dopbinwid:(fc+maxdop);
    [y,k]=max(lockdet);
    [yy,ii]=max(y);
    freqoffset=doppfreq(ii); % Frequency bin
    IF2 = freqoffset; % Found carrier frequency <-----
    % Let's find max_to_2nd_max: relation of the maximum to the 2-nd maximum
    max_to_2nd_max = MaxTo2ndMax(lockdet(:,ii), fs);
    if max_to_2nd_max < sqrt(5), % should be 5 for lockdet,~2
        return; % no more processing is necessary, we have a weak signal
    end

clear stime gpsdata cacode freqcaconj mixgps freqgps outinter
% Repeat everything one more time, to find PR, using correct frequency
stime=[0:1:(2^19-1)]/fs; % time scale
gpsdata = data(1:2^19);
cacode = zeros(1, 2^19); % log(2*NS1ms)/log(2) = 16.22 ~ 17
cacode(1:NS1ms) = cacode4(satprn, fs, NS1ms, coderate, 0); % Generate 1 ms of CA code
freqcaconj=conj(fft(cacode));
freq = IF2;
mixgps =gpsdata .* exp(-i*2*pi*freq*stime);
freqgps=fft(mixgps);
outinter=ifft(freqgps .* freqcaconj);
[y kk] = max(abs(outinter));
kk1 = mod(kk, 38192); % kk1 is the corr. peak maximum, or PR in samples <-----

```

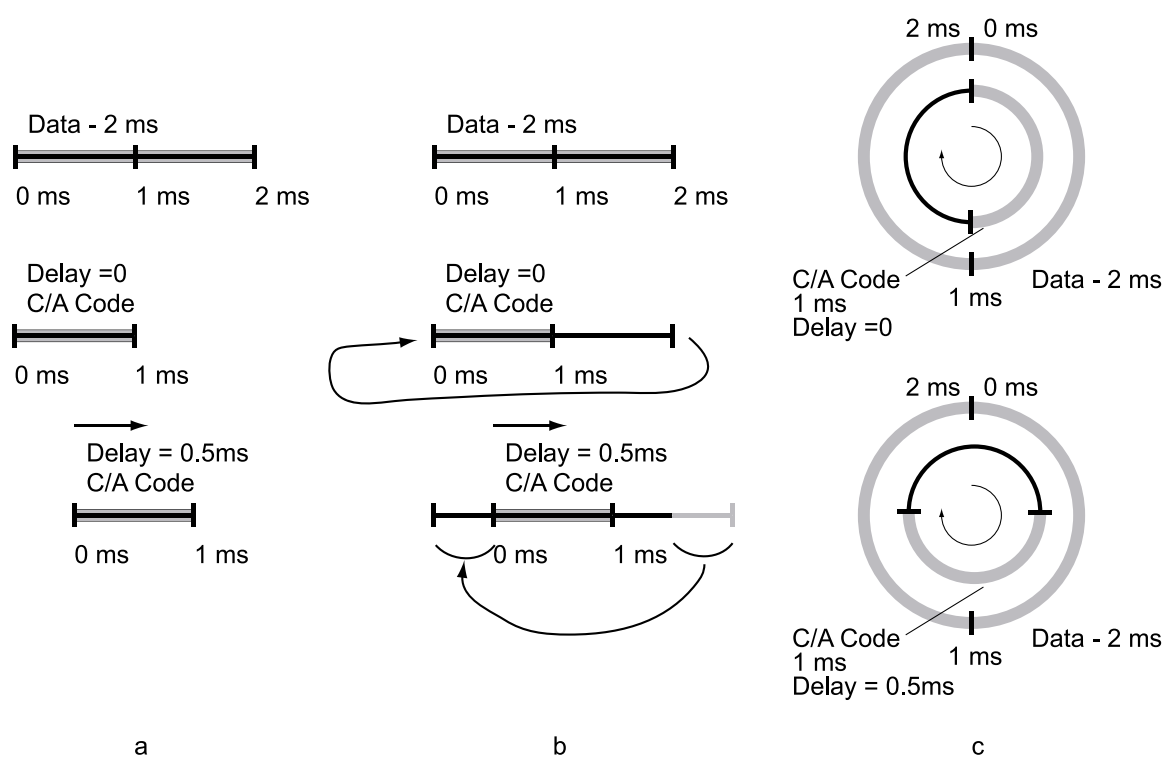
Figure 5.5: MATLAB code to search 1(2) ms of data for Doppler frequency and C/A code offset

operate.

A frequency/time search is performed in parallel in time delay domain, utilizing the FFT technique outlined in Section 4.3.2, and in series in frequency domain. The serial frequency domain search is done in steps of 250 Hz, and in the range of ± 8 kHz of the nominal center frequency. The chosen frequency search steps guarantee that when the search is completed and signal found, its apparent Doppler frequency would be known to within 250 Hz. This apparent Doppler frequency consists of two components. One is due to the real Doppler frequency of the signal, and the other due to errors in the receiver frequency. These frequency search numbers can be changed. The first number is defined by the frequency resolution that can be obtained from 1 ms of data. In theory it should be on order of 1 kHz, but in practice 250 Hz steps provide better resolution. This is explained by the fact that the actual amount of data used is more than 1 ms, as will be explained later. The frequency search window is defined by combination of possible signal Doppler frequencies and receiver clock instability.

As previously mentioned, the search is done over all possible Doppler frequencies (including receiver clock imperfections). To form in-phase and quadrature channels in complex form the input signal is multiplied by the carrier frequency ($\exp(-j2\pi ft)$). Here “ f ” is the residual carrier frequency plus possible frequency offsets. The span of which is searched for the correct offset. If this frequency were correct, perfect in-phase and quadrature signals would be formed. On each search step, a signal with this frequency is correlated to obtain the baseband signal (in-phase and quadrature channels) with the C/A code in order to obtain a correlation peak. The correlation peak is used for signal detection.

Because the GIDL receiver software already has the correct Doppler frequency for the signal coming from satellite, the C/A code rate is corrected by this frequency. For a 1 ms search it is an insignificant correction, but when the correlation is over 12 ms this correction provides some improvement to the frequency and delay measurement. Nominally the C/A code rate is 1.023 MHz, and it is coupled with the satellite carrier frequency. Due to the Doppler effect the satellite carrier frequency changes as seen from the ground, this causes a slight change in the C/A code rate. One can think about it as C/A code chip contains specified number of carrier cycles, and as carrier cycles compress or stretch so does C/A code.

**Figure 5.6:** Correlation and Circular correlation

In order to find the correlation peak, it is necessary to correlate baseband data with a local replica of the C/A code. To visualize this process, assume that we have 2 ms of the data available, and 1 ms (1 epoch) of the C/A code. To form a correlation we would slide this 1 ms of C/A code over the data, as shown in Figure 5.6a, and multiply the overlapping data and C/A code to compute a sum. By sliding it over all 2 ms of data we would get 1 ms of the correlation peak. This process is very computationally intensive. Now let's assume that we have same 1 ms of C/A code padded by zeros to form 2 ms sequence, shown in Figure 5.6b, and we do circular correlation.

After performing this circular correlation we would get 2 ms of the correlation. The first ms of this data is identical to the data that we obtained by sliding 1 ms of the C/A code. The representation of this correlation in circular form is in Figure 5.6c. If the circular correlation is performed as described it is also computationally inefficient. However, there is a way to efficiently calculate circular correlation. Regular correlation is really needed in order to obtain the correlation peak, but the first half of the circular correlation is equivalent to the regular correlation. This exact approach is implemented in GIDL calibration algorithm: a double length of the data is taken, and a length of C/A code is generated and padded by zeros to form two lengths. The circular correlation is computed and only the first half of it is taken as the real correlation.

The efficient way to compute circular correlation is by using the Fast (Discrete) Fourier Transformation (F(D)FT). Let us assume that we have two sequences $x_1[n]$, and $x_2[n]$. According to [156] circular convolution of these two sequences is

$$x_1[n] * x_2[n] = \sum_{m=0}^{N-1} x_2[m] x_1[(n-m)_N], \quad (5.1)$$

here $(\cdot)_N$ is modulus N . Correlation has the following property:

$$x_1[n] * x_2[n] \xleftrightarrow{DFT} DFT(x_1[n]) \cdot DFT(x_2[n]). \quad (5.2)$$

It is also possible to show that

$$IFFT(Conj(FFT(x_1[n]))) = x_1[(N-n)_N]. \quad (5.3)$$

From the last two equations it follows that circular correlation has the property:

$$\sum_{m=0}^{N-1} x_2[m] x_1[(m-n)_N] =$$

$$\sum_{m=0}^{N-1} x_2[m]x_1[((N - (n - m)))_N] \xleftrightarrow{DFT} DFT(x_1[n]) \cdot Conj(DFT(x_2[n])) \quad (5.4)$$

or

$$\sum_{m=0}^{N-1} x_2[m]x_1[((m - n))_N] = IFFT[DFT(x_1[n]) \cdot Conj(DFT(x_2[n]))]. \quad (5.5)$$

This property is used to efficiently calculate the circular correlation of the data and C/A code. By clever zero padding and throwing away the second half of the circular correlation, this correlation becomes plain linear correlation but efficiently computed.

For each frequency in the search region this correlation is computed and the maximum value is stored. When the search over all frequencies is completed, the table of corresponding maximum value of the correlation is examined. Then a simple maximum search is done over these maximums to find the corresponding frequency. This frequency is assumed to be the right carrier frequency (including clock errors). Lastly one more correlation that uses this frequency is calculated and location of the maximum of correlation peak is found. This location is the delay of the received C/A code expressed in number of samples, or PR (expressed in number of samples).

Another consistency check on the data is done. The absolute maximum of the first peak is compared to the second maximum. If this second maximum is significantly smaller than the previous maximum, the data is flagged as valid. If these maximums are close to each other, the data is not used for further processing.

Summarizing, this first step of the GIDL calibration algorithms finds a rough estimate of the carrier frequency as it seen by the receiver, and delay of the C/A code in the received data for each satellite in view. This data is refined in the next steps of calibration process and finally used to calibrate the GIDL receiver.

5.4.2 Detection of the GPS data bit flips in the collected data

The C/A code GPS signal is modulated by almanac data, which arrives at rate of 50 Hz or one data bit in 20 ms. Data bit flips happens synchronously with C/A code epochs. If one were to try to correlate more than one epoch of the C/A code with the data, there is a chance that a data bit flip would happen in the middle of the data, and no correlation

```

% Let's try to find data bit flip

stime=[0:1:(2^19-1)]/fs; % time scale
gpsdata = data(1:2^19); % Raw data from ADC is in data
cacode = zeros(1, 2^19); % log(2*NSims)/log(2) = 16.22 ~= 17
cacode(1:NSims) = cacode4(satprn, fs, NSims, coderate, 0); % Generate 1 ms
                                                    % (1 epoch of CA code)

freqcaconj=conj(fft(cacode));
freq = IF2; % Carrier frequency from the Code/Freq. Search step
mixgps =gpsdata .* exp(-i*2*pi*freq*stime);
freqgps=fft(mixgps);
outinter=ifft(freqgps .* freqcaconj);
[y kk] = max(abs(outinter));
kk1 = mod(kk, 38192); % C/A delay or pseudorange in samples

nn = [ 0:1:11];
peak = outinter(kk1+nn*NSims); % Contains all the correlation peaks
peak_angle = unwrap(angle(peak));
jump_det = peak_angle(2:12)-peak_angle(1:12-1);
jump_det = jump_det-mean(jump_det);
jump_det_bin= abs(round((jump_det * 180/pi)/100)); % Detect jumps of 100 deg. or more
jump_det_bin(jump_det_bin ~=0) = jump_det_bin(jump_det_bin ~=0)./ ... % <-----
                                                    jump_det_bin(jump_det_bin ~=0); % <-----
% Now jump_det_bin contains '1' in the epoch when new data bit starts % <-----

```

Figure 5.7: MATLAB code to detect data bit flips occurrence in the data

could be obtained. In order to utilize and correlate all the data obtained by the GIDL it is necessary to find data bit flip occurrences in the collected data. Because the sample length is 13.7 ms, and the data bit length is 20 ms, no more than one data bit flip could have occurred in the duration of the data sample.

To find data bit flips the same idea of circular correlation is used. The MATLAB code used to find data bit flips is present in Figure 5.7. For this process, all the collected data is utilized. The processing scheme is very similar to the one shown in Figure 5.4, with the difference that data length now is 13.7 ms and C/A code present for the first millisecond and then padded by zeros to form data set 13.7 ms in length. The raw data is mixed with complex carrier frequency. The frequency used for mixing is found in the first step of the processing algorithms and is known within 250 Hz from actual carrier frequency. After mixing, the baseband signal is correlated with the C/A code. The result of the correlation is the complex correlation peaks that retain phase information. A typical example of how I and Q channel data looks like is shown in Figure 5.8. Phasor angle is computed for each correlation peak. (This operation can be interpreted as sampling residual carrier frequency left in the signal at the baseband after mixing with a frequency of 1 kHz, determined from the length of 1 C/A code epoch. No aliasing would happen during this operation, because

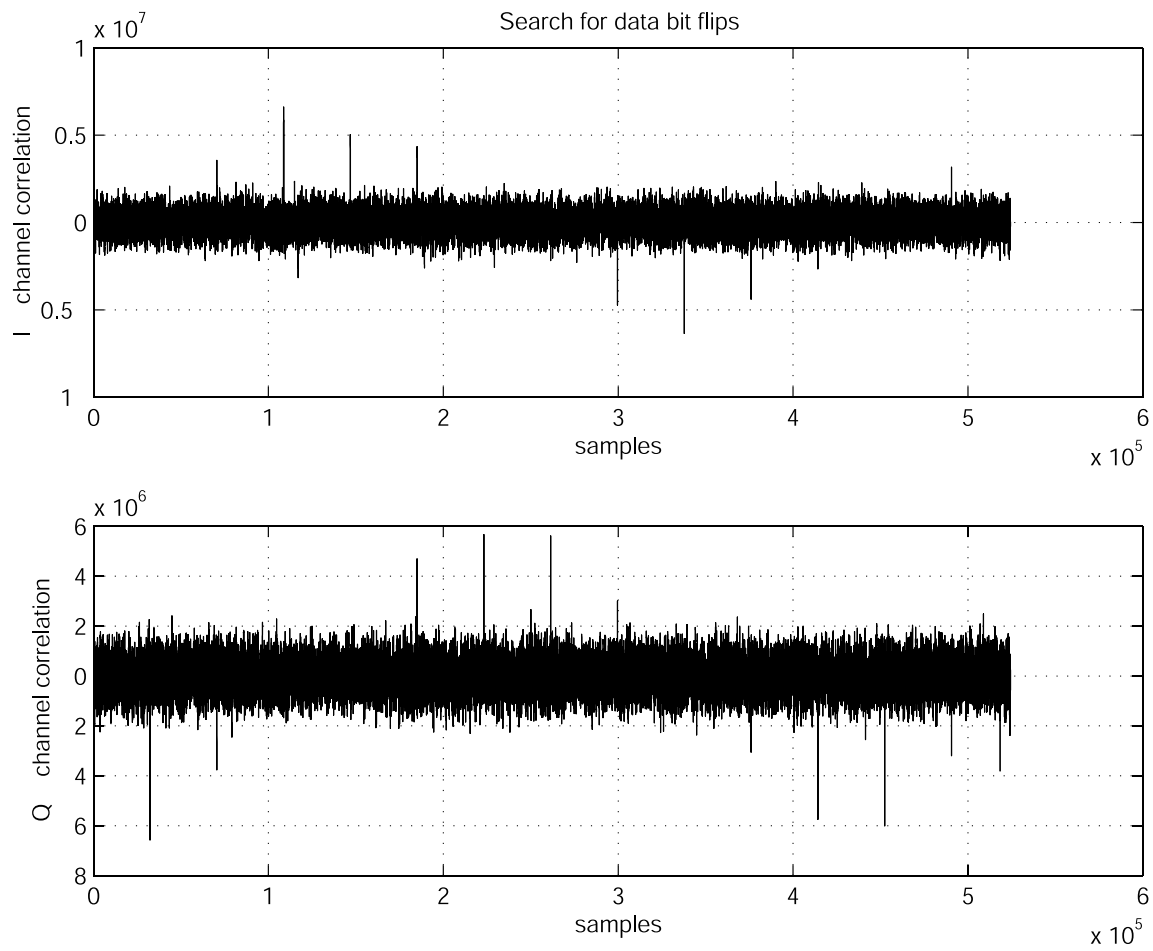


Figure 5.8: Typical complex correlation peaks for data bit flips detection

```

% Let's find carrier:
% size(cacode) = 38192, or 1 epoch, let's form 12 epochs of CA code:
% Out of 13.7 ms we can get for sure 12 full epochs
cacode1 = cacode4(satprn, fs, NSims*12, coderate, 0);
data_pol = 1;
for nepch=2:12,
    if jump_det_bin(nepch-1),
        data_pol = data_pol *(-1);
    end
    cacode1(1+NSims*(nepch-1):NSims*nepch) = data_pol * ...
        cacode1(1+NSims*(nepch-1):NSims*nepch);
end

postfft = fft(cacode1(1:12*NSims).* data(k(ii):12*NSims+k(ii)-1));

freqvec = (0:1:12*NSims-1)*fs/(12*NSims);
[fy fi] = max(abs(postfft(1:6*NSims)));
fft_freq = freqvec(fi);

% Let's find error in reference oscillator frequency:
DeltaFref = (L1+Fdopp-Fref0*287/3-fft_freq)*3/287; % <-----
fs_corr = (Fref0 + DeltaFref)*7/3;
freqvec_corr = (0:1:12*NSims-1)*fs_corr/(12*NSims);
fft_freq_corr = freqvec_corr(fi);

% Second order correction, DeltaFref should be good to 1e-3Hz
DeltaFref = DeltaFref+(L1+Fdopp-(Fref0+DeltaFref)*287/3-fft_freq_corr)*3/287; % <-----
fs_corr = (Fref0 + DeltaFref)*7/3;
freqvec_corr = (0:1:12*NSims-1)*fs_corr/(12*NSims);
fft_freq_corr = freqvec_corr(fi);

```

Figure 5.9: MATLAB Code to find master clock offset, and all relevant frequencies

the residual frequency is less than 250 Hz, and “sampling” frequency is 1 kHz.). The phasor angle is unwrapped such that there are no discontinuities at 0 and 2π radians. This data is then examined for discontinuities of approximately π radians. If no data bit flips occurred during the collected data sample, the phasor angle forms a monotonic curve, which should be close to a straight line. If a data bit flip happens then this line has a step at the occurrence.

Information about where the data bit flip occurred is stored and passed to the next step of the calibration algorithm. It will be used to form a C/A code sequence that can be correlated with the entire acquired data sequence. At the data bit flip occurrence the polarity of the generated C/A code would be reversed, as a match for the GPS data.

5.4.3 Carrier frequency calculation and master clock calibration

After executing the first and second steps of the calibration algorithms, we know the approximate value of the carrier frequency, approximate value of the C/A code delay (or pseudorange) and information about data bit flips in the collected data sample. At this step of the calibration routine, the exact value of the carrier frequency will be calculated, and the reference oscillator (or master clock) error also will be calculated, and used to calculate all system frequencies. This knowledge of the frequencies will later be used to find the best estimate of the pseudorange. It will also be used to calibrate GIDL timing for jammer localization. MATLAB code to calculate clock calibration is shown in Figure 5.9.

Initially, the carrier frequency of the GPS signal is determined as best as possible in terms of the internal clock frequency. In 13.7 ms of collected data it is possible to locate 12 full C/A code epochs. These twelve epochs are used to obtain an estimate of the carrier frequency. First twelve epochs of the C/A code (corrected for the satellite Doppler frequency shift) are generated. This sequence is corrected for the detected data bit flip (if one exists in the collected data sample). This combination of the C/A code and data (which is the spreading code for the GPS signal, and the despreading code in the receiver) is then multiplied by the sampled signal, effectively despreading it. In the ideal case, the result is the pure reconstructed carrier. In the case of a real signal, this reconstructed carrier contains noise. This is, however, the best estimate of the carrier that can be obtained from the available data. This reconstructed carrier is Fast Fourier transformed into the frequency domain and the maximum is extracted, which corresponds to the carrier frequency (Figure 4.5). The resolution of this frequency measurement equals the sampling frequency divided by the number of samples in the data set (12 epochs of 1 ms each: $\text{Resolution} = 38.192\text{MHz}/(12 \cdot 38192) = 83.33\text{Hz}$). The frequency of the reconstructed carrier, as seen by the receiver is known to within this accuracy (assuming the receiver master clock is perfect).

It is possible to use this data to calibrate the reference oscillator of the receiver. The frequency plan of the GIDL receiver is discussed in Section 3.3.2, and the system clock diagram is shown in Figure 3.11. Assume that the reference oscillator (TCXO) has some

error in generated frequency (this is the error we wish to calibrate): $f_{ref} = f_{ref0} + \Delta$. This frequency is used to generate the master or Local Oscillator (LO) frequency:

$$LO = \frac{280}{3}(f_{ref}) = \frac{280}{3}(f_{ref0} + \Delta), \quad (5.6)$$

and sampling frequency in turn is derived from this common frequency:

$$f_{sampl} = \frac{1}{40}LO = \frac{1}{40}\frac{280}{3}(f_{ref0} + \Delta) = \frac{7}{3}(f_{ref0} + \Delta). \quad (5.7)$$

From the frequency plan of the GIDL receiver it follows that the first intermediate frequency is: $IF_1 = (L_1 + F_{Dopp}) - LO$, where L_1 is nominal GPS carrier frequency of 1.57542 GHz, and F_{Dopp} is Doppler frequency offset due to satellite motion. The second Intermediate frequency is obtained after sampling signal with aliasing (bandpass sampling) as described in Section 3.1.4:

$$\begin{aligned} IF_2 &= IF_1 - f_{sampl} = (L_1 + F_{Dopp}) - \frac{280}{3}(f_{ref0} + \Delta) - \frac{7}{3}(f_{ref0} + \Delta) \\ &= (L_1 + F_{Dopp}) - \frac{287}{3}f_{ref0} - \frac{287}{3}\Delta \end{aligned} \quad (5.8)$$

For the nominal GPS carrier frequency and local oscillator the GIDL frequency plan is designed in such a way that GPS frequency would alias to the quarter of the sampling frequency, i.e.:

$$L_1 - \frac{287}{3}f_{ref0} = \frac{1}{4}\left(\frac{7}{3}f_{ref0}\right) \quad (5.9)$$

or

$$L_1 = \frac{287}{3}f_{ref0} + \frac{1}{4}\left(\frac{7}{3}f_{ref0}\right) = \frac{385}{4}f_{ref0} \quad (5.10)$$

Substituting this expression into expression for IF_2 one obtains:

$$\begin{aligned} IF_2 &= (L_1 + F_{Dopp}) - \frac{287}{3}f_{ref0} - \frac{287}{3}\Delta \\ &= F_{Dopp} + \frac{287}{3}f_{ref0} + \frac{1}{4}\left(\frac{7}{3}f_{ref0}\right) - \frac{287}{3}f_{ref0} - \frac{287}{3}\Delta \end{aligned} \quad (5.11)$$

From this, we find

$$IF_2 = F_{Dopp} + \frac{1}{4}\left(\frac{7}{3}f_{ref0}\right) - \frac{287}{3}\Delta. \quad (5.12)$$

Solving for Δ and using expression 5.9 for L_1 :

$$\Delta = \frac{3}{287} \left(F_{Dopp} + \frac{1}{4} \left(\frac{7}{3} f_{ref0} \right) - IF_2 \right) = \frac{3}{287} \left(F_{Dopp} + L_1 - \frac{287}{3} f_{ref0} - IF_2 \right). \quad (5.13)$$

In this equation F_{Dopp} is known, it is calculated from the satellite-antenna geometry. L_1 is also known and constant. f_{ref0} again is a known constant. IF_2 is measured, as previously described.

How accurate is the measurement of IF_2 , if the exact reference frequency is unknown? The actual sampling frequency is: $f_{sampl} = \frac{7}{3}(f_{ref0} + \Delta)$. The resolution of the FFT frequency measurement from 12 epochs of data is equal to

$$\frac{f_{sampl}}{N} = \frac{\frac{7}{3}(f_{ref0} + \Delta)}{12 \cdot 38192}.$$

To the first approximation it is still 38192 samples per 1 ms, thus

$$\frac{f_{sampl}}{N} = \frac{38192000 + \frac{7}{3}\Delta}{12 \cdot 38192} = \frac{1000}{12} + \frac{7}{3 \cdot 12 \cdot 38192}\Delta = 83.33 + 5.1 \cdot 10^{-6}\Delta.$$

From this expression it follows if Δ relatively small, on order of few hundred Hz (assured by the use of a TCXO), then the error in the IF_2 measurement due to the error in the TCXO is negligible.

Actual code to implement these calculations is shown in Figure 5.9. The first few lines of the code compute an estimate of the IF_2 . Then the correction to the TCXO is calculated. This process is iterated twice to improve convergence on IF_2 . This iteration could be continued, but it has been demonstrated in practice to converge after the second step, so no further calculation loops have been implemented.

This process is repeated for the each satellite in view and for the each GIDL channel. All individual clock error measurements are averaged over a whole ensemble to form a combined estimation of the TCXO correction.

5.4.4 Precise PR estimation and differential delay calculation

At this point in the process, all necessary data is available to find the best possible pseudorange estimate from the data. MATLAB code to perform this operation is shown in


```

% Let's find pseudorange as good as we can...

% Now using corrected values for fs, fft_freq, etc
fft_freq = fft_freq_corr;
NS1ms = round(fs_corr/1000); % Number of samples in 1 ms
stime=[0:1:(2^19-1)]/fs_corr; % New time scale
IF2 = L1 + Fdopp - (Fref0+DeltaFref)*287/3; % Including aliasing

% Let's find absolute max of the correlation peak in steps of 0.1 sample rate
cacode = zeros(1, 2^19);
outinter10 = zeros(10, NS1ms);
delay10 = zeros(10);
indd = 1;

gpsdata(1:2^19) = data;
mixgps =gpsdata .* exp(-i*2*pi*IF2*stime);
freqgps=fft(mixgps);

for delay = 0:0.1:0.9,

    delay10(indd) = delay;

    % Using 12 periods of CA code:
    cacode(1:round(12*fs_corr/1000)) = ...
        cacode4(satprn, fs_corr, round(12*fs_corr/1000), coderate, delay/fs_corr);

    % Need to correct CA code for data bit flips.
    % In this correction algorithm I can misplace up to ~2 samples
    % on the wrong side of the data bit. Should be insignificant
    data_pol = 1;
    for nepch=2:12,
        if jump_det_bin(nepch-1),
            data_pol = data_pol *(-1);
        end
        cacode(1+NS1ms*(nepch-1):NS1ms*nepch) = data_pol * ...
            cacode(1+NS1ms*(nepch-1):NS1ms*nepch);
    end

    freqcaconj=conj(fft(cacode));
    outinter=ifft(freqgps .* freqcaconj);
    outinter10(indd,:) = outinter(1:NS1ms); % Maximum for the given delay
    indd = indd + 1;
end % for delay

[y10 k10] = max((abs(outinter10.')));
[y k] = max(y10);
code_offset = k10(k)-1-delay10(k); % Code lock offset or PR <-----

```

Figure 5.10: Precise pseudorange estimation

Figure 5.10. First, the sampled GPS signal is mixed with the precise complex carrier signal, which is corrected for the Doppler frequency and errors in the receiver clock, to form inphase and quadrature channels. Second, a local replica of the C/A code is generated, which is corrected for the Doppler frequency and data bit flips. This C/A code is correlated with the mixed signal and correlation peak is formed. (Only 12 full C/A code epochs are used in order to simplify the code.) The maximum of the correlation peak corresponds to the best estimate of the pseudorange. Time resolution of this estimation is $1/f_{\text{sampl}} = 1/38192000 = 26.18 \text{ ns}$. Resolution can be improved. One way to improve resolution is to resample the correlation peak with a higher sampling rate. Another more natural way was implemented. This is to generate ten local replicas of the C/A code that are offset from each other by 0.1 samples, and then generate correlation peaks for the each of these replicas (replicas are sampled at the original sampling frequency, this idea is similar to the idea used in the GPS receiver correlators, where sampling rate is fixed, but C/A code can be generated with any delay to track satellite signal). The correlation with the highest peak corresponds to the best alignment of the generated C/A code and actual received code, and is taken as the best estimate of the pseudorange. If one looks only at the maximum of the correlation peak than this process is equivalent to the search of the maximum for the punctual correlator in a conventional GPS receiver; it shifts a local replica of the C/A code until a maximum is found.

The result of this process is shown in Figure 5.11. Plot on the left shows tips of the correlation peaks as “fine” delay increases from 0.0 to 0.9 samples. Plot on the right shows maximum of the obtained correlation peaks normalized to the largest maximum.

These plots has been obtained from the real data. After executing code in Figure 5.10 the following code was used to generate Figure 5.11:

```
subplot(121)
plot([32284-3:32284+3], (abs(outinter10(:,32284-3:32284+3).')), '-x');
grid
xlabel('Delay, samples')
ylabel('Correlation Mag.')
```

```
subplot(122)
plot([0:0.1:0.9], y10/max(y10), '-x')
```

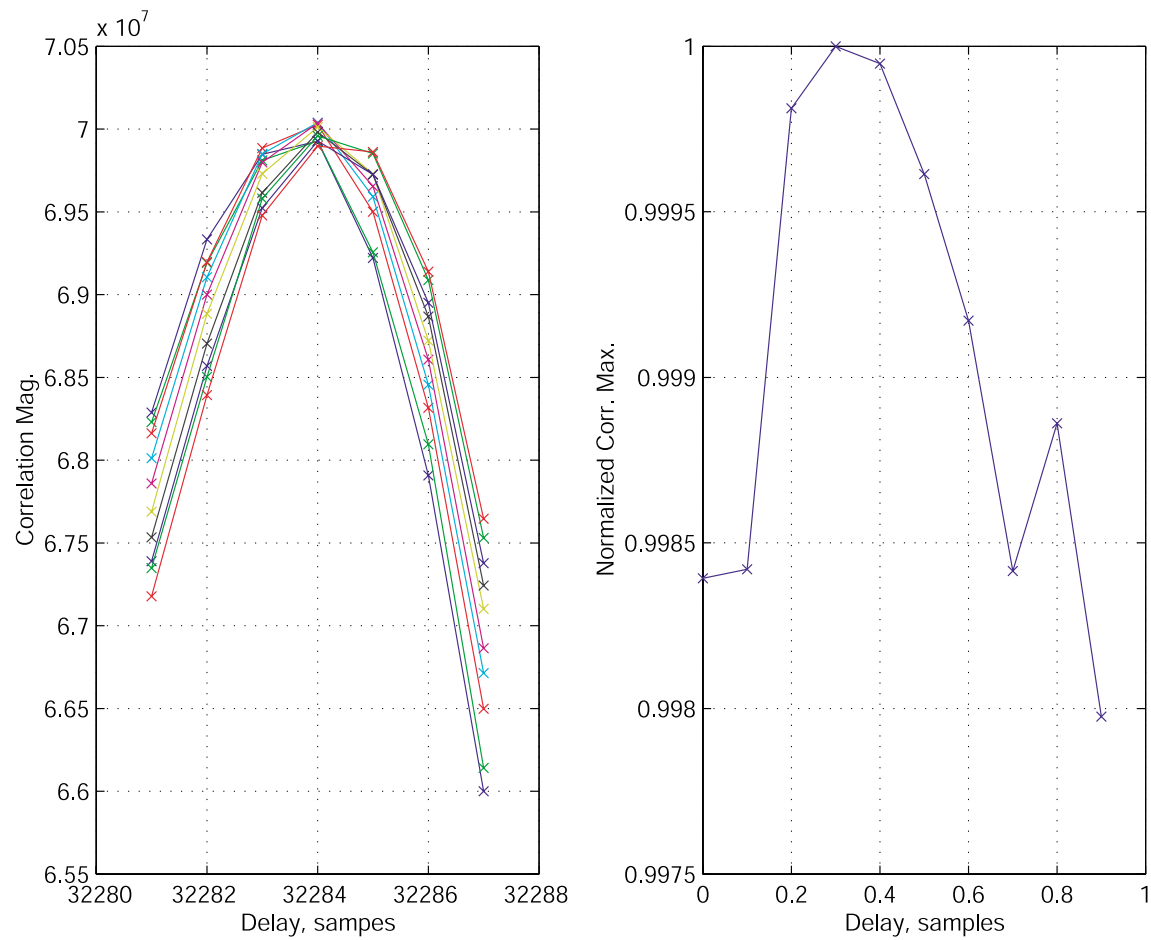


Figure 5.11: Correlation peaks and normalized maximums for the fine C/A code delay search

```

for k= 1:NSV, % Number of SV in view

% As PR using maximum of the correlation peak
Mes_Delay_M_m(1,k) = c*(code_offset(2,k) - code_offset(1,k))/fs_corr(1,k);
Mes_Delay_M_m(2,k) = c*(code_offset(3,k) - code_offset(1,k))/fs_corr(1,k);
Mes_Delay_M_m(3,k) = c*(code_offset(4,k) - code_offset(1,k))/fs_corr(1,k);

Error_M(1,k) = Delay(1,k) - Mes_Delay_M_m(1,k);
Error_M(2,k) = Delay(2,k) - Mes_Delay_M_m(2,k);
Error_M(3,k) = Delay(3,k) - Mes_Delay_M_m(3,k);

end %k

% Calibration coefficient, or system delays for the each BL
Delays(1) = mean(ValidError_M(1,:));
Delays(2) = mean(ValidError_M(2,:));
Delays(3) = mean(ValidError_M(3,:));

% Averaged TCXO frequency correction
DeltaFref = mean(mean(ValidDeltaFref));

% Saving calibration results:
save calibration DeltaFref Delays

```

Figure 5.12: Calibration coefficient calculation

```

grid
xlabel('Delay, samples')
ylabel('Normalized Corr. Max.')

```

This process of pseudorange estimation is repeated for each channel of the GIDL system and each satellite in view. The measured signal propagation delay for the each baseline is calculated by subtracting the master antenna (Antenna 1) pseudorange from the pseudorange for the each slave antenna (Antennae 2, 3, 4). This subtraction is done for each satellite in view also. These propagation delays for each baseline and each satellite in view constitute the required measurements for the calibration procedure.

5.4.5 Calibration Coefficient Calculation

Calibration coefficients, or GIDL system delays are calculated by subtracting the measured delay for each base line and each satellite from the calculated signal propagation delay and then averaging the results for each baseline. This process is shown in Figure 5.12. This process is repeated over several collected data sets, and the results stored and averaged.

5.5 Jammer Detection and TDOA Estimation

5.5.1 Jammer Detection

As stated in Section 2.2 the current GIDL configuration assumes that the jammer is a stationary white noise–like signal with no appreciative Doppler frequency shift between the various GIDL antennae.

The detection algorithm is optimized for this kind of a jammer. In future development of the GIDL it is anticipated that received signals would go through a number of jammer detection algorithms, each optimized for various types of jammers. This would allow jammer signal classification and then the utilization of specific localization algorithms for the specific types of jamming. To limit the scope of the thesis, only one kind of the jamming signal was considered.

The theoretical background for jammer detection is given in Section 2.2. From that discussion, it follows that in the particular case of a stationary Gaussian white noise jammer, it is enough to compute power spectral density (PSD) of the received signal and compare it with the threshold. This is precisely the algorithm that has been implemented. When data is collected, a PSD of the signal is computed in each GIDL channel individually, and then compared with the expected PSD absent a jammer. Whenever the PSD maximum is higher than PSD maximum with no jamming by approximately 3 dB, it is assumed that a jammer is present. Jammer detection is an “OR” function across all GIDL channels.

An example of the PSD of the received signal both when the jammer is absent and present is shown in Figure 5.13. Note the hump in the middle of the PSD for the case when jammer is absent (blue, or dash-dot line), this hump corresponds to the spectrum of the GPS signal or the combined energy from all the GPS satellites in view.

5.5.2 Jammer Signal TDOA Estimation

When this jammer is detected it must be located. The theory for jammer localization is discussed in Section 2.3. It follows from the theory that for the assumed jammer, it would be sufficient to estimate time differences of arrival of the jamming signal for each baseline formed by the master antenna and slave antennae, and then use these measured TDOAs

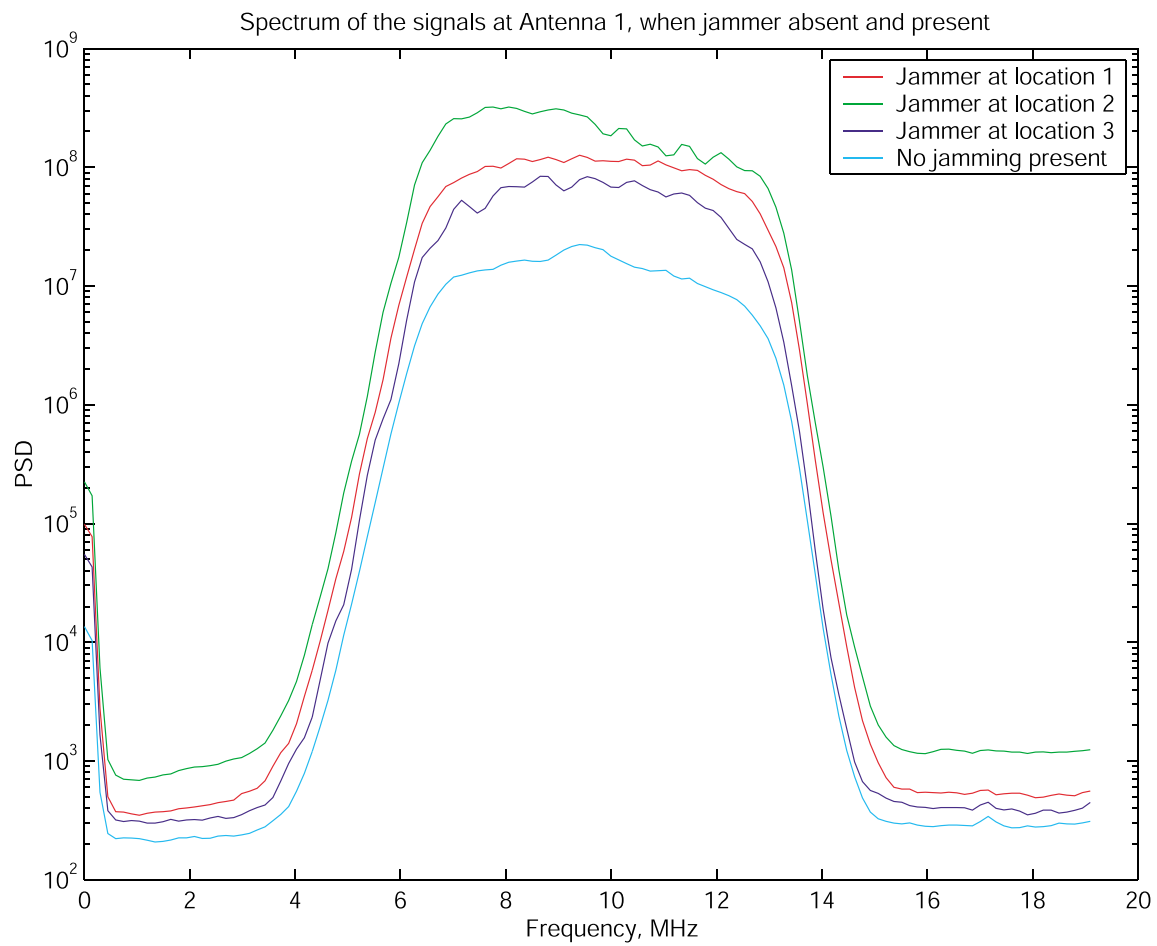


Figure 5.13: PSD of the signal in the absence and presence of the jammer

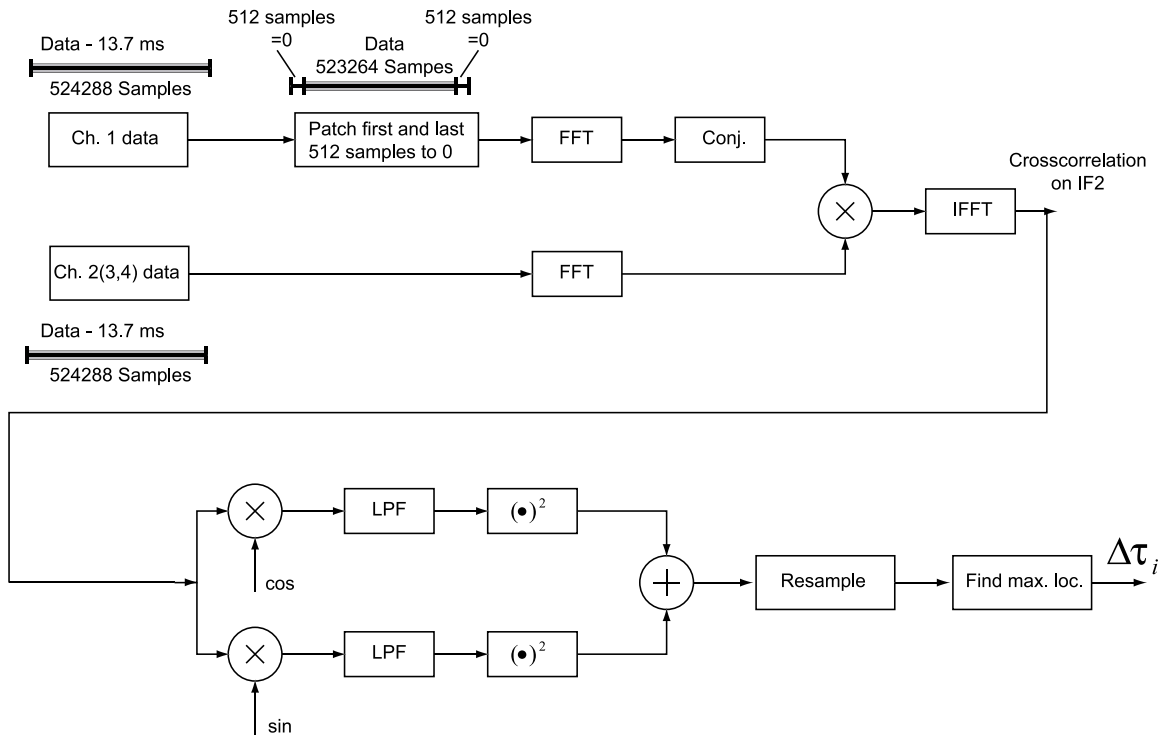


Figure 5.14: Process of the TDOA estimation for jamming signal

to locate the jammer. Coordinate transformation from the TDOAs to the range, azimuth and elevation, or to the (x, y, z) coordinates are considered in the Section 2.3, and they are generic in nature. Because there are only three TDOA measurements in the current GIDL configuration, analytical coordinate transformations from TDOA to range, azimuth, and elevation have been derived.

The most interesting part of the jammer localization is estimation of the actual TDOAs for the jamming signal. Again, from the theory chapter it follows that it could be done by simple correlation of the signals in the two channels, but in practice it is more involved than that. This section explains the actual procedure.

The process of the TDOA estimation of the jamming signal for the each baseline of the GIDL system is graphically represented in Figure 5.14, and MATLAB code to perform this process is shown in Figure 5.15.

In order to find TDOA it is necessary to calculate the correlation function between the signals in the master channel and the signals in the slave channel. The location of the

```

% fs = 38192000; % Nominal sampling frequency, Hz
fs = 38191891; % Sampling frequency after calibration
c = 299792458.0; % Speed of light, m/s

data1(1:2^19) = ICS650(1:2^19,1); % ICS650 is 524288x4 raw data array from ADCs
data2(1:2^19) = ICS650(1:2^19,2);
data3(1:2^19) = ICS650(1:2^19,3);
data4(1:2^19) = ICS650(1:2^19,4);
clear ICS650

% Let's correlate channel one data with Data from other channels I am interested
% only in correlation function near Zero delay +/- 512 samples.
data = data1;
data(1:512) = 0;
data(2^19-512+1:2^19) = 0;
datafft = fft(data);
data2fft = fft(data2);
data3fft = fft(data3);
data4fft = fft(data4);

data2dataxcorr = ifft(data2fft .* conj(datafft));
data3dataxcorr = ifft(data3fft .* conj(datafft));
data4dataxcorr = ifft(data4fft .* conj(datafft));

% Three cross-correlation functions, they are on IF.
d2dxcorr = [data2dataxcorr(2^19-512+1:2^19) data2dataxcorr(1:512)];
d3dxcorr = [data3dataxcorr(2^19-512+1:2^19) data3dataxcorr(1:512)];
d4dxcorr = [data4dataxcorr(2^19-512+1:2^19) data4dataxcorr(1:512)];

% In-phase and Quadrature components of the carrier for mixing
cosif = cos([0:1023]*pi/2);
sinif = sin([0:1023]*pi/2);

% fs/8 low pass filter. fs = 38.192 MHz; fs/8 = 4.7740 MHz
% Half a bandwidth of the signal is 6MHZ/2 = 3 MHz (IF filters are 6MHz wide)
B = fir1(1024, 0.25);

% In-phase and Quadrature components of the correlations:
I2 = cosif.*real(d2dxcorr); Q2 = sinif.*real(d2dxcorr);
I3 = cosif.*real(d3dxcorr); Q3 = sinif.*real(d3dxcorr);
I4 = cosif.*real(d4dxcorr); Q4 = sinif.*real(d4dxcorr);

% Filtered crosscorrelations:
d2dxcorr_f2 = filter2(B,I2).^2 + filter2(B,Q2).^2;
d3dxcorr_f2 = filter2(B,I3).^2 + filter2(B,Q3).^2;
d4dxcorr_f2 = filter2(B,I4).^2 + filter2(B,Q4).^2;

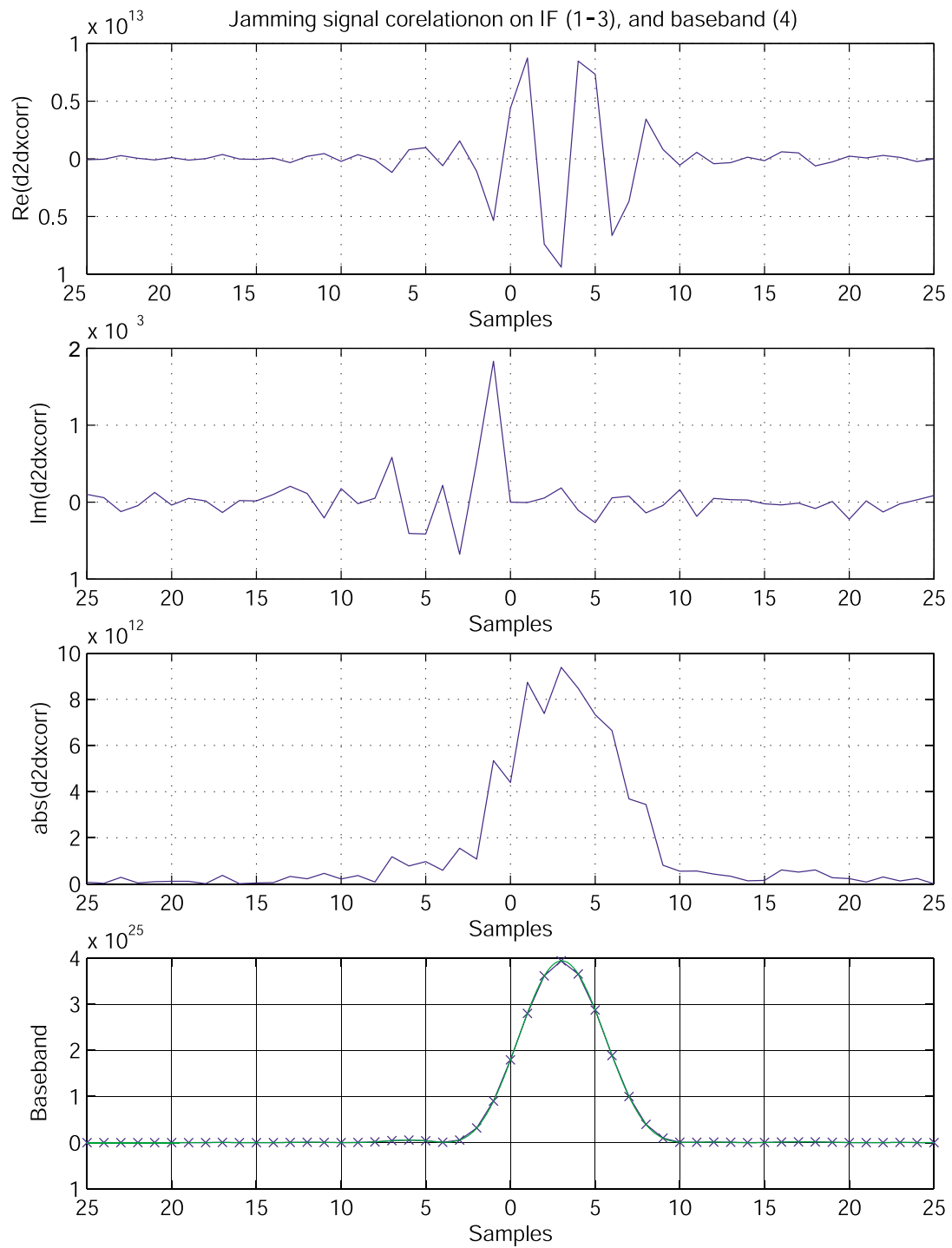
% resampling correlation peak:
NN = 20; % Resampling factor
d2dxcorr_f2_r = resample(d2dxcorr_f2, NN, 1);
d3dxcorr_f2_r = resample(d3dxcorr_f2, NN, 1);
d4dxcorr_f2_r = resample(d4dxcorr_f2, NN, 1);

[y(1) k(1)] = max(d2dxcorr_f2_r);
[y(2) k(2)] = max(d3dxcorr_f2_r);
[y(3) k(3)] = max(d4dxcorr_f2_r);

DeltaTauSamples = ( ((k-1)/NN+1) - 513); % TDOAs for each channel in samples <-----

```

Figure 5.15: MATLAB code to estimate jammer signal TDOAs for each baseline

**Figure 5.16:** Various stages of the obtaining jammer correlation

maximum of this correlation would correspond to the jamming signal propagation delay between two antennae or TDOA. As described earlier, the most efficient way to find circular correlation is by FFT. But regular, not circular correlation is needed in order to find the TDOA. It is possible to use exactly the same technique that has been used to obtain the initial guess of the C/A code phase; namely to pad data with zeros, and watch where circular correlation equals the regular correlation. In the current GIDL configuration, the base line length is approximately 100 meters or less, which corresponds to a possible time difference of $100 \text{ m} / 300000000 \text{ m/s} = 333.333 \text{ ns}$. At the GIDL sampling rate of 38.192 MHz, it corresponds to $38.192 \text{ MHz} \cdot 333.333 \text{ ns} = 12.7 \text{ samples}$. So only approximately 26 samples around zero of the correlation function are required.

To compute the correlation between the master and slave channels, the following operations are performed. Data from the master channel are padded by zeros at the beginning and at the end of the data set (an insignificant amount of data are lost). The circular correlation between padded master channel data and slave channel data is computed. Referring to the Figure 5.6c, the time delay around zero is equivalent of sliding the master data back and forth with respect to the slave data and computing correlation. Because 512 samples in the master channel have been nulled out on either side, that operation would produce correct correlation function between -512. . . +512 samples around zero delay. This correct correlation function is separated from the rest of the data in the next step.

Because all of the signals from the GPS band are mixed down to intermediate frequency and then sampled at that frequency, the obtained correlation is modulated by the intermediate frequency. This modulation must be removed from the correlation in order to obtain a better estimate of the TDOA. To do this, a correlation peak on the baseband frequency is mixed with the sine and cosine signals at one fourth the sampling rate, which corresponds to the IF frequency. Then in-phase and quadrature signals are filtered with low pass filter (LPF) whose bandwidth equals 1/8 of the sampling rate (4.7740 MHz). This bandwidth is adequate to the signal processed. IF filters used for the experiment in the GIDL receiver have a bandwidth of 6 MHz, which would make the signal bandwidth of 3 MHz on the baseband (this is due to “wrapping” of the signal spectrum around carrier frequency when mixed down to zero). The magnitude, or envelope, of the correlation signal is calculated using the simple equation: $\sqrt{I^2 + Q^2}$.

Because we are interested in the location of the maximum, and to simplify calculations, the square root operation is omitted.

As mentioned, the sampled signal has a bandwidth of 6 MHz. Because it is sampled above Nyquist rate all information about the signal is retained after sampling. To improve the timing resolution of the TDOAs, the correlation peak is resampled $\times 20$. The location of the maximum of the resampled correlation peak is used as an estimate of the TDOA for the given baseline. In Figure 5.16 (obtained from the real data) in the first plot shows the real component of the correlation on the IF (`real(d2dxcorr)`), the imaginary component of it on the second plot (`imag(d2dxcorr)`, its value should be small), and in the third the absolute value of correlation (`abs(d2dxcorr)`). On these plots it is easy to see oscillations which corresponds to the IF frequency. On the last plot in Figure 5.16, the squared magnitude of the correlation peak on baseband is shown, along with the resampled squared correlation peak (`d2dxcorr_f2` and `d2dxcorr_f2_r`). Points of the original peak are marked by “x” and connected by straight lines.

These differential jammer signal delay data are later corrected for the calibrated system delays (or the calibration values are set to zero if no calibration is available) and then used to calculate jammer locations. Code to perform this operation is shown in Figure 5.17.

5.6 Why GIDL needs a 12-bit ADC

This section explains why GIDL needs a 12-bit ADC. However, to do a full analysis of the receiver with the multi-bit ADC, to evaluate its performance, and to compute the receiver’s noise level would require at least a separate chapter. That is beyond the scope of this work. After sampling the data are converted to floating point numbers, rendering noise due to signal processing negligible and this noise would not be considered in this work also. (This section discuss only noise due to ADC effects, and does not cover noise due to analog and digital signal processing, such as noise in the amplifiers and cables, numerical noise due to round off errors, etc.)

Faster signal sampling reduces a noise floor because the noise is spread out over more frequencies. The total integrated noise remains constant but is now spread out over more frequencies that have benefits if the ADC is followed by a digital filter. The noise floor

```

% Using calibration data to correct delays
DeltaTau = DeltaTauSamples/fs;
dR1 = DeltaTau(1)*c + Delays(1);
dR2 = DeltaTau(2)*c + Delays(2);
dR3 = DeltaTau(3)*c + Delays(3);

load Ant_Locations_ENU.dat
x1 = Ant_Locations_ENU(2,1);
y1 = Ant_Locations_ENU(2,2);
z1 = Ant_Locations_ENU(2,3);
x2 = Ant_Locations_ENU(3,1);
y2 = Ant_Locations_ENU(3,2);
z2 = Ant_Locations_ENU(3,3);
x3 = Ant_Locations_ENU(4,1);
y3 = Ant_Locations_ENU(4,2);
z3 = Ant_Locations_ENU(4,3);

[xa, ya, za, xb, yb, zb, Det] = ...
    Find_XYZ(x1, y1, z1, x2, y2, z2, x3, y3, z3, dR1, dR2, dR3);

load ObserverLocationsENU.dat

% Vector from observer location
xo = xa - ObserverLocationsENU(2,1);
yo = ya - ObserverLocationsENU(2,2);
zo = za - ObserverLocationsENU(2,3);

% Direction from observer location:
[Beta, e, R] = cart2sph(xo, yo, zo);
Beta = pi/2 - Beta;

if Beta < 0,
    Beta = pi*2+Beta;
end
Beta = mod(Beta, 2*pi);

azimuth = ['Azimuth = ' num2str(Beta*180/pi) ' deg.'];
disp(azimuth)
range = ['Range = ' num2str(real(R)) ' m.'];
disp(range)

```

<-----
 % <-----
 % <-----
 % <-----
 % <-----

Figure 5.17: MATLAB code to calibrate TDOAs and find jammer location

(in dB) follows the equation: $Noise_Floor = 6.02 B + 1.8 + 10 \lg(F_s/2)$, where B is the number of bits in the ADC and F_s is the sampling frequency [157].

This equation represents the level of the quantization noise within the converter and shows the relationship between noise, number of bits, and the sample rate, F_s . Therefore, each time the sample rate is doubled, the effective noise floor improves by 3 dB! It shows that when the number of bits is increased by 1, the noise floor improves by 6 dB! Changing GIDL ADC from 8-bit to 12-bit yields a 24 dB improvement in the noise floor. This fact is important because the signals that GIDL detects and localizes are very close to the noise floor.

In the case of a GPS signal there is no information contained in the magnitude of the signal; information is only contained in the phase of the signal. In addition, the structure of the signal is known. Therefore, only a one-bit ADC is required to capture phase information and resolve the GPS signal. In the case of the GIDL no *a priori* information about jamming signal is available. Therefore, by obtaining additional information, for example better magnitude resolution, one could implement a wider range of processing algorithms. In the case of a white Gaussian jammer, information about magnitude is necessary to perform a correlation. A correlation is used to estimate the propagation delay of the unknown signal. Noise floor reduction in the ADC improves overall system noise floor and allows for detection and localization of weaker sources.

GIDL is similar to a phase array antenna (PAA). The basic idea behind a PAA is that the signals are collected from multiple antenna elements, undergo some delays and then are summed together to form the output signal. This process assumed that no information about the signal waveform is lost, only delays are introduced in the signal paths. So, if all processing in the array is done digitally it is necessary to ensure that the signals in each path are not distorted, and introduced noise would be minimized. To achieve that goal the signal should be sampled with the highest possible resolution and the highest possible sampling frequency. It is known from practice that digital phase array antennae start showing good performance when signals are sampled at 12 bits or more.

In practice, the performance of the GIDL with 8-bit ADCs was attempted and proven marginal. It detected and localized stronger signals, but failed to work for weaker ones, despite the weaker signals been theoretically detectable. After switching to 12-bit ADCs

the digital noise floor was reduced by 24 dB and these problems were solved. This switch was a major change in overall system architecture. The original ADCs were attached to a specialized digital signal processing board [158], while the new ADCs are data collection units only and forced all processing to be done on the main computer processor in MATLAB.

Chapter 6

Experimental Setup and Results

The concepts, theories and GIDL receiver described in the previous chapters were tested in a series of experiments conducted by the author and fellow researchers. Preliminary GIDL experiments and tests were performed first in the LAAS laboratory, using RF cables as delay lines and using only two channels to verify the concept. After successful experiments with the cables, the experimental setup was moved to the roof of the LAAS laboratory, allowing for experiments with real satellite signals, movable jammers, and pseudolites. The last set of the experiments was performed in the dry bed of Lake Lagunita on the Stanford campus. These experiments were designed to be as close to a real-life scenario as possible. This chapter describes the setup, testing, and results of these experiments.

6.1 Cable Experiments

These experiments were performed with the GIDL system to verify that the system was functioning properly and to make sure that the TDOA estimation algorithms for a non-moving jammer worked as expected. These experiments were complete end-to-end tests of the system and verified its performance before moving on to the field experiments. They also demonstrated the possible performance obtainable from the completed system.

The cable experiments were performed inside the LAAS lab. The test setup for these experiments was the following (see Figure 6.1). The signal from the -70 dBW/MHz jammer was split two ways by the RF splitter and then fed into two channels of the GIDL system.

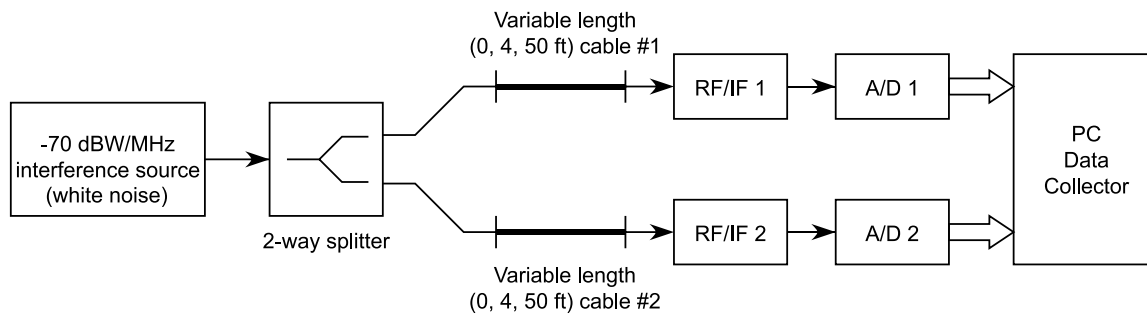


Figure 6.1: Experimental Setup for Cable Experiment

Cables of various length were inserted in the signal path in either channel (Cable 1 and Cable 2). Numerous experiments were performed with this setup, two of which will be described in detail in this section.

The first experiment was performed with so called “50 ft” cable which actual length was 49.5 ft. To obtain a reference delay in the correlation peak, zero-length cables (direct connections) were inserted in both channels, and data was collected. This data set was used as a calibration or reference data set. Then, in the first channel, Cable 1 with length “50 ft” was inserted, and data was collected. Lastly, Cable 1 was removed (set to 0 ft), inserted as Cable 2, and data was collected again.

Correlations of the signals in the first and second channels are shown in Figure 6.2. This figure presents “raw” correlation peaks, as they were obtained by direct correlation of the signals in channels 1 and 2. As theory shows (see Chapter 2), simple cross-correlation of signals from two channels is the optimal way to estimate TDOA in the case of a white noise jammer and white background noise, which is the case in these experiments.

The horizontal axis shows raw sample numbers, and the vertical axis shows the magnitude of the correlation peak in internal (relative) units. The scale factor is $1 \text{ V} = 2^{15}$ for the input signal but it is irrelevant for this experiment, because we are interested in the location of the correlation peak in time, not its absolute magnitude.) One can observe that the magnitude of the correlation peaks with the 50 ft cable inserted in either channel is smaller than that of the 0-ft cable. This is due to losses in the cable. RG-58 cable was used for this experiment, and it has an expected signal loss of approximately 9 dB per 50 ft of length at GPS frequency. To get a better sense of how far these correlation peaks are from

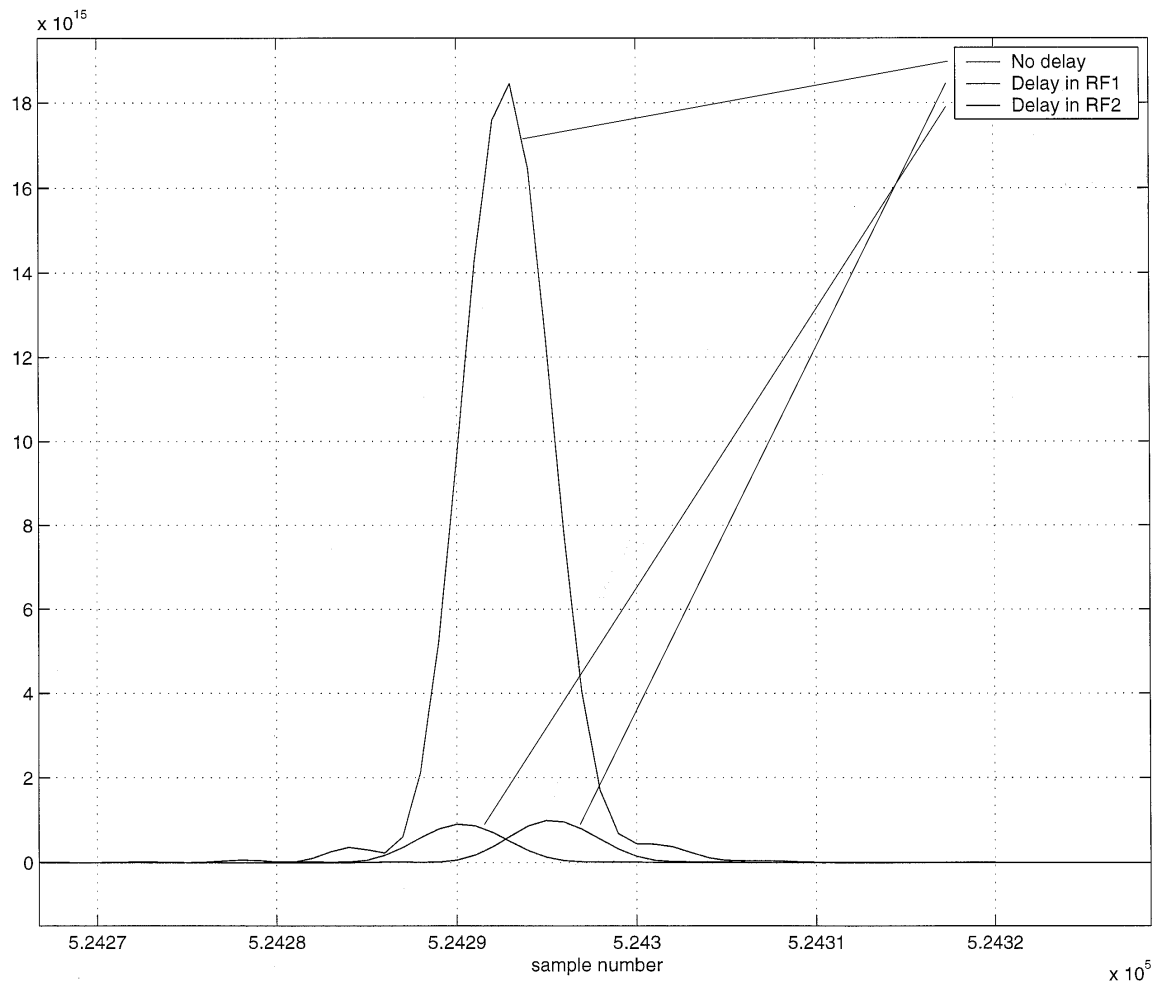


Figure 6.2: Correlation of the first and second channel data for experiment with 50 ft cable. Horizontal axis shows number of samples from the beginning of data set, and vertical axis shows amplitude of the correlation peaks in internal (relative) units.

each other, they were scaled such that the maximum value of each peak would be equal to one. These data are shown in Figure 6.3. Note, that to obtain these plots, the origin on the horizontal axes was moved. The maximum of the correlation peaks corresponds to the samples numbered 5242894, 5242919, and 5242944 of the unmoved data. This makes the distance between correlation peak without 50 ft cable insertion and the correlation peaks with the cable inserted equal to 25 samples.

As mentioned earlier, Belden 8219 RG-58 cable was used with a propagation speed in the cable approximately 73% of the speed of light (c). The effective sampling rate for the data is $3.8192 \cdot 10^8 \text{ Hz}$. From these numbers, it follows that the cable length $l = \frac{25 \cdot 0.73c}{3.8192 \cdot 10^8} = 14.34 \text{ m} \approx 47 \text{ ft}$. Recall that the actual cable length used was 49.5 ft. These numbers are close (the error is less than 10%), so this test is a success. To do a double-check of the numbers, it is possible to assume that the propagation speed in the cable is unknown but that the cable length is known (measured by the tape measure and equal to 49.5 ft). Then the propagation speed relative to the speed of light $\alpha = \frac{49.5 \cdot 12 \cdot 0.0254 \cdot 3.8192 \cdot 10^8}{25 \cdot c} = 0.7683$. This number is close to the number 73% given in the data sheet for the cable, which has 10% accuracy, giving a range 65% – 80%. The obtained result of 76.83% is well inside the possible range, so this test is a success.

Exactly the same experiment was performed with a cable of 4 ft length. This was a test of GIDL ability to resolve short ranges. Plots of the scaled correlation peaks are shown in Figure 6.4. (Again, to obtain this picture, the origin had to be moved.) The maximum of the correlation peaks corresponds to the samples numbered 5242917, 5242919, and 5242921 of the unmoved data. This makes the distance between correlation peak without the 4 ft cable insertion to correlation peaks with the inserted cable equal to 2 samples. Repeating the same calculations for $\alpha = 0.73$, one would get a cable length equal to 3.76 ft, and assuming the cable length is known, $\alpha = 0.7761$. This is a good result. This result also shows that one sample would correspond to 2.6183 ns in resolution in time for TDOA, which would correspond to 0.7855 m resolution of range difference in free space.

More complex data processing algorithms could be used to improve this resolution, such as dithering, averaging, etc., but even this resolution provides good accuracy for jammer detection, as was shown in Chapter 2.

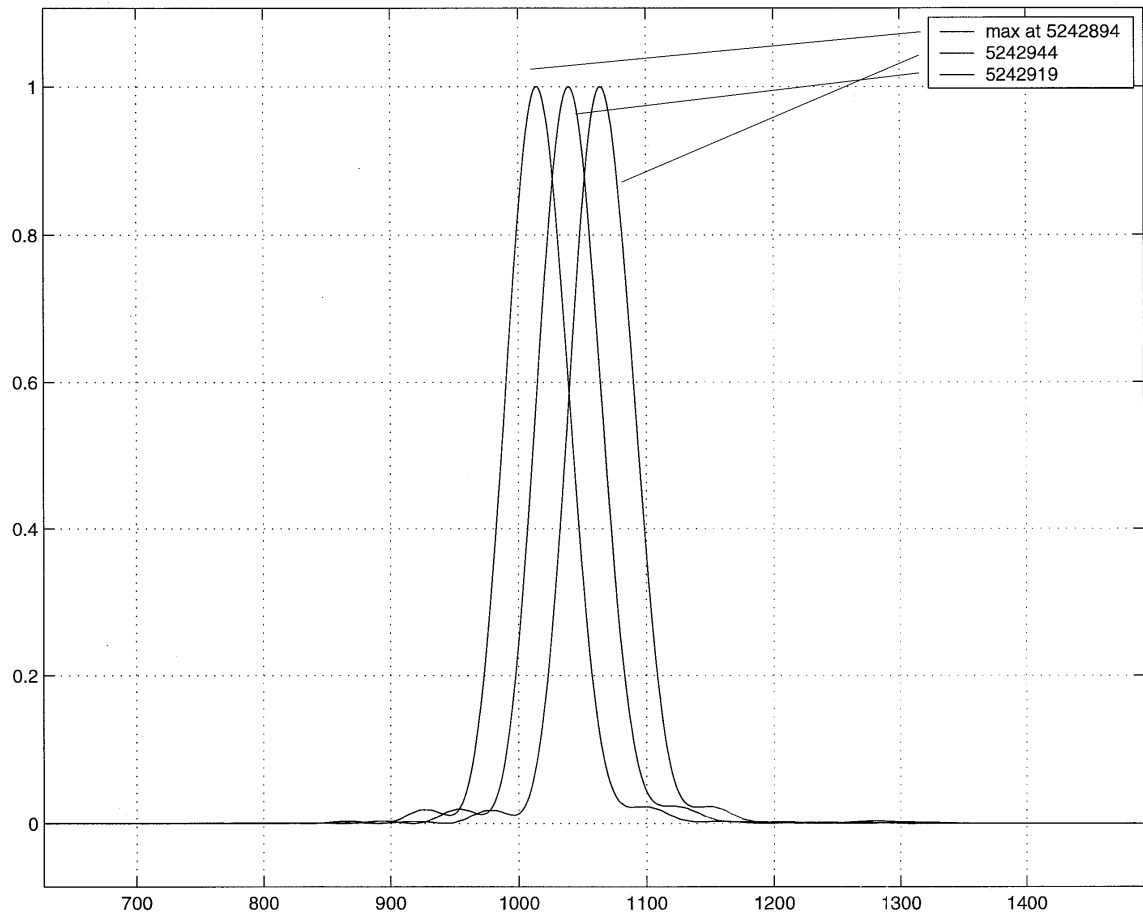


Figure 6.3: Scaled correlation of the first and second channel data for experiment with 50 ft cable. Horizontal axis shows number of samples from the beginning of data set, and vertical axis shows scaled amplitude of the correlation peaks such that maximum is equal to one.

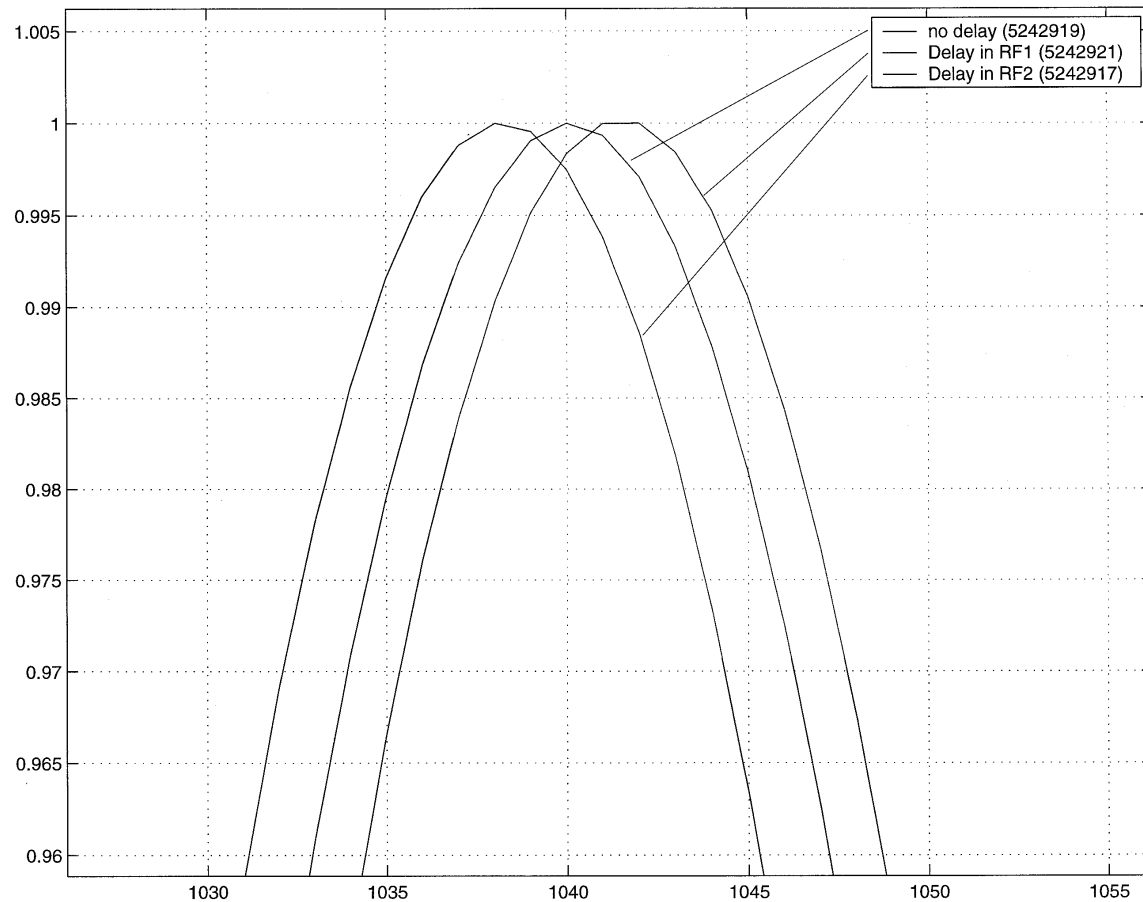


Figure 6.4: Scaled correlation of the first and second channel data for experiment with 4 ft cable. Horizontal axis shows number of samples from the beginning of data set, and vertical axis shows scaled amplitude of the correlation peaks such that maximum is equal to one.

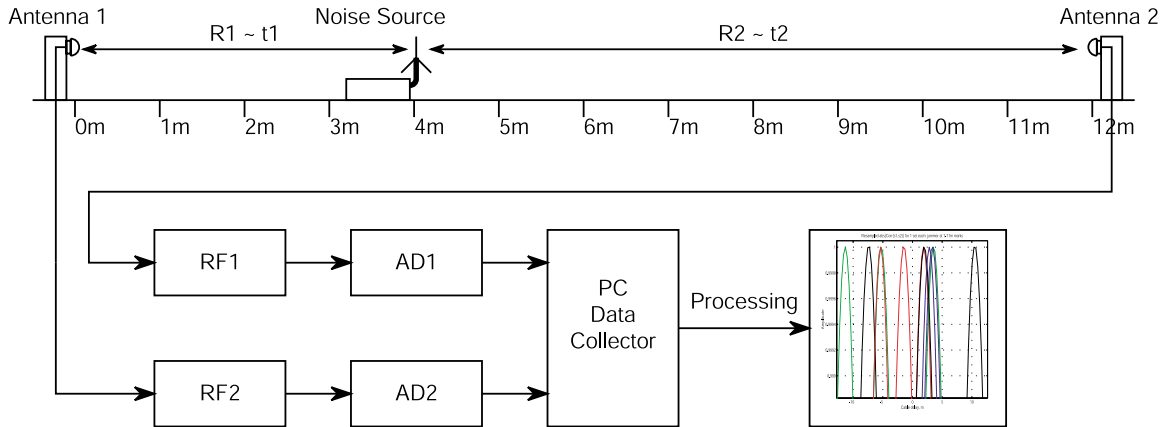


Figure 6.5: Rooftop Test Range 1

6.2 Roof-Top Experiments

After completing the cable experiments, but before moving to the full system field tests, another set of tests were performed in a more realistic but easily accessible environment. These are the experiments on the roof of the LAAS laboratory.

The experiments on the roof of the GPS lab simulate system operation in a real environment. The system configuration for the real operation of GIDL in the LAAS environment would include multiple antennae spaced a hundred meters or so apart on the airport property. Before going to the field, an attempt was made to do as many experiments in the lab environment as possible. A 12-meter test range was set up on the roof of the LAAS laboratory. The length of 12 meters was limited by the roof size. The GIDL system should demonstrate its capability of accurate estimation of signal time-of-arrival difference when the signal arrives from any direction. It is difficult to move a jammer around the roof in a circle, so it was decided to move the jammer on straight line between two antennae. Effectively, it is the same as moving the jammer around. By moving the jammer between antennae, one can create all possible differential times of arrival for the given antenna configuration.



Figure 6.6: Rooftop Test Range 2

The diagram for the test range is shown in Figure 6.5. There are two antennae located at the marks 0 m and 12 m plus the roving jammer, which may be placed anywhere between the two antennae. One-meter marks were painted between the two antennae and were used to set up the jammer in order to get repeatability in the results. To improve the antenna gain in the horizontal direction, antennae were mounted sideways looking toward the jammer in these experiments, and in other experiments, the antennae were vertically mounted. The signal from each antenna goes through the cable down to the lab into the GIDL receiver, where it is digitized and stored in the PC computer for post-processing. Pictures of the test range and each antenna are shown in Figure 6.6. The goal for this test is to evaluate how accurately one can measure $\tau = t_2 - t_1$, or differential range, $\Delta R = c\tau$, where c is the speed of light in the real environment and to evaluate potential problems.

Some results from this experiment are presented in Figure 6.7 in the form of the correlation plots for each jammer location from 1 to 11 m. When jammer was placed in each marked location, three data sets were collected. Each data set contains 524288 samples, which corresponds to 13.7 ms of data to process. The same results are presented in tabular form in Figure 6.8 and in graph form in Figure 6.9. The results for all data runs in each location are consistent and repeatable. Errors in the results at the 1, 2, 3, 4, and 5 meter marks are compatible with the length of one sample, which is 0.3142 m. For these experiments, the sample time was 2.5 times shorter than for the cable experiments, which gave a minimum resolution of 0.7855 m. This was done to accommodate the small baseline on

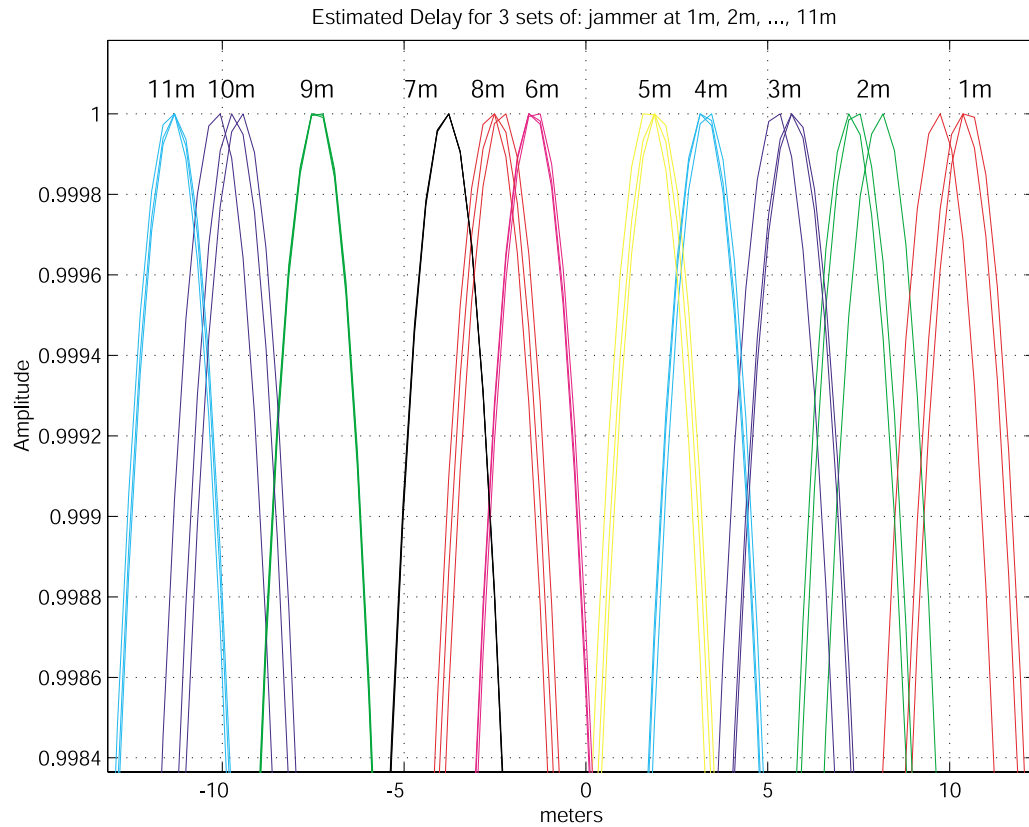


Figure 6.7: Plot of the Results from the Roof Experiments (1–5 m results are good, 6–11 m results are severely affected by multipath)

the roof of the LAAS lab. These are quite good results, and they demonstrate the potential of the system. There is one outlier in the position estimation, located at the 10 m mark, but this error is repeatable from test to test, so it appears that the measurements are being affected by multipath or some other external error source. Results in other locations have some errors but are also repeatable from test to test for the given location, so multipath again is the suspect. There are RF reflecting structures on the roof which corrupt results in the second half of the test range (delays from 0 to -10 m).

It was shown that it is possible to resolve range to 1 m in the open air. One meter of error on a 100-m baseline corresponds to an angular error in estimating direction of the signal of 0.6 degrees in the direction perpendicular to the baseline and 8 degrees in the direction parallel to the baseline. When using a multiple baseline system, this error

Jammer location, m	Expected Delay, m	Data Set #1			Data Set #2			Data Set #3		
		Delay, Sample	Delay, m	Error, m	Delay, Sample	Delay, m	Error, m	Delay, Sample	Delay, m	Error, m
1	10	10034	10.3686	0.3686	10034	10.3686	0.3686	10032	9.7402	-0.2598
2	8	10027	8.1692	0.1692	10025	7.5408	-0.4592	10024	7.2266	-0.7734
3	6	10018	5.3414	-0.6586	10019	5.6556	-0.3444	10019	5.6556	-0.3444
4	4	10012	3.4562	-0.5438	10011	3.142	-0.858	10011	3.142	-0.858
5	2	10007	1.8852	-0.1148	10007	1.8852	-0.1148	10006	1.571	-0.429
6	0	9996	-1.571	-1.571	9996	-1.571	-1.571	9997	-1.2568	-1.2568
7	-2	9989	-3.7704	-1.7704	9989	-3.7704	-1.7704	9989	-3.7704	-1.7704
8	-4	9993	-2.5136	1.4864	9993	-2.5136	1.4864	9994	-2.1994	1.8006
9	-6	9978	-7.2266	-1.2266	9977	-7.5408	-1.5408	9977	-7.5408	-1.5408
10	-8	9969	-10.0544	-2.0544	9970	-9.7402	-1.7402	9971	-9.426	-1.426
11	-10	9965	-11.3112	-1.3112	9965	-11.3112	-1.3112	9965	-11.3112	-1.3112

Note: 1 Sample = 0.3142 m **Very Good Results** **OK Results** **Bad results** - Suspected multipath

Figure 6.8: Summary of the Results from the Roof Experiments

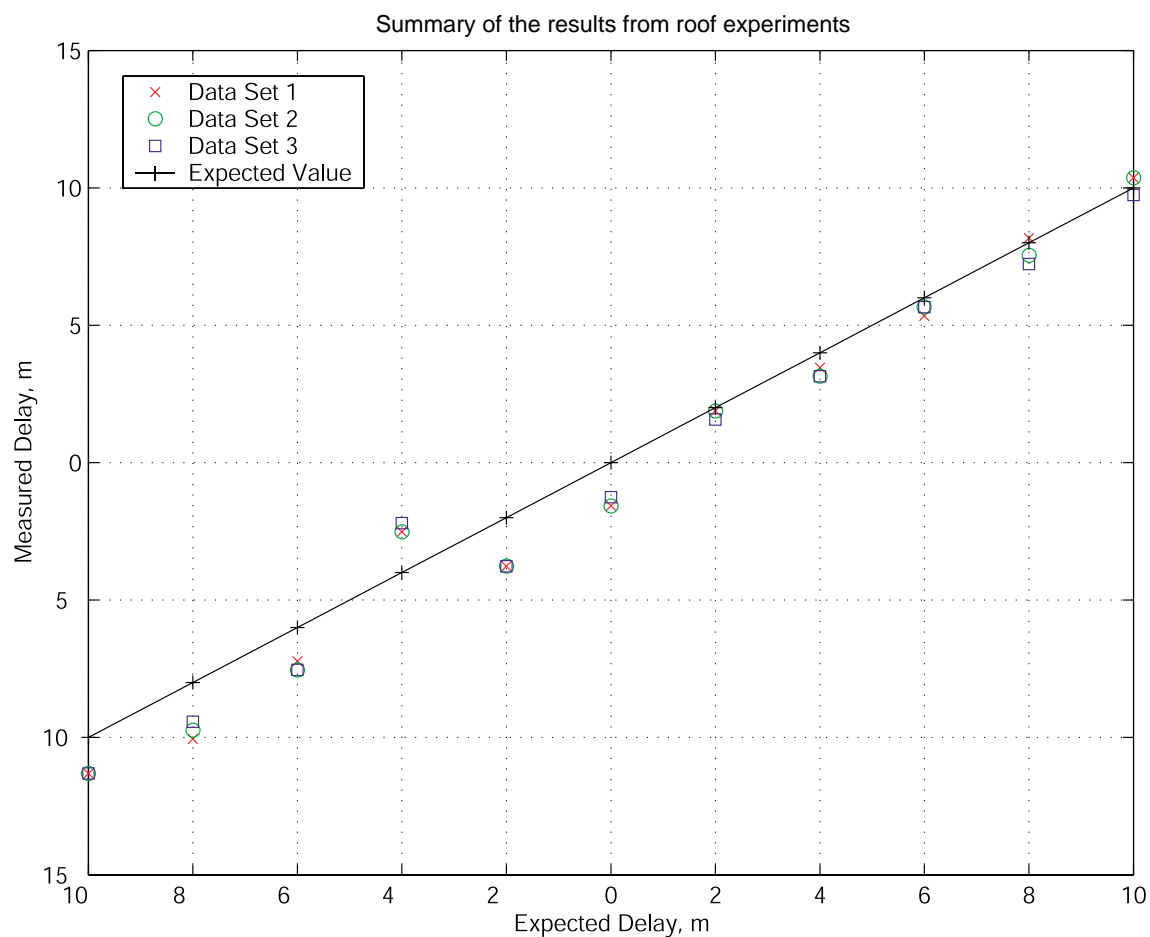


Figure 6.9: Summary of the Results from the Roof Experiments in Graph Form

could drop below 1 degree in any direction. This experiment was also a success and it demonstrated the readiness of the system for the full and final test and demonstration.

6.3 Experimental Setup for Full GIDL System Test

Full system tests of the GIDL were performed on the dry bed of Lake Lagunita on the Stanford campus. There were a number of reasons for choosing that test location. In particular the lake bed is below ground level with respect to the rest of campus; thus any jammer located in the lake bed would not be visible from the campus or other locations, and would not introduce any unwanted interference to nonparticipating parties. Also, the lake bed is open space and is a reasonable simulation of the real life LAAS installation. It was easy to find an elevated observer spot for independent jammer direction verification. The lake bed is not used for any sports or recreational activities when the lake is dry, so it was safe to install equipment and run cables without any expected interruptions from other users. Lastly, it had the advantage of being located right on the Stanford campus, making it relatively easy to move equipment to and from the laboratory.

There were two installations of the GIDL system on Lake Lagunita. One was temporary and was used only for one day and one series of experiments. It was the first full test of the GIDL system and a verification of the usefulness of the lake-bed setup. This first experiment was performed on August 22, 2000. Large amounts of data were collected and used in post processing for algorithm debugging and system tuning.

For all experiments on Lake Lagunita, the same -70 dBW/MHz white noise jammer was used with an extra 30 dB amplifier to scale the estimated jamming range to 316 m. The expected GIDL range for a jammer of that power is 505 m. The jamming signal is a white noise centered at the L1 frequency with a bandwidth greater than 24 MHz. This is a realistic type of jammer which could easily be built for under \$100 and poses a significant threat to GPS operations. The experimental jammer and amplifier is shown in Figure 6.10(b). The jammer power was so low that the GPS receiver installed in the GIDL base station was tracking satellites throughout all jamming experiments. This provided an additional assurance that no other user would be unintentionally jammed while GIDL experiments were being conducted.



(a) One of four GIDL receiving antennae (stations)



(b) Experimental Jammer: -40 dBW/MHz white noise source

Figure 6.10: GIDL Receive Antenna and Experimental Jammer

NovAtel 401 antennae were used as GIDL antennae (or stations) for both setups. Each GIDL antenna was connected to the GIDL receiver by an RF cable. The length of the cables was 100 m each, and they were cut to this size. This was done intentionally to allow some experiments to assume that the system delays were equal in each channel and therefore proceed without calibration. Because the cables were of significant length, extra in-line amplifiers after each antenna were used to cope with attenuation and signal degradation in the cables. Belden 9913 cable was used with approximate attenuation of 6 dB per 100 ft at GPS frequency, making each cable attenuation approximately equal to 20 dB. Starlink in-line amplifiers with 21 dB of gain were used. In the first GIDL experimental setup, the antennae were mounted on temporary mounts. In the second, semi-permanent setup, the antennae were installed on mounts permanently fixed in the ground. One of the GIDL antennae with an in-line amplifier attached to it is shown in Figure 6.10(a) on a permanent mount.

Location of the antennae and surveyed jammer locations for the first setup are shown in Figure 6.11(a). The second setup is shown in Figure 6.11(b). As mentioned, this setup was a semi-permanent setup, and numerous experiments were conducted on it. All antenna and jammer mounts in surveyed locations are aluminum posts driven about 70 cm deep into the ground with an antenna thread on top, making them virtually permanent installations.

For proper GIDL operation, it is necessary to know the exact relative geometry of the GIDL antennae, and it is convenient (and necessary for calibration by GPS) to know how internal GIDL coordinates (i.e., antenna geometry) relate to some common coordinate reference. Thus, extra care was taken in surveying the GIDL antenna locations. For both setups, antenna locations were surveyed using Trimble 4000 series survey receivers. Three jammer locations also were marked and surveyed to be used as “truth” for the jammer localization algorithms. The GIDL finds and locates jammers, but it is necessary to know how accurately it is doing its job. Thus, independent ways of locating jammers for test purposes must be available. These surveyed jammer locations were used to collect statistics of GIDL errors in jammer localization.

For the semi-permanent setup, the so-called observer location was also surveyed. For a visual consistency check and for demonstration purposes, an optical direction finder was installed in that location, and all directions to the jammers were calculated relative to this

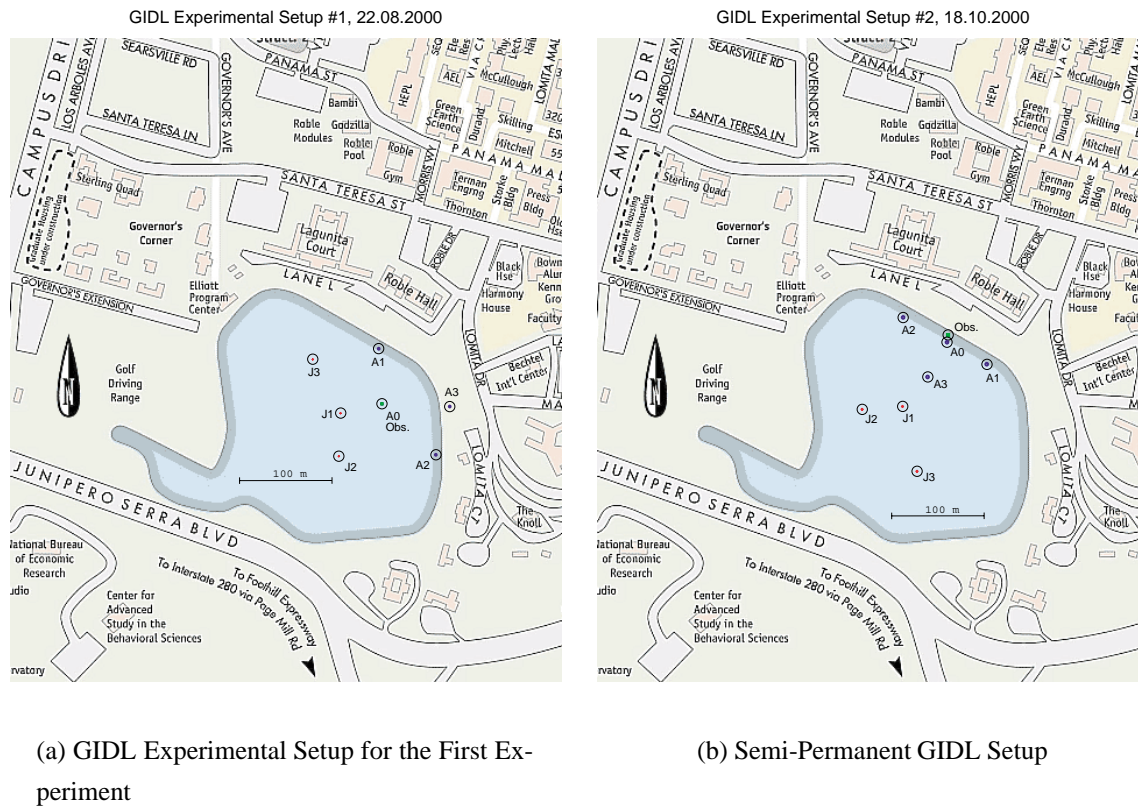


Figure 6.11: GIDL Experimental Setups on Lake Lagunita; A0, A1, A2, A3—GIDL Antenna Locations; J1, J2, J3—Surveyed Locations of the Jammer; Obs.—Direction Finder (Observer) Location

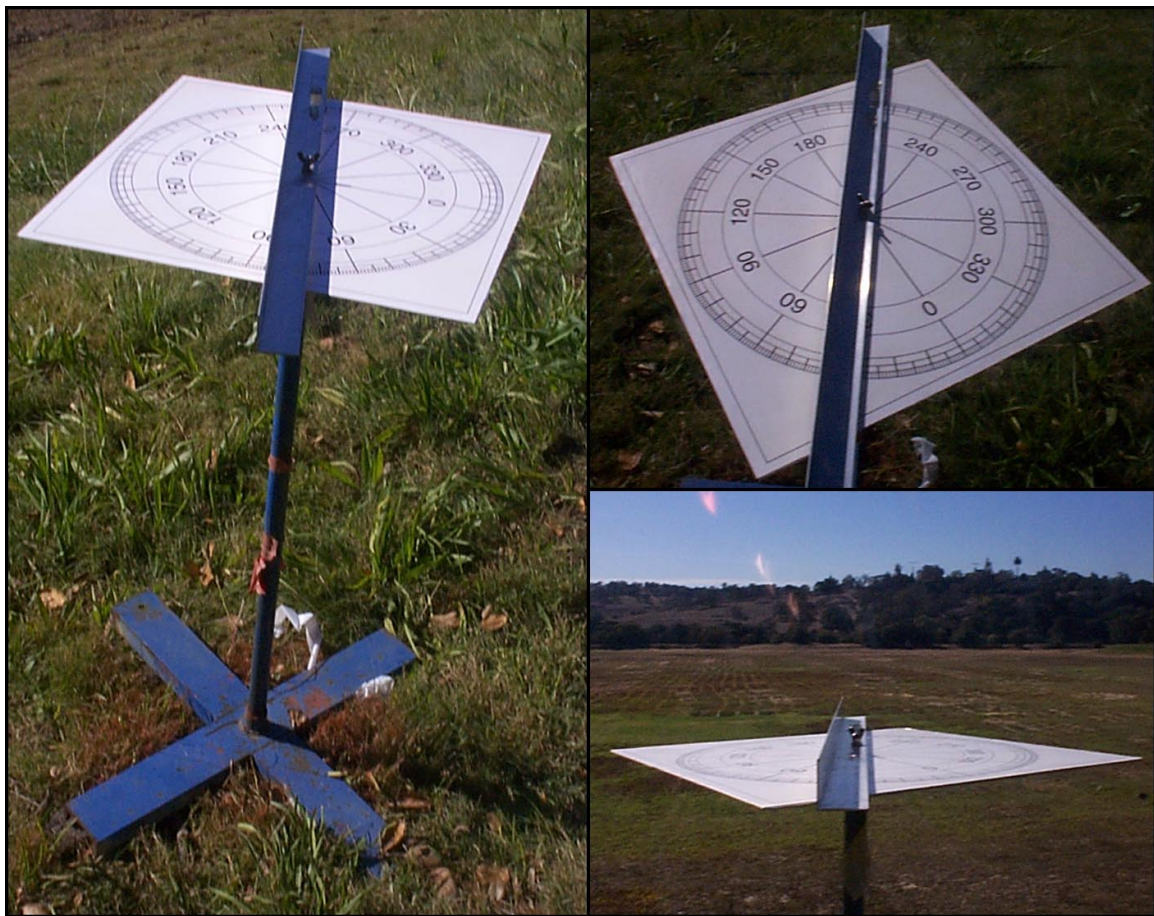


Figure 6.12: Optical Direction Finder, Used for Independent Jammer Azimuth Verification

point such that an independent observer can quickly check the GIDL performance. Various views of this direction finder are shown in Figure 6.12.

After moving all equipment into the field, GIDL antennae were installed on the mounts. One-hundred-meter antenna cables were then run from each antenna to the GIDL base station. For most experiments the GIDL equipment was installed in the back of a truck and consisted of the GIDL receiver, processing computer, and the Garmin GPS receiver (used for calibration and jammer power monitoring), as shown in Figure 6.13. The base station, i.e., the complete GIDL system, was powered by a gas generator. Thus, it had an independent power source and could be moved to different locations if necessary.



Figure 6.13: GIDL base station (GIDL receiver, processing computer, etc.) was located in the bed of HEPL truck during experiments at Lake Lagunita

6.4 Data Collection and Demonstration Modes

There were two major operation modes for the GIDL system: data collection and demonstration modes. In the data collection mode, software was set up to collect 50 individual data sets for system calibration or jammer localization and to save all raw data to the hard drive for post processing and statistical analysis. The number 50 was chosen due to the limited capacity of the hard drive. When data analysis occurred in post processing or when various algorithms were tested, the following mode of operation was adapted. The GIDL was installed on the test range, and the jammer was turned off. Then 50 calibration data sets were collected. These data sets include raw data from the ADCs in each GIDL channel, time stamped by the GPS time, and satellites in view and ephemeris data from the GPS receiver. The jammer was then moved to the first surveyed location, turned on, and another 50 data sets were collected, this time gathering only raw data from ADCs in each GIDL channel. After this data collection, the jammer was again turned off, and another calibration data set was collected. The jammer was then moved to a second surveyed location and

50 jammer data sets were collected. The same procedure was repeated for the jammer at the third surveyed location. Lastly, another 50 calibration data sets were collected. Using these data, all experimental result plots were generated, and all statistics were obtained. To do so, the first calibration data set was used to calibrate the system clock and biases in the system. The jammer data were then processed using the GIDL detection and localization algorithm, taking into account the calibration results.

A second mode of GIDL operation is the demonstration mode. This mode is used to demonstrate system performance, do a quick assessment of the system accuracy, and to “show off” the system. In this mode, a few calibration data sets are collected at the beginning of operation (and could be collected at any time to recalibrate the system during the demonstration) and are then processed and stored as parameters for the real-time jammer localization code. After that, the jammer localization code can be run. One option is to run the jammer detection and localization code continuously. In this case, the display described in Chapter 3 is shown collects data sets and tries to detect a jammer. If a jammer is detected, location, azimuth and range are displayed on the screen along with expected errors for its location. Another option is to run the algorithm in single runs. Then, on command from the operator, a data set is collected, jammer detection/localization is performed, and results including jammer location (if present) are displayed.

To verify how well the system performs without calibration, it can be run in demonstration mode while setting all calibration coefficients to zero. It takes about 55 seconds to collect and process one data set in demonstration mode, i.e., in that time, data is collected, stored to the hard drive, read into MATLAB, and then processed by the GIDL algorithms implemented in MATLAB. This process could be sped up (see Section 8.2.6 for suggestions).

6.5 Experimental Results of Jammer Localization

In Figures 6.14–6.19, jammer localization results are shown. The Figures 6.14, 6.16, and 6.18 shows a “bird’s-eye” view of the experimental results, and the Figures 6.15, 6.17, and 6.19 zooms in on the jammer which has been localized. Known GIDL antenna locations are shown by the bold circles on the plots, while estimated jammer locations are

	Surveyed		GIDL		Estimated		Test	
	Az, deg	Range, m	Measured Mean Az, deg	Range, m	Error $\sigma(Az)$, deg	$\sigma(R)$, m	Statistics $\sigma(Az)$, deg	$\sigma(R)$, m
Jam. 1	214.69	117.92	214.70	118.15	0.61	4.39	0.21	2.09
Jam. 2	231.65	163.35	231.70	163.95	0.65	7.83	0.30	5.12
Jam. 3	193.07	200.11	193.04	200.89	0.56	11.51	0.16	4.93

Table 6.1: Results of the Experiment Performed October 18, 2000. Azimuth and Range Referenced to Antenna 0; Measured values are mean and standard deviation of 50 runs for each jammer location.

shown by the regular circles for uncalibrated data and by the small crosses for calibrated data. Also, hyperbolas used for jammer localization are shown (these are so-called “surfaces of position”), along with expected error boundaries for each hyperbola. There is also a predicted 1σ error ellipse shown for the given jammer location.

From these plots, it is easy to see that all calibrated jammer location estimates fell within predicted error boundaries (boundaries on each side of the ellipses of jammer location for each pair of antennae) and correspond to the predicted 1σ error ellipse (these are 1σ boundaries on statistical data, so one would expect about 37% of the data points to lie outside the 1σ boundaries). From the plots it is easy to see that the system performs very well and as predicted.

Looking at the uncalibrated data, it is possible to observe that azimuth estimation remains strong in these results while the ranging information is almost lost. So it is possible to conclude that calibration is more important for finding the range and less important for finding azimuth.

The measured mean and standard-deviation values of jammer localization at each jammer location for 50 data sets are shown in Table 6.1 and in graphical form in Figure 6.20, along with the values predicted by the theoretical analysis in Chapter 2. In this result, the azimuth and range of the jammer location is referenced to Antenna Number 0 of the GIDL system.

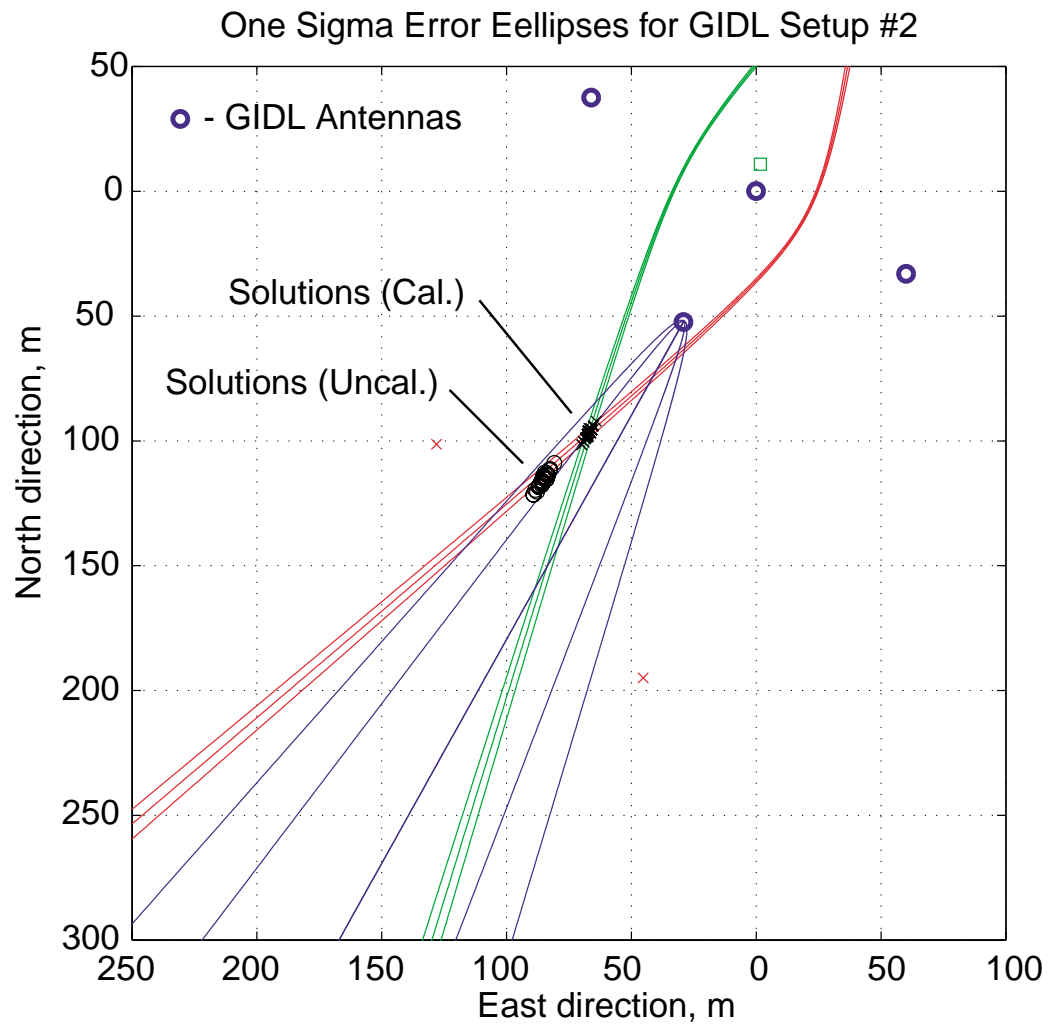


Figure 6.14: Jammer localization results on October 18, 2000, with jammer at location 1, summary of 50 independent experiments

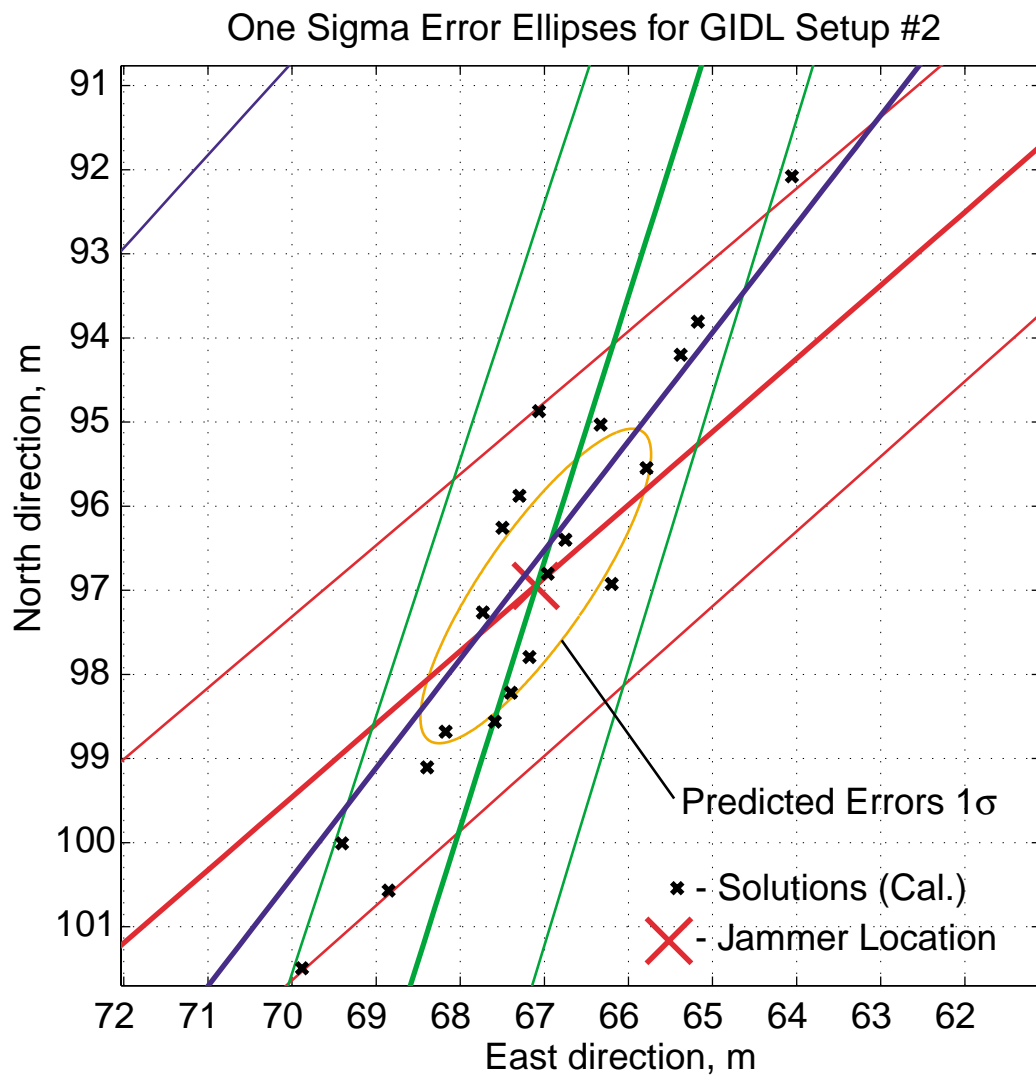


Figure 6.15: Jammer localization results on October 18, 2000, with jammer at location 1, summary of 50 independent experiments (zoomed)

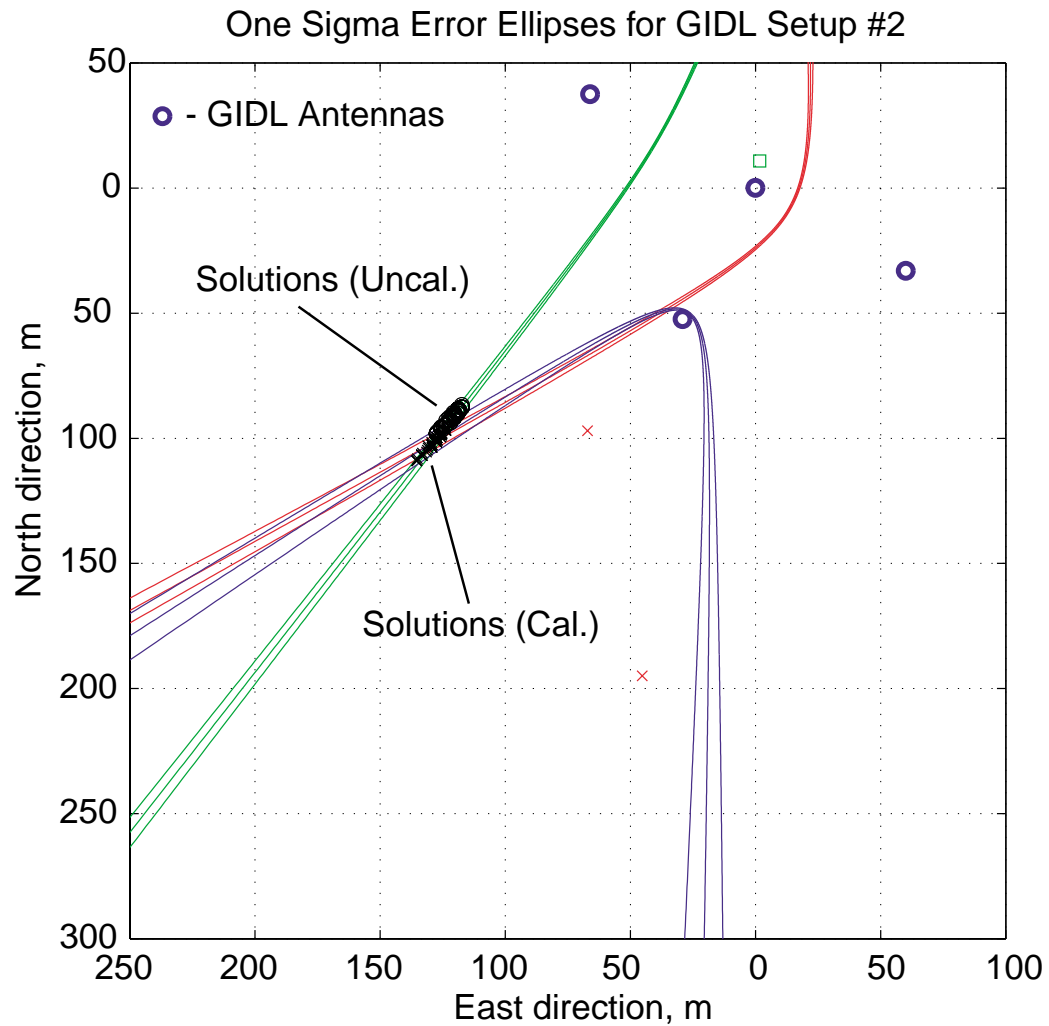


Figure 6.16: Jammer localization results on October 18, 2000, with jammer at location 2, summary of 50 independent experiments

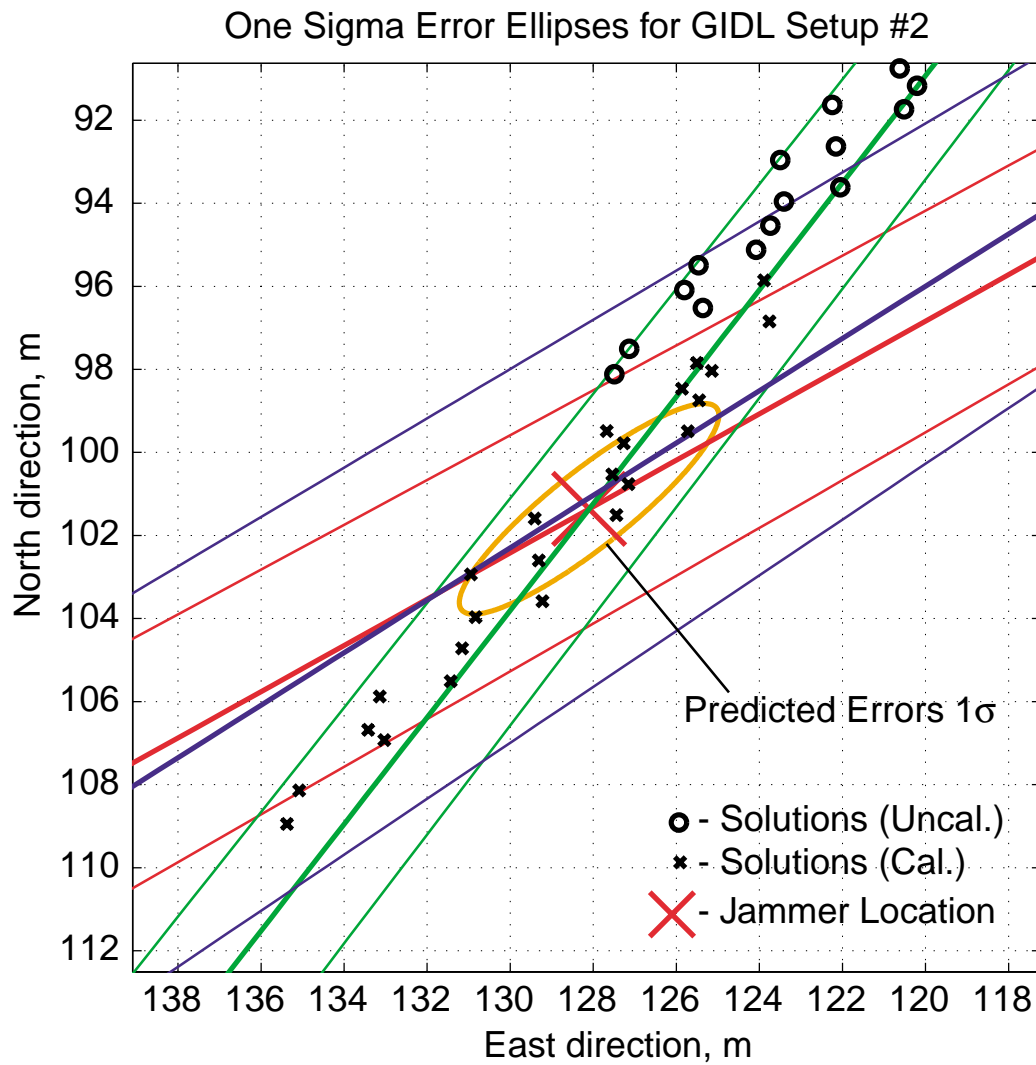


Figure 6.17: Jammer localization results on October 18, 2000, with jammer at location 2, summary of 50 independent experiments (zoomed)

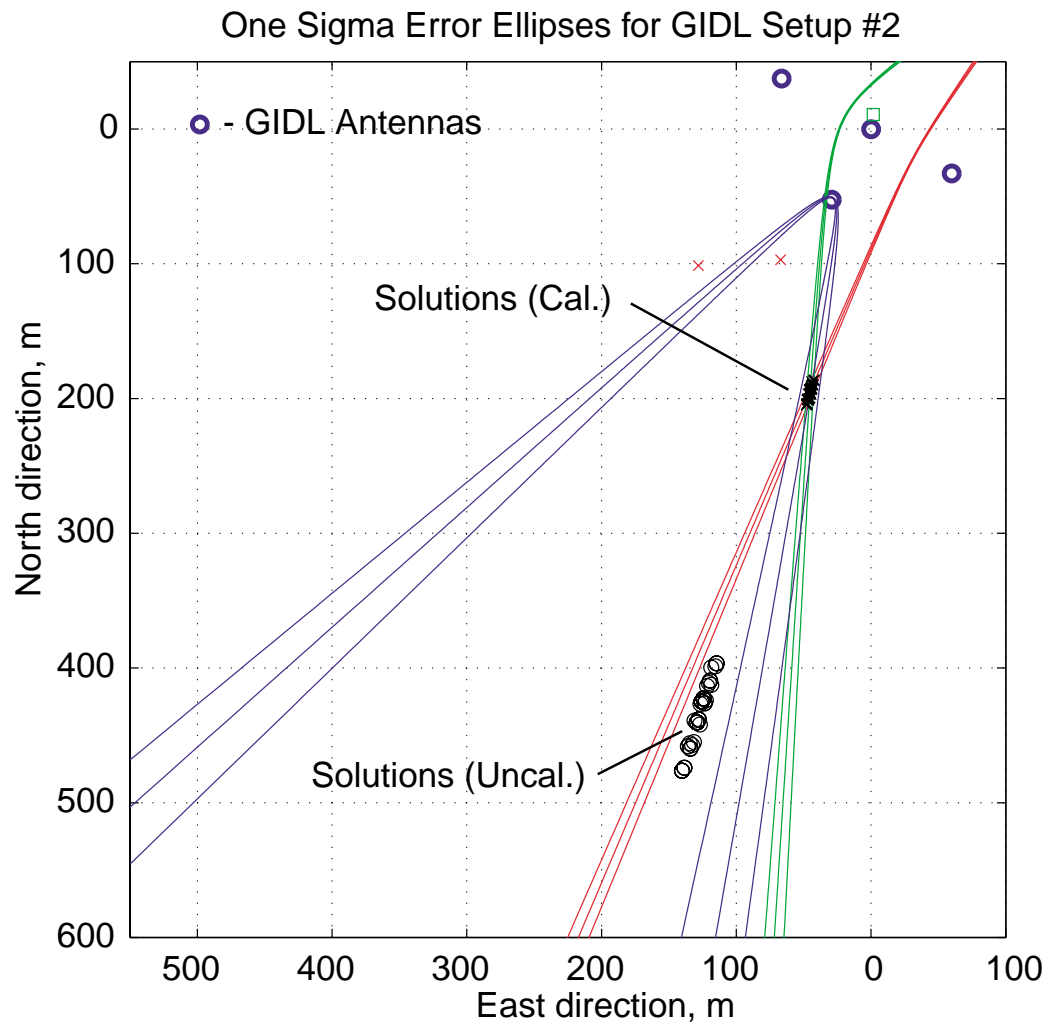


Figure 6.18: Jammer localization results on October 18, 2000, with jammer at location 3, summary of 50 independent experiments

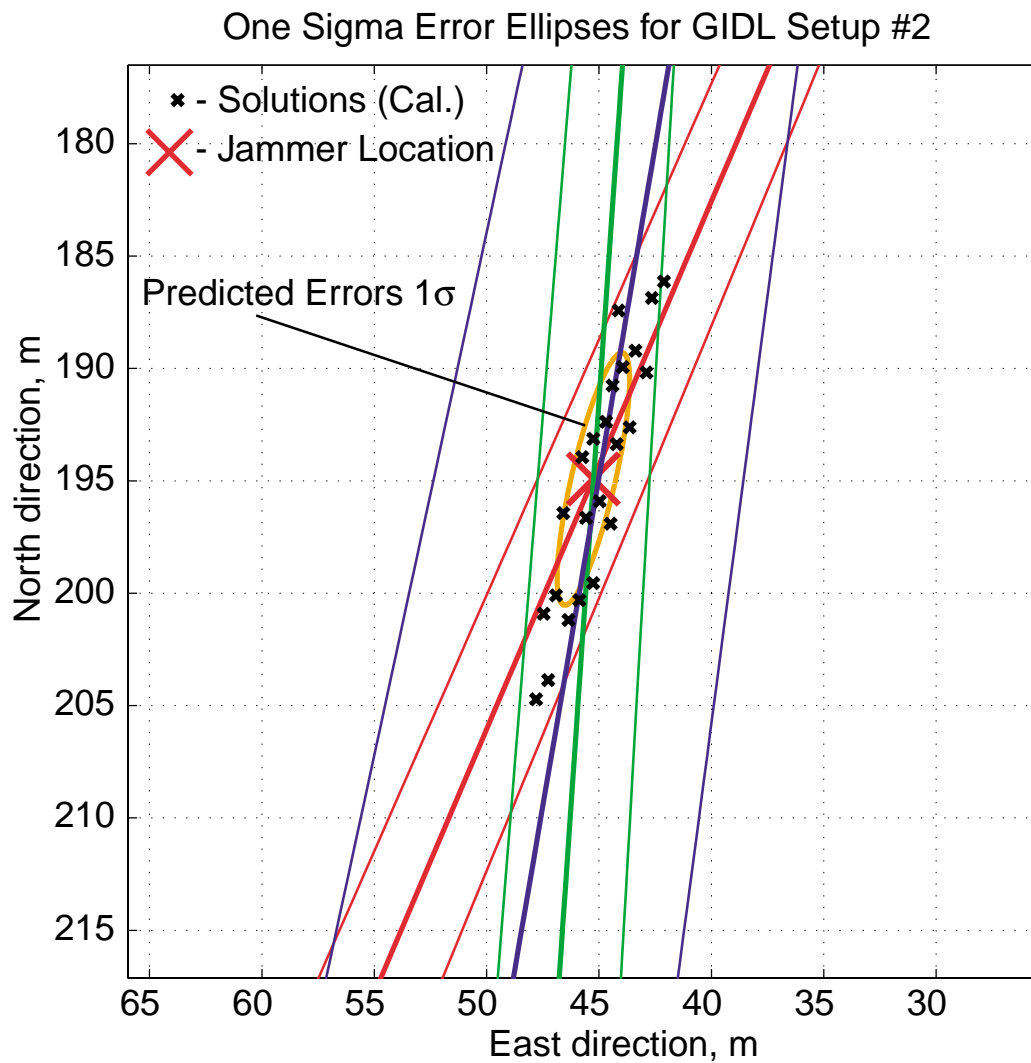


Figure 6.19: Jammer localization results on October 18, 2000, with jammer at location 3, summary of 50 independent experiments (zoomed)

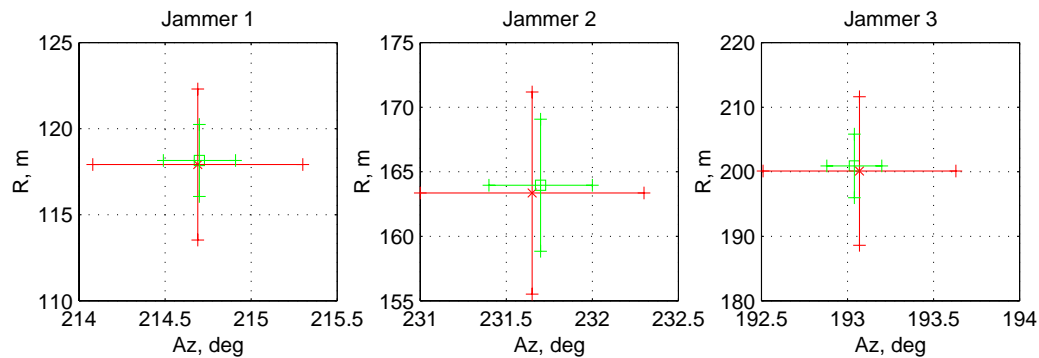


Figure 6.20: Results of the Experiment Performed October 18, 2000. Surveyed (red \times) and GIDL measured mean location (green \square) for each jammer with corresponding $\pm 1\sigma$ error bars.

	GIDL Reported Location		Surveyed Location	
	Range, m	Az, deg	Range, m	Az, deg
Jammer 1	55.1578	255.6821	45.9234	257.2396
Jammer 2	86.031	219.4568	73.3871	219.4165
Jammer 3	96.6923	-56.6896	88.8767	-57.2878

Table 6.2: Uncalibrated Jammer Localization in Demonstration Mode During First GIDL Experiment at Lake Lagunita

Table 6.2 and Figure 6.21 shows results obtained in the demonstration mode for jammer localization during the first GIDL experiment at Lake Lagunita on August 22, 2000. To obtain these results, no calibration data were used. Instead, data were obtained immediately after turning GIDL on for the first time on the lake-bed.

Table 6.3 and Figure 6.22 shows results obtained in the demonstration mode during the second experiment on the lake. Again, no calibration data were used to obtain these results.

These results show that GIDL performs well in finding the azimuth of the jammer even without calibration. This could be useful in localizing jammers, if they are present at the time of GIDL activation.

All the data in this chapter show that the GIDL performs well and roughly as expected

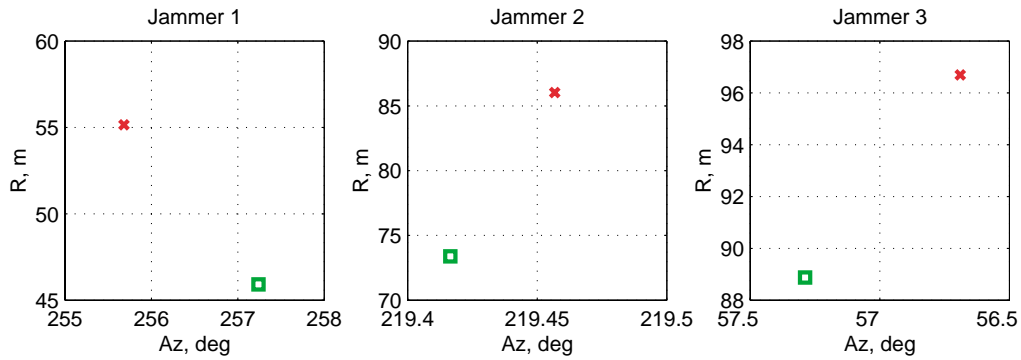


Figure 6.21: Uncalibrated Jammer Localization in Demonstration Mode During First GIDL Experiment at Lake Lagunita. Surveyed (red \times) and GIDL measured location (green \square) for each jammer.

	GIDL Reported Location		Surveyed Location	
	Range, m	Az, deg	Range, m	Az, deg
Jammer 1	153	213	127.9494	212.5391
Jammer 2	167	229	171.5574	229.1565
Jammer 3	386	196	211.0717	192.8428

Table 6.3: Uncalibrated Jammer Localization in Demonstration Mode During Second GIDL Experiment at lake Lagunita

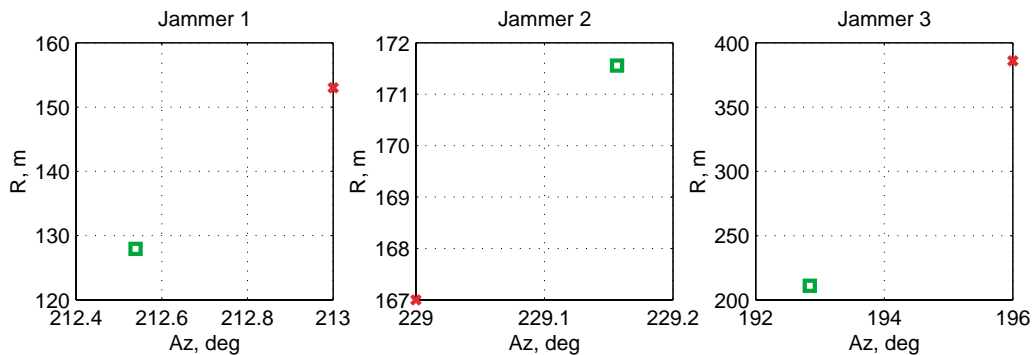


Figure 6.22: Uncalibrated Jammer Localization in Demonstration Mode During Second GIDL Experiment at lake Lagunita. Surveyed (red \times) and GIDL measured location (green \square) for each jammer.

in localizing a jammer. This conclusion applies even at ranges when the jammer is not affecting or not completely jamming the protected GPS receiver and with jamming power comparable to the noise floor. It takes only 55 seconds to detect and locate a jammer.

}

Chapter 7

GIDL Applications

The GIDL system is built as a four-channel software radio which operates in the GPS frequency band. What it does with received signals completely depends on the software loaded into it. In this work, jammer detection and localization algorithms along with software for this receiver were developed and tested. This receiver and developed software works as an interference detection and localization system. This system originally was intended for integration with LAAS as one of the subsystems, to protect airports from GPS interference. But this system has utility on its own and could be used for various other applications. Besides the entire system applying to various applications, the receiver itself proves to be a valuable research platform for a different set of applications.

7.1 Applications to LAAS

The GIDL system can be implemented in parallel with a three- or four-receiver LAAS ground facility (sharing some components with the LAAS reference receivers and processors) or as a separate installation to support nearby LAAS and WAAS sites. While LAAS would detect interference on its own, the GIDL would improve overall LAAS availability through timely detection and localization of a jammer source so that the interference is removed as quickly as possible.

7.2 Aircraft Application

It may be possible to use the GIDL on an airborne craft to find sources of interference to GPS. It could be used for flight inspection or for rapid jammer localization in the areas where a GIDL is not permanently installed. (This idea has been suggested by Professor D. Powell during a private conversation.) The GIDL could be installed on the bottom of an airplane forward and back of the fuselage and at the tips of the wings. It could then be used for flight inspection to find the location of any transmitters in the GPS band, particularly sources of interference and jammers.

Currently GIDL data processing is implemented as batch processing. It takes only about 14 ms to collect raw data from the GIDL receiver, and then about 1 minute to process this data by MATLAB software (this processing time could be improved see Section 8.2.6). For airborne jammer localization it also would be necessary to know attitude and location of the aircraft in the moment of data collection. So it is possible to rapidly collect number of data sets in the region of interest and then obtain jammer location in the postprocessing, or to implement number of processors that would process data sets in succession (for example if 10 processors would be utilized with no changes in the current software new data points would be obtained each 6 seconds).

For this application GIDL approach to the jammer localization could be combined with approach studied by Shau-Shiun Jan [104] by providing bearing and Doppler frequency of the jammer. Utilizing jammer range measurements provided by the GIDL could further enhance it.

Another application of GIDL to aviation is the installation of some version of the GIDL system at airports which do not have LAAS but are going to utilize WAAS for navigation and landing. The GIDL system should be inexpensive to install and maintain so that almost any general aviation airport should be able to afford it. Such an installation should increase the protection against interference at this airport. If all airports in the area had a GIDL system installed, then these systems could combine within the network, potentially protecting large regions from jamming or interference.

7.3 Other Applications

The GIDL could be used as an interference monitoring, detection and localization tool, whenever it is required. It could be installed on vehicles for use on demand whenever a GPS interference problem is suspected. In this mode of operation, only directional data could be used. By moving the vehicle, it would be possible to triangulate the source of interference.

Temporary interference problems have happened on various occasions. One example is the installation of a remote TV camera on the Durand building on the Stanford campus. For some reason, this camera was transmitting in the GPS frequency band and was interfering with several GPS antenna installations at Stanford. The GIDL was not available then and it took some time to locate this source of interference to GPS. Using the GIDL, it could have been done in a much shorter amount of time.

7.4 GIDL Hardware as a Flexible Research Platform

The GIDL receiver has found number of interesting applications in other research conducted in the LAAS and WAAS laboratories. Several people have already used it in their experiments.

7.4.1 Experiment on Aided GPS Signal Detection

The ability to detect and process weak Global Navigation Satellite System (GNSS) signals is extremely valuable, as the specified received power levels of such signals are already quite low. (The GPS-SPS signal specification indicates the signal power at the antenna will be -130 dBm.) Weak detection techniques would be of importance for a number of applications. To collect data and study these weak detection techniques, two channels of the GIDL receiver system were utilized. For a detailed description of this GIDL experiment, see [90].

7.4.2 SQM Application

A primary design goal for the use of the Local Area Augmentation System (LAAS) for aircraft precision approach and landing is to assure that failures occurring in the ground or space segments be eliminated by the ground system before differential corrections are broadcast to users. One means for checking the ground segment is to compare the measurements generated by redundant reference stations and to eliminate receivers whose measurements on one or more satellite channels exceed detection and isolation thresholds (so-called “ground screening”). Multiple receiver failures pose a problem for this type of monitor; thus additional checks on the reference receiver outputs and signal processing are needed to insure that such an event is extremely improbable. They must also protect against “common mode” failures originating in the space segment. These checks taken together comprise Signal Quality Monitoring (SQM), which occurs before measurements from redundant receivers are compared in the final stage of ground integrity testing. SQM activities occur primarily in parallel with reference receiver functioning and also exist within the ground software that collects and process the individual receiver inputs. To limit the scope of this thesis work, SQM is not considered in any detail (for reference on SQM for example see [23, 159, 160, 161]).

The GIDL receiver could be used as an extension of the SQM receiver. A GIDL receiver has four channels, and all of them could be utilized for signal quality monitoring. This could be useful, when not only satellite signals have to be monitored, but also pseudolite signals.

Another application related to SQM is collection of the raw data from one-time events for detailed post processing. One example of such an event is the end of life switch on PRN 19 back to its faulted section, which caused distortion of the GPS signal and errors in the performance of differential GPS. It has been proposed that to analyze the satellite fault mode which happened with PRN 19, the SV would be switched back to the faulty section before its decommissioning. This faulty GPS signal would then be available for a short time and would provide a valuable data set for detailed post processing. Another example of a one-time event application would be continuous raw data collection by the GIDL receiver with simultaneous “strange event” detection by a monitor algorithm in a regular receiver.

Data are only kept for times when such events occur, for example, the clock event detected by WAAS on 10 March 1998 on SV 27 [162].

7.4.3 Modifications for Multiple Frequencies

With slight modifications, the GIDL receiver could be used to collect GPS data on multiple frequencies. It is interesting to study multiple GPS frequencies for a number of reasons: ionospheric correction, the carrier cycle ambiguity resolution using multiple frequencies, etc. Attempts to collect such multifrequency data have been performed using one of the versions of the current GIDL receiver employing the “Stanford Dish” high-gain parabolic antenna. This experiment showed the utility of the GIDL receiver to collect multifrequency data and to capture clean GPS signals for later analysis. Detailed results of this experiment are presented in [163].

7.4.4 Experiments With New GPS Signals

The GIDL could easily be modified to collect and process new GPS signals such that performance testing could occur before specialized new receivers were built. This feature could also be used to study various pseudolite signals to test their performance characteristics and their level of interference on the GPS satellite signals.

}

Chapter 8

Conclusions and Future Work

A four-channel, common-clock software defined radio (SDR) which operates in the L1 GPS band has been developed. The primary intended use for this receiver is the Generalized Interference Detection and Localization (GIDL) System and development of new localization algorithms. GIDL signal processing algorithms which allow interference detection, TDOA estimation of weak unknown jamming signals, and their source localization have been developed and tested.

The GIDL receiver is a valuable development platform, first for interference detection and localization and also as a software radio. It can be used for weak GPS signal detection experiments, multi-frequency experiments (with slight modifications), and other current and future experiments.

Jammer localization and GIDL interface display software were developed and tested during field experiments and GIDL real-time demonstrations. Field tests of the GIDL demonstrated detection of weak signals as well as determining azimuth and range to their source in real time with experimental results matching the predicted performance. The GIDL demonstrated that it is capable of jammer localization in less than one minute with an azimuthal accuracy better than 0.30 degrees (Table 6.1) when the largest antenna baseline was 76 meters and distance to the jammer was 200 meters (antenna baseline was $0.38 \times$ the distance to the jammer).

The demonstrated GIDL system is compatible with the currently recommended LAAS

installation and can improve overall LAAS availability by detecting the presence of a jammer and finding the direction and/or location of detected interference sources.

8.1 Specific Contributions

The newly developed Generalized Interference Detection and Localization System provides the solutions to constantly monitor the GPS signal environment and detect interference as soon as it appears. When interference is detected, GIDL estimates the direction to the source of interference and its location. The developed GIDL hardware allows for the development and testing of numerous detection and localization algorithms spanning different numbers and types of sources. It performs the role of a flexible development platform as well as solution for the jammer threat.

The specific contributions of this research are the following:

1. Developed the first Time Difference of Arrival (TDOA) system to find the location of GPS jammers that is compatible with the currently recommended LAAS installation. The system experimentally demonstrated detection of weak interference signals, finding azimuth and range to their source in real time, and included localization of a moving jammer.
2. GIDL signal processing algorithms were developed to detect the presence of interference in the GPS band and to estimate the location of the jammer. These developed algorithms include algorithms to estimate and measure the Time Difference of Arrival (TDOA) for unknown weak signals (jamming signals), and algorithms to estimate range and direction to the the source of interference from measured TDOA.
3. Developed Software GPS Receiver algorithms to calibrate the GIDL system delays and clock offsets using the GPS satellite signals.
4. Designed, developed, and built flexible a research platform for the GIDL system development and digital signal processing of signals in the GPS frequency band. This

platform is a completely digital, common clock, four-channel digital signal processing receiver solution. A user friendly graphical interface to the GIDL programmed in MATLAB was also developed for easy user interaction.

8.2 Recommendations for Future Research

This research has demonstrated the feasibility of developing a system using stationary non-directional antennae and DSP-based signal processing capable of detecting and localizing sources of jamming and interference to GPS-based systems. However, it has hardly begun to explore the opportunities that this idea and hardware presents. This section discusses some recommendations for further research.

There are a number of things planned for the developed hardware which will improve system performance. These include: a short-baseline direction finder and antenna array; a distributed GIDL system; the verification of system performance on different types of interference sources and different configurations of antenna arrays; detection algorithms to estimate number of interferers; operational procedures for GIDL operation; integration of the GIDL subsystem with the Integrity Monitoring Testbed, and evaluation of overall system performance.

8.2.1 Short Baseline System to Mitigate CW Interference

One can move the GIDL antennae closer to each other to form a phased array antenna. This new configuration could, for example, solve cycle ambiguities which would arise when the basic GIDL is used to locate CW interference. (Current GIDL algorithms rely on correlating jamming signal received by antennae. Multiple correlation peaks of equal magnitude would exist in case of the CW jammer due to periodic nature of the signal. These multiple peaks would cause ambiguity in TDOA estimation.) This short-baseline system would be used in parallel with the existing GIDL system. Another application for short-baseline systems is a mobile direction-only finder installed, for example, on a car. Combined with a low-accuracy positioning system (not GPS based), the two could find the

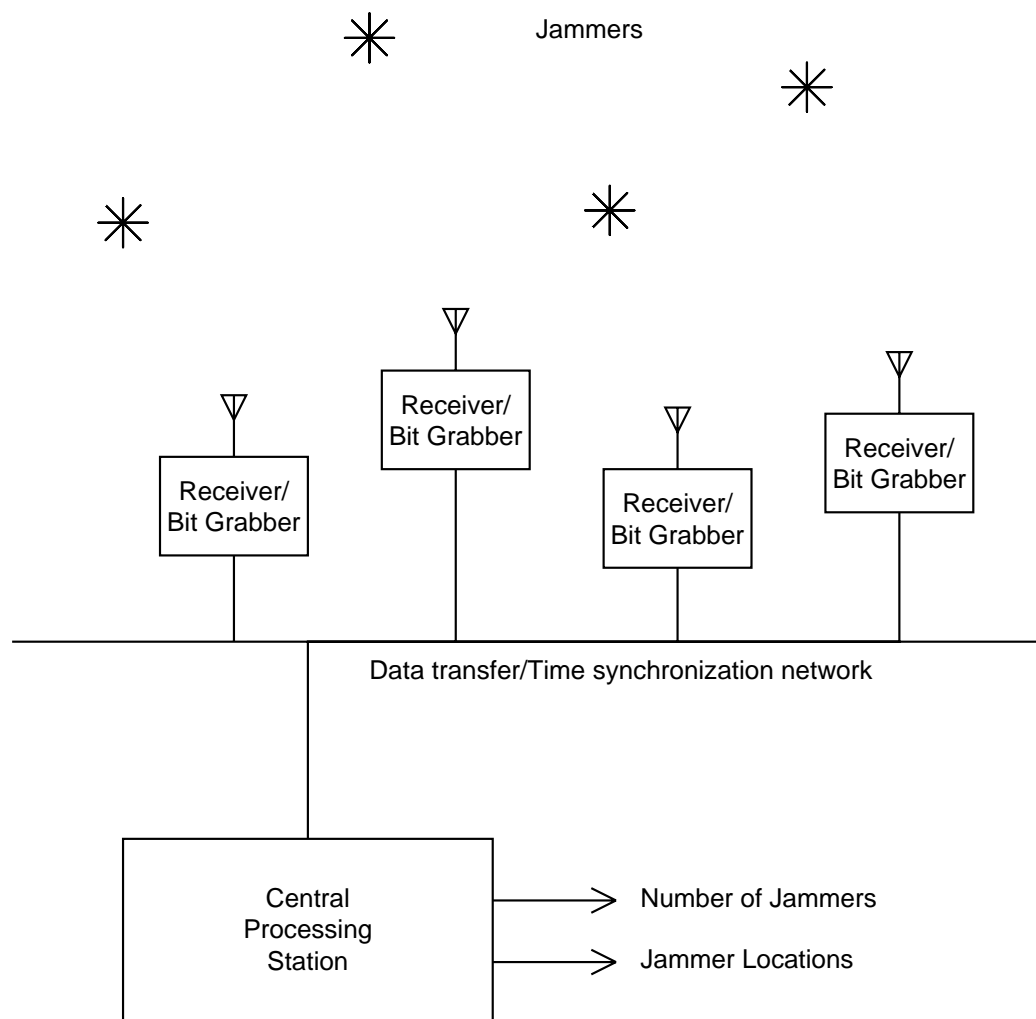


Figure 8.1: Distributed GIDL System

direction to a source of interference from multiple locations and subsequently determine its location.

8.2.2 Distributed GIDL System Concept

A distributed GIDL system could be formed by connecting and synchronizing simple receivers, or bit grabbers, in a network covering a large area (Figure 8.1). This is one of the possible extensions to the GIDL. In the current configuration, all hardware and software processing in the GIDL are colocated; thus the antenna configuration and coverage pattern

is limited by the length of the RF cables, which cannot exceed a few hundred meters. (Similar distributed jammer localization system based on the network of bearing sensors has been proposed and analyzed by Shau-Shiun Jan [104].)

In the proposed concept of the distributed GIDL system, one would put data transmission and time synchronization on a network, which would have a number of nodes — single channel GIDL receivers, or bit grabbers — which would collect data simultaneously and then send it to the main processing station, or even do some preliminary processing on each node.

This distributed GIDL system configuration has a number of advantages and differences compared to the original multichannel GIDL system:

- The distributed system would be a collection of independent receivers. Each receiver (bit grabber) is inexpensive and easy to build.
- The location of each receiver must be known for the network of such receivers to be able to provide good jammer localization performance.
- It could cover and protect large areas from the threat of jamming.
- Configuration of the distributed system by “bit grabber” placement could be tailored to the specific areas to be protected.
- This configuration is easy to extend if the need should arise to cover a larger area than originally intended. Extension would be relatively simple: only few new “bit grabbers” would have to be added to the network. This feature also allows for multistep deployment of the distributed GIDL, should it be necessary.
- The distributed GIDL would have improved jammer localization accuracy compared to basic GIDL because of its increased number and variety of vectors to the unknown jammer location.
- This system would degrade more gracefully compared to the basic GIDL. The system would not fail completely if one of the “bit grabbers” failed but would be able to operate in a reduced configuration and continue to provide useful data.

Along with these advantages come distinct problems which would have to be solved, namely how to synchronize all these receivers and how to transmit large amounts of generated data. A further issue arises as one designs computationally efficient algorithms to process all of the additional data.

8.2.3 Incorporation into Integrity Monitoring Testbed

The GIDL could be integrated with an Integrity Monitoring Testbed (IMT) to form another version of the prototype LAAS system for development and testing. One of the major concerns in the current LAAS configuration is what to do with interference. The GIDL helps to answer this question; thus an integration of the GIDL and LAAS is a reasonable (but not mandatory) step in LAAS development.

8.2.4 Test on Various Single Jammers

The system has been tested extensively on white-noise type jammers, but it has the capability to locate other types of jammers as well. More testing is required to determine the maximum capability of this system on non-white interference.

8.2.5 Test on Multiple Jammers

As in the previous subsection, the system has been mainly tested on the localization of one jammer when it is actually capable of locating multiple sources. More experiments and development are needed in this area.

8.2.6 Optimization of Algorithms

Most of the processing algorithms for this system have been written in MATLAB because it was a demonstration system. For a fully operational system, these algorithms should be rewritten in C or another efficient programming language to improve performance and streamline operation. For example, it takes about 55 seconds to collect and process one data set in demonstration mode. In that time, data is collected, stored to the hard drive, read into MATLAB, and then processed by GIDL algorithms implemented in MATLAB.

This process could be sped up significantly if intermediate writing onto the hard drive were avoided and/or if the processing algorithms were rewritten in something faster than MATLAB, for example C.

8.3 Summary

The goal of this research was to make interference detection and localization useful in the real world to protect GPS-based systems from interference and jamming. This goal has been accomplished through the development of the prototype GIDL system. The first practical GIDL system for this application has been developed and demonstrated. Design requirements and recommendations for the next generation of this system have been presented as a number of likely extensions to the technology. This technology is no longer a research topic; an accurate Generalized Interference Detection and Localization System is available for use and for further development.

}

Appendix A

Glossary

ADC Analog-to-Digital Converter

ADP Antenna Directivity Pattern

AGC Automatic Gain Control

AIAA American Institute of Aeronautics and Astronautics

AOA Angle of Arrival

ASIC Application-Specific Integrated Circuit

ATC Air Traffic Control

AWGN Additive White Gaussian Noise

bps bits per second

C/A-code Coarse/Acquisition code (1.023 MHz)

C/A Coarse/Acquisition

CDMA Code Division Multiple Access

CRB Cramer-Rao Lower Bound

CW Continuous Wave

dBW decibels relative to one Watt

dB decibels (logarithmic measurement of power or gain ratios)

dBm decibels relative to one milliwatt

DFT Discrete Fourier Transform

deg degree

DH Decision Height

DLL Delay Lock Loop

DoD Department of Defense

DSP Digital Signal Processing

ECM Electronic Countermeasures or Error Covariance Matrix

EMI Electromagnetic Interference

FAA Federal Aviation Administration

FCC Federal Communications Commission

FFT Fast Fourier Transform

FIM Fisher Information Matrix

GDOP Geometric Dilution of Precision

GHz Gigahertz (billions of cycles per second)

GIDL Generalized Interference Detection and Localization

GNSS Global Navigation Satellite System

GPS-PPS Global Positioning System — Precise Positioning Service

GPS-SPS Global Positioning System — Standard Positioning Service

GPS Global Positioning System

HDTV High Definition Television

HEPL W.W. Hansen Experimental Physics Laboratory, Stanford University

HMI Hazardously Misleading Information

ICAO International Civil Aviation Organization

ICD Interface Control Document

IDF Interference Direction Finder

IDFT Inverse Discrete Fourier Transform

IEEE Institute of Electrical and Electronics Engineers, Inc.

IF Intermediate Frequency

ILS Instrument Landing System

IMT Integrity Monitoring Testbed

ION Institute of Navigation

KREMS Kiernan Reentry Measurement Site

L-band all frequencies between 1 and 2 GHz

L1 first L-band GPS frequency: 1575.42 MHz (154×10.23 MHz)

LAAS Local Area Augmentation System

LF Likelihood Function or Likelihood Functional

LNA Low Noise Amplifier

LOS Line of Sight

LO Local Oscillator

LPF Low Pass Filter

m meters

Mbps megabits per second

MEDLL Multipath Estimating Delay Lock Loop

MHz megahertz (millions of cycles per second)

ML Maximum Likelihood

MMS Multistatic Measurement System

MSRS Multisite Radar System

MSS Mobile Satellite Systems

MUSIC Multiple Signal Classification

mW milliwatt

OCS Operational Control Segment

PAA Phased Antenna Array

PCI Peripheral Component Interconnect

PDF Probability Density Function

PLSS Precision Location/Strike System

PR Pseudorange

PRIME Polynomial Root Intersection for Multidimensional Estimation

PRN Pseudo-Random Noise (a digital code with noise-like properties)

PSD Power Spectral Density

RD Range Difference

RFI Radio Frequency Interference

RF Radio Frequency

r.m.s. root mean square

RVR Runway Visual Range

SDR Software Defined Radio

SNR Signal-to-Noise Ratio

SOP Surface of Position

SQM Signal Quality Monitoring

SRC Space Resolution Cell

SV Satellite (e.g., Space Vehicle)

TCXO Temperature Controlled Crystal Oscillator

TDOA Time Difference of Arrival

TOA Time of Arrival

UHF Ultra High Frequency (all frequencies between 300 MHz and 3 GHz)

USAF United States Air Force

VPL Vertical Protection Limit

WAAS Wide Area Augmentation System

}

Bibliography

- [1] T. Corrigan, J. Hartranft, L. Levy, K. Parker, J. Pritchett, A. Pue, S. Pullen, and T. Thompson, *GPS Risk Assessments Study Final Report*. John Hopkins University, 1999.
- [2] B. W. Parkinson and J. J. Spilker, Jr, eds., *Global Positioning System: Theory and Applications I*, vol. 163 of *Progress in Aeronautics and Astronautics*. AIAA, 1996.
- [3] B. W. Parkinson and J. J. Spilker, Jr, eds., *Global Positioning System: Theory and Applications II*, vol. 164 of *Progress in Aeronautics and Astronautics*. AIAA, 1996.
- [4] *Global Positioning System*, vol. 1. Washington, DC: Institute of Navigation, 1980.
- [5] *Global Positioning System*, vol. 2. Washington, DC: Institute of Navigation, 1984.
- [6] *Global Positioning System*, vol. 3. Washington, DC: Institute of Navigation, 1986.
- [7] *Global Positioning System*, vol. 4. Washington, DC: Institute of Navigation, 1994.
- [8] ARINC Research Corporation, *ICD-200 NAVSTAR GPS User Interfaces*, July 1993. Rev B-PR-002.
- [9] Federal Aviation Administration, Washington, DC, *Advisory Circular 120-28C: Criteria for Approval of Category III Landing weather Minima*, Mar. 1984.
- [10] J. M. Davis and R. J. Kelly, “RNP Tunnel Concept for Precision Approach with GNSS Application,” in *ION 49th Annual Meeting*, (Cambridge, Massachusetts), Institute of Navigation, June 1993.

- [11] Federal Aviation Administration, Satellite Navigation Program Office, *Operational Requirements Document: Local Area Augmentation System*, February 28 1995.
- [12] International Civil Aviation Organization (ICAO), *International Standards, Recommended Practices and Procedures for Air Navigation Services—Annex 10*, Apr. 1985.
- [13] D. Girts, “Presentation to Boeing GPS Landing System (GLS) Requirements Group.” Honeywell Corporation, February 14 1995.
- [14] J. P. Fernow, “FAA SOIT Consensus on Requirements for the Local Area Augmentation System (LAAS) ORD.” Presented to RTCA Special Committee 159 Working Group 4, April 19 1995. Washington DC.
- [15] RTCA, *Minimum Operations Performance Standards (MOPS) for LAAS (DO-253)*, Jan. 2000.
- [16] J. J. Spilker, Jr, “GPS Signal Structure and Characteristics,” in *Global Positioning System I*, vol. 1, Washington, DC: Institute of Navigation, 1980.
- [17] A. Pinker, D. Walker, and C. Smith, “Jamming the GPS Signal,” in *ION 55th Annual Meeting*, (Cambridge, Massachusetts), Institute of Navigation, June 1999.
- [18] R. S. Littlepage, “The Impact of Interference on Civil GPS,” in *ION 55th Annual Meeting*, (Cambridge, Massachusetts), Institute of Navigation, June 1999.
- [19] G. Colby, M. Smith, F. Ventrone, and J. Linehan, “GPS Anomaly Investigation Report.” First Interim Report, U.S. Naval Air Warfare Center and DoD Joint Spectrum Center, July 1996.
- [20] R. Swider, *Recommended LAAS Architecture*. Federal Aviation Administration, Anaheim, California, November 12 1996. Presented to RTCA SC-159 WG-4.
- [21] RTCA, *Minimum Aviation System Performance Standards for the Local Area Augmentation System (RTCA DO-245)*, September 28 1998. Washington, D.C.

- [22] T. Upadhyay, D. G., F. W., and D. Weed, "Test Results on Mitigation of SATCOM-Induced Interference to GPS Operation," in *Proceedings of the ION Global Positioning System GPS-95 Conference*, (Palm Springs, California), Institute of Navigation, Sept. 1995.
- [23] A. Ndili, *Robust GPS Autonomous Signal Quality Monitoring*. PhD thesis, Department of Mechanical Engineering, Stanford University, August 1998.
- [24] J. I. Glaser, "Fifty Years of Bistatic and Multistatic Radar," *IEE Proceedings*, vol. 133, no. 7, pp. 596–603, 1986.
- [25] N. J. Willis, *Bistatic Radar*. Norwood, Massachusetts: Artech House, 1991.
- [26] J. W. Caspers, "Bistatic and Multistatic Radar," in *Radar Handbook* (M. I. Skolnik, ed.), McGraw-Hill, 1970.
- [27] B. Gumble, "Air Force Upgrading Defenses at NORAD," *Defense Electronics*, vol. 17, pp. 86–100, 1985.
- [28] "Lockheed Wins Air Force Approval to Build Precision Location and Strike System," *Microwaves*, vol. 16, no. 11, p. 14, 1977.
- [29] R. Hartman, "Budget Cuts Miss Most Electronic Programs," *Defense Electronics*, vol. 14, no. 10, pp. 125–127, 1982.
- [30] "Lockheed Prepared for TP-I Production," *Aviation Week and Space Technology*, vol. 110, no. 26, p. 60, 1979.
- [31] W. J. Bangs and P. M. Schultheiss, "Space-Time Signal Processing for Optimal Parameter Estimation," in *Signal Processing* (J. W. R. Griffiths, P. L. Stocklin, and C. van Schooneveld, eds.), New York: Academic Press, 1973. pp. 577–590.
- [32] G. C. Carter, "Variance Bounds for Passively Locating an Acoustic Source with a Symmetric Line Array," *J. Acoust. Soc. Am.*, vol. 62, pp. 922–926, Oct. 1977.
- [33] N. L. Owsley and G. Swope, "Time Delay Estimation in a Sensor Array," *IEEE Trans. Acoust., Speech, Sig. Proc.*, vol. ASSP-29, June 1979.

- [34] A. V. Dubrovin and Y. G. Sosulin, "One-Stage Estimation of the Location of a Radio Source by a Passive System," *Journal of Communication Technology and Electronics*, vol. 43, no. 12, pp. 1388–1396, 1998.
- [35] M. Wax and T. Kailath, "Optimum Localization of Multiple Sources in Passive Arrays," *IEEE Trans. Acoust., Speech, Sig. Proc.*, vol. ASSP-31, Oct. 1983.
- [36] A. Farina and E. Hanle, "Position Accuracy in Netted Monostatic and Bistatic Radar," *IEEE Transactions on Aerospace and Electronic Systems*, vol. 19, July 1983.
- [37] W. R. Hahn, "Optimum Signal Processing for Passive Sonar Range and Bearing Estimation," *J. Acoust. Soc. Am.*, vol. 58, pp. 201–207, July 1975.
- [38] E. Weinstein, "Optimal Source Localization and Tracking from Passive Array Measurements," *IEEE Trans. Acoust., Speech, Sig. Proc.*, vol. ASSP-30, Feb. 1982.
- [39] L. C. Ng and Y. Bar-Shalom, "Multisensor Multitarget Time Delay Vector Estimation," *IEEE Trans. Acoust., Speech, Sig. Proc.*, vol. ASSP-34, Aug. 1986.
- [40] J. D. Brad, "Time Difference of Arrival Dilution of Precision and Applications," *IEEE Transactions on Sig. Proc.*, vol. 47, Feb. 1999.
- [41] Y. T. Chan, "A Simple and Efficient Estimator for Hyperbolic Localization," *IEEE Transactions on Sig. Proc.*, vol. 42, Aug. 1994.
- [42] W. R. Hahn and S. A. Tretter, "Optimum Processing for Delay-Vector Estimation in Passive Signal Arrays," *IEEE Trans. Inform. Theory*, vol. IT-19, pp. 608–614, Sept. 1973.
- [43] W. R. Hahn, "Optimum Signal Processing for Passive Sonar Range and Bearing Estimation," *J. Acoust. Soc. Am.*, vol. 58, pp. 201–207, July 1975.
- [44] L. C. Ng and Y. Bar-Shalom, "Multisensor Multitarget Time Delay Vector Estimation," *IEEE Trans. Acoust., Speech, Sig. Proc.*, vol. ASSP-34, August 1986.
- [45] E. L. Lehmann, *Theory of Point Estimation*. New York, New York: John Wiley and Sons, 1983.

- [46] S.-K. Chow and P. M. Schultheiss, "Delay Estimation Using Narrow-Band Processes," *IEEE Trans. Acoust., Speech, Sig. Proc.*, vol. ASSP-29, June 1981.
- [47] J. P. Ianniello, "Large and Small Error Performance Limits for Multipath Time Delay Estimation," *IEEE Trans. Acoust., Speech, Sig. Proc.*, vol. ASSP-34, Apr. 1986.
- [48] A. Weiss and E. Weinstein, "Fundamental Limitations in Passive Time Delay Estimation-Part 1: Narrow-Band Systems," *IEEE Trans. Acoust., Speech, Sig. Proc.*, vol. ASSP-31, pp. 472–485, 1983.
- [49] J. P. Ianniello, "Comparison of the Ziv-Zakai Lower Bound on Time Delay Estimation with Correlator Performance," in *IEEE Int. Conf. Acoust. Speech, Sig. Proc.*, (Boston, Massachusetts), 1983.
- [50] S. Bellini and G. Tartara, "Bounds on Error in Signal Parameter Estimation," *IEEE Trans. Comm.*, vol. COM-22, pp. 340–342, Mar. 1974.
- [51] D. Chazan, M. Zakai, and J. Ziv, "Improved Lower Bounds on Signal Parameter Estimation," *IEEE Trans. Inform. Theory*, vol. IT-21, pp. 90–92, Jan. 1975.
- [52] J. Ziv and M. Zakai, "Some Lower Bounds on Signal Parameter Estimation," *IEEE Trans. Inform. Theory*, vol. IT-15, pp. 386–391, May 1969.
- [53] B. P. Bogert, M. J. R. Healy, and J. W. Tukey, "The Quefrency Analysis of Time Series for Echoes: Cepstrum, Pseudo-Autocovariance, Cross-Cepstrum and Saper Cracking," in *Symp. Time Series Analysis* (M. Rosenblatt, ed.), 1963.
- [54] B. P. Bogert and J. F. Ossanna, "The Heuristics of Cepstrum Analysis of a Stationary Complex Echoed Gaussian Signal in Stationary Gaussian Noise," *IEEE Trans. Inform. Theory*, vol. IT-12, pp. 373–380, July 1966.
- [55] J. C. Hassab, "Time Delay Processing Near the Ocean Surface," *J. Acoust. Soc. Am.*, vol. 35, no. 4, pp. 489–501, 1974.
- [56] J. C. Hassab and R. Boucher, "A Probabilistic Analysis of Time Delay Extraction by the Cepstrum in Stationary Gaussian Noise," *IEEE Trans. Inform. Theory*, vol. IT-22, pp. 444–454, July 1976.

- [57] J. P. Lanniello, "High Resolution Multipath Time Delay Estimation for Broadband Random Signals," in *IEEE Int. Conf. Acoust. Speech, Sig. Proc.*, pp. 12.4.1–12.4.4, Apr. 1987.
- [58] R. C. Kemerait and D. G. Childers, "Signal Detection and Extraction by Cepstrum Techniques," *IEEE Trans. Inform. Theory*, vol. IT-18, Nov. 1972.
- [59] H. Zi-qiang and W. Zhen-dong, "A Method for High Resolution Multipath Estimation of Time Delay," in *IEEE Int. Conf. Acoust. Speech, Sig. Proc.*, (Paris, France), Apr. 1982.
- [60] T. J. Abatzoglou, "A Fast Local Maximum Likelihood Estimator for Time Delay Estimation," *IEEE Trans. Acoust., Speech, Sig. Proc.*, vol. ASSP-34, Apr. 1986.
- [61] G. C. Carter, "Coherence and Time Delay Estimation," *Proc. IEEE*, vol. 75, pp. 236–255, Feb. 1987.
- [62] J. C. Hassab and R. Boucher, "Optimum Estimation of Time Delay by a Generalized Correlator," *IEEE Trans. Acoust., Speech, Sig. Proc.*, vol. ASSP-27, Aug. 1979.
- [63] S. Holm and G. Ottesen, "Bias in the Cross Spectrum and Time Delay Estimates Due to Misalignment," *IEEE Trans. Acoust., Speech, Sig. Proc.*, vol. ASSP-34, Dec. 1986.
- [64] C. H. Knapp and G. C. Carter, "The Generalized Correlation Method for Estimation of Time Delay," *IEEE Trans. Acoust., Speech, Sig. Proc.*, vol. ASSP-23, Aug. 1976.
- [65] M. Wax, "The Estimate of Time Delay Between Two Signals with Random Relative Phase Shift," *IEEE Trans. Acoust., Speech, Sig. Proc.*, vol. ASSP-29, June 1981.
- [66] D. M. Etter and S. D. Sterns, "Adaptive Estimation of Time Delay in Sampled Data Systems," *IEEE Trans. Acoust., Speech, Sig. Proc.*, vol. ASSP-29, June 1981.
- [67] P. L. Feintuch, N. J. Bershad, and F. A., "Reed Time Delay Estimation Using the LMS Filter—Static Behavior," *IEEE Trans. Acoust., Speech, Sig. Proc.*, vol. ASSP-29, June 1981.

- [68] P. L. Feintuch, N. J. Bershad, and F. A. Reed, "Time Delay Estimation Using the LMS Filter—Dynamic Behavior," *IEEE Trans. Acoust., Speech, Sig. Proc.*, vol. ASSP-29, June 1981.
- [69] B. Friedlander and J. O. Smith, "Multipath Delay Estimation." SCT Technical Memo 5466-04, Systems Control Technology, Inc., Palo Alto, California, Dec. 1983.
- [70] H. Messer and Y. Bar-Ness, "Closed-Loop Least Mean Square Time-Delay Estimator," *IEEE Trans. Acoust., Speech, Sig. Proc.*, vol. ASSP-35, Apr. 1987.
- [71] J. O. Smith and B. Friedlander, "Adaptive Interpolated Time-Delay Estimation," *IEEE Trans. Aerosp. Electro. Syst.*, vol. AES-21, pp. 180–199, March 1985.
- [72] J. O. Smith and B. Friedlander, "Adaptive Multipath Delay Estimation," *IEEE Trans. Acoust., Speech, Sig. Proc.*, vol. ASSP-33, Aug. 1985.
- [73] B. Friedlander, "On the Cramer-Rao Bound for Time Delay and Doppler Estimation," *IEEE Trans. Inform. Theory*, vol. IT-30, pp. 575–580, May 1984.
- [74] E. Weinstein, "Optimal Source Localization and Tracking from Passive Array Measurements," *IEEE Trans. Acoust., Speech, Sig. Proc.*, vol. ASSP-30, Feb. 1982.
- [75] G. C. Carter, "Sonar Signal Processing for Source State Estimation," in *IEEE Int. Conf. Acoust. Speech, Sig. Proc.*, pp. 386–395, 1979.
- [76] P. M. Schultheiss, "Locating a Passive Source with Array Measurements: A Summary of Results," in *IEEE Int. Conf. Acoust. Speech, Sig. Proc.*, 1979.
- [77] P. M. Schultheiss and E. Weinstein, "Lower Bounds on the Localization Errors of a Moving Source Observed by a Passive Array," *IEEE Trans. Acoust., Speech, Sig. Proc.*, vol. ASSP-29, June 1981.
- [78] K. B. Theriault and R. M. Zeskind, "Inherent Bias in Wavefront Curvature Ranging," *IEEE Trans. Acoust., Speech, Sig. Proc.*, vol. ASSP-29, June 1981.

- [79] R. M. Zeskind, K. B. Theriault, and P. Moss, "Accuracy of Linearized Performance Predictions for Wavefront Curvature Ranging Systems," in *IEEE Int. Conf. Acoust. Speech, Sig. Proc.*, (Boston, Massachusetts), pp. 879–882, 1983.
- [80] L. C. Ng, *Optimum Multisensor, Multitarget Localization and Tracking*. PhD thesis, Univ. Conn. Storrs, 1983.
- [81] B. Porat and B. Friedlander, "Estimation of Spatial and Spectral Parameters of Multiple Sources," *IEEE Trans. Inform. Theory*, vol. IT-29, pp. 412–425, May 1983.
- [82] A. Nehorai, G. Su, and M. Morf, "Estimation of Time Differences of Arrival by Pole Decomposition," *IEEE Trans. Acoust., Speech, Sig. Proc.*, vol. ASSP-31, Dec. 1983.
- [83] R. O. Schmidt, "Multiple Emitter Location and Signal Parameter Estimation," in *RADC Spectrum Estimation Workshop*, pp. 243–258, 1979.
- [84] R. Roy, A. Paulraj, and T. Kailath, "Comparative Performance of ESPRIT and MUSIC for Direction-of-Arrival Estimation." Submitted IEEE ASSP, 1987.
- [85] J. P. V. Etten, "Navigation Systems: Fundamentals of Low and Very Low Frequency Hyperbolic Techniques," *Electrical Commun.*, vol. 45, no. 3, pp. 192–212, 1970.
- [86] B. Forssell, *Radionavigation Systems*. Englewood Cliffs, New Jersey: Prentice-Hall, June 1991.
- [87] P. M. Janiczek, ed., *Global Positioning System*. Washington, DC: The Institute of Navigation, 1980.
- [88] A. Ndili and P. Enge, "Receiver Autonomous Interference Detection," in *Institute of Navigation Annual Meeting*, (Santa Monica, California), Institute of Navigation, Jan. 1997.
- [89] D. M. Akos, *A Software Radio Approach To Global Navigation Satellite System Receiver Design*. PhD thesis, Department of Electrical Engineering, Ohio University, August, 1997.

- [90] D. M. Akos, P.-L. Normark, J.-T. Lee, K. G. Gromov, J. B. Y. Tsui, and J. Schamus, "Low Power Global Navigation Satellite System (GNSS) Signal Detection And Processing," in *Proceedings of the ION Global Positioning System GPS-2000 Conference*, (Salt Lake City, Utah), Institute of Navigation, Sept. 2000.
- [91] M. S. Braasch, D. M. Akos, J. Caschera, M. H. Stockmaster, and J. B. Y. Tsui, "Test Results From A Direct L-Band Digitizing GPS/Glonass Receiver," in *Institute of Navigation Annual Meeting*, (Santa Monica, California), Institute of Navigation, Jan. 1997.
- [92] D. M. Akos and M. S. Braasch, "A Software Radio Approach to Global Navigation Satellite System Receiver Design," in *Institute of Navigation Annual Meeting*, (Cambridge, Massachusetts), Institute of Navigation, June 1996.
- [93] D. M. Akos and M. H. Stockmaster, "Direct Sampling of Three or More Frequency Separated Bandpass Signals at RF with a Minimum Sampling Rate." Wright Laboratories, Wright-Patterson AFB, Patent Pending.
- [94] A. Brown and B. Wolt, "Digital L-Band Receiver Architecture with Direct RF Sampling," in *IEEE 1994 Position Location and Navigation Symposium*, (Las Vegas, Nevada), April 11-15 1994.
- [95] D. M. Akos and J. B. Y. Tsui, "Design and Implementation of a Direct Digitization GPS Receiver Front End," *IEEE Transactions on Microwave Theory and Techniques*, Dec. 1996.
- [96] J. B. Y. Tsui, *Digital Techniques for Wideband Receivers*. Artech House, 1995.
- [97] J. Mitola, "The Software Radio Architecture," *IEEE Communications Magazine*, vol. 33, pp. 26-38, May 1995.
- [98] S.-C. Leung, R. DiEsposti, C. Giron, and I. Weiss, "Analysis of Algorithms for GPS Interferer Direction Finding," in *Proceedings of the ION Global Positioning System GPS-97 Conference*, (Kansas City, Missouri), Institute of Navigation, Sept. 1997.

- [99] E. M. Geyer, B. M. Winer, and R. Frazier, "Airborne GPS RFI Localization Algorithms," in *Proceedings of the ION Global Positioning System GPS-97 Conference*, (Kansas City, Missouri), Institute of Navigation, Sept. 1997.
- [100] D.-J. Moelker, "Multiple Antennas for Advanced GNSS Multipath Mitigation and Multipath Direction Finding," in *Proceedings of the ION Global Positioning System GPS-97 Conference*, (Kansas City, Missouri), Institute of Navigation, Sept. 1997.
- [101] J. Blas, R. Blazquez, and J. Alonso, "A Low Cost Adaptive Antenna Array," in *Proceedings of the ION National Technical Meeting NTM-99*, (San Diego, California), Institute of Navigation, Jan. 1999.
- [102] A. Brown, D. Reynolds, D. Roberts, and S. Serie, "Jammer and Interference Location System – Design and Initial Test Results,," in *Proceedings of the ION Global Positioning System GPS-99 Conference*, (Nashville, Tennessee), Institute of Navigation, Sept. 1999.
- [103] J. E. Wohlfel and B. Tanju, "Location of GPS Interferers," in *Proceedings of the ION Global Positioning System GPS-99 Conference*, (Nashville, Tennessee), Institute of Navigation, Sept. 1999.
- [104] S.-S. Jan and P. Enge, "Finding Source of Electromagnetic Interference (EMI) to GPS Using a Network Sensors," in *Proceedings of the ION National Technical Meeting NTM-2000*, (Long Beach, California), Institute of Navigation, Jan. 2001.
- [105] V. S. Chernyak, "Optimal Signal Detection in Systems with Spatially Separated Receivers," *Voprosi Radioelektroniki, Seriya Obshchetechnicheskaya*, no. No. 11, pp. 17–28, 1970. (in Russian).
- [106] V. S. Chernyak, "Synthesis of Optimum Signal Temporal Parameter Estimators for a System with Spatially Separated Receivers," in *Proceedings 4th Conference on Information Transmission and Coding Theory*, (Moscow-Tashkent), 1969. Section 2, pp. 221–225, (in Russian).

- [107] V. S. Chernyak, "About the Use of the Fisher Information Matrix for Maximum Attainable Accuracy Analysis of Maximum Likelihood Estimates in the Presence of Stray Parameters," *Radiotekhnika i Elektronika*, vol. 16, no. 6, pp. 956–966, 1971. (in Russian).
- [108] V. S. Chernyak, L. P. Zaslavsky, and L. V. Osipov, "Multistatic Radars and Systems (Review)," *Zarubezhnaya Radioelektronika*, no. 1, pp. 9–69, 1987.
- [109] V. S. Chernyak, *Multistatic Radars and Multiradar Systems*. Moscow: Radio i Svyaz, 1993. (in Russian).
- [110] V. S. Chernyak, *Fundamentals of Multisite Radar Systems: Multistatic Radars and Multiradar Systems*. G & B Science Pub, July 1998.
- [111] R. A. Monzingo and T. W. Miller, *Introduction to Adaptive Arrays*. New York, New York: John Wiley and Sons, 1980.
- [112] I. Y. Kremer *et al.*, *Space-Time Signal Processing*. Moscow: Radio i Svyaz, 1984. (in Russian).
- [113] S. E. Fal'kovich and E. N. Khomyakov, *Statistical Theory of Measurement Radiosystems*. Moscow: Radio i Svyaz, 1981. (in Russian).
- [114] Y. D. Shirman and V. N. Manzhos, *Theory and Techniques of Radar Information Processing in a Background of Interferences*. Moscow: Radio i Svyaz, 1981. (in Russian).
- [115] R. S. Berkowitz, ed., *Modern Radar*. New York, New York: John Wiley and Sons, 1965.
- [116] Y. D. Shirman *et al.*, *Theoretical Foundations of Radar*. Moscow: Soviet Radio, 1970. (in Russian).
- [117] A. A. Korostelev *et al.*, *Theoretical Foundations of Radar*. Moscow: Soviet Radio, 1970. (in Russian).
- [118] C. W. Helstrom, *Statistical Theory of Signal Detection*. Pergamon Press, 1960.

- [119] B. R. Levin, *Theoretical Foundations of Statistical Radioengineering*, vol. Part 1. Moscow: Soviet Radio, 1966. (in Russian).
- [120] V. G. Repin and G. P. Tartakovsky, *Statistical Synthesis Under Condition of a priori Uncertainty and Adaptation of Information Systems*. Moscow: Soviet Radio, 1977. (in Russian).
- [121] H. L. Van Trees, *Detection, Estimation and Modulation Theory*, vol. Part 1. New York, New York: John Wiley and Sons, 1969.
- [122] N. A. White, P. S. Maybeck, and S. L. DeVilbiss, "MMAE Detection of Interference/Jamming and Spoofing in a DGPS-Aided Inertial System," in *Proceedings of the ION Global Positioning System GPS-98 Conference*, (Nashville, Tennessee), Institute of Navigation, Sept. 1998.
- [123] K. W. Shallberg and D. T. Cox, "Interference Monitoring at WAAS Reference Stations," in *Proceedings of the ION Global Positioning System GPS-98 Conference*, (Nashville, Tennessee), Institute of Navigation, Sept. 1998.
- [124] D. K. Faddeev and V. N. Faddeeva, *Calculation Methods of the Linear Algebra*. Moscow: Fizmatgiz, 1960. (in Russian).
- [125] V. I. Tikhonov, *Statistical Radioengineering*. Moscow: Radio i Svyaz, 2nd edition ed., 1982. (in Russian).
- [126] V. V. Karavaev and V. V. Sazonov, *Statistical Theory of Passive Location*. Moscow: Radio i Svyaz, 1987. (in Russian).
- [127] V. C. Kondratyev, A. F. Kotov, and L. N. Markov, *Multistatic Radio Systems*. Moscow: Radio i Svyaz, 1986. (in Russian).
- [128] Y. T. Chan and K. C. Ho, "A Simple and Efficient Estimator for Hyperbolic Location," *IEEE Trans. on Signal Processing*, vol. SP-42, no. 8, pp. 1905–1915, 1994.
- [129] W. R. Hahn, "Optimum Signal Processing for Passive Sonar Range and Bearing Estimation," *J. Acoust. Soc. Ani*, vol. 58, no. 1, pp. 201–207, 1975.

- [130] H. Cramer, *Mathematical Methods of Statistics*. Princeton University Press, 1946.
- [131] S. E. Fal'kovich, *Signal Parameter Estimation*. Moscow: Soviet Radio, 1970. (in Russian).
- [132] S. Z. Kuzmin, *Design Fundamentals of Radar Information Digital Processing*. Moscow: Radio i Svyaz, 1986. (in Russian).
- [133] M. R. Buchner, "A Multistatic Track Filter With Optimal Measurement Selection," in *International Radar Conference, "Radar '77"*, (London, UK), pp. 72–75, 1977.
- [134] D. Willner, C. B. Chang, and K. P. Dunn, "Kalman Filter Algorithms for a Multi-sensor System," in *15th IEEE Conf. on Decision and Control*, (Clearwater, Florida), 1976.
- [135] D. J. Torrieri, "Statistical Theory of Passive Location Systems," *IEEE Trans. on Aerospace and Electronic Systems*, vol. AES-20, no. 2, pp. 183–198, 1984.
- [136] V. I. Pagurova, *Tables of Incomplete Gamma-Function*. Computer Centre of the Academy of Science USSR, 1963. (in Russian).
- [137] B. D. Sivazlian and R. E. Green, "Effect of Instrument Siting and Coordinate Selection on GDOP in Target Tracking," in *IEEE Nat. Aerospace and Electron. Conf.*, (Dayton, Ohio), pp. 142–147, NAECON, 1976.
- [138] H. B. Lee, "Accuracy Limitations of Hyperbolic Multilateration Systems," *IEEE Trans. on Aerospace and Electronic Systems*, vol. AES-11, no. 1, pp. 16–29, 1975.
- [139] C. Yin, S. Xu, and D. Wang, "Location Accuracy of Multistatic Radars (TR_n) Based on Ranging Information," in *CIE Int. Conf. of Radar*, (China, Beijing), pp. 34–38, ICR, 1996.
- [140] W. H. Foy, "Position-Location Solutions by Taylor Series Estimation," *IEEE Transactions on Aerospace and Electronic Systems*, vol. AES-12, no. 2, pp. 187–193, 1976.

- [141] H. L. Groginsky, "Position Estimation Using Only Multiple Simultaneous Range Measurements," *IRE Trans. on Aeronautical and Navigational Electronics*, vol. ANE-6, no. 5, pp. 178–187, 1959.
- [142] M. Wax, "Position Location from Sensors with Position Uncertainty," *IEEE Trans. on Aerospace and Electronic Systems*, vol. AES-19, no. 5, pp. 658–662, 1983.
- [143] M. P. Dana, *Registration: a Prerequisite for Multiple Sensor Tracking, in Multitarget-Mullisensor Tracking: Advanced Applications*, vol. 1. Norwood, Massachusetts: Artech House, 1990.
- [144] J. A. Wepman, "Analog-to-Digital Converters and Their Application in Radio Receivers," *IEEE Communications Magazine*, vol. 33, pp. 39–45, May 1995.
- [145] R. Vaughan, N. Scott, and D. White, "The Theory of Bandpass Sampling," *IEEE Trans. on Signal Processing*, vol. 39, pp. 1973–1984, Sept. 1991.
- [146] G. Hill, "The Benefits of Undersampling," *Electronic Design*, pp. 69–70, July 11 1994.
- [147] T. Lewis, "The Nethead Gang," *IEEE Computer*, vol. 28, pp. 8–10, Dec. 1995.
- [148] D. L. Sharpin and J. B. Y. Tsui, "Analysis of the Linear Amplifier/Analog-Digital Converter Interface in a Digital Microwave Receiver," *IEEE Trans. Aerospace and Electronic Systems*, vol. 31, pp. 248–256, Jan. 1995.
- [149] P. Vizmuller, *RF Design Guide—Systems, Circuits, and Equations*. Artech House, 1995.
- [150] RTCA, *Minimum Aviation System Performance Standards (MASPS) for LAAS (DO-245)*, Sept. 1998.
- [151] D. V. Sarwate and M. B. Pursley, "Crosscorrelation Properties of Pseudorandom and Related Sequences," in *Proceeding of the IEEE*, May 1980.
- [152] W. Zhuang, *Composite GPS Receiver Modeling, Simulations and Applications*. PhD thesis, University of New Brunswick, October 1992.

- [153] S. S. Rappaport and D. M. Grieco, "Spread-Spectrum Signal Acquisition: Methods and Technology," *IEEE Communications Magazine*, vol. 22, pp. 6–21, June 1984.
- [154] V. M. Jovanovic, "Analysis of Strategies for Serial-Search Spread-Spectrum Code Acquisition—Direct Approach," *IEEE Transactions on Communications*, vol. COM-36, pp. 1208–1220, Nov. 1988.
- [155] C.-L. Soong, "Fast Time-Domain-Based GPS Acquisition," Master's thesis, Department of Electrical Engineering, Ohio University, June 1996.
- [156] A. V. Oppenheim and R. Schaffer, *Discrete-Time Signal Processing*. Englewood Cliffs, New Jersey: Prentice-Hall, 1989.
- [157] B. Brannon, "Basics of Designing a Digital Radio Receiver (Radio 101)." Analog Devices Inc., CD-ROM, Advanced Signal Processing for Wireless, Spring 2001.
- [158] K. Gromov, D. M. Akos, S. Pullen, P. Enge, B. Parkinson, and B. Pervan, "Interference Direction Finding for Aviation Applications of GPS," in *Proceedings of the ION Global Positioning System GPS-99 Conference*, (Nashville, Tennessee), Institute of Navigation, Sept. 1999.
- [159] A. M. Mitelman, R. E. Phelts, D. M. Akos, S. P. Pullen, and P. K. Enge, "A Real-Time Signal Quality Monitor for GPS Augmentation Systems," in *Proceedings of the ION Global Positioning System GPS-2000 Conference*, (Salt Lake City, Utah), Institute of Navigation, Sept. 2000.
- [160] R. E. Phelts, D. M. Akos, and P. Enge, "Robust Signal Quality Monitoring and Detection of Evil Waveforms," in *Proceedings of the ION Global Positioning System GPS-2000 Conference*, (Salt Lake City, Utah), Institute of Navigation, Sept. 2000.
- [161] C. Macabiau and E. Chatre, "Signal Quality Monitoring for Protection of GBAS Users Against Evil Waveforms," in *Proceedings of the ION Global Positioning System GPS-2000 Conference*, (Salt Lake City, Utah), Institute of Navigation, Sept. 2000.

- [162] H. S. Cobb, D. G. Lawrence, J. R. Christie, T. F. Walter, Y. Chao, J. D. Powell, and B. W. Parkinson, "Observed GPS Signal Continuity Interruptions," in *Proceedings of the ION Global Positioning System GPS-95 Conference*, (Palm Springs, California), Institute of Navigation, Sept. 1995.
- [163] D. M. Akos, K. Gromov, T. Walter, and P. Enge, "A Prototype 3-Frequency SBAS Receiver and Test Results," in *ION 57th Annual Meeting*, (Albuquerque, New Mexico), Institute of Navigation, June 2001.